Università degli Studi di Ferrara

DOTTORATO DI RICERCA IN
"SCIENZE DELL'INGEGNERIA"

CICLO XXV

COORDINATORE Prof. Stefano Trillo

Nonlinear analysis of structures on elastic half-space by a FE-BIE approach

Settore Scientifico Disciplinare ICAR/09

Dottorando
Dott. Baraldi Daniele

Tutore
Prof. Tullini Nerio

Anni 2010/2012

Nonlinear analysis of structures on elastic half-space by a FE-BIE approach

PhD Thesis by Daniele Baraldi

Supervisor
Prof. Nerio Tullini

March 2013

Università degli Studi di Ferrara
Dottorato di Ricerca in Scienze dell'Ingegneria
Ingegneria Civile − Tecnica delle Costruzioni
XXV ciclo

Examiners:

Prof. Antonio Tralli,	Università di Ferrara
Prof. Fabio Conti,	Università dell'Insubria
Prof. Giorgio Novati,	Politecnico di Milano
Prof. Mira Petrovic,	Institut Català de Recerca – Girona (Spagna)

Contents

Introdutcion 1

1 Stability of Euler-Bernoulli beams and frames resting on elastic half-plane..5

1.1 Introduction 5

1.2 Basic relationships... 7

1.3 Discrete model... 9

1.4 Comparison of the present model with a traditional FE model 12

1.4.1 Convergence test for a beam with free ends 13

1.5 Buckling analysis of beams resting on elastic half-plane 17

1.5.1 Analytic solution for the buckling of a beam of infinite length resting on an elastic half-plane... 17

1.5.2 Beam of finite length with sliding ends 20

1.5.2.1 Modal shapes... 23

1.5.2.2 Beam with sliding ends on Winkler-type half-space 26

1.5.3 Beam of finite length with pinned ends 30

1.5.3.1 Modal shapes... 33

1.5.3.2 Bosakov's solution (1994) 37

1.5.3.3 Gallagher's solution (1974).. 38

1.5.3.4 Beam with pinned ends on Winkler-type half-space 41

1.5.4 Beam of finite length with free ends.. 44

1.5.4.1 Modal shapes... 46

1.5.4.2 Beam with free ends on Winkler-type half-space.................................. 48

1.5.5 Beam of infinite length with various end restraints 51

1.5.6 Buckling of a beam with a weakened section at midpoint........................ 53

1.6 Analysis of a compressed beam on half-plane loaded at midpoint............... 58

1.6.1 Incremental analysis of a compressed beam on half-plane loaded at midpoint... 62

1.7 Rectangular pipe resting on elastic half-plane 64

1.7.1 Buckling of rectangular pipes with free and pinned foundation beam ends 65

1.7.1.1 Buckling of rectangular pipes on half-plane modelled with traditional FEs... 70

1.7.2 Nonlinear incremental analyses of rectangular pipes 73

2 Stability of Timoshenko beams resting on elastic half-plane..... 77
2.1 Introduction 77
2.2 Basic relationships..... 79
2.3 Discrete model..... 81
2.4 Comparison of the present model with a classical FE model 84
2.4.1 Convergence test for a beam with free ends 84
2.5 Buckling analysis of beams with different end restraints 87
2.5.1 Beam of finite length with pinned ends 87
2.5.1.1 Modal shapes..... 91
2.5.1.2 Two-dimensional FE model results 94
2.5.1.3 Buckling of a beam with pinned ends on Winkler half-space 97
2.5.2 Beam of finite length with free ends..... 100
2.5.2.1 Modal shapes..... 103
2.5.2.2 Two-dimensional FE model results 106
2.5.2.3 Buckling of a beam with free ends on Winkler half-space..... 109
2.5.2.4 First critical load determined with different beam models..... 111
2.6 Coupling of 2D plane elements and boundary integral equations..... 112
2.6.1 Basic relationships..... 112
2.6.2 Discrete model..... 114
2.6.3 Static analysis of a layer resting on an elastic half-plane 116
2.6.4 Buckling analysis of 2D beams with free ends on half-plane..... 119

3 Analysis of slender beams and frames resting on elastic half-plane including material nonlinearity..... 125
3.1 Introduction 125
3.2 Semi-rigid analysis for a beam-column element..... 127
3.2.1 Monforton-Wu-Xu model for a beam with semi-rigid ends..... 127
3.2.2 Shakourzadeh model for a beam with semi-rigid ends..... 129
3.3 Plasticity model for a beam-column element..... 133
3.4 Analysis of beams on elastic half-plane including material nonlinearity... 136
3.4.1 Beam with plastic hinges on elastic half-plane..... 136
3.4.2 Incremental analysis of beams on half-plane including material nonlinearity..... 137
3.4.3 Incremental analysis of beams on half-plane including material and geometric nonlinearity..... 144

3.5 Incremental analysis of frames on half-plane including material nonlinearity 146
3.5.1 Description and design of the structure 146
3.5.2 Description of the discrete model 150
3.5.3 Numerical examples: pipe loaded by increasing service loads 152
3.5.3.1 Example 1: pipe loaded by a distributed force along the upper beam .. 152
3.5.3.2 Example 2: pipe loaded by self-weight and service load along the upper beam 154
3.5.3.3 Example 3: pipe loaded by dead loads and increasing service loads 156

4 Static and buckling analysis of beams resting on 3D elastic half-space 161
4.1 Introduction 161
4.2 Half space model 163
4.3 Galerkin boundary element method 164
4.3.1 Surface discretization 165
4.3.2 Rigid rectangular punch on elastic half-space 168
4.3.3 Uniform pressure 176
4.4 Beam model 183
4.4.1 Analytical formulation 183
4.4.1.1 Kinematical model 184
4.4.1.2 Constitutive laws 187
4.4.1.3 Formulation of the linearized stability problem 188
4.4.2 Beam discrete model 191
4.4.2.1 Interpolating shape functions 192
4.5 Beam on 3D half space 194
4.5.1 Variational formulation 195
4.5.2 Discrete model 197
4.6 Static analysis of beams on 3D elastic half-space 201
4.6.1 Foundation beam loaded by a concentrated force at midpoint 201
4.6.2 Foundation beam loaded by a uniform force distribution 210
4.6.3 Foundation beam loaded by a concentrated moment at midpoint 213
4.7 Buckling analysis of beams on 3D elastic half-space 217
4.7.1 Beam with sliding ends 217
4.7.2 Beam with pinned ends 219

4.7.3 Beam with free ends 223
4.7.4 Critical loads of a beam on stiff half-space varying *L*/*b* ratio 226

Conclusions 229

Appendix A1 – Discrete model for a beam on 2D half-space 233
Appendix A2 – Discrete model for a beam on Winkler half-space 234
Appendix A3 – Discrete model for a layer on 2D half-space 236
Appendix A4 – Discrete model for a beam with semi-rigid ends (Monforton-Wu-Xu) 238
Appendix A5 – Discrete model for a beam on 3D half-space 240

References 243

Introduction

The analysis of the interaction between deformable bodies represent a problem with both a mathematical and an engineering interest. In the engineering field, such interaction problems include, for example, the study of structural shallow foundations, floating structures, laminated or composite materials, sandwich panels, indentation problems. In the civil engineering field, the analysis of the interaction between structural foundations and the supporting soil is important to both structural and geotechnical engineering. Results of soil-structure interaction (SSI) analyses provide information which may be used in structural design of the foundation or of the entire structure, or in the analysis of stresses and deformation within the soil. Even if many studies are devoted to the elastic analysis of the interaction problem, the subject is continually being extended in order to include, for example, material and geometric nonlinearity. The aim of this thesis is to extend an existing numerical approach for studying the SSI problem of beams and frames on elastic half-space, including geometric and material nonlinearities and considering two different types of half-space model.

In the civil engineering field, the SSI problem assumes that the soil can be adequately represented by an elastic medium occupying a half-space region. In this thesis, models of half-space response which exhibit linear elastic characteristics are considered. The linear elastic idealization of the supporting medium is often represented by a mathematical model which describes the particular characteristics of the behaviour of the half-space. Some idealizations have been developed during years. The simplest soil or half-space model was defined by Winkler (1867), who assumed that the surface displacement of the half-space at every point is proportional to the pressure applied at the same point and it is independent of pressures and displacements at other surface points. Winkler-type half-space is physically represented by a distributed set of springs under the supported structure and it is often adopted to describe, for example, the behaviour of floating structures, railroad tracks and road pavements. Since the deflections in a Winkler model are limited to the loaded region, this reduce the applicability of the model, which turn out to be quite different than the real behaviour of a half-space characterized by transmissibility of applied forces such as the soil medium, the core of a sandwich panel or the elastic support of a thin film. In these cases, an elastic continuum model may be defined. The initial

studies in this context were done by Boussinesq (1885), who analyzed the problem of a semi-infinite homogeneous and isotropic linear elastic solid subject to a concentrated force acting normal to the its surface. A similar case is given by the plane problem of a concentrated normal line load applied to the surface of the half-space, which was studied for the first time by Flamant (Timoshenko and Goodier 1970, Johnson 1985). Moreover, it must be noted that the incapacity of the Winkler model in determining the continuous behaviour of real supports and the complexity of the continuum models caused the development of many other simple half-space response models in the past. Some examples are given by the two-parameter elastic models, which are characterized by two independent elastic constants (Hetenyi 1946, Pasternak 1954, Vlasov and Leonitiev 1966).
The interaction between foundations and the supporting soil medium is often analyzed by coupling finite element (FE) and boundary element (BE) methods (Brebbia and Georgiou 1979, Mendonca and Paiva 2003, Gonzalez et al. 2007). FE method is appropriate for structural analysis, whereas BE method is appropriate for studying unbounded domains. Moreover, adopting symmetric Galerkin BEM-FEM coupling procedures (Leung et al. 1995, Springhetti et al. 2007), symmetric coefficient matrices may be obtained for the BE formulations. BE formulation was adopted to study layered soils (Maier and Novati 1987), whereas BEM-FEM coupling may be also adopted for studying fracture mechanics problems (Frangi et al. 2002, Frangi and Novati 2003).
Considering the elastic half-plane or half-space, the BE formulation may be simplified by adopting a simple fundamental solution such as Boussinesq or Flamant solution, respectively. In these cases, the discretization of the contact surface generates a symmetric and positive definite system matrix. The first application of the FE-BE approach was carried out by Cheung and Zinkiewicz (1965) for the static analysis of plates on elastic foundations. The authors discretized the soil reaction with concentrated forces at plate sub-element nodes and obtained the flexibility matrix of the soil by using both Boussinesq and Winkler solutions. In the latter case, the flexibility matrix was purely diagonal. Cheung and Zinkiewicz showed that the stiffness matrix of the soil may be obtained by inverting the flexibility matrix and adding it to the stiffness matrix of the foundation, the total stiffness of the system may be obtained. The same approach was adopted by Cheung and Nag (1968) for the determination of the stiffness matrix of an elastic half-plane (Flamant solution) and half-space (Boussinesq solution). The flexibility matrix of the soil was also used by

Rajapakse and Selvadurai (1986) for studying Mindlin plate elements, whereas Guarracino et al. (1992) studied three-dimensional frames with rigid footings on half-space.

A SSI problem may be studied efficiently adopting a mixed variational formulation, which assumes as independent functions both structure displacements and soil or half-space contact pressures. Kikuci (1980) adopted a mixed variational formulation for studying beams resting on Pasternak soil, whereas Bjelak and Stephan (1983) adopted this formulation for Pasternak soil model and averaging Boussinesq solution. Tullini and Tralli (2010) studied Timoshenko beams on elastic half-plane by coupling beam FEs and boundary integral equation for the half-plane and adopting a mixed variational formulation. The same approach has been adopted by Tullini et al. (2012a) for studying axially loaded thin structures bonded to a homogeneous elastic half-plane.

In the first chapter of this thesis, the simple and efficient numerical model, introduced by Tullini and Tralli (2010), is extended to the buckling analysis of Euler-Bernoulli (E-B) beams on half-plane and to incremental analysis of E-B beams and frames including geometric nonlinearity. The stability of beams on elastic half-plane is important in many engineering fields, such as the design of structural sandwich panels (Allen 1969) and the buckling analysis of thin films in electronic industry (Shield 1994; Volynskii et al. 2000). The stability and the non-linear geometric analysis of frames on elastic half-plane may be very important for the design of subways or box-culverts. Moreover, the coupling of foundation FEs with a structure described by traditional beam elements, including geometric nonlinearity, represents a promising aspect of this work. In the second chapter, buckling analysis of beams on half-plane is applied to the Timoshenko beam model, which is well suited to study structural foundations with low slenderness. The results showed in first and second chapter have recently been published (Tullini et al. 2013, Tullini et al. 2012b).

In the third chapter, the analysis of E-B beams and frames on elastic half-plane is carried out including structural material nonlinearity. The non-linear behaviour of beams in bending is considered and for simplicity it is lumped at beam ends and represented by plastic hinges. For this purpose, an efficient model, commonly used to represent semi-rigid connection behaviour (Monforton and Wu 1963, Shakourzadeh et al. 1999), is adopted for representing the non-linear moment-rotation behaviour of beam cross-sections, following the approach of Hasan et al. (2002) for the pushover analysis of frames. Analysis of foundation beams including material nonlinearity are performed by defining a-priori the position of potential plastic hinges. Then, a box-culvert designed to grant the flow of a river under a railway line is studied and an incremental analysis is performed.

Finally, in the fourth chapter, the three-dimensional (3D) half-space model is considered and the flexibility matrix of the soil represented by Boussinesq solution is determined. The Galerkin boundary element method is firstly applied for solving problems related to rigid indenters on elastic half-space and uniform pressures over rectangular areas. Then, static and buckling analysis of beams on elastic soil is considered and the stiffness matrix of the soil is determined. Foundation beams of 3D frames on elastic soil may be discretized by adopting a beam model based on Timoshenko bending theory and Reissner (1952) torsion theory, following the model described by Minghini et al. (2008). However, for simplicity, foundation beams with rectangular cross-section are considered for static and buckling analysis, whereas surface pressures are discretized by adopting constant shape functions and subdividing the contact surface in both directions. Static analysis results for beams loaded by many load configurations are discussed and buckling analysis results are compared against those obtained with the two-dimensional half-space model.

1 Stability of Euler-Bernoulli beams and frames resting on elastic half-plane

1.1 Introduction

The stability of Euler-Bernoulli beams and frames resting on substrate or soil is important in many engineering fields and, in the past, this has been the subject of many works. In the civil engineering field, examples of this problem are the lateral buckling of welded railway rails (Kerr 1974, 1978) and the stability of road pavements (Kerr 1984). In this context, the pioneering works of Wieghardt (1922) and Prager (1927) are based on the assumption that the half-space under the beam is modelled as a continuously distributed set of springs (Winkler 1867). In 1937, Biot studied the problem of an infinite beam resting on elastic half-plane loaded by vertical forces. Biot compared beam bending moments with the ones obtained with the Winkler soil model and determined a relation between the Winkler subgrade modulus and the elastic modulus of the half-plane. After Biot, Reissner (1937) was the first to study the stability problem of an infinite beam resting on an elastic half-plane. Identical results were obtained by Murthy (1970, 1973b) who studied the stability of continuously supported beams on elastic half-plane and on a Wieghardt-type half-space. After Reissner results, the interest in this problem grew, motivated by early structural problems of sandwich elements, and Gough et al. (1940) extended Biot and Reissner results to include various conditions of contact between the infinite beam and the elastic half-plane. The study of sandwich elements continued up to recent years (Allen 1969; Ley et al 1999; Davies 2001). Recently, the main interest has been motivated by thin film buckling and by the research driven by the developments in the electronic industry (Shield 1994; Volynskii et al. 2000). The case of buckling without delamination is often called wrinkling.

In Timoshenko and Gere (1961), the buckling of a simply supported Euler-Bernoulli beam on Winkler soil is studied. Other boundary conditions, such as beam with clamped ends and beam with free ends, were studied and compared with the former (Hetenyi 1946). Moreover, the buckling conditions of beam on Winkler half-space with various end restraints were recently resumed by Wang et al. (2005). In the sandwich plates context, Goodier and Hsu (1954) underlined the presence of nonsinusoidal local buckling modes with large deflections at beam ends.

Assuming the more realistic relationship between foundation pressure and beam displacement defined by Wieghardt, Smith (1969), determined the buckling loads of a beam with pinned ends. Gallagher (1974) was the first to study the buckling of a beam with finite length and pinned ends on elastic half-plane adopting Chebyshev polynomials. The same problem was studied by Bosakov (1994) who applied the Ritz method to solve the stability problem of a simply supported beam.

In this chapter, the critical loads of Euler-Bernoulli beams with finite length resting on an elastic half-plane are evaluated by using the Finite Element-Boundary Integral Equation (FE-BIE) coupling method proposed by Tullini and Tralli (2010), where static analysis is performed. Making use of a parameter that takes into account both beam slenderness and half-plane stiffness, comparisons with analytical solutions and traditional two-dimensional (2D) FEs are given. Then, buckling loads and mode shapes are determined for different beam end restraints. The results are also compared with the corresponding ones obtained with a Winkler half-space model. Moreover, rectangular frames on elastic half-plane with compressed columns are considered. Buckling loads and mode shapes are determined for two different restraint conditions and varying soil stiffness. In addition, the geometric nonlinear behaviour of the frames is investigated and the load multipliers at limit point are compared with the buckling loads, showing that some pipes stiffer than the soil may exhibit snapthrough instability. Results relative to beam and frame buckling have recently been presented and discussed by Tullini et al. (2013).

1.2 Basic relationships

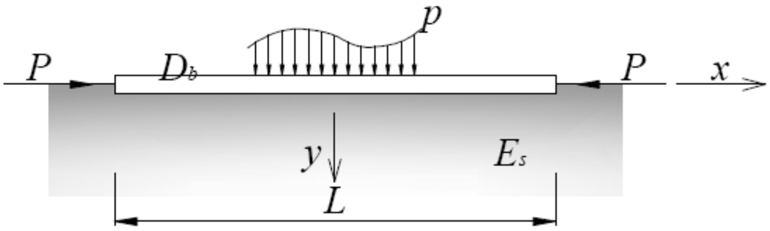

Fig. 1.1 – Beam on elastic half plane subject to external load $p(x)$ and compressive force P.

An elastic beam of length L, cross-section height h and width b, resting on a semi-infinite linearly elastic substrate in plane state, is referred to a Cartesian coordinate system (0; x, y), where x coincides with both the centroidal axis and the boundary of the half-plane and y is directed downwards. In the following, E_b and E_s indicate the Young moduli of beam and substrate, respectively. Analogously, Poisson's ratios of beam and substrate are denoted by ν_b and ν_s, respectively. Generalized plane stress or plane strain regime is considered; in the latter case, the width b of both beam and half-plane is assumed unitary. The beam is loaded at the ends by a compressive force P as shown in Fig. 1.1. A distributed vertical external load $p(x)$ can also be applied along the beam axis x. In the interface between beam and soil, frictionless and bilateral conditions are assumed. Consequently, a vertical soil reaction $r(x)$ is enforced to both beam and substrate and the vertical displacement $v(x)$ of the beam coincides with that of the half-plane boundary.

The total potential energy Π_b of the Euler-Bernoulli beam resting on the elastic half plane is given by the strain energy of the beam including second order effects (Bazant and Cedolin 1991), the work of external loads $p(x)$ and half-space reactions $r(x)$. Then, it can be written as:

$$\Pi_b = \frac{1}{2} \int_L \{D_b [v''(x)]^2 - P[v'(x)]^2\} \, \mathrm{d}x - b \int_L [p(x) - r(x)] \, v(x) \, \mathrm{d}x \tag{1.1}$$

where prime denotes differentiation with respect to x and $D_b = E_0 \, bh^3/12$ is the bending stiffness, with $E_0 = E_b$ or $E_0 = E_b/(1-\nu_b^2)$ for a generalized plane stress or plane strain state, respectively.

The potential energy of the half-space is given by:

$$\Pi_S = U_S - b\int_L r(x)\, v(x)\, \mathrm{d}\, x\,. \tag{1.2}$$

Considering the Clapeyron's theorem, the strain potential energy of the half-space is equal to half the work of the contact stresses at the beam soil interface (Tullini and Tralli 2010):

$$U_S = \frac{b}{2}\int_L r(x)\, v(x)\, \mathrm{d}\, x\,. \tag{1.3}$$

Then, the total potential energy of the half-space turns out to be:

$$\Pi_s = -\frac{b}{2}\int_L r(x)\, v(x)\, \mathrm{d}\, x = -\frac{b}{2}\int_L r(x)\, \mathrm{d}\, x \int_L g(x,\hat{x})\, r(\hat{x})\, \mathrm{d}\, \hat{x} \tag{1.4}$$

where the vertical displacement $v(x)$ is replaced by the boundary integral equation known as Flamant's solution (Timoshenko and Gere 1961; Johnson 1985), which uses the Green function $g(x,\hat{x})$ corresponding to the solution of the elastic problem for a homogeneous isotropic half-plane loaded by a point force normal to its boundary:

$$g(x,\hat{x}) = -\frac{2}{\pi\, E}\ln|x-\hat{x}|\,. \tag{1.5}$$

The generic elastic modulus of the half space E is equal to E_s or $E_s/(1-\nu_s^2)$ for a generalized plane stress or plane strain state, respectively.

Constraint equations $R_i(v,\, v') = 0$ between displacements or rotations, may be assigned along the beam axis, especially at beam ends. For example, a beam with pinned ends requires the equation $v(L/2) - v(-L/2) = 0$. These constraint equations can be included in the total potential energy Π of the beam-substrate system by means of a penalty approach (Reddy 2006):

$$\Pi(v,r) = \Pi_b(v,r) + \Pi_s(r) + \frac{k}{2}\sum_i [R_i(v,v')]^2 \tag{1.6}$$

where k is the penalty parameter whose value should be large enough to satisfy the constraint equations accurately. For beams with free ends, rigid-body displacement related to Flamant's solution can be removed by choosing an arbitrary abscissa $\bar{x}$ where a null value of $v(\bar{x})$ is forced.

1.3 Discrete model

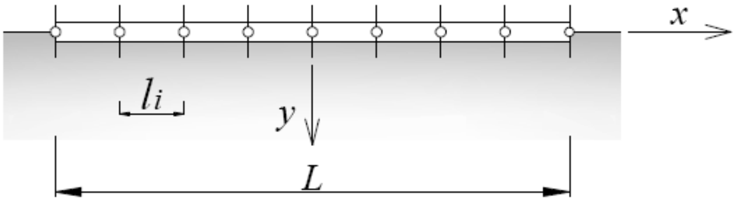

Fig. 1.2 – Beam on elastic half plane subdivided into 8 equal FEs

A simple discretization of the beam can be created by subdividing the beam into FEs of length l_i (Fig. 1.2), then beam displacements and rotations are discretized in the usual form as follows

$$\mathbf{d}(\xi) = \mathbf{N}(\xi)\, \mathbf{q}_i \tag{1.7}$$

where $\xi = x/l_i$, $\mathbf{d} = [v, \varphi]^{\mathrm{T}}$ collects the unknown displacement function, $\mathbf{q}_i = [v_1, \varphi_1, v_2, \varphi_2]^{\mathrm{T}} = [v_1, v'_1, v_2, v'_2]^{\mathrm{T}}$. Beam shape functions collected in the matrix $\mathbf{N}(\xi)$ are the classical Hermitian polynomials and the corresponding derivatives:

$$\begin{aligned}
&N_{11} = 1 - 3\xi^2 + 2\xi^3; && N_{21} = 6\xi\,(1-\xi)/l_i;\\
&N_{12} = -l_i\,\xi\,(1-\xi)^2; && N_{22} = 3\,\xi^2 - 4\,\xi;\\
&N_{13} = 3\xi^2 - 2\xi^3; && N_{23} = -6\xi\,(1-\xi)/l_i;\\
&N_{14} = l_i\,\xi^2\,(1-\xi); && N_{24} = 3\,\xi^2 - 2\,\xi.
\end{aligned} \tag{1.8}$$

Half-plane pressures are discretized considering a piecewise constant soil reaction inside each element (Tullini and Tralli 2010):

$$r(\xi) = [\boldsymbol{\rho}(\xi)]^{\mathrm{T}}\, \mathbf{r}_i, \tag{1.9}$$

where $\mathbf{r}_i$ denotes the vector components of nodal soil reaction and $\boldsymbol{\rho}$ assembles constant shape functions. One, two or four subdivisions can be considered inside each element.

Substituting Eqs. 1.8 and 1.9 into variational principal (Eq. 1.6), the total potential energy Π written in discrete form takes the expression:

$$\Pi(\mathbf{q},\mathbf{r}) = \frac{1}{2}\mathbf{q}^T\mathbf{K}_b\,\mathbf{q} - b\mathbf{q}^T\mathbf{F} + b\mathbf{q}^T\mathbf{H}\mathbf{r} - \frac{1}{2}b\mathbf{r}^T\mathbf{G}\mathbf{r} \tag{1.10}$$

where, the penalty function in discrete form is included into the beam stiffness matrix $\mathbf{K}_b$.

Then, the stationarity condition of the total potential energy Π written in discrete form provides the following system:

$$\begin{bmatrix} \dfrac{D_b}{L^3}\left(\widetilde{\mathbf{K}}_b - \dfrac{PL^2}{D_b}\widetilde{\mathbf{K}}_g\right) & b\mathbf{H} \\ b\mathbf{H}^{\mathrm{T}} & -\dfrac{b}{E}\widetilde{\mathbf{G}} \end{bmatrix} \begin{Bmatrix} \mathbf{q} \\ \mathbf{r} \end{Bmatrix} = \begin{Bmatrix} b\mathbf{F} \\ \mathbf{0} \end{Bmatrix} \tag{1.11}$$

where the vector **q** collects nodal displacements, **r** denotes the vector of constant soil reactions, **F** is the external load vector, $D_b/L^3\widetilde{\mathbf{K}}_b$ is the elastic stiffness matrix of the beam, $P/L\widetilde{\mathbf{K}}_g$ is the geometric (or incremental) matrix. The elements of matrices **H** and $\widetilde{\mathbf{G}}$, together with the element matrices $\widetilde{\mathbf{K}}_{bi}$ and $\widetilde{\mathbf{K}}_{gi}$, are reported in the appendix A1.

System in Eq. 1.11 yields the following solution:

$$\mathbf{r} = E\,\widetilde{\mathbf{G}}^{-1}\mathbf{H}^{\mathrm{T}}\mathbf{q}. \tag{1.12}$$

$$\left[\widetilde{\mathbf{K}}_b - \lambda\widetilde{\mathbf{K}}_g + \widetilde{\mathbf{K}}_{\mathrm{soil}}\right]\mathbf{q} = \mathbf{F}\frac{bL^3}{D_b} \tag{1.13}$$

where $\widetilde{\mathbf{K}}_{\mathrm{soil}}$ is the stiffness matrix of the half-plane

$$\widetilde{\mathbf{K}}_{\mathrm{soil}} = (\alpha L)^3\mathbf{H}\widetilde{\mathbf{G}}^{-1}\mathbf{H}^{\mathrm{T}} \tag{1.14}$$

and load multiplier λ, and parameter α*L* are defined as follows;

$$\lambda = \frac{PL^2}{D_b}, \qquad \alpha L = \sqrt[3]{\frac{E\,b\,L^3}{D_b}}. \tag{1.15a,b}$$

According to references (Biot 1937; Vesic 1961; Tullini and Tralli 2010), the parameter αL in Eq. 1.15b describes the beam-substrate system. Low values of αL characterise short beams stiffer than the soil, whereas higher values of αL describe more flexible beams, this latter case is suitable to represent long beams resting on stiff soil.

The adopted mixed finite element model is particularly simple and effective, as shown in Tullini and Tralli (2010) for the static case, where the numerical properties of the present FE model are also discussed. As for the determination of critical load P_{cr}, a homogeneous system associated to Eq. 1.13 must be considered and the buckling loads are given by the roots λ_{cr} of the equation $\det[\widetilde{\mathbf{K}}_b - \lambda \widetilde{\mathbf{K}}_g + \widetilde{\mathbf{K}}_{\mathrm{soil}}] = 0$, which can be suitably reduced to a standard eigenvalue problem. Making use of Eq. 1.15a and the definition of Euler critical load:

$$P_{\mathrm{cr,E}} = \frac{\pi^2 D_b}{L^2}, \tag{1.16}$$

dimensionless buckling loads are defined as $P_{\mathrm{cr}}/P_{\mathrm{cr,E}} = \lambda_{\mathrm{cr}}/\pi^2$.

In the case of a structure connected to the foundation beam, system (Eq. 1.13) can be partitioned as shown in (Tullini and Tralli 2010), where nodal displacements without or with nodes shared with the foundation beam are selected. Moreover, the element geometric matrix of each beam FE is dealt with as usual.

1.4 Comparison of the present model with a traditional FE model

Taking into account two different αL values, representing a rather stiff beam (αL = 5) and a flexible beam (αL = 25), a convergence test is done in order to compare the present model with a classical model that uses 2D elastic elements to describe the soil. In both cases, the foundation beam is modelled as Euler-Bernoulli beam subdivided into equal FEs, with a number of elements n_{el} equal to powers of two up to 512 FEs. Each beam element of the present model includes one soil element, whereas in the 2D model the soil is modelled by a square mesh of quadrilateral elements in plane state. The mesh of the soil has a total width equal to 8L, and zero horizontal and vertical displacements are imposed at vertical and lower boundaries, respectively. Two nested square meshes, which width equal to 4L and 2L, are taken close to the foundation beam, and each quadrilateral element side of the smaller mesh has the same size of the beam element. This type of mesh does obviously require a mix of triangular and quadrilateral elements, in order to avoid hanging nodes and to reduce the total number of degrees of freedom with respect to a mesh of quadrilateral elements only.

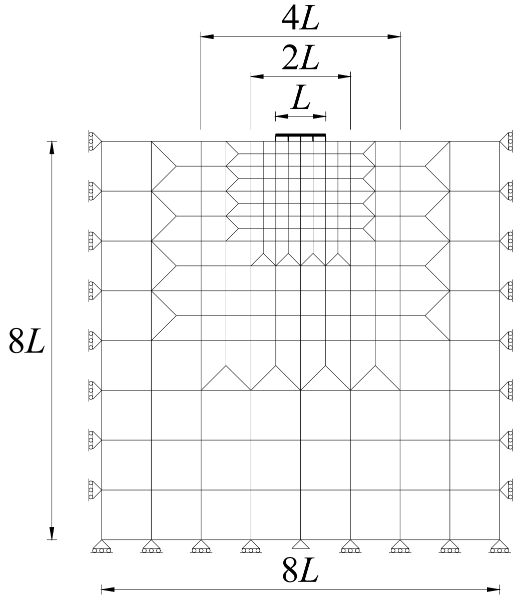

Fig. 1.3 – Mesh adopted for the 2D model with foundation beam subdivided into 4 equal FEs.

In Fig. 1.1.3, the case of the foundation beam subdivided in 4 beam FEs is shown. The frictionless connection between beam and soil nodes is established by vertical master-slave links. The adopted 2D code uses geometric matrix also for 2D soil FEs.

1.4.1 Convergence test for a beam with free ends

Fig. 1.4a shows the number of equations for the two models, with respect to the number of FEs adopted for the beam. Fig. 1.4b shows the number of equations of the two models with respect to the number of equations of the present model. In both figures the line with crosses is used for the present model and the line with dots regards the 2D model. Adopting axis in logarithmic scale, each set of points lie on a straight line in both figures and the corresponding slope can be calculated through least-squares method. Therefore, the ratio between the number of equations of the two models can be easily determined. Tab. 1.1 collects the number of equations of the 2D model and the present model varying the number of beam elements. The slope of the line with dots in Fig. 1.4b is 2.04, whereas the slope of the line with crosses is obviously equal to 1. The same number can be obtained by determining the ratio between the slopes A of the straight lines in Fig. 1.4a.

$$A^{\mathrm{2D}} / A^{\mathrm{PA}} = 1.94/0.95 = 2.04 \tag{1.17}$$

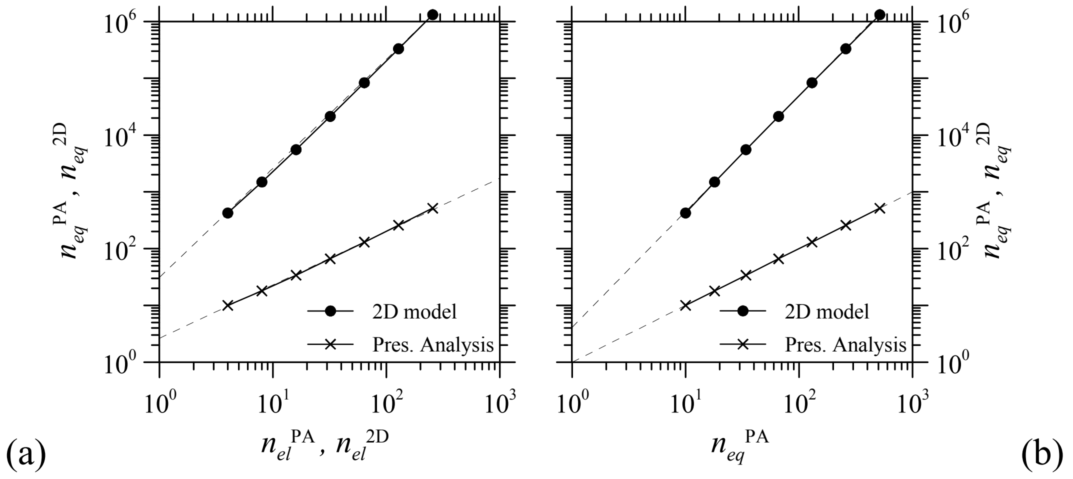

Fig. 1.4 – Number of equations of 2D model and present model as a function of beam FEs (a) and number of equations of the present model (b).

n_{el}	n_{eq}	
	2D model	Present Analysis
2^2	424	10
2^3	1488	18
2^4	5536	34
2^5	21312	66
2^6	83584	130
2^7	331008	258
2^8	1317376	514

Tab. 1.1 – Number of equations for the two models considered, with respect to the number of beam FEs

Therefore, the number of equations of the 2D model n_{eq}^{2D} is related to the number of equations of the present analysis n_{eq}^{PA} by means of the following relation:

$$n_{eq}^{\mathrm{2D}} \cong 2\,(n_{eq}^{\mathrm{PA}})^2. \tag{1.18}$$

where $n_{eq}^{\mathrm{PA}} = 2\,n_{el} + 2$ as usual, as it can be seen in Tab. 1.1.

The present analysis performed with a beam having 2,048 FEs and one soil reaction under each beam element is used as reference to determine the first three buckling loads $P_{\mathrm{cr}}^{\mathrm{REF}}$. Figs. 1.5a and b show the relative error $\delta P_{\mathrm{cr}} = (P_{\mathrm{cr}}^{\mathrm{FEM}} - P_{\mathrm{cr}}^{\mathrm{REF}})/P_{\mathrm{cr}}^{\mathrm{REF}}$ as a function of n_{el} for $\alpha L = 5$ and 25. Figs. 1.5c and d show the absolute values of the relative error δP_{cr} in logarithmic scale, in order to obtain the convergence rates for the critical loads. Lines with dots represent errors for the 2D model, whereas lines with crosses represent errors for the present analysis. It is clear that the first and the second buckling loads obtained with the two models converge with the same rate, which is less than n_{el}^{-1}. The third buckling load converge for both models with a rate larger than the previous one, which is less than n_{el}^{-2}. Both methods converge with a rate less than n_{el}^{-1} for the first two eigenvalues, but CPU time t^{2D} of the 2D model is bigger than $5\,(t^{\mathrm{PA}})^{2.5}$, where t^{PA} is the CPU time of the present analysis.

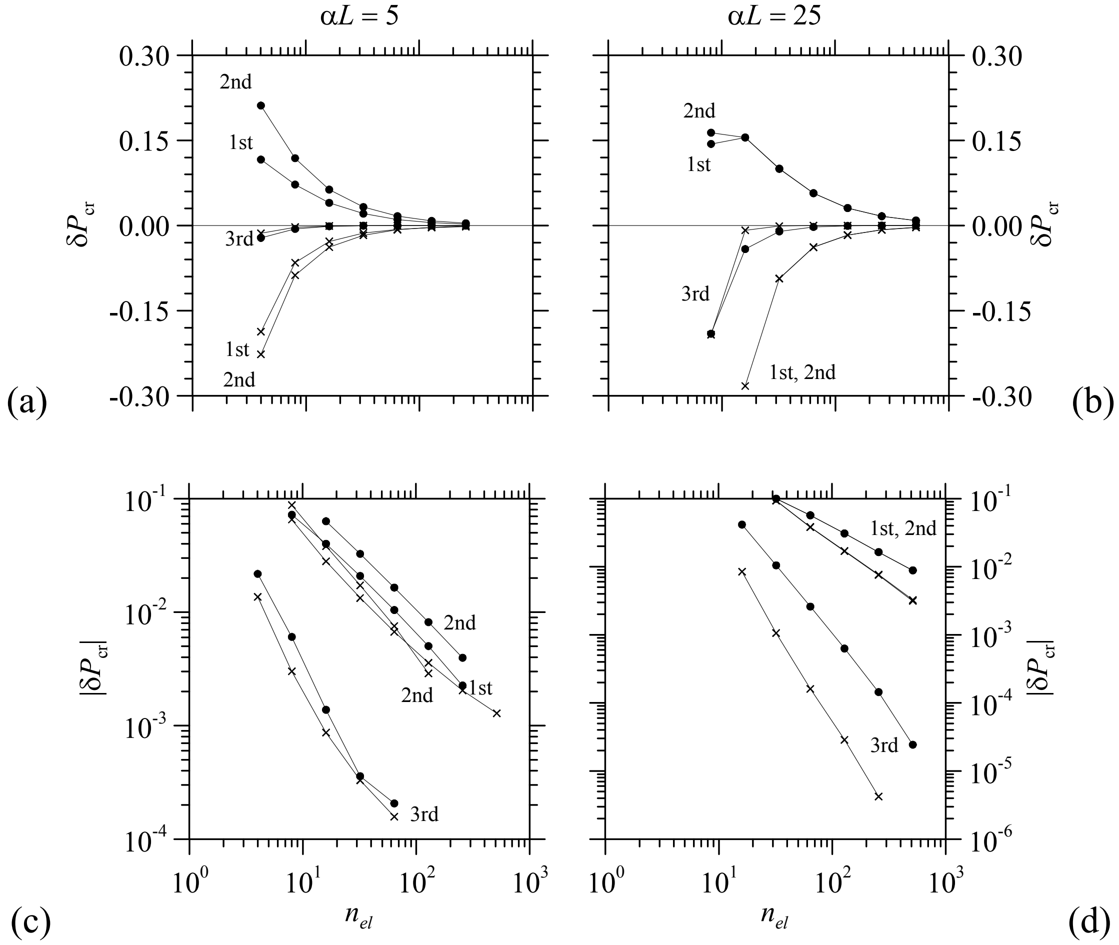

Fig. 1.5. Relative errors δP_{cr} for first three buckling loads as a function of n_{el} for $\alpha L = 5$ (a) and $\alpha L = 25$ (b). Absolute relative errors in bi-logarithmic scale for first three buckling loads $\alpha L = 5$ (c) and $\alpha L = 25$ (d).

Lines with crosses or dots correspond to the present analysis or 2D models, respectively.

(a)

n_{el}	$\alpha L = 5$					
	PA			2D		
	1	2	3	1	2	3
2^2	1.688	1.889	4.956	2.267	2.939	4.917
2^3	1.880	2.131	5.008	2.159	2.630	4.993
2^4	1.949	2.233	5.019	2.087	2.474	5.017
2^5	1.977	2.279	5.022	2.046	2.396	5.022
2^6	1.990	2.300	5.023	2.025	2.356	5.022
2^7	1.996	2.311	5.023	2.014	2.337	5.022
2^8	1.999	2.316	5.023	2.008	2.327	5.022
2^{11}	2.004	2.318	5.023	-	-	-

(b)

n_{el}	$\alpha L = 25$					
	PA			2D		
	1	2	3	1	2	3
2^2	6.776	9.240	29.469	19.454	25.481	46.132
2^3	23.811	23.849	65.543	60.796	62.307	65.650
2^4	40.582	40.645	77.512	61.605	61.686	75.049
2^5	47.595	47.662	78.084	57.851	57.892	77.357
2^6	50.138	50.201	78.155	55.208	55.257	77.965
2^7	51.186	51.248	78.165	53.714	53.768	78.118
2^8	51.663	51.724	78.167	52.926	52.982	78.156
2^{11}	52.059	52.114	78.167	-	-	-

Tab.2. First three dimensionless critical loads $P_{\mathrm{cr}}/P_{\mathrm{cr,E}}$ corresponding to the present analysis (PA) or 2D models as a function of n_{el} for αL equal to 5 and 25.

Moreover, relative errors are lower than 1% with at least 128 beam FEs for αL = 5 and with at least 256 beam FEs for αL = 25. Thus, the present model can be considered effective for the determination of buckling loads and mode shapes, and a number of 256 equal FEs are adopted for all cases reported in this section.

1.5 Buckling analysis of beams resting on elastic half-plane

In the following, beams with finite length and with different boundary conditions are discussed (sliding-sliding, pinned-pinned and free-free) and for each case, critical loads and modal shapes are determined for increasing values of α*L*. Moreover, analytic solutions of similar problems such as the ones studied by Reissner (1937), Gallagher (1974) and Bosakov (1994) are present in order to have a comparison for the present analysis.

1.5.1 Analythic solution for the buckling of a beam of infinite length resting on an elastic half-plane

Reissner (1937) studied the stability of a beam of infinite length resting on an elastic half-plane (Fig. 1.6), starting from the differential equation of an Euler-Bernoulli beam on elastic half-plane, including second order effects due to axial load *P* (Eqs. 1.19a and b).

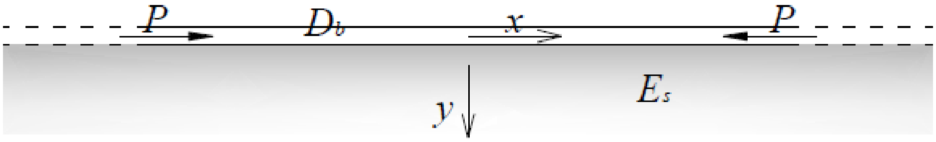

Fig. 1.6 – Beam of infinite length on elastic half space subject to axial load.

$$D_b \frac{d^4 v(x)}{dx^4} + P \frac{d^2 v(x)}{dx^2} = -r(x) \tag{1.19a}$$

$$v(x) = \int_{-\infty}^{+\infty} g(x,\hat{x})\, r(\hat{x})\, d\hat{x} = \int_{-\infty}^{+\infty} g(|x-\hat{x}|)\, r(\hat{x})\, d\hat{x} \tag{1.19b}$$

Substituting Eq. 1.19a with Eq. 1.19b and differentiating with respect to *x*, the following expression is obtained:

$$\frac{d\,v(x)}{dx} = -\int_{-\infty}^{+\infty} \frac{d\,g(|x-\hat{x}|)}{dx} \left[D_b \frac{d^4 v(\hat{x})}{dx^4} + P \frac{d^2 v(\hat{x})}{dx^2} \right] d\hat{x} \,. \tag{1.20}$$

Reissner assumed a solution which satisfies the conditions of vertical displacement and curvature equal to zero for $x_n = \pm nL$, with $n = 1, 2, 3..$. A sine-type solution satisfies these conditions:

$$v(x) = \sin\frac{m\pi x}{L} \quad \text{for } m = 1, 2, 3, .. \tag{1.21}$$

This solution represents a beam which is freely supported at the points x_n, then the original problem of an infinite beam supported by an elastic half plane becomes the problem of an infinite beam resting on elastic half plane supported by an infinite set of equidistant supports. It is worth noting that the buckling modes corresponding to this solution are sinusoidal with constant amplitude. Considering Eq. 1.21, Eq. 1.19 becomes

$$\frac{m\pi}{L}\cos\frac{m\pi x}{L} = -\int_{-\infty}^{+\infty}\frac{d\,g(|x-\hat{x}|)}{dx}\left[-D_b\left(\frac{m\pi}{L}\right)^4 + P\left(\frac{m\pi}{L}\right)^2\right]\sin\frac{m\pi\hat{x}}{L}\,d\hat{x}\,. \tag{1.22}$$

Setting $x-\hat{x}=u$, the previous equation can be simplified as follows:

$$\cos\frac{m\pi x}{L} = \frac{m\pi}{L}\left[-D_b\left(\frac{m\pi}{L}\right)^2 + P\right]\cos\frac{m\pi x}{L}\int_{-\infty}^{+\infty}\frac{d\,g(|u|)}{du}\sin\frac{m\pi u}{L}\,du \tag{1.23a}$$

$$1 = \frac{m\pi}{L}\left[-D_b\left(\frac{m\pi}{L}\right)^2 + P\right]\bar{g}\left(\frac{m\pi}{L}\right) \tag{1.23b}$$

Introducing the expression of g (Eq. 1.5)

$$\frac{d\,g(|u|)}{du} = \frac{2}{\pi E u} \tag{1.24a}$$

$$\bar{g}\left(\frac{m\pi}{L}\right) = \int_{-\infty}^{+\infty}\frac{d\,g(|u|)}{du}\sin\frac{m\pi u}{L}\,du = \frac{2}{\pi E}\int_{-\infty}^{+\infty}\frac{\sin(m\pi u/L)}{u}\,du = \frac{2}{E} \tag{1.24b}$$

Then, substituting Eq. 1.24b into Eq. 1.23b, the critical load P is given by

$$P = P_{cr,m} = D_b\left(\frac{m\pi}{L}\right)^2 + \frac{1}{\frac{2}{E}\frac{m\pi}{L}} = D_b\left(\frac{m\pi}{L}\right)^2 + \frac{E}{2}\frac{L}{m\pi} \quad \text{for } m = 1, 2, 3, \tag{1.25}$$

Finally, introducing in Eq. 1.25 the expression of the Euler load (Eq. 1.16), the critical loads of a beam of infinite length resting on a two-dimensional half-space and on an infinity of equidistant supports turn out to be:

$$P_{\mathrm{cr},m} = P_{\mathrm{cr,E}}\left[m^2 + \frac{(\alpha L)^3}{2m\pi^3}\right] \quad \text{for } m = 1, 2, 3, \ldots \tag{1.26}$$

It is worth noting that the last simplification shows that critical loads of a beam on elastic half-plane depend directly on the beam-subgrade parameter αL.

For any given m, Eq. 1.26 provides the smallest critical load $P_{\mathrm{cr,R}}$ when $\alpha L = \sqrt[3]{4}\,\pi m$ that substituted in Eq. 1.26 yields

$$P_{\mathrm{cr,R}} = 3\,m^2 P_{\mathrm{cr,E}} = \frac{3}{\sqrt[3]{16}\,\pi^2} P_{\mathrm{cr,E}}(\alpha L)^2 = 0.121\,P_{\mathrm{cr,E}}(\alpha L)^2, \tag{1.27}$$

The same result was obtained by Murthy (1970, 1973b) who studied the buckling of continuously supported beams on a semi-infinite elastic continuum. Murthy considered a cosine series solution (Eq. 1.28) by applying the same procedure adopted in a previous paper (Murthy 1973a) for the case of a beam on Pasternak foundation.

$$v(x) = \sum_{n=0}^{\infty} w_n \cos(a_n x) \tag{1.28}$$

For $\alpha L = 0$, i.e. for a beam without supporting soil, Eq. 1.26 provides buckling loads of a beam with sliding ends as well as of a simply supported beam (Eq. 1.30), and the first mode shape corresponds to the longest wavelength permitted by the end restraints.

Furthermore, Eq. 1.27 allows the evaluation of the critical stress of the beam cross-section in a form frequently used in the design of structural sandwich panels (Gough et al 1960; Allen 1969; Ley et al. 1999; Davies 2001):

$$\sigma_{\mathrm{cr,R}} = \frac{P_{\mathrm{cr,R}}}{b\,h} = \frac{3^{2/3}}{4}\sqrt[3]{E^2\,E_0} = 0.52\,E^{2/3}\,E_0^{1/3}. \tag{1.29}$$

1.5.2 Beam of finite length with sliding ends

The case of a beam with sliding ends is considered first (Fig. 1.7). This case may refer to a rectangular pipe with a top beam simply supported on rigid columns; thus, the structure prevents rotations at the ends of the foundation beam but allows independent vertical displacements.

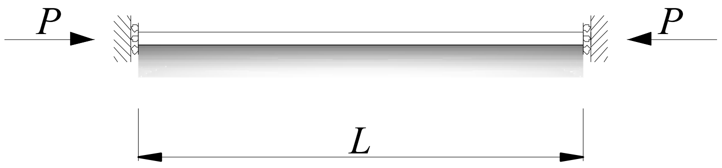

Fig. 1.7 – Beam with sliding ends subject to axial load P.

The constraint equations that have to be used in Eq. 1.6 are $R_1 = v'(L/2) - v'(-L/2) = 0$ and $R_2 = v'(L/2) + v'(-L/2) = 0$, which turn out to be equal to $v'(\pm L/2) = 0$. Applying a penalty parameter $k = 10^9\, l_i\, D_b/L^3$, an error less than 10^{-5} is obtained for the first ten eigenvalues.

Fig. 1.8a shows the first six dimensionless buckling loads $P_{\mathrm{cr}}/P_{\mathrm{cr,E}}$ versus the parameter αL^3. Alternatively, Fig. 1.8b shows the first six dimensionless buckling loads $P_{\mathrm{cr}}/P_{\mathrm{cr,E}}$ versus the parameter αL. Continuous lines represent dimensionless buckling loads obtained with the present model, whereas dashed lines represent Reissner's solution. For $\alpha L = 0$, critical loads converge to the buckling loads of a beam with sliding ends without supporting medium:

$$P_{\mathrm{cr},m}(0)/P_{\mathrm{cr,E}} = m^2 \quad \text{with } m = 1, 2, 3\ldots \tag{1.30}$$

Normalized critical loads turn out to be proportional to the square of the beam-subgrade parameter αL. Fig. 1.8c shows the ratio $P_{\mathrm{cr}}/[P_{\mathrm{cr,E}}\,(\alpha L)^2]$ versus the parameter αL; for increasing αL, the ratios corresponding to the first and second smallest eigenvalues converge to a constant value equal to 0.121, this value is coincident with the coefficient obtained in Eq. 1.27. Comparing the numerical solution with the one determined by Reissner (1937), for αL values up to 5 (short beams and/or soft soil), the numerical solution is in good agreement with Eq. 1.26, whereas for the high values of αL (long beams and/or stiff soil) the numerical solution is well approximated by Eq. 1.27.

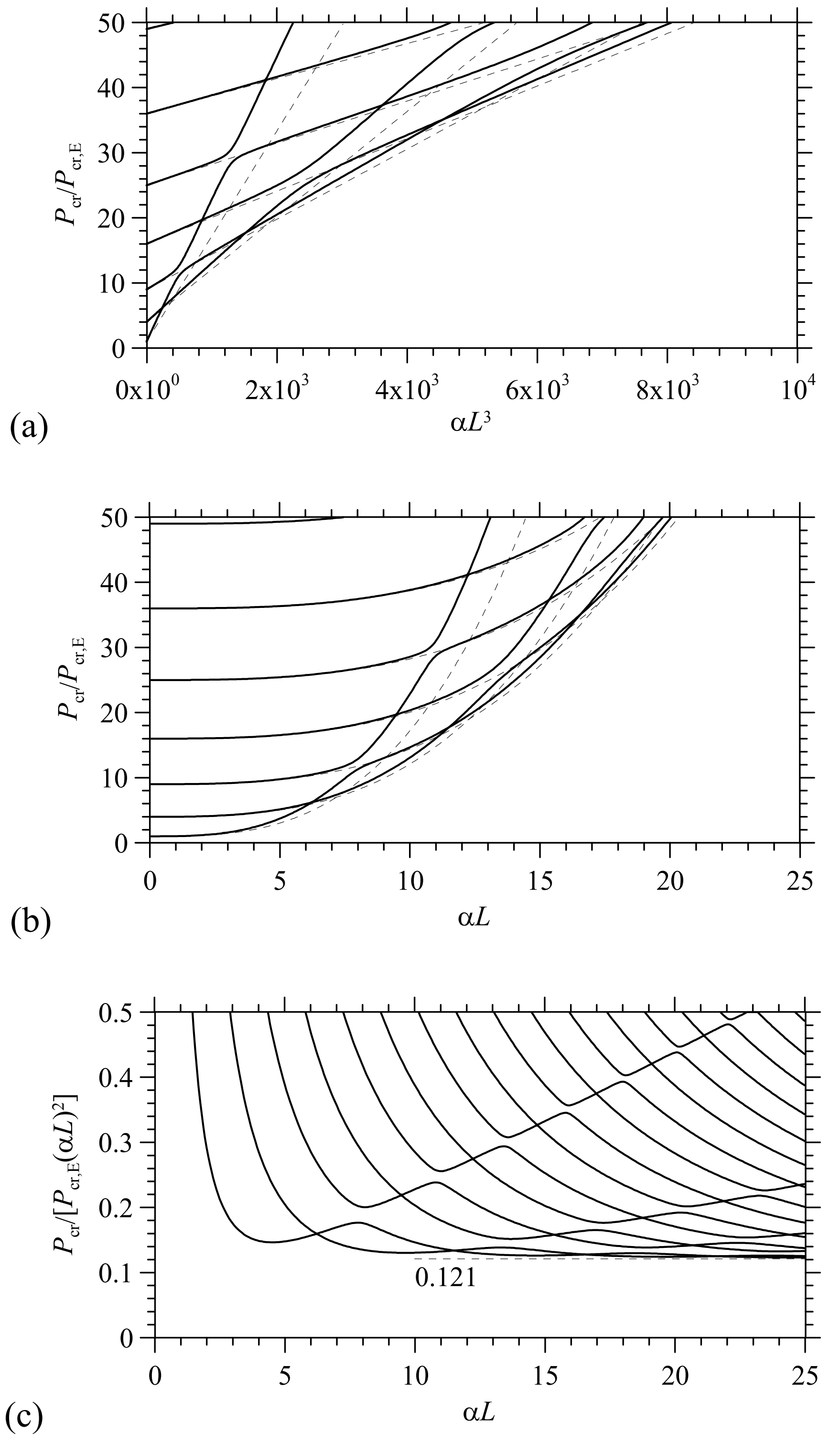

Fig. 1.8 – Dimensionless critical loads P_{cr} (continuous lines) and $P_{\mathrm{cr},m}$ (dashed lines) versus αL for a beam with sliding ends.

The curves in Figs. 1.8a, b and c, exhibit curve veering and crossing points which interchange themselves for increasing values of αL. The coordinates of crossing points can be determined approximately by refining the αL values in proximity of each point and searching coincident eigenvalues. Tab. 1.3 shows the coordinates of the first four crossing points for the first two curves, which are also depicted with crosses in Fig. 1.9.

Point	1	2	3	4
αL	6.232	11.735	16.573	21.633
$P_{cr}/P_{cr,E}$	6.200	17.511	35.092	58.546

Tab. 1.3 – Coordinates of the first four crossing points between the first and second eigenvalues for a beam with sliding ends on elastic half-plane.

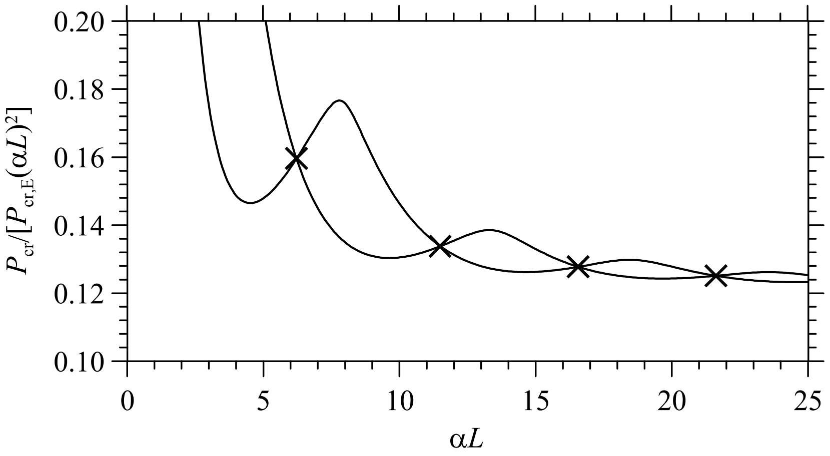

Fig. 1.9 – First and second critical loads of a beam with sliding ends on elastic half-plane (continuous lines) with the first four crossing points (crosses).

The behaviour of a beam with sliding ends on elastic half plane is found to be quite analogous to a beam with sliding ends resting on Winkler soil (Hetenyi 1946; Timoshenko and Gere 1961; Bazant and Cedolin 1991),where coordinates of intersection points may be exactly known, but curve veering is not present. Moreover, the curve representation shown in Figs. 1.8a, b and c, was introduced for the first time by Ratzersdorfer (1936) for the case of the beam on Winkler soil.

1.5.2.1 Modal shapes

The modal shapes of a beam with sliding ends on elastic half-plane turn out to be sinusoidal. The number of half-waves and their amplitude depends on the αL parameter. In the following figures, modal shapes are shown for increasing αL values; displacements are normalized putting the maximum absolute beam deflection equal to 1; moreover, the corresponding soil reactions are shown.

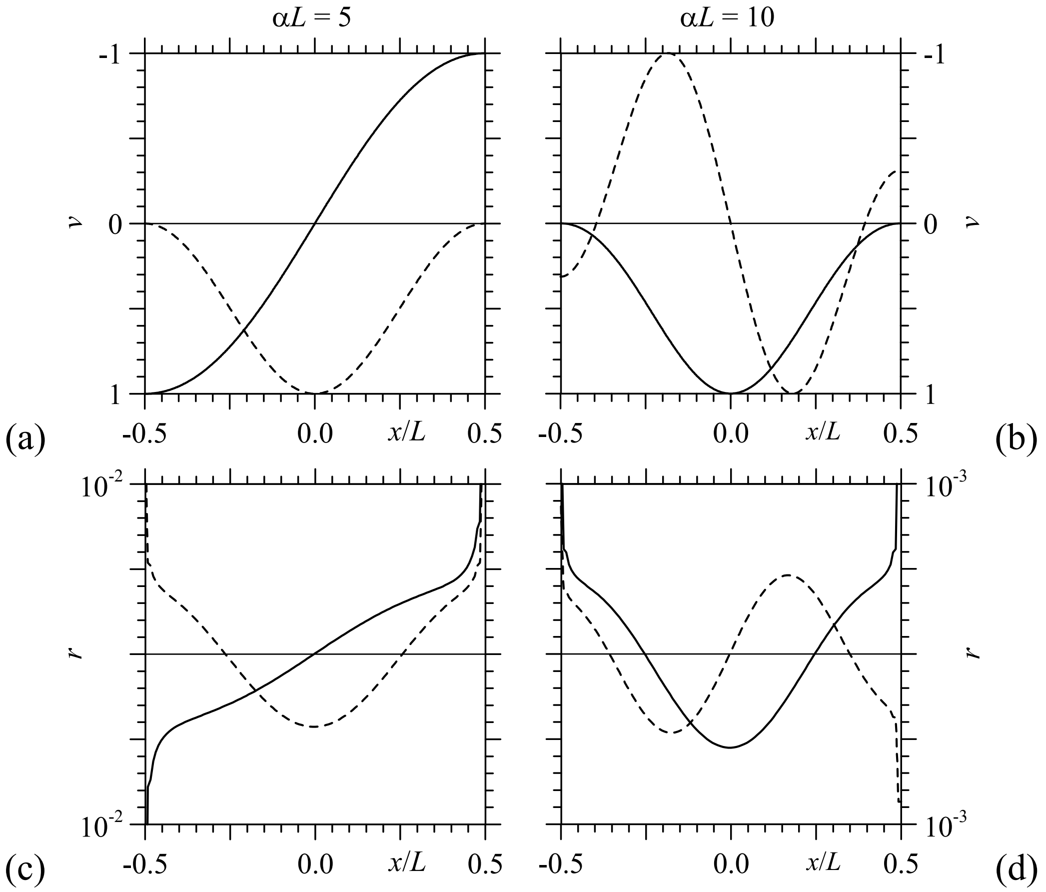

Fig. 1.10 – First (continuous line) and second (dashed line) mode shapes for a beam with sliding ends and αL equal to 5 (a), 10 (b). Soil reactions corresponding to the first (continuous line) and second (dashed line) mode shapes for a beam with sliding ends and αL equal to 5 (c), 10 (d).

For $\alpha L = 5$, Fig. 1.10a shows the first two mode shapes which are characterized by one and two half-waves; whereas, for $\alpha L = 10$, two and three half-waves are observed (Fig. 1.10b). Fig. 1.10c and d show the corresponding soil reactions. For $\alpha L = 10$, the first mode shape (Fig. 1.10b, continuous line) is similar to the second one obtained for $\alpha L = 5$ (Fig. 1.10a, dashed line), however, the second mode shape for $\alpha L = 10$ is different than the first one for $\alpha L = 5$. Therefore, even if the first and second critical load curves (Figs. 1.8a, b and c) interchange themselves, the corresponding buckling modes do not interchange each other. For αL = 15 and 20, Figs. 1.11a and b show the first two mode shapes, respectively, whereas Figs. 1.11c and d show the corresponding soil reactions. The first mode shape for αL = 15 is characterized by three half-waves and for αL = 20 it is characterized by four half-waves. Hence, after each intersection point (Tab. 1.3), every mode shape changes and the number of half-waves increases.

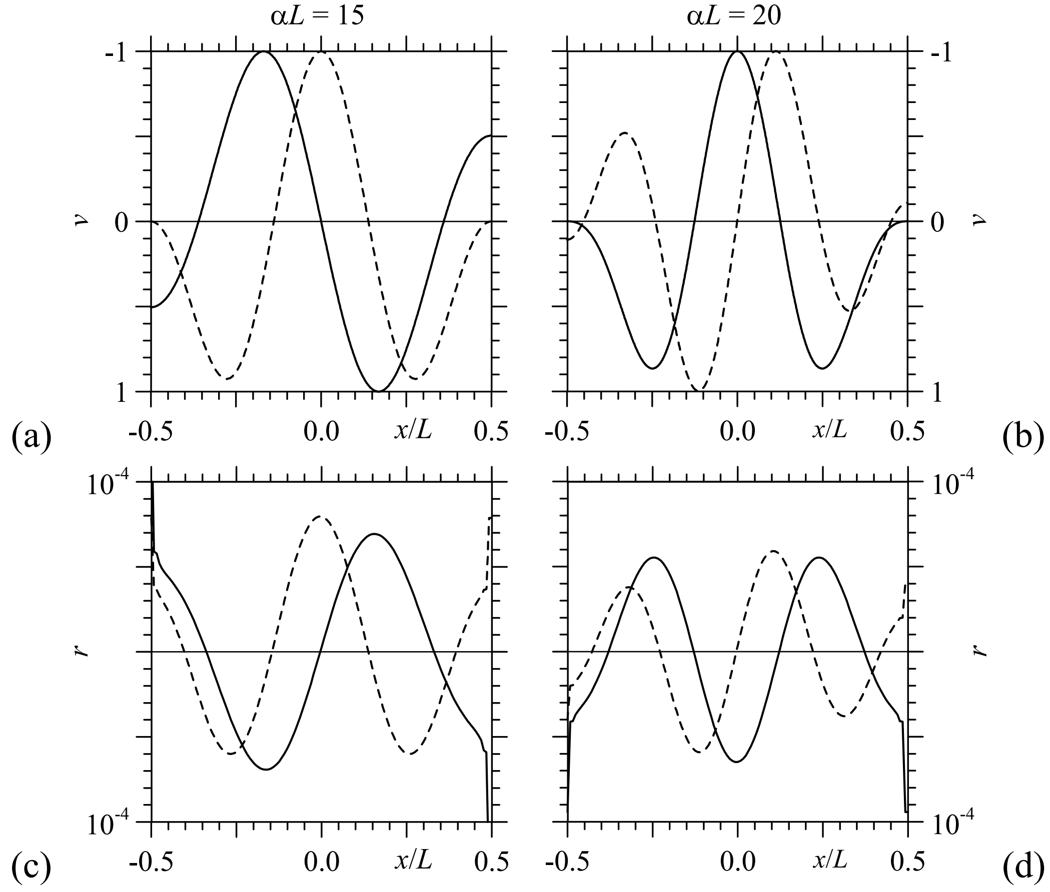

Fig. 1.11 – First (continuous line) and second (dashed line) mode shapes for a beam with sliding ends and αL equal to 15 (a), 20 (b). Soil reactions corresponding to the first (continuous line) and second (dashed line) mode shapes for a beam with sliding ends and αL equal to 15 (c), 20 (d).

Figs. 1.10, 1.11 and 1.12 clearly show that for increasing αL, the number of half-waves for the first two mode shapes increases and short wavelengths are obtained. Furthermore, mode shapes amplitude is not constant and for increasing αL it tends to reach maximum values close to beam midpoint. A different behaviour can be detected in beam on Winkler soil (Timoshenko and Gere 1961;

Bazant and Cedolin 1991), where mode shapes amplitude is constant, as shown in the following paragraph.

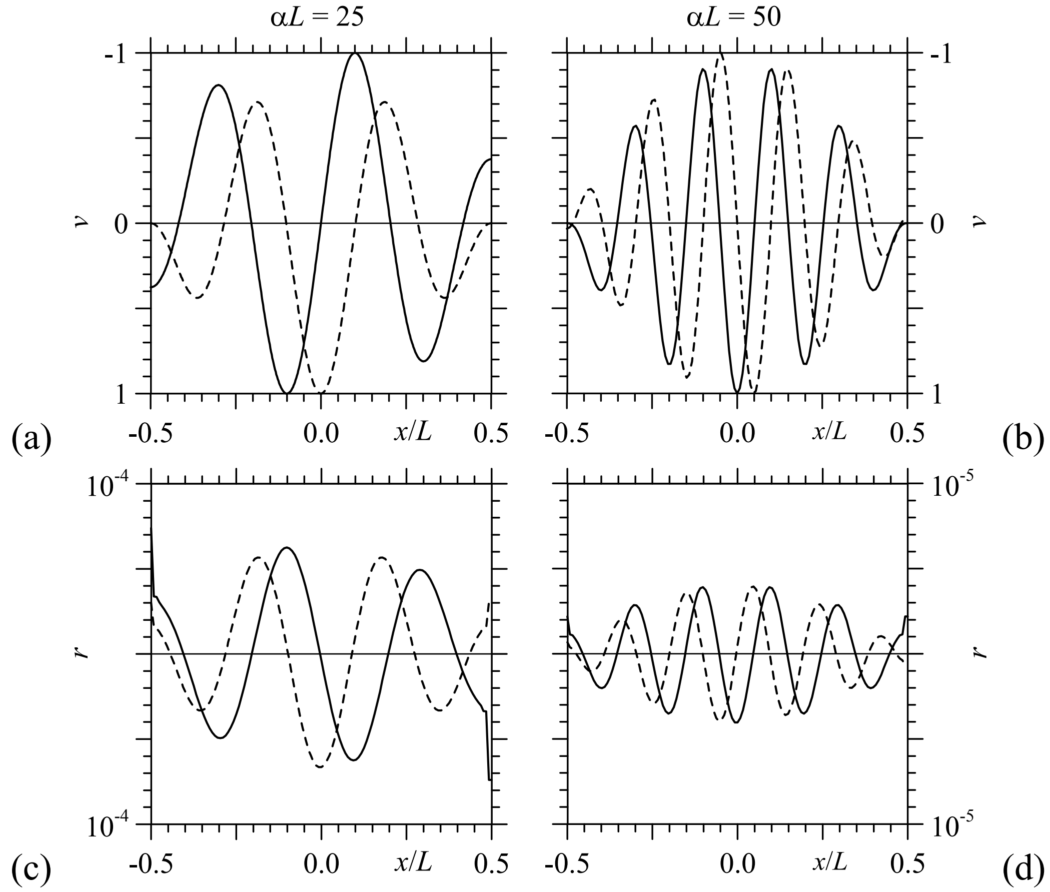

Fig. 1.12 – First (continuous line) and second (dashed line) mode shapes for a beam with sliding ends and αL equal to 25 (a), 50 (b). Soil reactions corresponding to the first (continuous line) and second (dashed line) mode shapes for a beam with sliding ends and αL equal to 25 (c), 50 (d).

The critical wavelength $\Lambda_{\mathrm{cr,R}}$ of the sinusoidal waveform assumed by Reissner (1937) is equal to (Volynskii et al, 2000):

$$\Lambda_{\mathrm{cr,R}} = 2\pi\, h \sqrt[3]{\frac{E_0}{3E}} = \frac{2\pi \sqrt[3]{4}}{\alpha} = \frac{9.97}{\alpha} \;, \tag{1.31}$$

where direct proportionality between the wavelength $\Lambda_{\mathrm{cr,R}}$ and the thickness h of the beam is predicted. Eq. 1.31 was used in advanced metrology methods to measure the elastic modulus of polymeric thin film (Stafford et al, 2004). Excluding the half-waves close to beam ends, the present analysis predicts a constant critical wavelength equal to $\Lambda_{\mathrm{cr,R}}$ for at least the first two mode shapes checked. Thus, the eigenvectors shown in Fig. 1.12b have almost-constant wavelength and variable amplitude, unlike the mode shape assumed in Reissner 1937 (Eq. 1.21), which is sinusoidal with constant amplitude and wavelength.

1.5.2.2 Beam with sliding ends on Winkler-type half-space

The analysis of a beam resting on a Winkler-type half space (1867) is briefly described in the appendix A2. It is well known that the idealized model of half-space proposed by Winkler assumes that the deflection v at a point of the surface is directly proportional to the stress or soil pressure r applied at the same point and independent of stresses applied at other locations:

$$r(x) = c \cdot v(x) \tag{1.32}$$

where c is a constant known as Winkler constant or modulus of subgrade reaction.

Critical loads of a beam with sliding ends on Winkler-type soil are equal to critical loads of a beam with pinned ends and are given by (Hetenyi 1948, Bazant and Cedolin 1991, Wang et al. 2005):

$$P_{\mathrm{cr,W}} = P_{\mathrm{cr,E}}\left[m^2 + \frac{\gamma^2}{m^2 \pi^4} \right] \quad \text{for } m = 1, 2, 3, \ldots \tag{1.33}$$

where

$$\gamma = \sqrt{\frac{c L^4}{D_b}} \tag{1.34}$$

describes the beam-subgrade system for the Winkler-type half-space and it corresponds to αL parameter for the beam resting on half-plane.

Considering the beam discrete model described in §1.3 and applying it to the case of a beam on Winkler-type soil (as shown in the appendix A2), critical loads may be determined and compared with the analytic solution (Eq. 1.33). Figs. 1.13a and b show dimensionless critical loads $P_{\mathrm{cr}}/P_{\mathrm{cr,E}}$, determined with the discrete model adopted, for increasing γ^2 and γ, respectively. Results turn out to be coincident with the analytic solution (Fig. 1.13b).

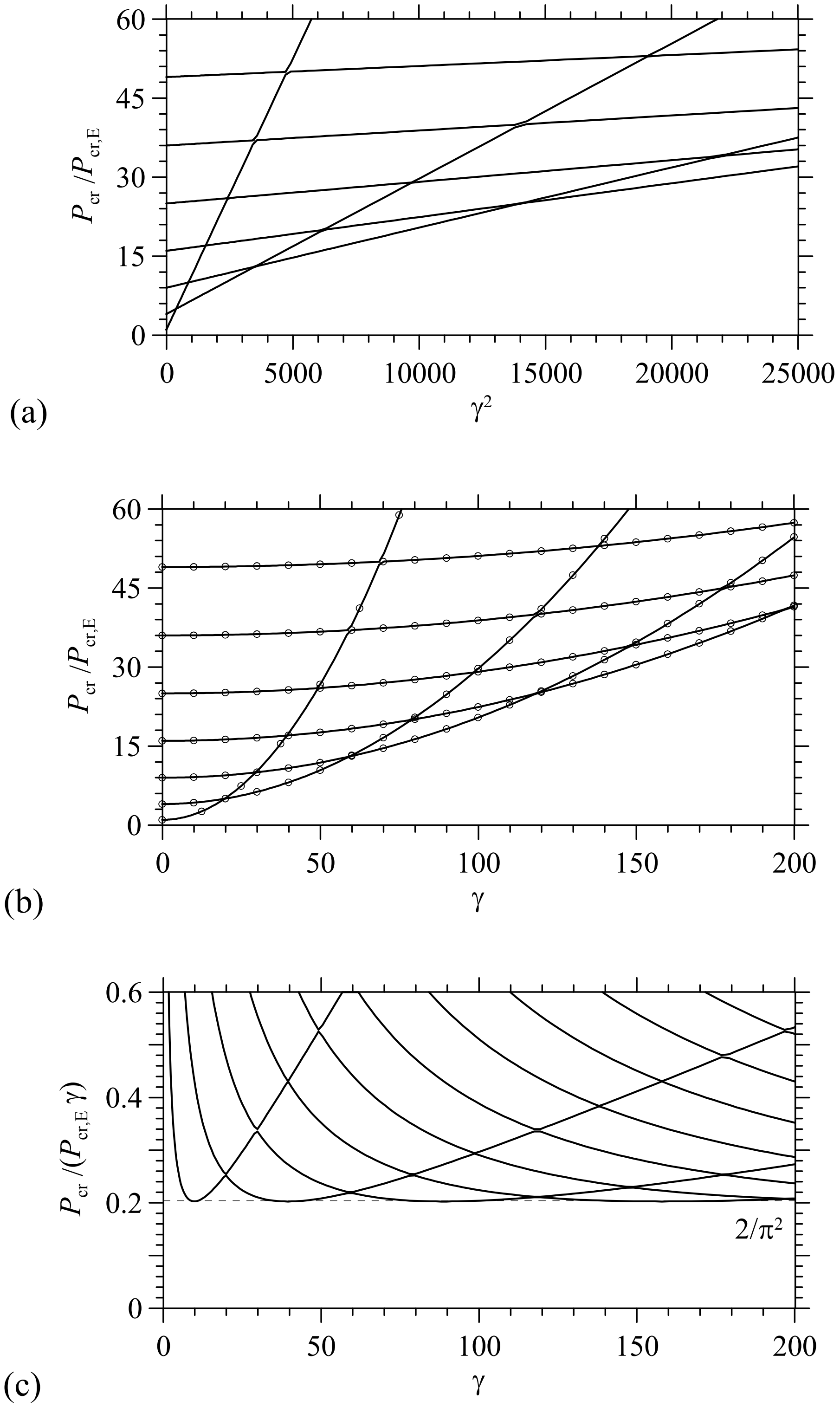

Fig. 1.13 – Dimensionless critical loads P_{cr} (continuous lines) and $P_{cr,W}$ (circles) versus γ for a beam with sliding ends on Winkler-type half space.

Fig. 1.13c shows that dimensionless critical loads are proportional to γ and the smallest critical load tends to:

$$P_{\mathrm{cr,W,min}} = P_{\mathrm{cr,E}} \frac{2\gamma}{\pi^2}, \tag{1.35}$$

which can also be obtained from Eq. 1.33.

The behaviour showed in Figs. 1.13a, b and c is quite similar to the one obtained for the beam on elastic half-plane. In this case, however, curves present crossing points but curve veering is not present. Minimum critical load $P_{\mathrm{cr,W,min}}$ for increasing γ (Eq. 1.35) may be compared with the corresponding one of the beam on half-plane $P_{\mathrm{cr,R}}$ (Eq. 1.27). Then, a ratio between the modulus of subgrade reaction c and half plane modulus E can be determined:

$$P_{\mathrm{cr,E}} \frac{2\gamma}{\pi^2} = P_{\mathrm{cr,E}} \frac{3}{\sqrt[3]{16}\,\pi^2} (\alpha L)^2 \rightarrow c = \frac{9}{2^{14/3}} \left[\frac{E^4\, b^4}{D_b} \right]^{1/3} = 0.354 \left[\frac{E^4\, b^4}{D_b} \right]^{1/3}. \tag{1.36}$$

The coefficient in Eq. 1.36 is larger than the one obtained by Biot (1937), who determined the relation between the foundation modulus c and the half plane modulus E in order to obtain the same maximum bending moment of an infinite beam loaded by a concentrated force at midpoint:

$$c = \frac{0.710}{2^{4/3}} \left[\frac{E^4\, b^4}{D_b} \right]^{1/3} = 0.282 \left[\frac{E^4\, b^4}{D_b} \right]^{1/3}. \tag{1.37}$$

However, if results showed in Figs. 1.13a, b and c are scaled taking into account Eq. 1.36, minimum critical loads tend to be coincident with the ones obtained for the beam on elastic half-plane for large values of αL (Fig. 1.14).

Figs. 1.15a and b show the first and second mode shapes for γ equal to 15 and 400, which correspond to αL close to 5 and 25, respectively (Eq. 1.36). For the case of a beam resting on soft support (Fig. 1.15a), the first and second mode shapes are characterized by one and two half-waves, respectively, and they are almost coincident with results obtained for the beam resting on half-plane (Fig. 1.10a). For a beam resting on stiff support (Fig. 1.15b), the first and second mode shapes are sinusoidal with constant wavelength and amplitude, whereas the corresponding case for beam resting on half-plane is characterized by sinusoidal mode shapes with different amplitude along beam length (Fig. 1.12a).

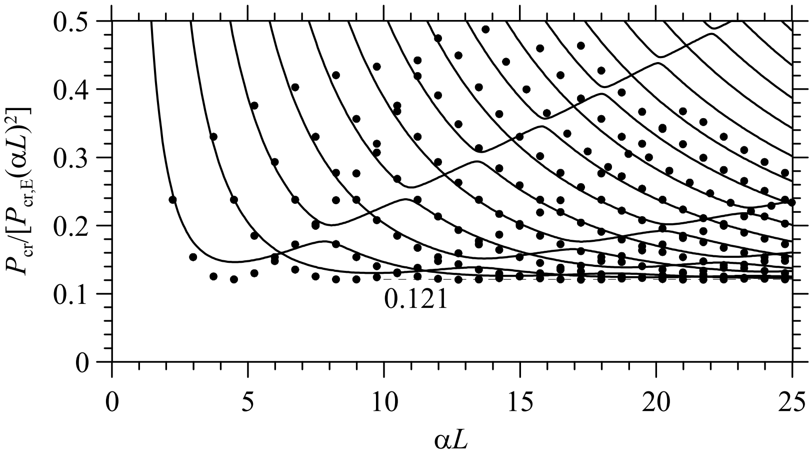

Fig. 1.14 – Dimensionless critical loads Pcr for a beam with sliding ends on elastic half plane (continuous lines) and on Winkler half-space (dots).

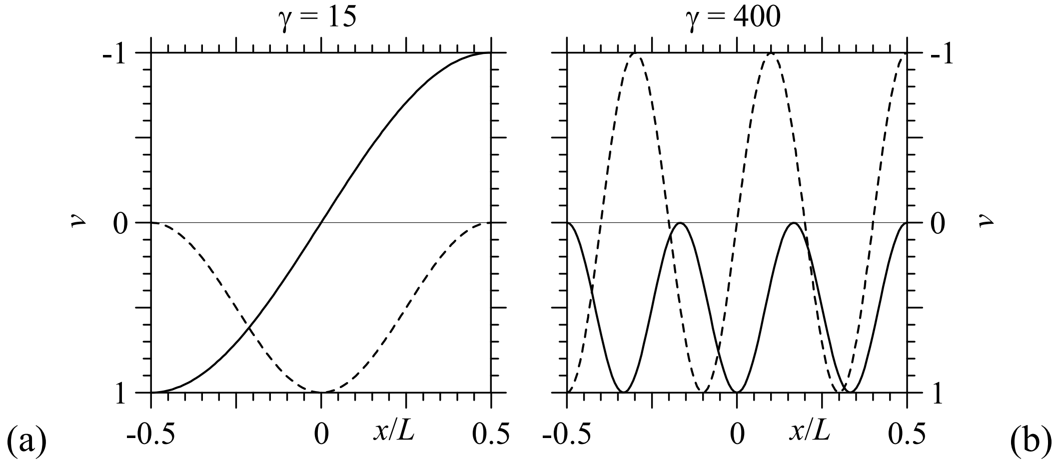

Fig. 1.15 – First (continuous line) and second (dashed line) mode shapes for a beam with sliding ends on Winkler-type half-space for γ = 15 (a) and 400 (b).

1.5.3 Beam of finite length with pinned ends

The case of a foundation beam with pinned ends (Fig. 1.16) may refer to a rigid portal frame whose columns are hinged to the foundation beam; thus, the structure enforces zero relative displacement between beam ends, but allows independent rotations.

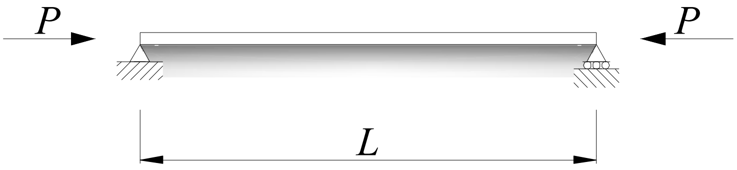

Fig. 1.16 – Beam with pinned ends subject to axial load *P*.

It is worth noting that the constraint equations must not be the typical equations of a beam with simple supported ends $R_1 = v(L/2) = 0$, $R_2 = v(-L/2) = 0$, because the behaviour of a beam on 2D half-plane is always characterized by a rigid body displacement, which cannot be set equal to zero a priori. Then, the constraint equation that has to be applied to Eq. 1.6 is $R_1 = v(L/2) - v(-L/2) = 0$. Adopting a penalty parameter $k = 10^6\, D_b/L^3$, an error less than 10^{-3} is obtained for the first ten eigenvectors.

In Figs. 1.17a and b, the first seven dimensionless buckling loads $P_{\text{cr}}/P_{\text{cr,E}}$ are plotted versus the parameter αL^3 and αL, respectively. For $\alpha L = 0$, numerical results coincide both with critical loads of a beam with pinned ends and with analytic solutions given by Reissner's solution (Eq. 1.26), moreover for low αL values, numerical results are quite close to Reissner's solution (dashed lines). For increasing αL, Figs. 1.17a and b show that the first and second critical loads tend to separate from other critical loads and the corresponding values are lower than Eq. 1.26, which correspond to the values obtained for the beam with sliding ends.

On the other hand, the third and fourth eigenvalues remain close to Reissner's solution (dashed lines), and the curves after the third one are characterised by veering and crossing points, similarly to the previous case of a beam with sliding ends.

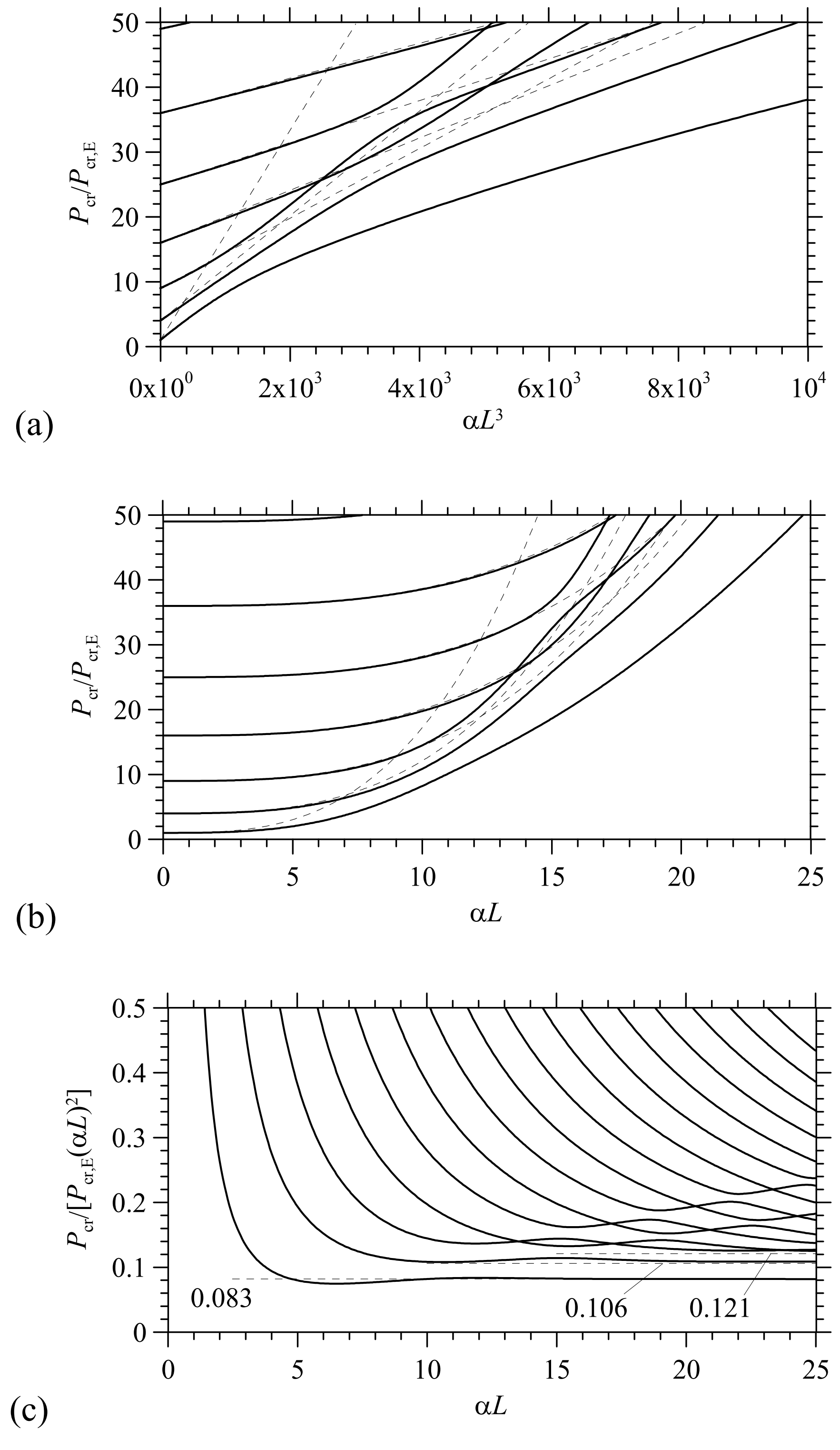

Fig. 1.17 – Dimensionless critical loads P_{cr} (continuous lines) and $P_{\mathrm{cr},m}$ (dashed lines) versus αL for a beam with pinned ends.

Fig. 1.17c shows the ratio $P_{cr}/[P_{cr,E}\,(\alpha L)^2]$ versus the parameter αL; for increasing αL the first and the second eigenvalues converge to:

$$P_{cr,1} = 0.083\,P_{cr,E}\,(\alpha L)^2, \tag{1.38}$$

$$P_{cr,2} = 0.106\,P_{cr,E}\,(\alpha L)^2, \tag{1.39}$$

whereas the third and fourth critical loads turn out to be very close to Reissner's solution and converge to Eq. 1.27. Therefore, the existence of critical loads lower than $P_{cr,R}$ in Eq. 1.27 is clearly shown. In particular, Eqs. 1.38 and 1.39 yield the following critical stresses:

$$\sigma_{cr,1} = \frac{P_{cr,1}}{b\,h} = 0.36\,E^{2/3}\,E_0^{1/3}. \tag{1.40}$$

$$\sigma_{cr,2} = \frac{P_{cr,2}}{b\,h} = 0.46\,E^{2/3}\,E_0^{1/3}. \tag{1.41}$$

which may be very important for the design of sandwich panels.

1.5.3.1 Modal shapes

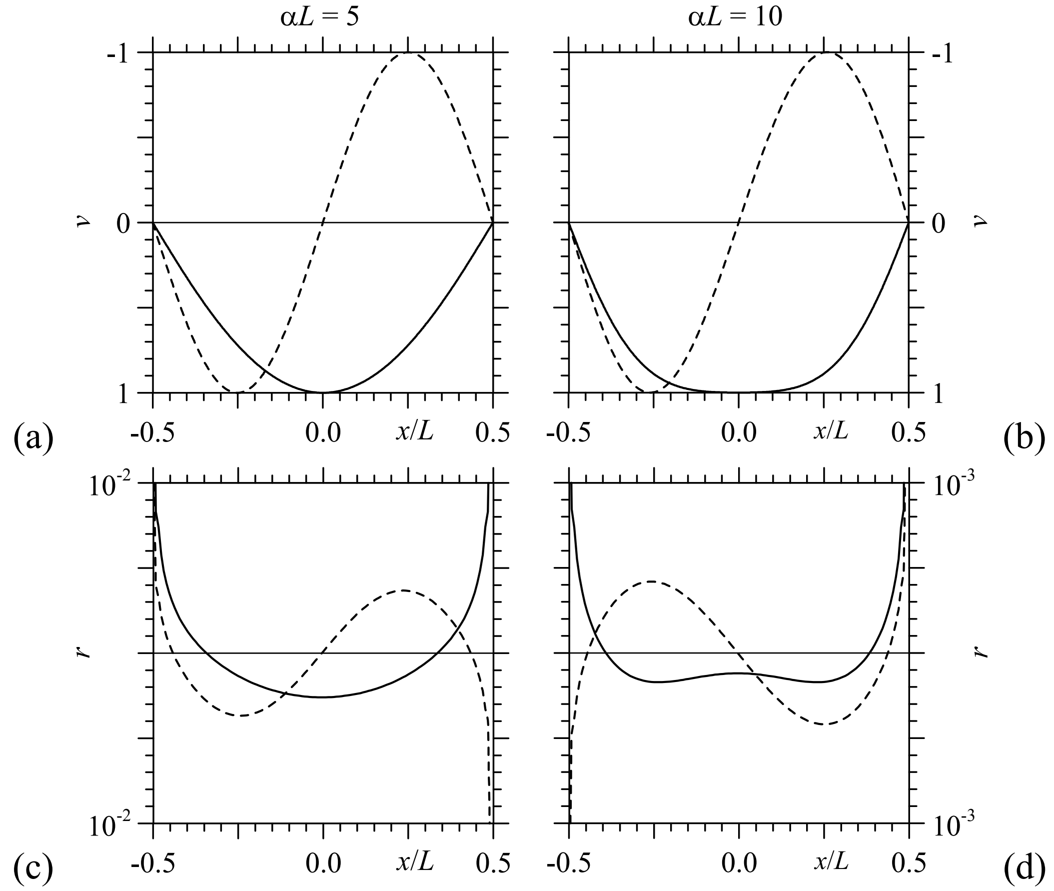

Fig. 1.18 – First (continuous line) and second (dashed line) mode shapes for a beam with pinned ends and αL equal to 5 (a), 10 (b). Soil reactions corresponding to the first (continuous line) and second (dashed line) mode shapes for a beam with pinned ends and αL equal to 5 (c), 10 (d).

For αL = 5, Fig. 1.18a shows that the first and second mode shapes present one and two half-waves, respectively, and they are clearly sinusoidal. For αL = 10 (Fig. 1.18b) the first mode shape is quite different from the one obtained for αL = 5 and it can not be described by a sine or cosine function, while the second mode shape is, indeed, sinusoidal with two half-waves. The difference between the first mode shapes obtained for αL = 5 and 10 can be described considering Figs. 1.17a and b. For αL = 5, the first and second critical loads are still in good agreement with Reissner's solution (Eq. 1.26), whereas for αL = 10 the first critical load is lower than Eq. 1.26.

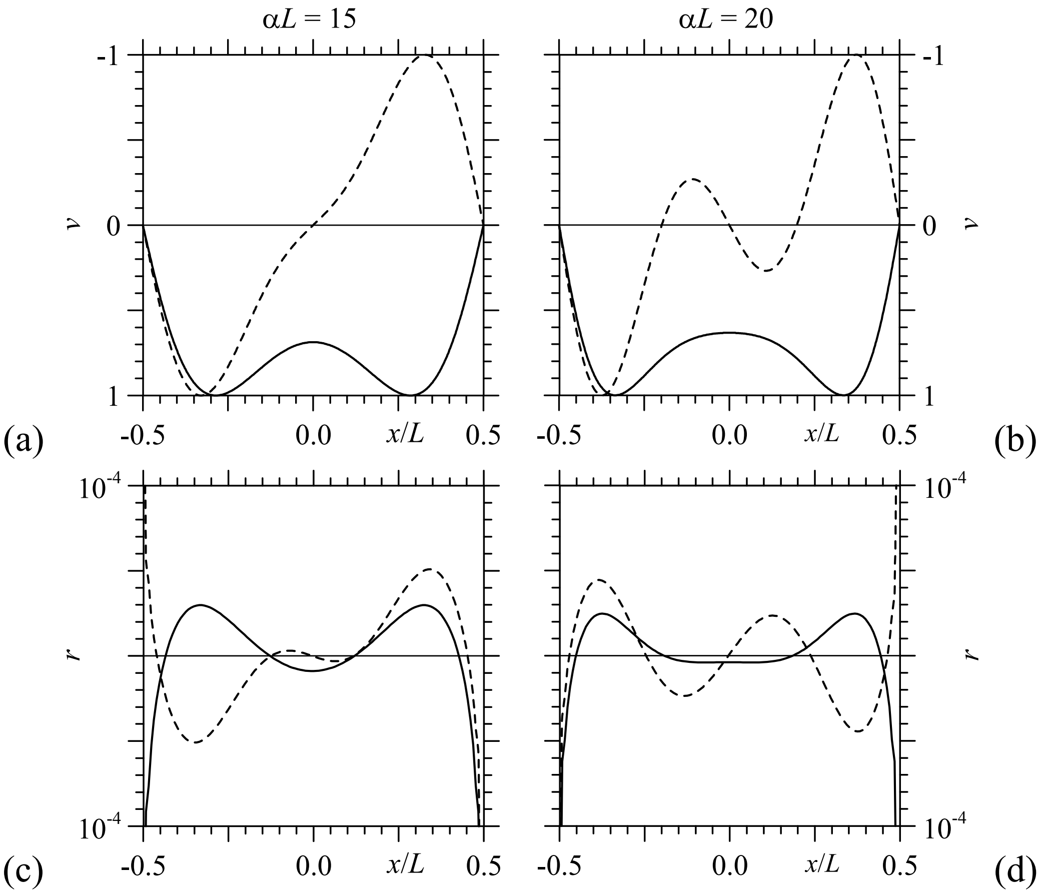

Fig. 1.19 – First (continuous line) and second (dashed line) mode shapes for a beam with pinned ends and αL equal to 15 (a), 20 (b). Soil reactions corresponding to the first (continuous line) and second (dashed line) mode shapes for a beam with pinned ends and αL equal to 15 (c), 20 (d).

For increasing αL (Figs. 1.19a and b), half-waves cannot be easily defined like in previous cases and buckling modes have large amplitudes near beam ends. Indeed, the critical loads in Eqs. 1.38 and 1.39 correspond to these localized buckling modes. It is interesting to note that the first mode shapes shown in Figs 1.18-1.20 are symmetric, whereas the second mode shapes are antisymmetric and, in fact, the first and second curves in Figs. 1.17a, b and c do not have any intersection point.

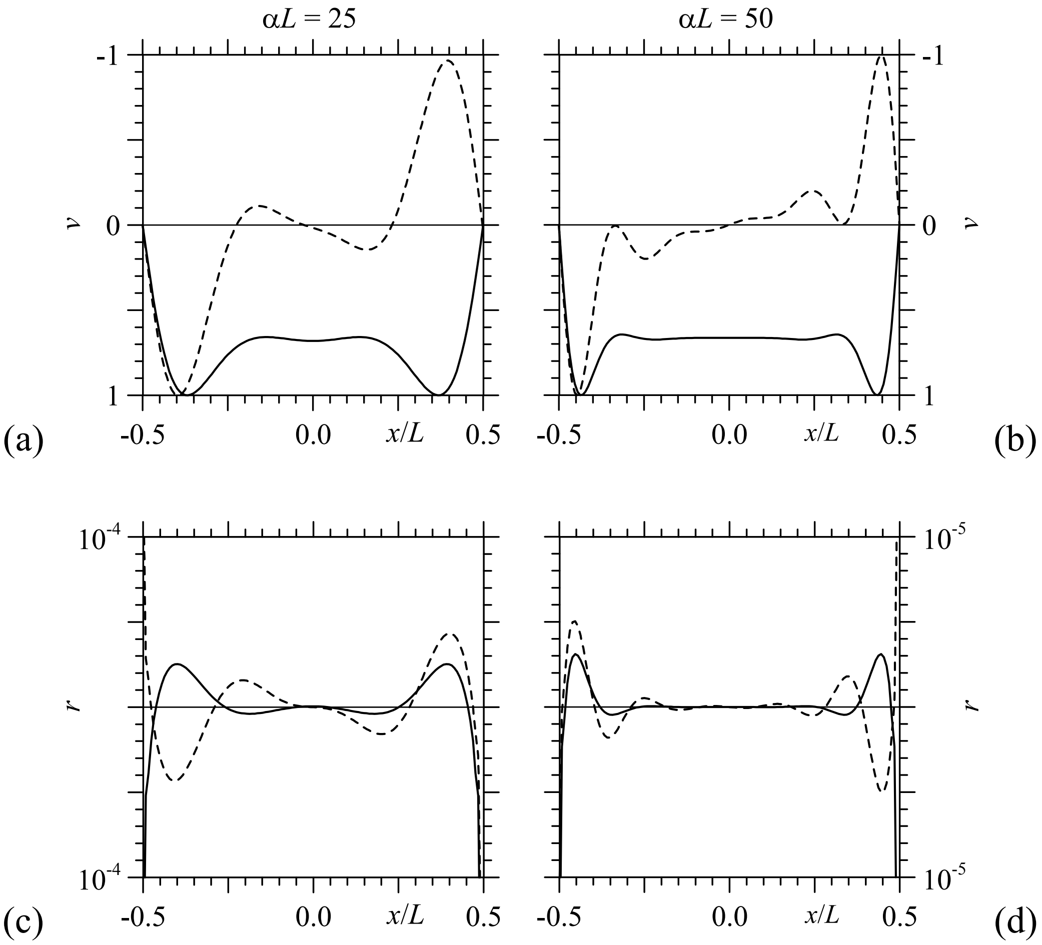

Fig. 1.20 – First (continuous line) and second (dashed line) mode shapes for a beam with pinned ends and αL equal to 25 (a), 50 (b). Soil reactions corresponding to the first (continuous line) and second (dashed line) mode shapes for a beam with pinned ends and αL equal to 25 (c), 50 (d).

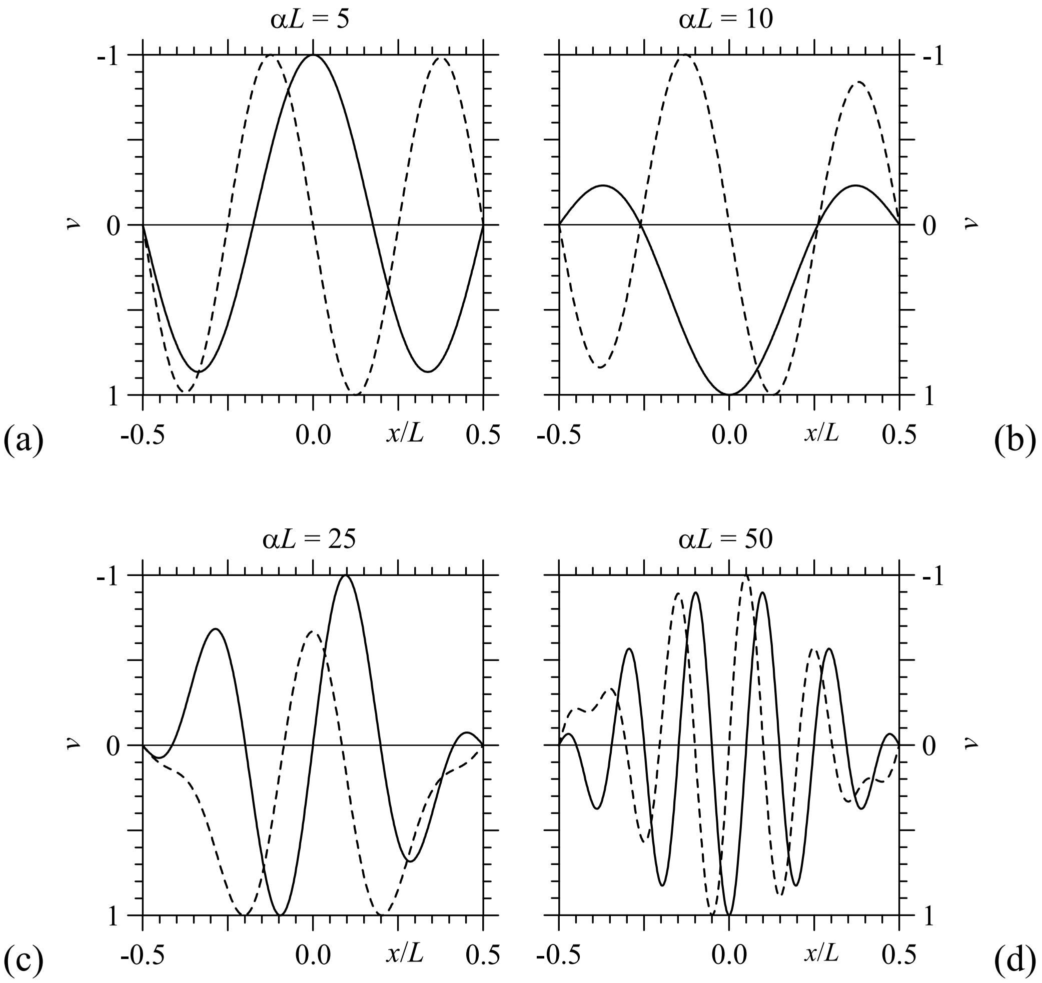

Fig. 1.21 – Third (continuous line) and fourth (dashed line) mode shapes for a beam with pinned ends and αL equal to 5 (a), 10 (b), 25 (c) and 50 (d).

The first and second eigenvectors are different than the following ones, in fact Figs. 1.21a-d show the third and fourth mode shapes for increasing αL values, which are sinusoidal with increasing half-waves number and varying amplitude along beam length. For αL = 25 and 50 (Figs. 1.21c, d), the third and fourth mode shape, excluding deformations at beam ends, are quite similar to the first and second mode shapes obtained for the beam with sliding ends (Figs. 1.12a and b). Then, the behaviour of a beam with pinned ends on elastic half-space is found to be quite different from the previous case of beams with sliding ends, which does not present localized eigenmodes for increasing values of αL (long beam and/or stiff soil).

As for Winkler soils, reference is usually made to Hetenyi (1946), where the solution of the beam with pinned ends converges to the same critical load of the beam with clamped ends (Hetenyi 1946, Simitses 1976). Nonetheless, for beams on Winkler soil with pinned ends, Goodier and Hsu (1954) reported the presence of mode shapes localized at beam ends.

1.5.3.2 Bosakov's solution (1994)

The stability of a beam with pinned ends resting on elastic half-plane was studied by Bosakov (1994) by adopting symmetric cosine functions:

$$P_{\mathrm{cr,B}} = P_{\mathrm{cr,E}}\left[(2m+1)^2 + \frac{2(\alpha L)^3}{(2m+1)\pi^3}F(m,m,0)\right] \quad \text{for } m = 0, 1, 2, \ldots \tag{1.42}$$

where $F(m, m, 0)$ is a function reported in the original paper (Bosakov 1994), based on Bessel functions of the first kind. Eq. 1.42 is compared with critical loads obtained with the present model and results are shown in Figs. 1.22a and b.

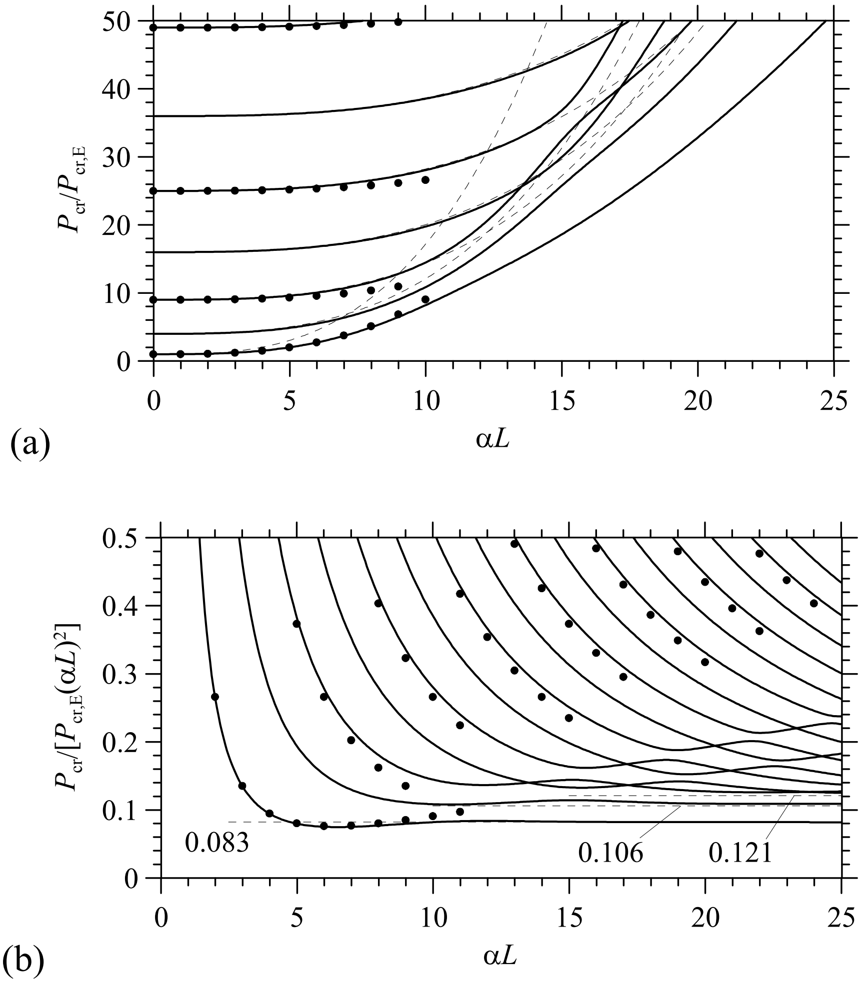

Fig. 1.22 – Dimensionless critical loads P_{cr} (continuous lines), $P_{\mathrm{cr},m}$ (dashed lines) and $P_{\mathrm{cr,B}}$ (dots) versus αL for beam with pinned ends.

The first buckling load is well approximated by Eq. 1.42 for α*L* < 7 (see dots in Figs. 1.22a and b), and by Eq. 1.26 for α*L* < 3. Moreover, Figs. 1.22a, b and c show that Eq. 1.42 is unable to provide eigenvalues corresponding to antisymmetric buckling and for large values of α*L*, as Bosakov's solution is not able to provide the first and second critical loads obtained with the present model.

1.5.3.3 Gallagher's solution (1974)

Another solution for the buckling of a beam with pinned ends under axial compression on elastic half-plane was determined by Gallagher (1974). The solution is based on Chebyshev polynomials of the first and second kind:

$$T_r = \cos r\theta, \quad U_r = \frac{\sin[(r+1)\theta]}{\sin\theta} \tag{1.43a,b}$$

and considering separately the even modes (Eq. 1.44) and the odd modes (Eq. 1.45) of buckling.

$$v'(\xi) = \sum_{n=1}^{\infty} a_{2n-1} T_{2n-1}(\xi) \tag{1.44}$$

$$v'(\xi) = \sum_{n=0}^{\infty} a_{2n} T_{2n}(\xi) \tag{1.45}$$

where $\xi = 2x/L$ and prime represents differentiation with respect to *x*.

The relation between beam displacement and half-space pressure considered by Gallagher is given by the following relation (Muskhelishvili 1963):

$$r(x) = \frac{E_0}{2\pi}\sqrt{L^2 - 4x^2} \int_{-L/2}^{L/2} \frac{v'(\hat{x})}{\sqrt{L^2 - 4\hat{x}^2}\,(\hat{x} - x)} d\hat{x} \tag{1.46}$$

Gallagher adopted the same beam-subgrade parameter α*L* considered in the present model and determined numerically the first six eigenvalues by substituting Eqs. 1.44, 1.45 and 1.46 in the differential equation of the beam on elastic half-plane with second order effects due to the axial load *P*. The author stopped the series in Eqs. 1.44 and 1.45 at $n = 36$ and found a linear relationship between critical loads and αL^3, but only for certain ranges of α*L*, depending on the mode. Moreover, considering even modes and odd modes separately, the curves corresponding to dimensionless critical loads (λ, αL^3 or λ, αL) never intersect. However, for simplicity, the following relation between critical loads and αL was adopted to describe the results:

$$P_{\mathrm{cr,G}} = P_{\mathrm{cr,E}}\left[m^2 + \frac{(\alpha L)^3}{2\pi^2} C_m\right] \quad \text{for } m = 1, 2, 3, \ldots \tag{1.47}$$

where C_m is a constant depending on the mode number; the values of $(m\pi/2)^2 C_m$ are listed in Tab. 1.4 for the first six buckling modes.

m	1	2	3	4	5	6
$\left(\frac{m\pi}{2}\right)^2 C_m$	1.05	1.77	2.66	3.39	4.23	4.97

Tab. 1.4 – Values of $(m\pi/2)^2 C_m$ for the first six buckling modes (Gallagher 1974).

Figs. 1.23 a, b and c show critical loads given by Eq. 1.47 with triangles, and these results are compared with the ones obtained with the present model for the same beam case (continuous lines, as already shown in Figs. 1.17a, b and c). It is clear that $P_{\mathrm{cr,G}}$ (Eq. 1.47) for m = 1, 2 does not converge to the first and second eigenvalues obtained with the present model, but it converges to the third and fourth eigenvalues. Moreover, Fig. 1.23c clearly shows that minimum values of $P_{\mathrm{cr,G}}$ (Eq. 1.47) converge to Eq. 1.27 for increasing αL.

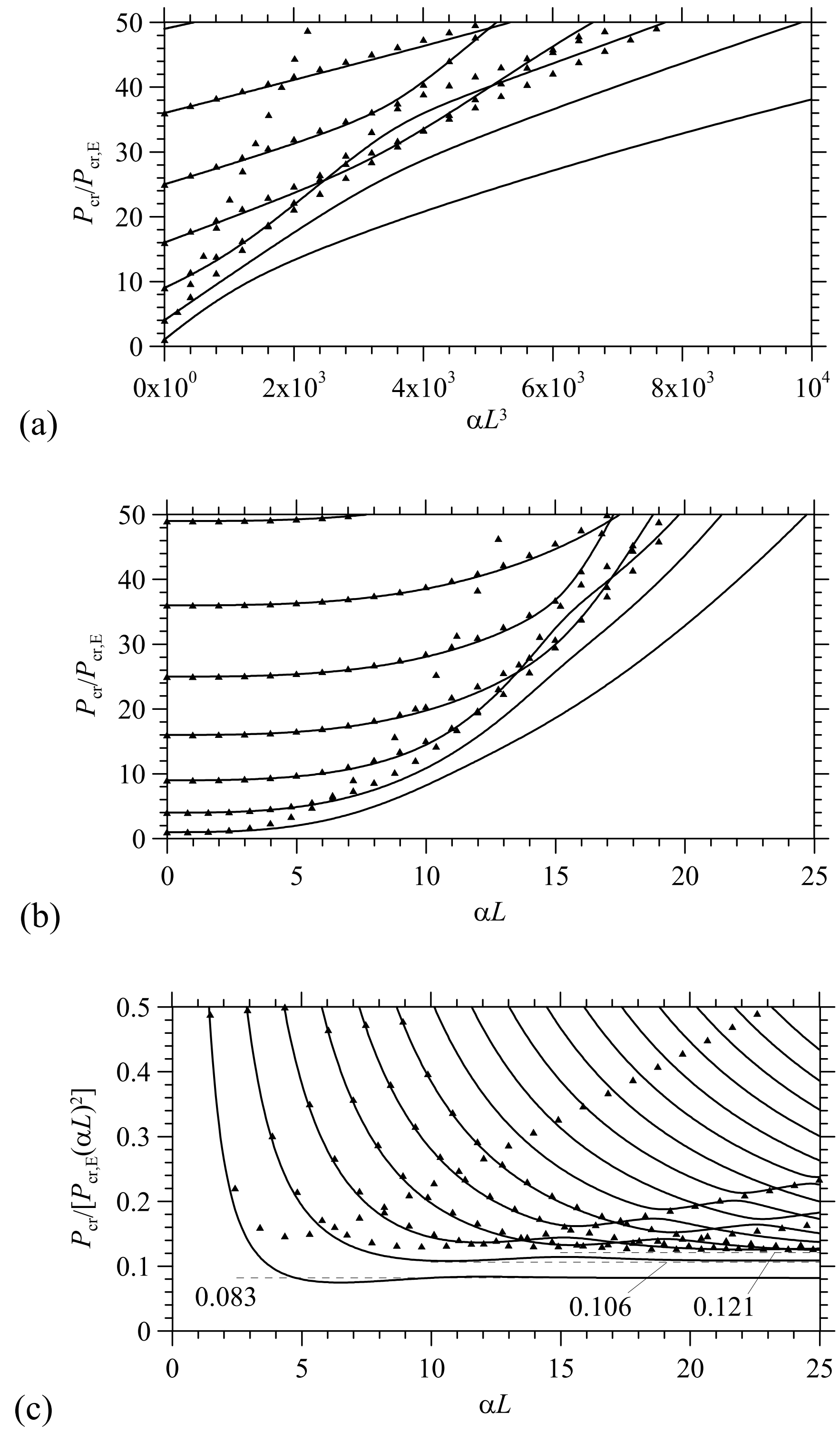

Fig. 1.23 – Dimensionless critical loads P_{cr} (continuous lines) and $P_{cr,G}$ (triangles) versus αL for a beam with pinned ends.

The critical loads determined by Gallagher are found to be very close to the ones obtained for the case of a beam with sliding ends. Figs. 1.24a and b show $P_{cr,G}$ (Eq. 1.47) with triangles which are practically coincident with the dimensionless critical loads already shown in Figs. 1.8b and c (continuous lines). The solution proposed by Gallagher is not able to describe the buckling localized at beam ends (Figs 1.20a and b), which characterizes the first and second critical loads for increasing αL.

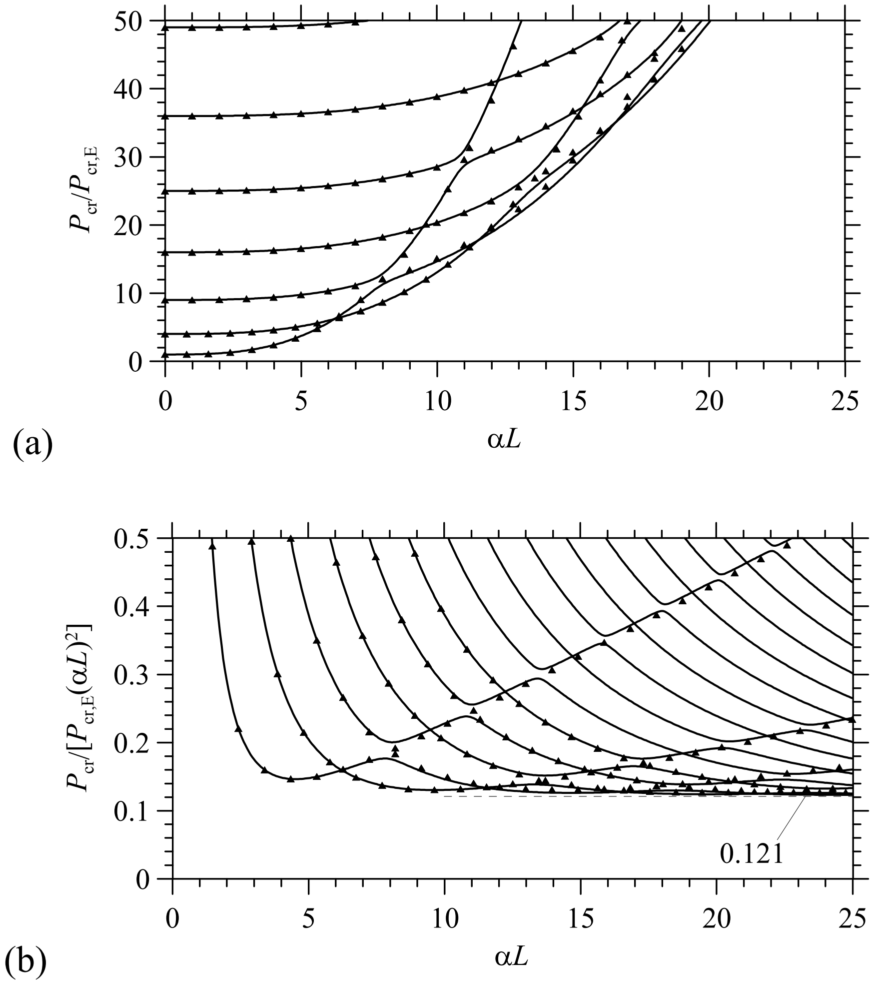

Fig. 1.24 – Dimensionless critical loads P_{cr} (continuous lines) for a beam with sliding ends and $P_{cr,G}$ (triangles) versus αL for a beam with pinned ends.

1.5.3.4 Beam with pinned ends on Winkler-type half-space

The most known solution for the buckling of a beam with pinned ends on Winkler-type half-space is coincident with the one defined for the beam with sliding ends (Eq. 1.33, Hetenyi 1948, Timoshenko and Gere 1961, Wang et al. 2005). However, this solution is obtained by satisfying the boundary condition $v(-L/2) = v(L/2) = 0$, which neglects rigid body displacement a priori.

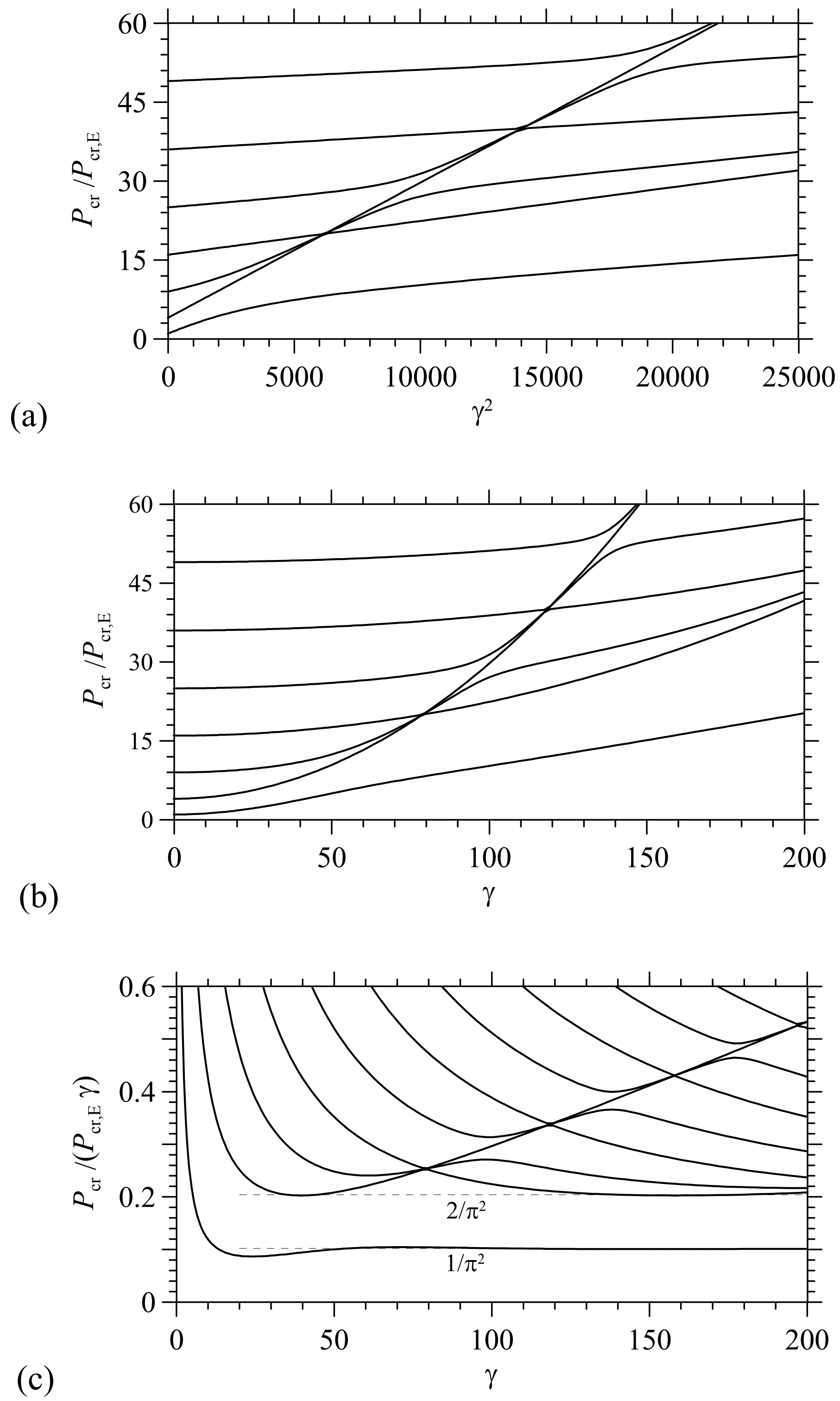

Fig. 1.25 – Dimensionless critical loads P_{cr} versus γ for a beam with pinned ends on Winkler-type half space.

If the condition $v(-L/2) = v(L/2)$ is adopted, critical loads turn out to be different than Eq. 1.33. Figs. 1.25 a and b show dimensionless critical loads $P_{\mathrm{cr}}/P_{\mathrm{cr,E}}$, determined with the discrete model adopted, for increasing γ^2 and γ, respectively, whereas Fig. 1.25 c shows the ratio $P_{\mathrm{cr}}/(P_{\mathrm{cr,E}}\,\gamma)$ for increasing γ. It is clear that the first critical load increasing γ is less than the other critical loads, which, moreover, turns out to converge to one half of the first critical load of a beam with sliding ends:

$$P_{\mathrm{cr,W,1}} = P_{\mathrm{cr,E}} \frac{\gamma}{\pi^2}, \tag{1.48}$$

whereas second and third critical loads converge to Eq. 1.35.

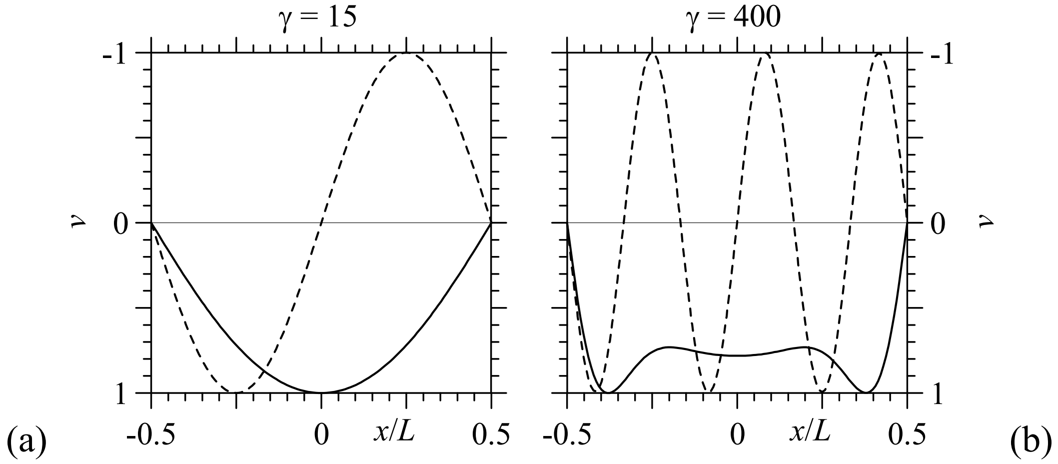

Fig. 1.26 – First (continuous line) and second (dashed line) mode shapes for a beam with pinned ends on Winkler-type half-space for γ = 15 (a) and 400 (b).

Considering a beam resting on soft support, Fig. 1.26a shows the first and second mode shapes which are characterized by one and two half-waves, respectively, and are almost coincident to the results obtained for the beam resting on elastic half-plane. However, for a beam resting on stiff support, Fig. 1.26b shows that the first mode shape is symmetric and characterized by large deflections close to beam ends, whereas the second mode shape is sinusoidal with almost constant amplitude and wavelength. The first mode shape for the stiffer support case can not be represented by sinusoidal functions, which behaviour was depicted by Goodier and Hsu (1954) studying the nonsinusoidal buckling modes of sandwich plates.

Considering the first critical load and the corresponding mode shape for increasing γ, the buckling of a beam with pinned ends on Winkler-type half-space is quite similar to the buckling of the same beam on elastic half-plane. In this case, however, an antisymmetric buckling mode with large deflections close to beam ends is not present.

1.5.4 Beam of finite length with free ends

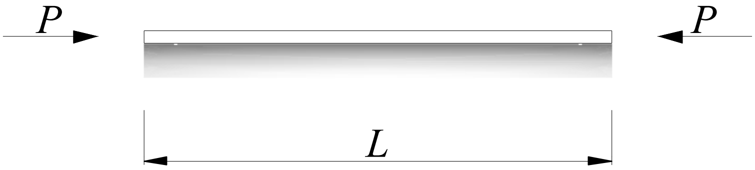

Fig. 1.27 – Beam with free ends subject to axial load *P*.

The stability of a beam with free ends on elastic half-plane (Fig. 1.27) is then considered. In Figs. 1.28a and b, dimensionless critical loads $P_{cr}/P_{cr,E}$ are plotted versus αL^3 and αL values, respectively; the dashed line shows the function given by Eq. 1.27. Fig. 1.28c shows the ratio $P_{cr}/[P_{cr,E}\,(\alpha L)^2]$ versus the parameter αL. Similarly, in the case of the beam with pinned ends, the first and second eigenvalues appear quite far from other results, whereas the third and fourth eigenvalues are close to Reissner's solution and converge to the value given in Eq. 1.27. In this case, however, for increasing αL, the first and second critical loads are coincident and converge to $P_{cr,1}$ (Eq. 1.38), obtained for the beam with pinned ends. In fact, it is worth noting that a beam with free ends and symmetrical behaviour is practically coincident with a beam with pinned ends.

It is interesting to observe that the first and second eigenvalues are quite different for the very small values of αL and present some intersection points, which are presented in Tab. 1.5, whereas for $\alpha L \geq 10$, they both converge to the value given in Eq. 1.38. The other critical loads present crossing points and veering, similarly to the beam with sliding ends case.

point	1	2	3
αL	4.500	10.514	15.217
$P_{cr}/P_{cr,E}$	1.728	9.157	19.115

Tab. 1.5 - Coordinates of the first three crossing points between the first and second eigenvalues.

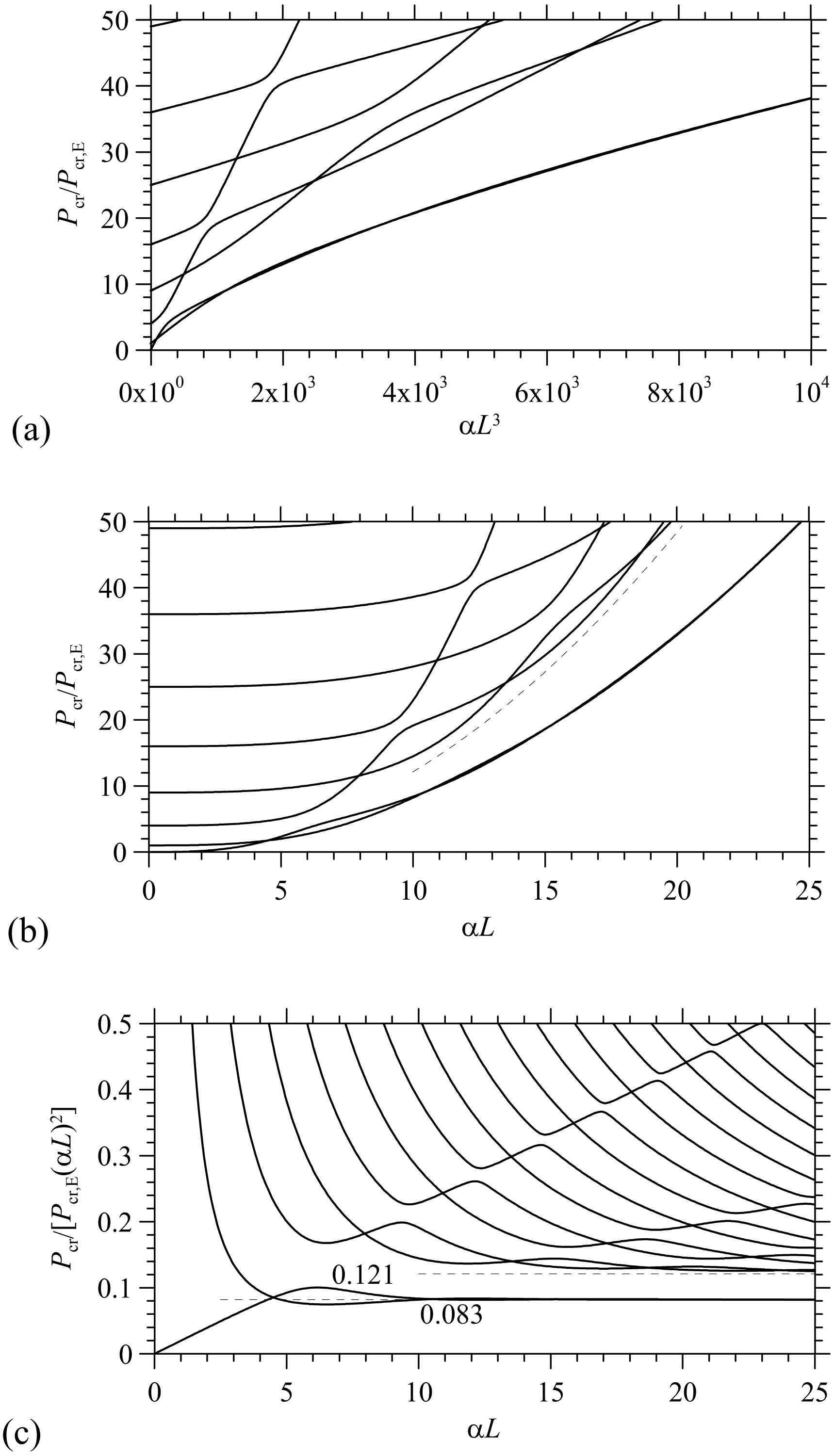

Fig. 1.28 – Dimensionless critical loads P_{cr} (continuous lines) and $P_{cr,R}$ (dashed line) versus αL for beam with free ends.

1.5.4.1 Modal shapes

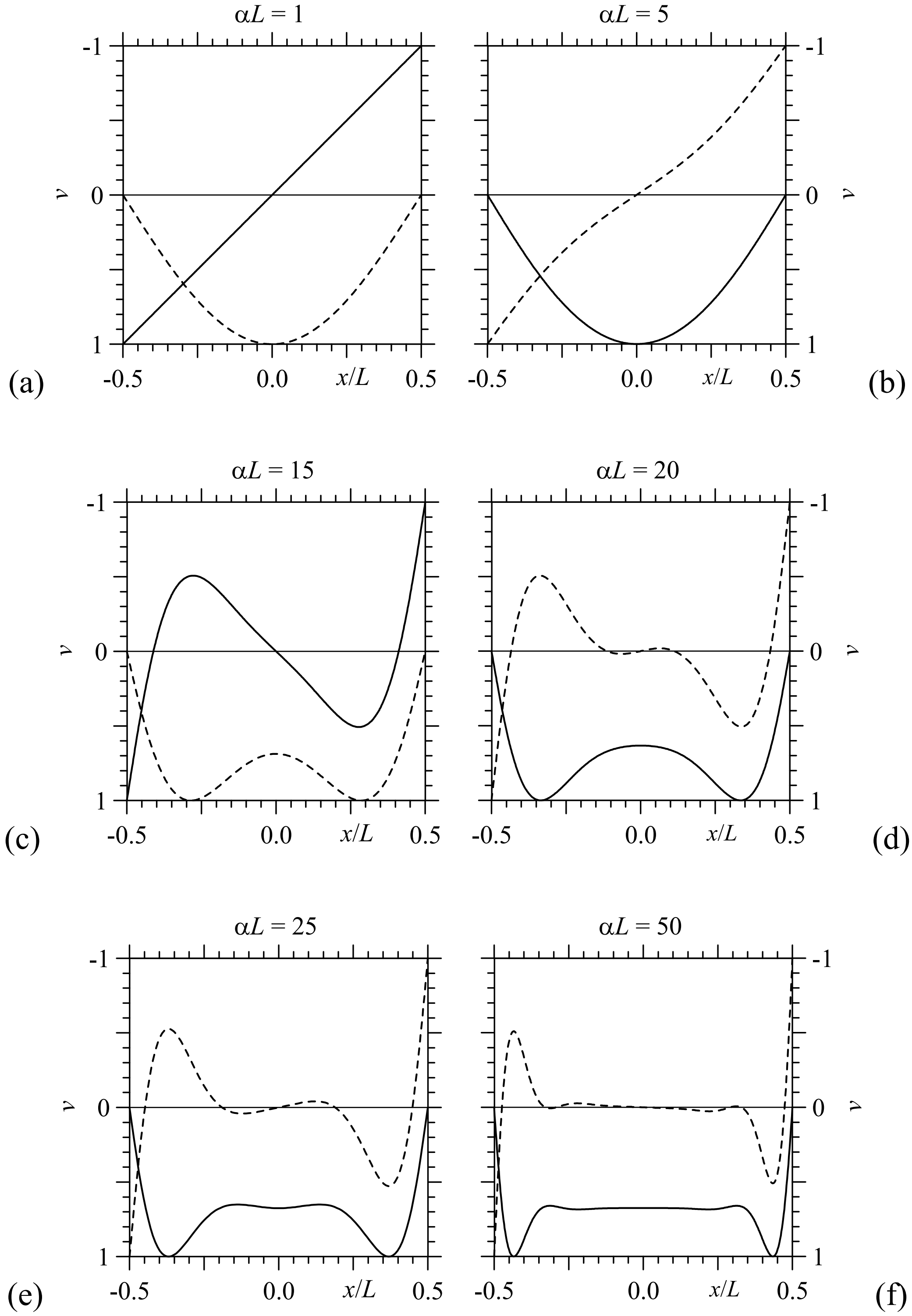

Fig. 1.29 – First (continuous line) and second (dashed line) mode shapes for a beam with free ends and αL equal to 1 (a), 5 (b), 10 (c), 20 (d), 25 (e) and 50 (f).

In absence of soil, the critical load value of a beam with free ends is obviously zero, but for very short beams or very soft soil ($\alpha L = 1$), the first mode shape is antisymmetric and represents a rigid body rotation, whereas the second one is symmetric and sinusoidal with one half-wave (Fig. 1.29a). For α*L* = 5, after the first crossing point, the first mode shape becomes symmetric and the second one antisymmetric (Fig. 1.29b). For α*L* = 15, after the second crossing point, the first mode shape is again antisymmetric and the second one is symmetric (Fig. 1.29c). For α*L* ≥ 15, the first and second critical loads are very close to the one given in Eq. 1.38 and both mode shapes tend to have large displacements localized near the beam ends, as shown for α*L* = 20, 25 and 50 in Figs. 1.29d, e and f, respectively, where the first mode shape is coincident with the one found for the beam with pinned ends (Fig. 1.20a).

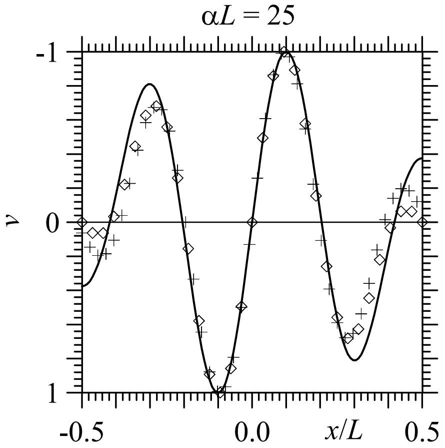

Fig. 1.30 – First mode shape for a beam with sliding ends (continuous line), and third mode shape for beam with pinned (symbol ◊) and free (symbol °) ends resting on stiff soil (α*L* = 25).

Fig. 1.30 shows the first mode shape for a beam with sliding ends and the third mode shape for beams with pinned and free ends resting on stiff soil (α*L* = 25). Eigenvectors are practically coincident in the neighbourhood of beam midpoint and present small differences at beam ends, due to the different restraints.

The behaviour of the beam with free ends resting on elastic half-space is quite similar to the corresponding case of the beam on Winkler soil, where the first and second critical loads converge to one half of the smallest critical load of a beam with clamped or sliding ends (Hetenyi 1946, Simitses 1976, Bazant and Cedolin 1991), as shown in the following paragraph.

1.5.4.2 Beam with free ends on Winkler-type half-space

Critical loads of a beam with free ends on a Winkler-type half space have to satisfy the following condition (Hetenyi 1948):

$$\frac{\sin(1/2\,\sqrt{2\gamma+\lambda})}{\sinh(1/2\,\sqrt{2\gamma-\lambda})} = \pm\frac{(\gamma-\lambda)\,\sqrt{2\gamma+\lambda}}{(\gamma+\lambda)\,\sqrt{2\gamma-\lambda}}, \tag{1.49}$$

Where γ is defined by Eq. 1.34 and λ is given by Eq. 1.15a. The above expression ensues from the solution of the differential equation of a beam on Winkler foundation subject to axial load.

Figs. 1.31a and b show dimensionless critical loads $P_{cr}/P_{cr,E}$, determined with the discrete model adopted, for increasing γ^2 and γ, respectively, whereas Fig. 1.31c shows the ratio $P_{cr}/(P_{cr,E}\ \gamma)$ for increasing γ. Results satisfy Eq. 1.49. In this case, the first and second critical loads are less than other results and interchange themselves up to γ close to 100; then, they tend to coincide and converge to $P_{crW,1}$. It is clear that the second critical load is coincident with the first critical load for the beam with pinned ends. Other critical loads are characterized by curve veering. Third and fourth critical loads converge to $P_{cr,W}$ for increasing γ.

The first mode shape for a stiff beam resting on soft support represents a rigid rotation, whereas the second mode shape is sinusoidal with one half-wave (Fig. 1.32a). For γ equal to 15, the first mode shape is sinusoidal and the second one is antisymmetric (Fig. 1.32b). For a beam resting on quite stiff soil, the first and second mode shapes are not sinusoidal and are characterized by large deflections close to beam ends (Fig. 1.32c). Finally, for a beam resting on very stiff soil, the first and second mode shapes present large deflections at beam ends and negligible deflections close to beam midpoint (Fig. 1.32d). It is clear that the first and second mode shapes for increasing γ present a behaviour similar to the corresponding ones of the beam with free ends on elastic half-plane. However, adopting the relation between c and E determined by Biot (1937) or determined for the beam with sliding ends, $P_{cr,W,1}$ turns out to be different than $P_{cr,1}$ (Eq. 1.38).

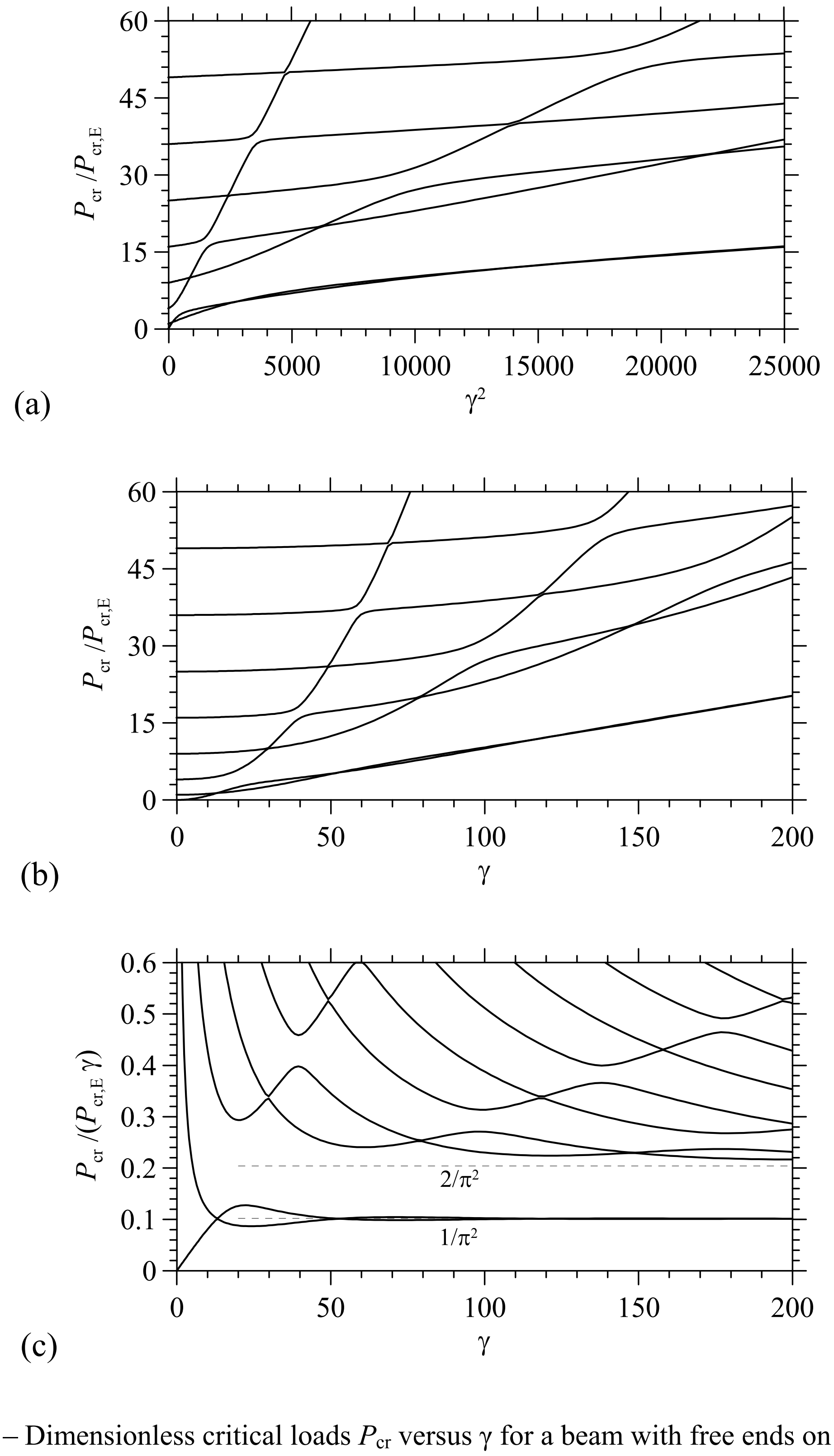

Fig. 1.31 – Dimensionless critical loads P_{cr} versus γ for a beam with free ends on Winkler-type half space.

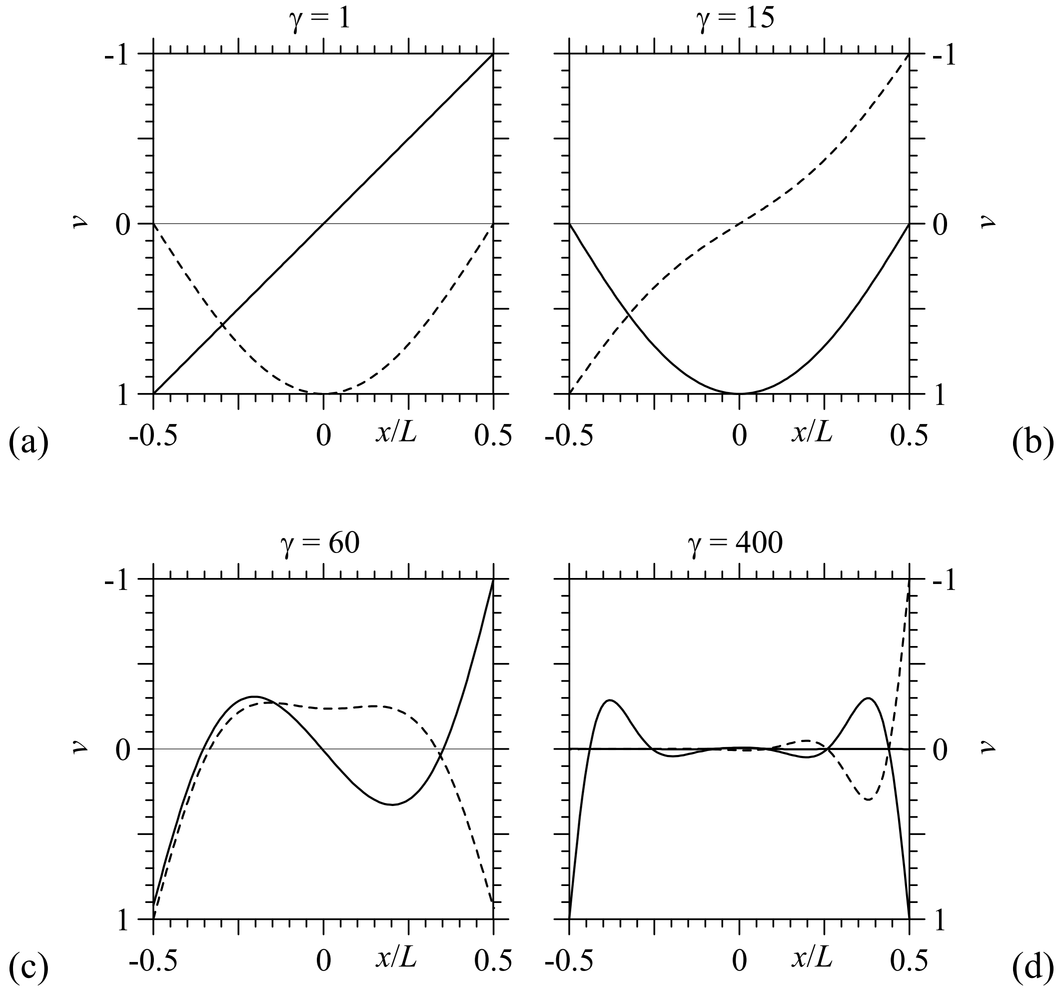

Fig. 1.32 – First (continuous line) and second (dashed line) mode shapes for a beam with free ends on Winkler-type half-space for γ equal to 1 (a), 15 (b), 60 (c) and 400 (d).

1.5.5 Beam of infinite length with various end restraints

Figs. 1.8c, 1.17c and 1.28c, clearly show that dimensionless critical loads converge to well definite limits for large values of αL, which correspond to the case of a very long beam resting on stiff soil. These figures show that critical loads values depend on beam end restraints. Table 6 collects the first four dimensionless critical loads $P_{\mathrm{cr},}/[P_{\mathrm{cr,E}}(\alpha L)^2]$ for beam with $\alpha L = 50$ and different boundary conditions. In particular, in the sliding–pinned case, the constraint equations that must be used in Eq. 1.6 are $R_1 = v(L/2) - v(-L/2) = 0$ and $R_2 = v(-L/2) - [v(-L/2) - v(L/2)]/L = 0$, whereas in the sliding–free case, the constraint equation is $R_1 = v(-L/2) = 0$. In this case, the first buckling mode is localized at the free end and a new value is obtained:

$$P_{\mathrm{cr},1} = 0.094 P_{\mathrm{cr,E}} (\alpha L)^2 . \tag{1.50}$$

The first and second mode shapes for increasing αL are shown in Fig. 1.33.

Beam end restraints	$P_{\mathrm{cr,min}}/[P_{\mathrm{cr,E}}(\alpha L)^2]$			
	1st	2nd	3rd	4th
Free-free	0.083	0.083	0.121	0.121
Pinned-pinned	0.083	0.106	0.121	0.121
Sliding-free	0.083	0.121	0.121	0.125
Sliding-pinned	0.094	0.121	0.121	0.125
Sliding-sliding	0.121	0.121	0.125	0.125

Tab. 1.6 – First four dimensionless critical loads for beam on elastic half-plane with various end restraints and $\alpha L = 50$.

Moreover, Tab. 1.6 shows that the first dimensionless critical load is conditioned by the less restrictive end restraint applied to the beam, for example, if the beam is characterized by at least one free end, the first dimensionless critical load converges to 0.083 $P_{\mathrm{cr,E}}(\alpha L)^2$.

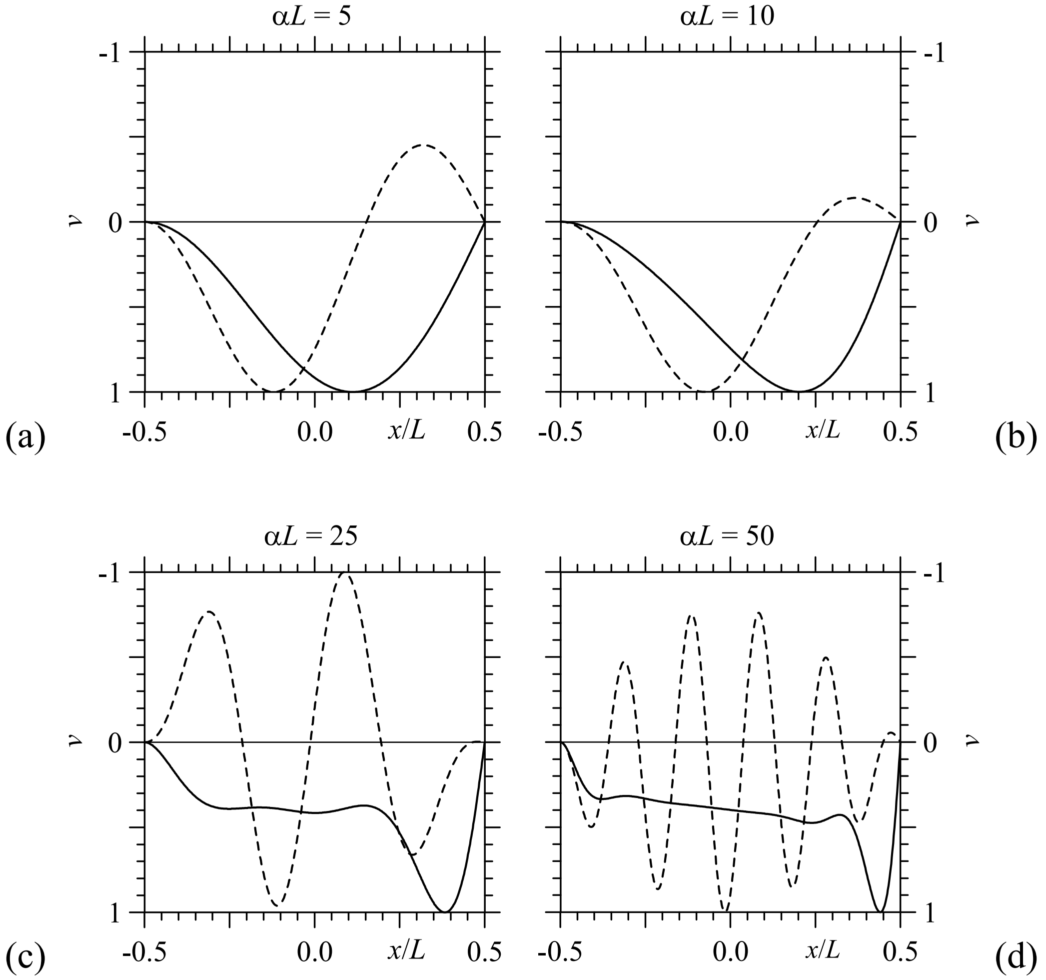

Fig. 1.33 – First (continuous line) and second (dashed line) mode shapes for a beam with sliding-pinned ends and αL equal to 1 (a), 5 (b), 10 (c), 20 (d), 25 (e) and 50 (f).

1.5.6 Buckling of a beam with a weakened section at midpoint

In some cases, a beam supported or not by an elastic half-plane, may not have continuous slope due to weakened joints or partial cracks along its length. In this paragraph, the buckling of a beam with free ends and with a hinge at midpoint is considered (Fig. 1.34). A similar problem was studied by Wang (2010) who considered an infinite beam on Winkler-type half-space, with up to three symmetric weakened joints. Wang determined critical loads by analytically solving the differential equation of the beam and the corresponding mode shapes characterized by large deflections close to weak sections.

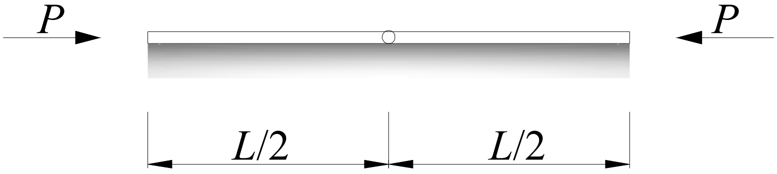

Fig. 1.34 – Beam with free ends and with a weakened joint at midpoint on elastic half-plane subject to axial load.

The weak section is introduced in the present discrete model by modifying the matrices of the beam elements converging at the midpoint node, following the method described in chapter 3 for taking into account the semi-rigid behaviour of a connection.

In Figs. 1.35a and b, dimensionless critical loads $P_{\mathrm{cr}}/P_{\mathrm{cr,E}}$ are plotted versus αL^3 and αL values, respectively; whereas Fig. 1.35c shows the ratio $P_{\mathrm{cr}}/[P_{\mathrm{cr,E}}\,(\alpha L)^2]$ versus the parameter αL.

In this case, the first, second and third eigenvalues appear quite far from other results, in particular, the second and third critical loads appear coincident with the first and second critical loads for the beam with free ends and converge to $P_{\mathrm{cr},1}$ (Eq. 1.38). The first critical load is less than the second and third critical loads; it does not intersect other curves, and for increasing αL it converges to a new value:

$$P_{\mathrm{cr},0} = 0.069\,P_{\mathrm{cr,E}}(\alpha L)^2, \qquad (1.51)$$

The fourth and fifth eigenvalues are close to Reissner's solution and converge to the value given by Eq. 1.27.

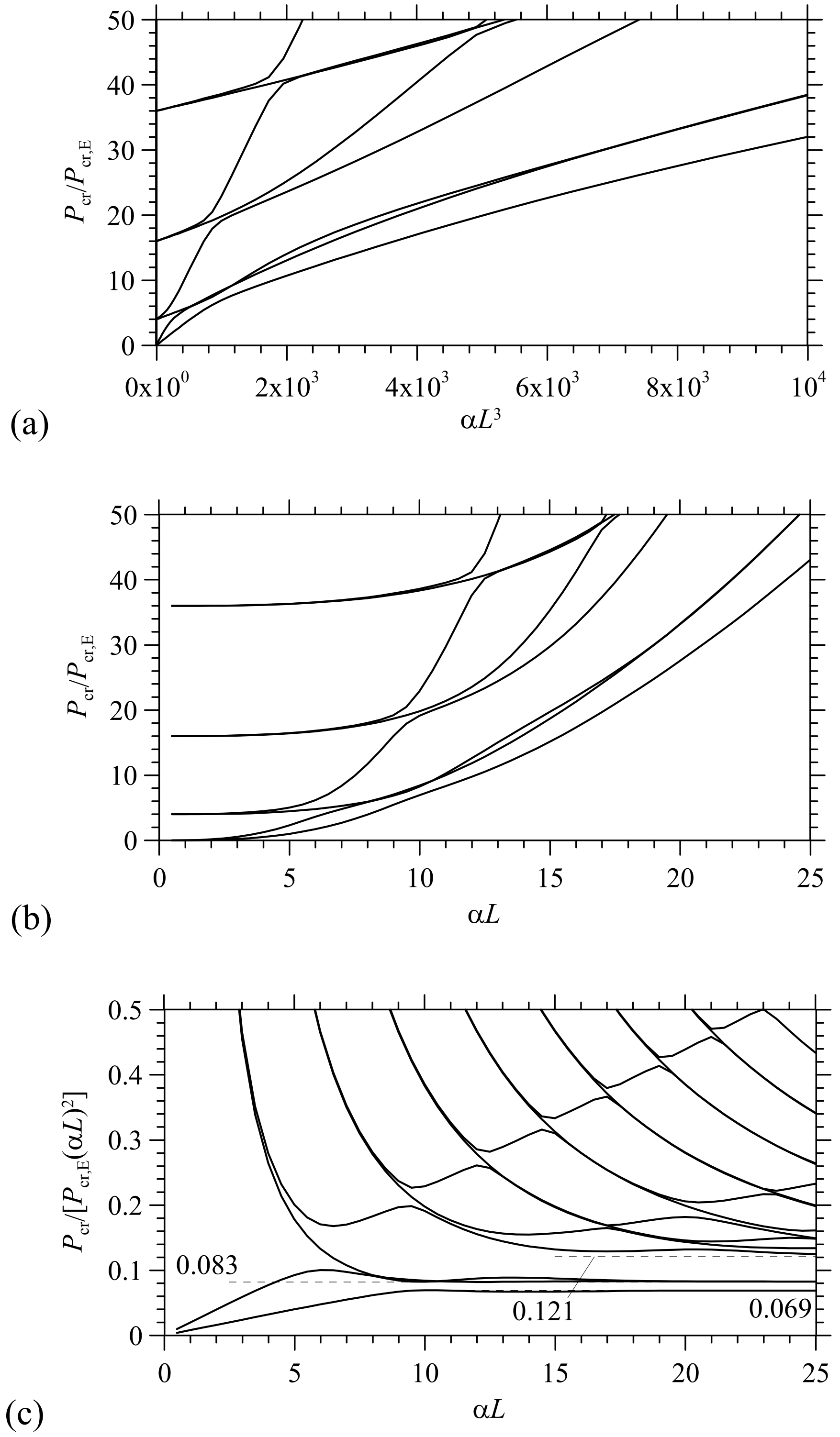

Fig. 1.35. Dimensionless critical loads P_{cr} versus αL for beam with free ends and a weakened joint at midpoint.

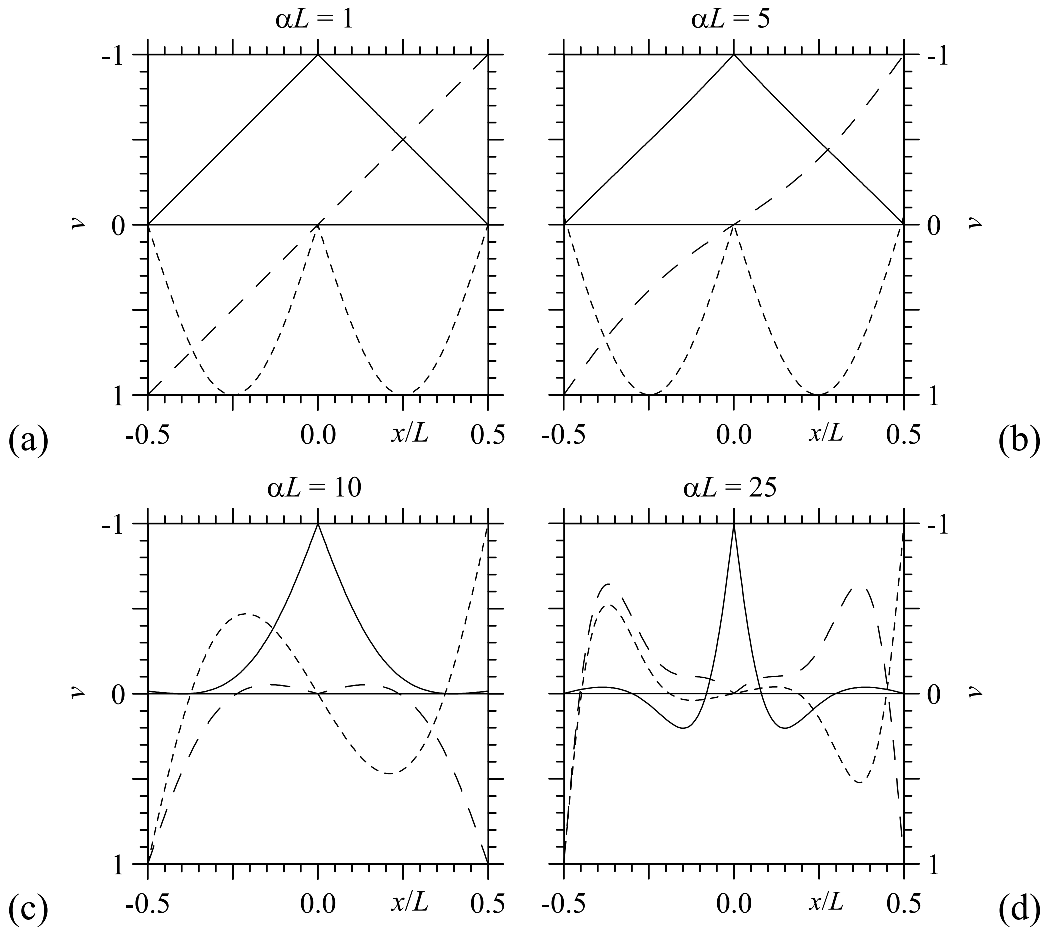

Fig. 1.36 – First (continuous line), second (large dashed line) and third (small dashed line) mode shapes for a beam with free ends and a weak section at midpoint for αL equal to 1 (a), 5 (b), 10 (c) and 25 (d).

Figs 1.36 a-d show the first three mode shapes for increasing αL. For $\alpha L = 1$ (Fig. 1.36a) the first mode shape is symmetric and characterized by the rigid body rotation of each part of the beam with respect to beam midpoint, whereas the second mode shape is a rigid rotation of the entire beam and it is coincident with the first mode shape for the beam with free ends. The third mode shape is sinusoidal with one half-wave for each part of the beam. For $\alpha L = 5$ (Fig. 1.36b), the first and the third mode shapes are similar to the corresponding ones obtained for $\alpha L = 1$, whereas the second mode shape is coincident with the first mode shape for the beam with free ends. For $\alpha L = 10$ and 25, the second and third mode shapes are coincident with the first and second mode shapes for the beam with free ends, whereas the first mode shape is characterized by large deflections close to the weak section. It is worth noting that the first mode shape corresponding to each half of the beam for $\alpha L = 10$ and 25 has never been obtained with other beam end restraints.

The buckling of a beam resting on elastic half-plane with a weak section at midpoint turns out to be similar to the corresponding case on a Winkler-type soil (Wang 2010). However, in the latter case, the first, second and third critical loads tend to be coincident for increasing γ, as shown in Figs. 1.38a, b and c, and converge to $P_{\mathrm{cr,W},1}$ (Eq. 1.48). Then, Figs. 1.37a and b show the first, second and third mode shapes for a beam on Winkler half-space with a weak connection at midpoint. For the beam on soft Winkler half-space, mode shapes are similar to the beam on half-plane case, whereas for the beam on stiff Winkler half-space, the first mode shape is characterized by large deflection at beam ends and midpoint. In this case, the first mode shape on each half of the beam is coincident with the entire mode shape obtained for the beam with free ends on quite stiff half-space (Fig. 1.32c).

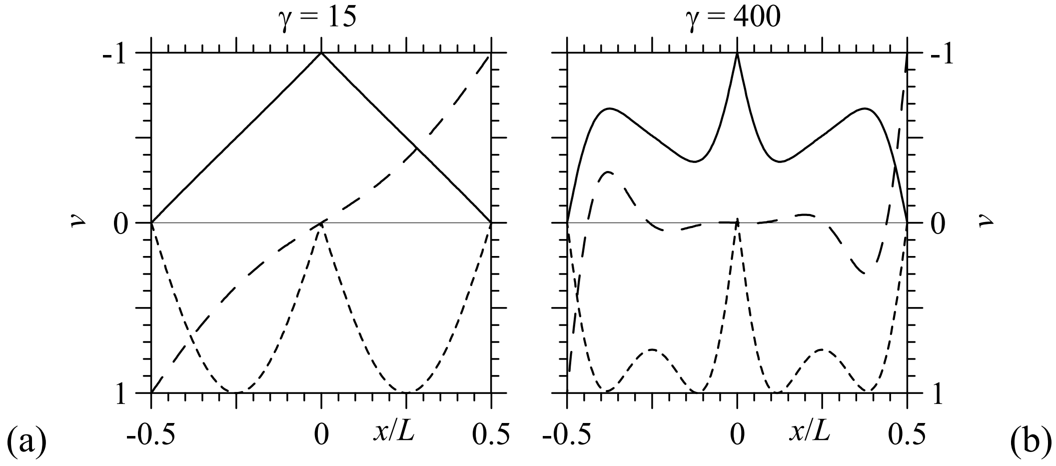

Fig. 1.37 – First (continuous line), second (large dashed line) and third (small dashed line) mode shapes for a beam with free ends and a weak section at midpoint for γ equal to 15 (a) and 400 (b).

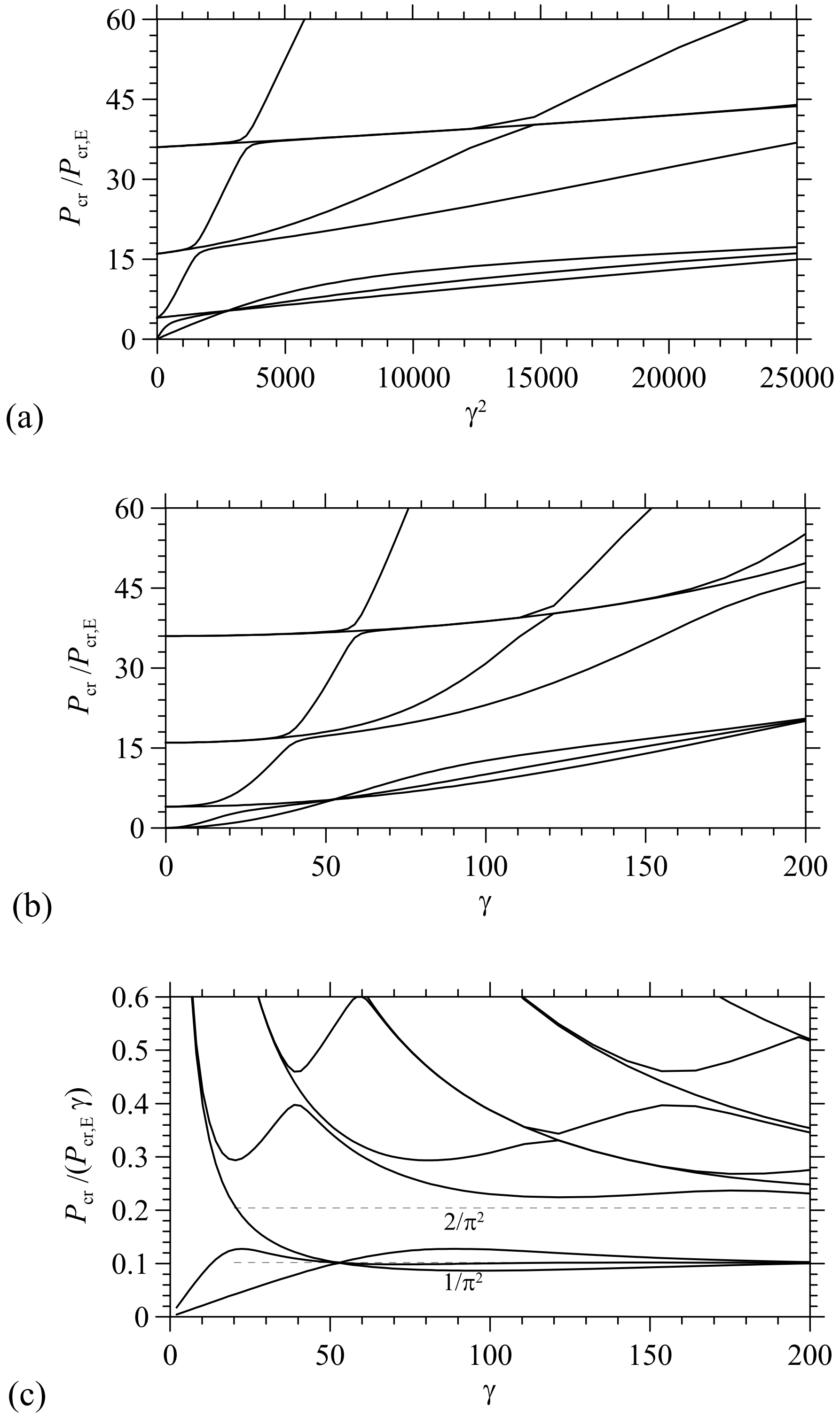

Fig. 1.38 – Dimensionless critical loads P_{cr} versus γ for a beam with free ends and a weak section at midpoint on Winkler-type half space.

1.6 Analysis of a compressed beam on half-plane loaded at midpoint

A beam resting on elastic half-plane is often used for representing the behaviour of sandwich panels (Gough et al. 1940; Allen 1969), however, in some cases, the simpler Winkler half-space model is adopted to represent the behaviour of the sandwich core (Davies 2001). Considering a simply supported panel subject to a concentrated or distributed load (Fig. 1. 1.39a), the upper face is compressed and it may suffer of buckling (Fig. 1. 1.39b). A similar case is represented by a supported panel, where the support reaction becomes a concentrated force for the panel. Then, the face sheet of the sandwich panel may fail at a support or under a load by buckling and bending failure of the face (Fig. 1.40).

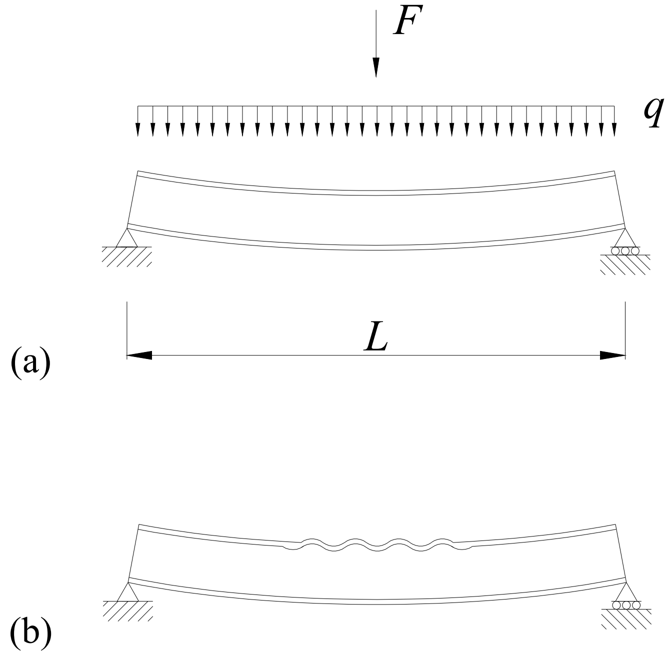

Fig. 1.39 – Structural behaviour of a simply supported sandwich panel (a), subject to local buckling of the upper face (b).

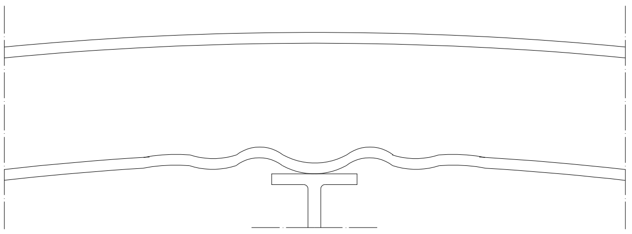

Fig. 1.40 – Buckling and bending failure of a sandwich face over a support.

The simple case of a beam with free ends resting on elastic half-plane loaded by a concentrated force F at midpoint and subject to a compressive force P (Fig. 1.41), is then considered in order to study the behaviour of a sandwich panel with a compressed face sheet. Moreover, the present model allows to study structures including second order effects due to axial load. Then, the beam characterized by an increasing axial load P is considered.

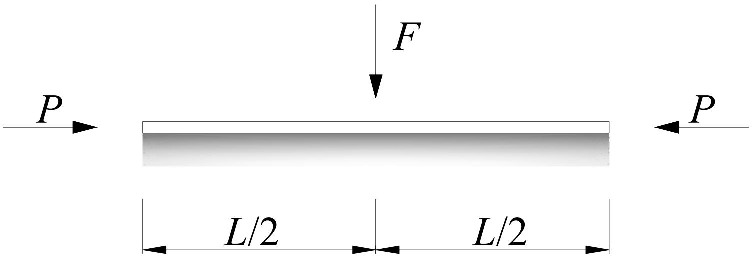

Fig. 1.41 – Beam with free ends loaded at midpoint and subject to axial load.

Considering the relation between subgrade parameter c of a Winkler support and the elastic modulus of an elastic half-plane E (Eq. 1.37) determined by Biot (1937), the analysis of a beam with free ends, including second order effects due to axial load, is carried out following Davies (2001) example and comparing results obtained with the two half-space models. In the following, beam deflections, half-space reactions and bending moments for the beam without axial load and with P equal to one half of the first critical load P_1 are determined. Results are first evaluated for the case of a beam resting on quite stiff support ($\alpha L = 10$ corresponding to $\gamma = 53$) and are shown in Figs. 1.42 a-f. Without axial load effects (dashed lines), the results obtained with both half-space models are quite similar. Including axial load effects (continuous lines), displacements, reactions and bending moments obtained with the beam on half-plane, are larger than those obtained by applying the Winkler model. Then, results are evaluated for the case of a beam on stiff support ($\alpha L = 50$ corresponding to $\gamma = 1330$) and are shown in Figs. 1.43 a-f. In this case, displacements and reactions for the beam on half-plane are larger than the corresponding results for the beam on Winkler-type half-space, with and without axial load effects. Moreover, in the latter case, displacements and reactions tend to be negligible and far from beam midpoint. Bending moments obtained with both models, present however very small differences. Then, Biot's expression (Eq. 1.37) turns out to be efficient for static analyses with second order effects and for the determination of beam bending moment.

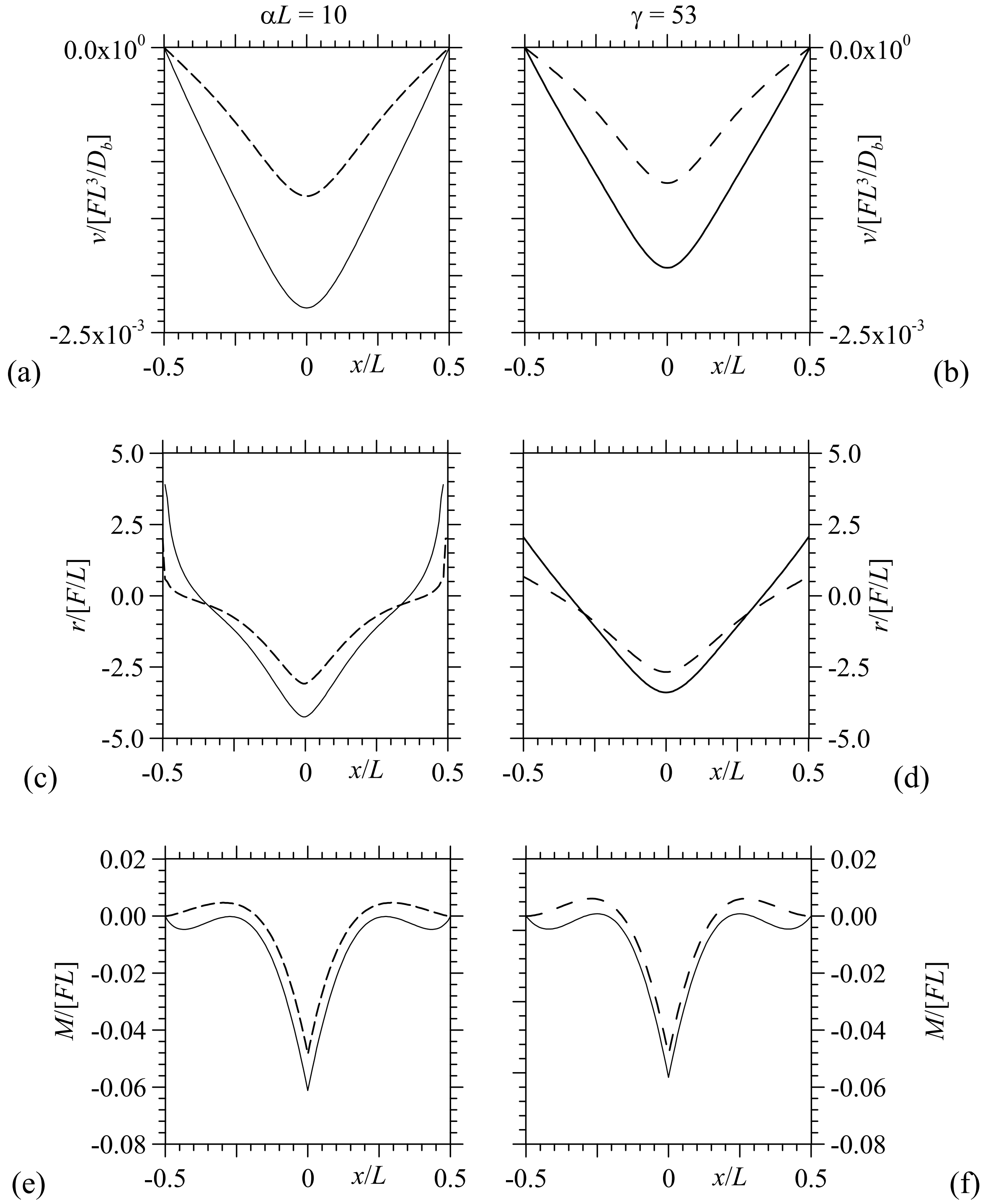

Fig. 1.42 – Beam on elastic support loaded by a concentrated force at midpoint on half plane (a, c, e) and Winkler soil (b, d, f). Vertical displacement (a,b), half-space reaction (c,d), bending moment (e,f). Dashed lines for $P = 0$, continuous lines for $P = 0.5\ P_1$

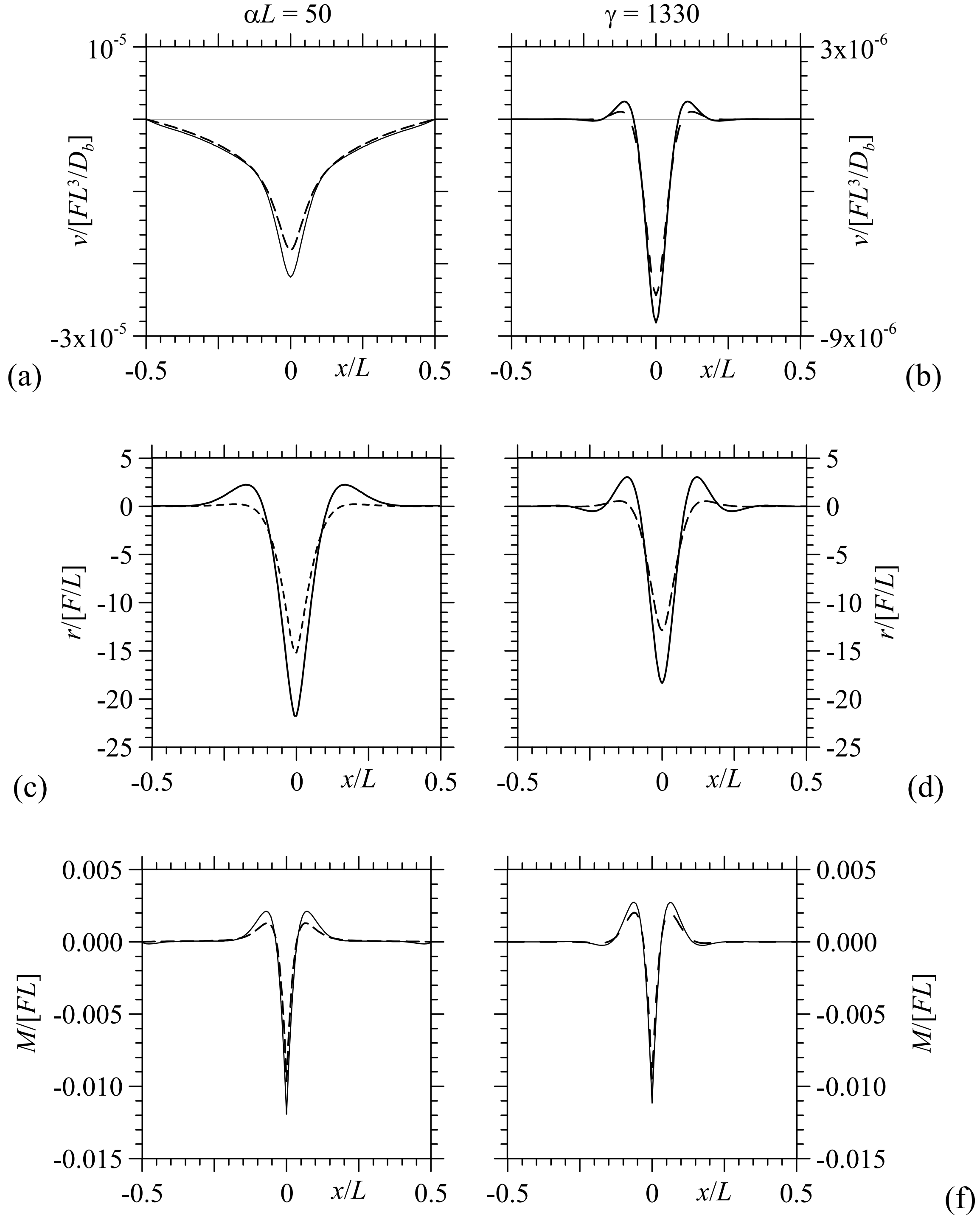

Fig. 1.43 – Beam on elastic support loaded by a concentrated force at midpoint on half plane (a, c, e) and Winkler soil (b, d, f). Vertical displacement (a,b), half-space reaction (c,d), bending moment (e,f). Dashed lines for $P = 0$, continuous lines for $P = 0.5\ P_1$

1.6.1 Incremental analysis of a compressed beam on half-plane loaded at midpoint

Considering a beam with free ends on elastic half-plane, loaded by a concentrated force *F* at midpoint and subject to axial load *P* (Fig. 1.41), the vertical displacement at beam midpoint *d* is evaluated for increasing *P* and for different α*L* values (without increasing *F*). A similar example was studied by Yankelewsky and Eisenberger (1986), where Winkler's hypothesis were adopted to represent the elastic half space. The system is symmetric, then the beam with free ends behaves like a beam with pinned ends.

In absence of soil (α*L* = 0), the case of a beam with pinned ends is considered. The displacement at midpoint $d_0 = d(0) = FL^3/(24\ D_b)$ is obtained without second order effects, then, by increasing *P*, the displacement *d* increases following the well-known relation (Timoshenko and Gere 1961):

$$d(P) = \frac{d(0)}{1 - P/P_{\text{cr,E}}} \tag{1.52}$$

Fig. 1.44a shows dimensionless axial load $P/P_{\text{cr,E}}$ with respect to dimensionless displacement at beam midpoint d/d_0. For α*L* = 0, and that the axial load converges to the Euler buckling load for the beam and the results given by the incremental analysis are in good agreement with Eq. 1.52 (line with crosses, Fig. 1.44a), which can also be written as $P/P_{\text{cr,E}} = 1 - d_0/d$.

For α*L* ≠ 0 and increasing α*L*, the displacement at beam midpoint without axial load is obviously smaller than d_0 and diminishes while increasing α*L*. For each value of the parameter α*L*, the axial load converges to the critical load corresponding to the first symmetric eigenvector, which is not always the first critical load for the case of the beam with free ends. For example, considering Fig. 1.28a or b for α*L* = 2, the first critical load is equal 0.158 $P_{\text{cr,E}}$, but it corresponds to an asymmetric mode shape. The incremental analysis performed for α*L* = 2, converges, in fact, to the second critical load, equal to 0.991 $P_{\text{cr,E}}$.

Fig. 1.44b shows dimensionless axial load $P/[P_{\text{cr,E}}(\alpha L)^2]$ with respect to dimensionless displacement at beam midpoint d/d_0. Axial loads converge to Eq. 1.38 for increasing α*L*.

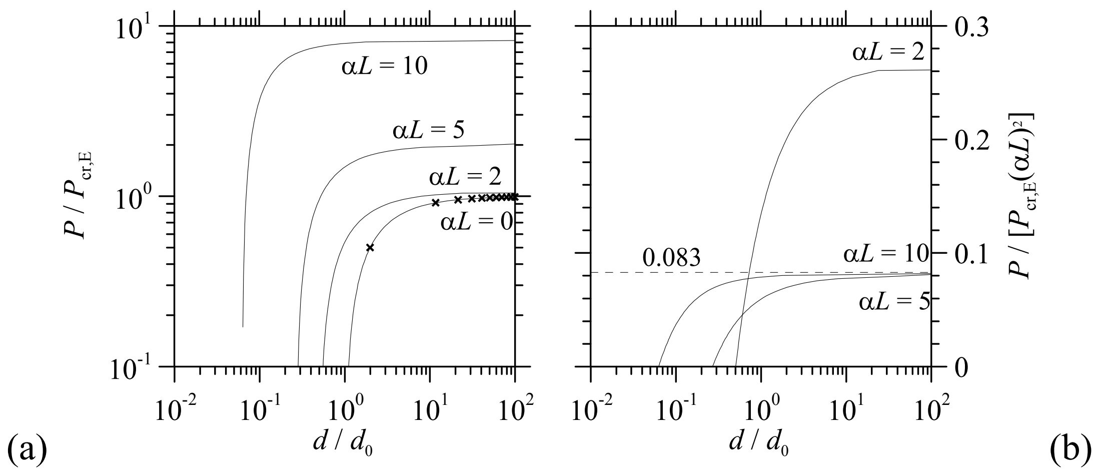

Fig. 1.44 – Dimensionless beam displacement at midpoint for increasing axial load for different αL values. Line with crosses for $P/P_{cr,E} = 1- d_0/d$.

Beam displacement at midpoint for increasing axial load and varying the parameter αL, turns out to have a behaviour similar to the case of the beam with pinned ends and without soil (Eq. 1.52). However, the expression in Eq. 1.52 can not be adopted to the case of the beam on elastic half plane. Fig. 1.45 shows dimensionless axial loads $P/P_{cr,E,\alpha L}$ with respect to dimensionless displacements $d/d(0)$, in order to obtain curves starting from (1,0) and converging to 1. Increasing αL values, curves are different than the one obtained with αL = 0.

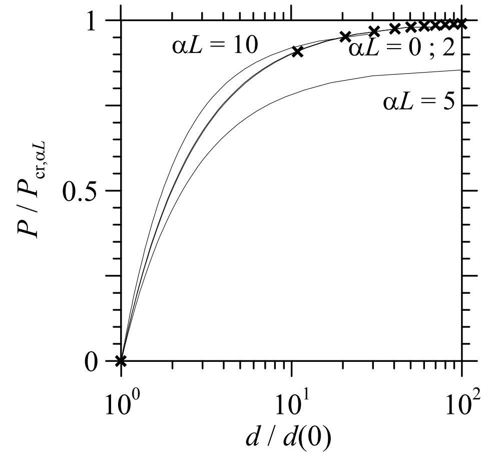

Fig. 1.45 – Dimensionless beam displacement at midpoint for increasing axial load for different αL values. Line with crosses for $P/P_{cr,E} = 1- d_0/d$.

1.7 Rectangular pipe resting on elastic half-plane

As suggested in the static case (Tullini and Tralli 2010), the present model gives the possibility to easily study the coupling of the foundation beam with structures described by traditional FEs. Buckling analysis and geometric nonlinear analysis can be carried out, taking into account second order effects due to axial load on structural elements and in particular on the foundation element.

The discrete problem is characterized by the separation of the degrees of freedom of the foundation beam (1) and the remaining degrees of freedom of the structure (2) as shown in the following system (Tullini and Tralli 2010):

$$\begin{bmatrix} (\mathbf{K}_b+\mathbf{K}_g)_{11} & (\mathbf{K}_b+\mathbf{K}_g)_{12}^T & b\mathbf{H} \\ (\mathbf{K}_b+\mathbf{K}_g)_{12} & (\mathbf{K}_b+\mathbf{K}_g)_{22} & \mathbf{0} \\ b\mathbf{H}^T & \mathbf{0} & -\frac{b}{E}\mathbf{G} \end{bmatrix} \begin{Bmatrix} \mathbf{q}_1 \\ \mathbf{q}_2 \\ \mathbf{r} \end{Bmatrix} = \begin{Bmatrix} b\mathbf{F}_1 \\ b\mathbf{F}_2 \\ \mathbf{0} \end{Bmatrix} \tag{1.53}$$

In the following, a rectangular frame of length L and high L_p is considered (Fig. 1.46).

This kind of frame in plane strain state may refer to the structure of a long subway resting on soil, then the deformations along its length become negligible with respect to in-plane deformations. Then, a pipe resting on elastic half-plane can represent the structural scheme of an underground canal or a subway.

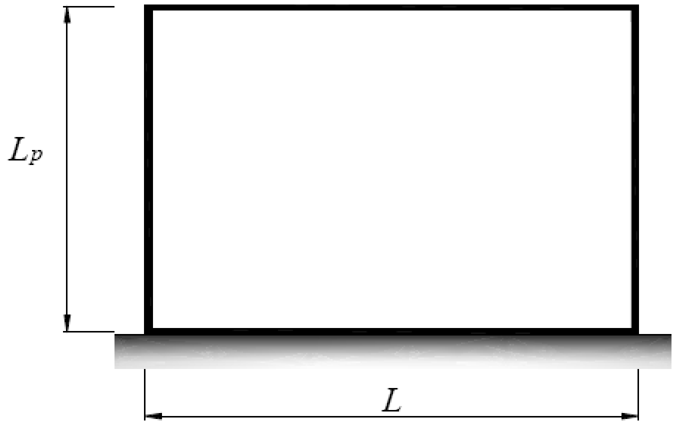

Fig. 1.46 – Rectangular pipe resting on elastic half-plane.

In this case, both the foundation and the top beam have the same bending stiffness D_b, whereas D_p indicates the column bending stiffness. Concentrated forces P are applied at upper column ends (Fig. 1.46). In the following, by introducing dimensionless parameters

$$\eta = \frac{L}{L_p}, \qquad \rho = \frac{D_b}{D_p}, \qquad \psi = \frac{\rho}{\eta}, \qquad \lambda_p = \frac{PL_p^2}{D_p} = \frac{\rho}{\eta^2}\lambda, \tag{1.54}$$

two cases with $\psi = 0.5$ ($\rho = 1$, $\eta = 2$) and $\psi = 2.0$ ($\rho = 4$, $\eta = 2$) are considered. A number of 32 equal FEs is adopted for the foundation beam, whereas the other frame elements are subdivided into 16 equal FEs. Moreover, a pipe resting on half-space modelled with traditional FEs is considered.

1.7.1 Buckling of rectangular pipes with free and pinned foundation beam ends

Buckling analyses are restricted to the determination of the first two critical loads and the corresponding mode shapes. Free and pinned foundation beam ends are considered. The second case may refer to a pipe supported by piles at foundation beam ends, and the penalty function R_1 introduced in section 1.3 is used.

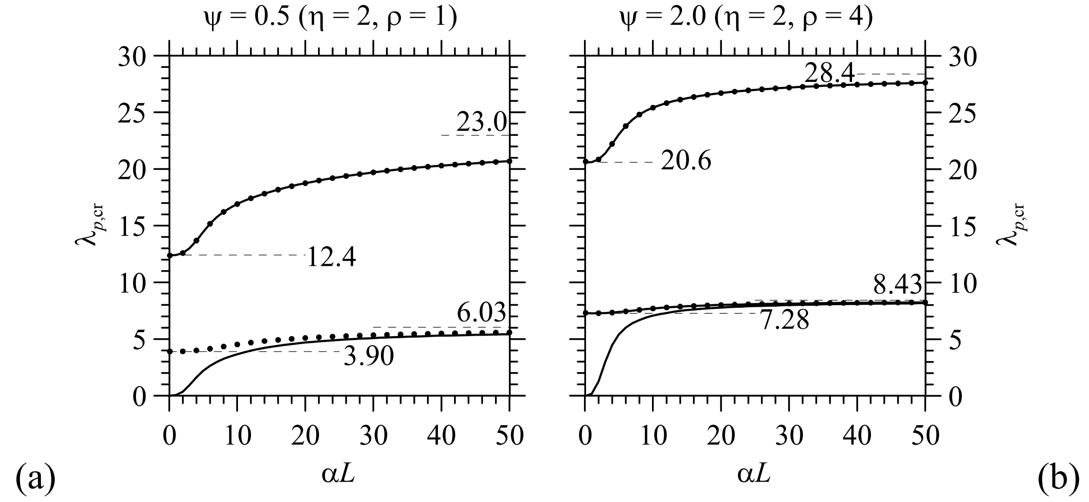

Fig. 1.47 – Rectangular pipe with $\psi = 0.5$ (a) and 2.0 (b). First and second dimensionless critical loads $\lambda_{p,\mathrm{cr}}$ for increasing αL. Continuous lines and dots describe pipe with free and pinned foundation ends, respectively.

Figs. 1.47a and b show the first and second dimensionless critical loads $\lambda_{p,\mathrm{cr}}$ increasing of αL for $\psi = 0.5$ and $\psi = 2.0$, respectively. Continuous lines represent critical loads of the pipe with free foundation ends, whereas dots represent the critical loads of pipes with pinned foundation ends. For very soft soil and free foundation ends, the first critical load tends to zero and the corresponding mode shape is a rigid body rotation (Fig. 1.48a); whereas for a pipe with pinned foundation ends, the first critical load is close to the analytical solution of the rectangular pipe without supporting soil, i.e. $\lambda_{p,\mathrm{cr}} = 3.90$ for $\psi = 0.5$ and $\lambda_{p,\mathrm{cr}} = 7.28$ for $\psi = 2.0$, and the corresponding mode shape (Fig. 1.48b) is antisymmetric.

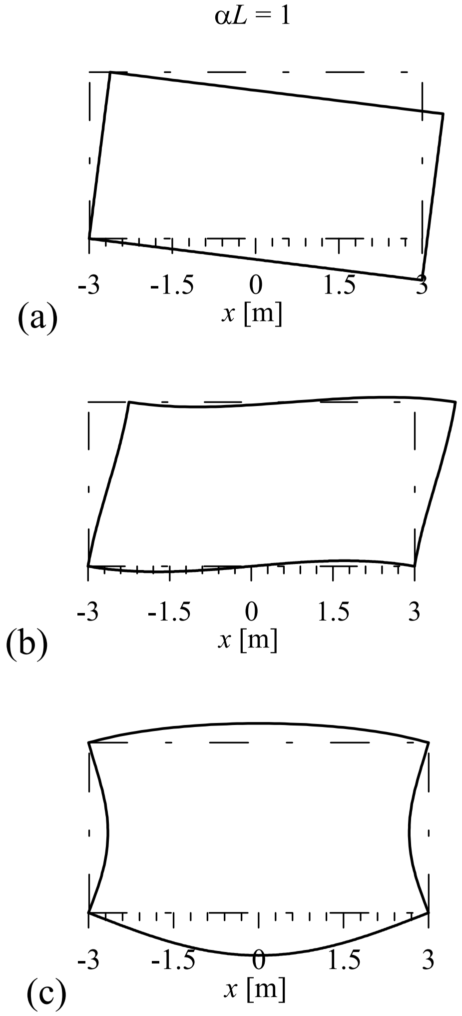

Fig. 1.48 – Rectangular pipe with $\psi = 0.5$. Mode shapes for $\alpha L = 1$. First mode shape for a pipe with free (a) and pinned ends (b) foundation ends. Second mode shape (b) for a pipe with either free or pinned foundation ends.

Considering the second critical load, for very soft substrate, soil reactions extend along the whole foundation length (Fig. 1.49a), whereas for large values of αL, reactions tend to concentrate at foundation ends and are close to zero along beam length (Fig. 1.49b). Therefore, for very soft substrate, the second critical load can be overestimated by the corresponding value $\lambda_{p,\mathrm{cr,sup}}$ of a pipe without supporting soil and it can be underestimated by the critical load $\lambda_{p,\mathrm{cr,inf}}$ of a self-equilibrate pipe having concentrated forces at top column ends and a distributed load equal to $2P/L$ on foundation beam, which simulates constant soil reactions. For $\psi = 0.5$ and αL tending to zero, the second critical load tends to $\lambda_{p,\mathrm{cr}} = 12.4$ (Fig. 1.47a), bounded by $\lambda_{p,\mathrm{cr,inf}} = 11.6$ and $\lambda_{p,\mathrm{cr,sup}} = 13.5$, whereas for $\psi = 2.0$ and αL tending to zero, the second critical load tends to $\lambda_{p,\mathrm{cr}} = 20.6$ (Fig. 1.47b), bounded by $\lambda_{p,\mathrm{cr,inf}} = 20.3$ and $\lambda_{p,\mathrm{cr,sup}} = 21.6$. The corresponding mode shape is characterized by a horizontal and a vertical axis of symmetry (Fig. 1.48c).

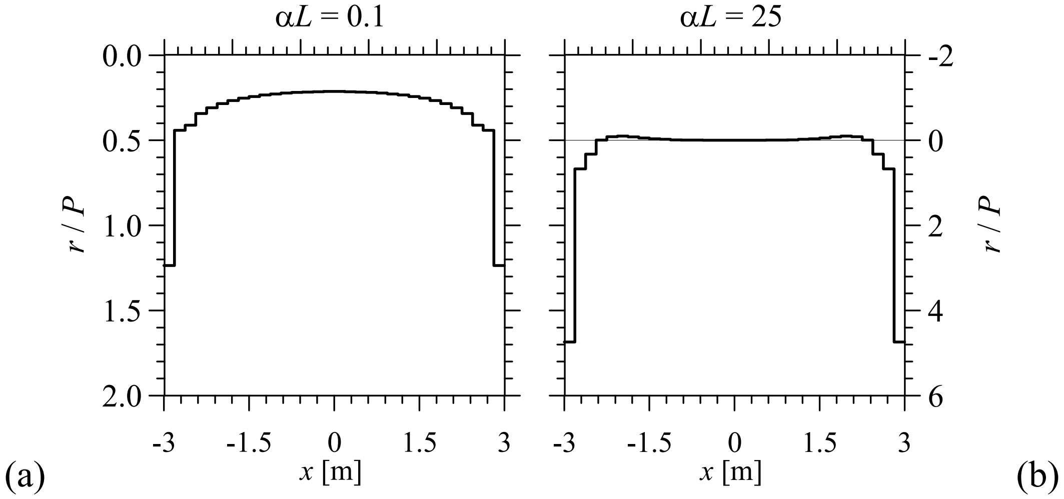

Fig. 1.49 – Half plane pressure generated by a pipe with columns compressed by P for αL = 0.1 (a) and 25 (b).

For quite soft soil (αL = 5), the first mode shape for the pipe with free foundation ends is antysymmetric and characterized by a rigid body rotation and small deformation of beams and columns (Fig. 1.50a). The first mode shape for the pipe with pinned foundation ends (Fig. 1.50b) is analogous to the one obtained in the previous case and, moreover, the corresponding critical load is not much larger than the one determined for αL = 1 (Figs. 1.47a and b). The second mode shape (Fig. 1.50c) is in this case characterized by one (vertical) axis of symmetry and it is clear that the effect of the half-plane is to reduce foundation beam deflection with respect to top beam.

For very stiff soil (αL = 25), the first mode shape obtained with both restraint conditions are coincident, foundation deflections are small (Figs. 1.51a and b) and the corresponding eigenvalue converges to the critical load of a portal frame with built-in bases ($\lambda_{p,\mathrm{cr}}$ = 6.03 for ψ = 0.5 and $\lambda_{p,\mathrm{cr}}$ = 8.43 for ψ = 2.0). It is worth noting that the first critical load for the second pipe (ψ = 2.0) converges faster to the analytic solution with respect to the first pipe.

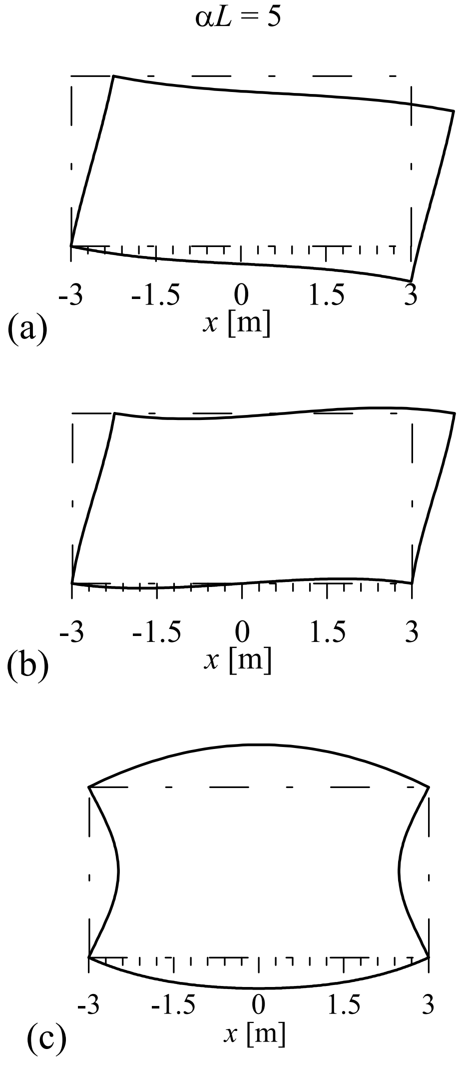

Fig. 1.50 – Rectangular pipe with ψ = 0.5. Mode shapes for αL = 5 . First mode shape for a pipe with free (a) and pinned (b) foundation ends. Second mode shape (c) for a pipe with either free or pinned foundation ends.

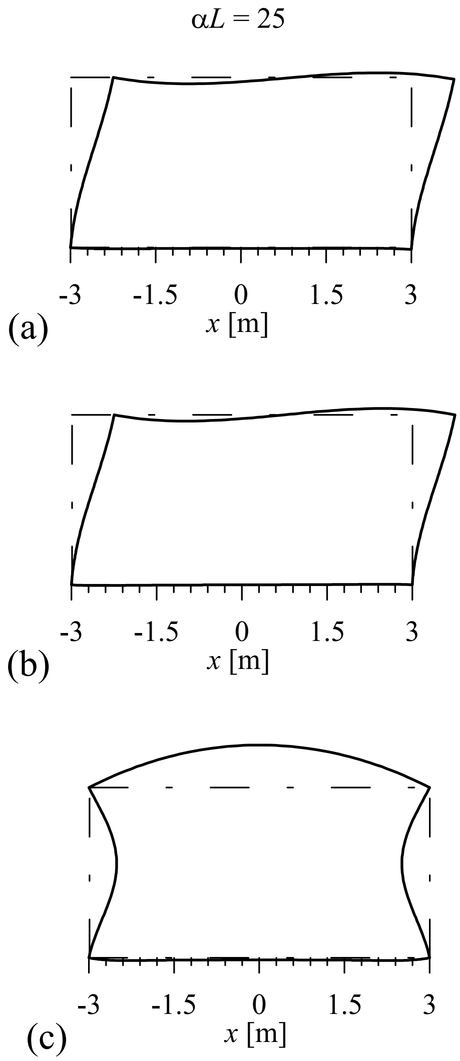

Fig. 1.51 – Rectangular pipe with $\psi = 0.5$. Mode shapes for $\alpha L = 25$. First mode shape for a pipe with free (a) and pinned (b) foundation ends. Second mode shape (c) for a pipe with either free or pinned foundation ends.

Considering the second eigenvalue, both restraint conditions give equal buckling loads and identical mode shapes (Fig. 1.51c). For increasing αL, the second critical load converges to the corresponding value of a portal frame with built-in bases ($\lambda_{p,\mathrm{cr}} = 23.0$ for $\psi = 0.5$, $\lambda_{p,\mathrm{cr}} = 28.4$ for $\psi = 2.0$). However, convergence is slow for $\psi = 0.5$ (Fig. 1.47a) and the mode shape depicted in Fig. 1.51c is characterized by small foundation deflections. Hence, the larger the pipe foundation length with respect to the height, the larger the soil stiffness necessary to converge to a portal frame with built-in bases.

1.7.1.1 Buckling of rectangular pipes on half-plane modelled with traditional FEs

The pipe on elastic half-plane is also modelled with traditional FEs. In particular, the pipe is modelled by beam FEs and a mesh of 2D FEs is created for representing the half-plane as it has been done for the convergence test for the beam with free ends (§1.4). It is worth noting that the traditional model takes into account the geometric matrix for both beam and 2D FEs.

Figs. 1.52a and b show the first and second dimensionless critical loads $\lambda_{p,\mathrm{cr}}$ of a pipe resting on elastic half-plane with $\psi = 0.5$ ($\rho = 1$, $\eta = 2$), increasing αL. Lines with crosses show the results obtained with the traditional FE model $\lambda_{p,\mathrm{cr}}^{\mathrm{2D}}$, whereas continuous lines and dots represent the results obtained with the present model $\lambda_{p,\mathrm{cr}}^{\mathrm{PA}}$. It is worth noting that the first and second critical loads for the traditional model are determined by selecting the eigenvalues corresponding to the eigenvectors similar to the ones obtained with the present model. For low αL, small eigenvalues are obtained and the corresponding eigenvectors are characterized by large half-space displacements close to foundation beam ends (see Fig. 1.53b for example). Then, buckling analysis of a pipe on half-plane modelled by traditional FEs may not be able to converge to accurate results for soft half-space cases.

Considering the traditional FE model, the first critical load for the pipe with free ends is quite close to the one obtained with the present model (Fig. 1.52a, line with crosses). However, the first critical load for the pipe with pinned ends is close to the present model only for $\alpha L > 7$. For $\alpha L < 7$ traditional FE analyses do not furnish accurate results and the eigenvectors are characterized by large half-space displacements close to foundation beam ends. The second critical load obtained with the traditional model (Fig. 1.52b, line with crosses) is easily determined for $\alpha L > 7$ and it is close to the present results for $\alpha L > 15$.

Figs. 1.53a and b show the first and second mode shapes, respectively, for a pipe with free foundation ends with $\psi = 0.5$ ($\rho = 1$, $\eta = 2$) and $\alpha L = 5$; both mode shapes are characterized by local deformations on half space near foundation beam ends. The first mode shape (Fig. 1.53a) represents a rigid rotation and it is similar to the one obtained with the present model (Fig. 1.50a). The corresponding eigenvalue $\lambda_{p,\mathrm{cr1}}^{\mathrm{2D}} = 1.82$ is quite close to $\lambda_{p,\mathrm{cr1}}^{\mathrm{PA}} = 2.20$. The second mode shape (Fig. 1.53b) is characterized by large local deformations on half space close to foundation beam ends and the corresponding eigenvalue $\lambda_{p,\mathrm{cr}}^{\mathrm{2D}} = 2.02$ can not be considered an accurate solution. For α*L* = 5, the buckling analysis with the traditional FE model is not able to determine a value close to $\lambda_{p,\mathrm{cr2}}^{\mathrm{PA}} = 14.45$ also if the first 100 eigenvalues are calculated. Figs. 1.53c and d show the first and fourth mode shapes, respectively, for α*L* = 10. In this case, the fourth critical load determined by the buckling analysis is taken as second critical load. However, $\lambda_{p,\mathrm{cr2}}^{\mathrm{2D}} = 15.5$ is lower than $\lambda_{p,\mathrm{cr2}}^{\mathrm{PA}} = 16.9$. Finally, considering the pipe on stiff soil (α*L* = 25), the first and the second mode shapes shown in Figs. 1.53e and f are coincident with the corresponding ones determined with the present model (Fig. 1.51).

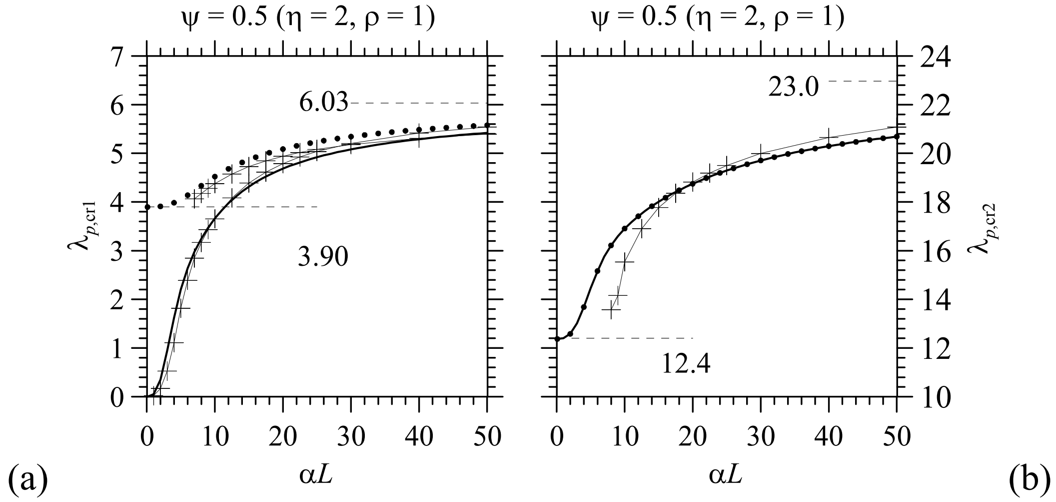

Fig. 1.52 – First (a) and second (b) dimensionless critical load of a pipe on elastic half plane. Continuous and dotted lines for the present model, line with crosses for the traditional FE model.

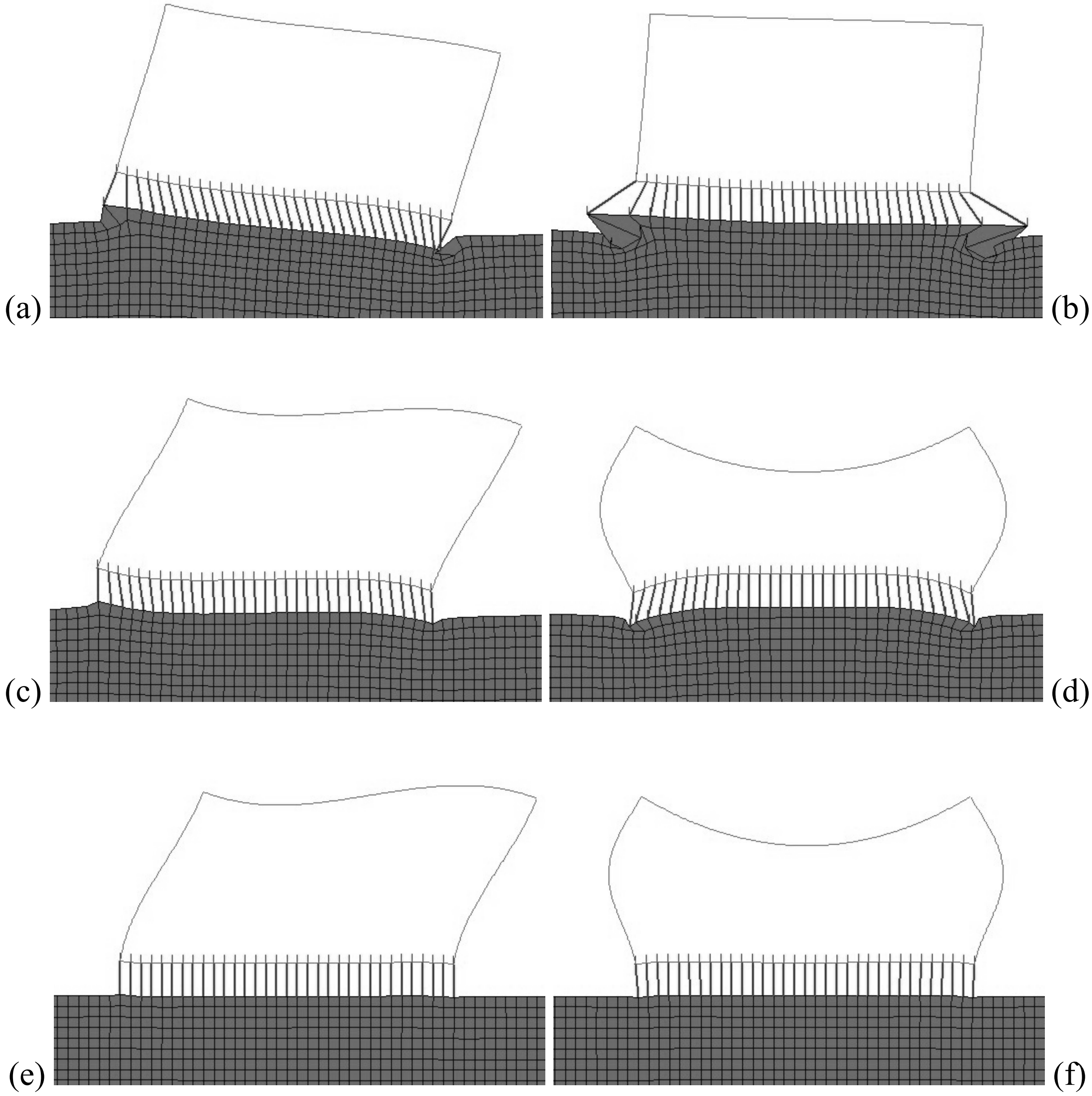

Fig. 1.53 – First (a, c, e) and second (b, d, f) mode shapes for a pipe on half-plane modelled with traditional FEs for αL = 5 (a, b), 10 (c, d) and 25 (e, f).

1.7.2 Nonlinear incremental analyses of rectangular pipes

Considering the pipe with compressed columns resting on elastic half-plane, it is worth noting that the axial forces in columns are statically determinate and equal to P, but the axial forces in top and foundation beams are statically indeterminate and depend nonlinearly on the load multiplier λ_p; thus, a snapthrough instability is to be expected (Bazant and Cedolin 1991). In order to obtain a more correct study of pipe stability, nonlinear incremental analyses are carried out, taking into account the axial force variation in top and foundation beams. To this purpose, axial degrees of freedom are added to beam FEs and element stiffness matrix is modified as usual (Reddy 2006); axial to bending stiffness ratio E_0bh/D_b is taken equal to $12/h^2$ with beam slenderness $L/h = 10$.

In the following, three types of analysis are carried out: the first is a simple linear static analysis (curve 1 in Fig. 1.54); the second is a static analysis which takes into account second order effects due to axial loads, but it considers axial loads proportional to the static solution during the entire analysis (curve 2 in Fig. 1.54); and the third takes into account the second order effects due to axial loads and update them during each analysis step (curve 3 in Fig. 1.54). For the third analysis type, displacement control has been adopted using the formulation proposed by Batoz and Dhatt (1979).

Considering the pipe with $\rho = 1$, $\eta = 2$ ($\psi = 0.5$) and $\alpha L = 1$, Fig. 1.54a shows load multiplier λ_p as a function of the rotation ϕ at the foundation beam end. In particular, line 1 represents the linear analysis and it is straight as expected, curve 2 corresponds to the incremental analysis that takes into account second order effects, but assumes axial forces proportional to those obtained with the linear analysis; then the load multiplier λ_p converges to $\lambda_{p,\mathrm{cr}} = 12.4$, determined with the buckling analysis. The analysis described by curve 3, which upgrades the axial forces in each load step, furnishes a load multiplier λ_p that reaches the limit point $\lambda_{p,\mathrm{lim}} = 5.2$ and then decreases. $\lambda_{p,\mathrm{lim}}$ is 58% lower than $\lambda_{p,\mathrm{cr}} = 12.4$ determined with the buckling analysis. Fig. 1.54b shows load multiplier λ_p as a function of dimensionless axial force in foundation beam $N_b L_p^2/D_p$ (positive sign for compression), and N_b increases more than linearly with respect to the load multiplier λ_p, up to attainment of the buckling load of the foundation beam.
Considering the pipe with $\rho = 1$, $\eta = 2$ ($\psi = 0.5$) and $\alpha L = 5$, Fig. 1.54c shows

that the geometric nonlinear analysis that upgrades axial forces attains the limit point $\lambda_{p,\mathrm{lim}} = 7.0$, 48% lower than $\lambda_{p,\mathrm{cr}} = 14.4$.
Similar results are shown in Figs. 1.55a and b for the pipe having $\rho = 4$, $\eta = 2$ ($\psi = 2.0$) and $\alpha L = 1$.

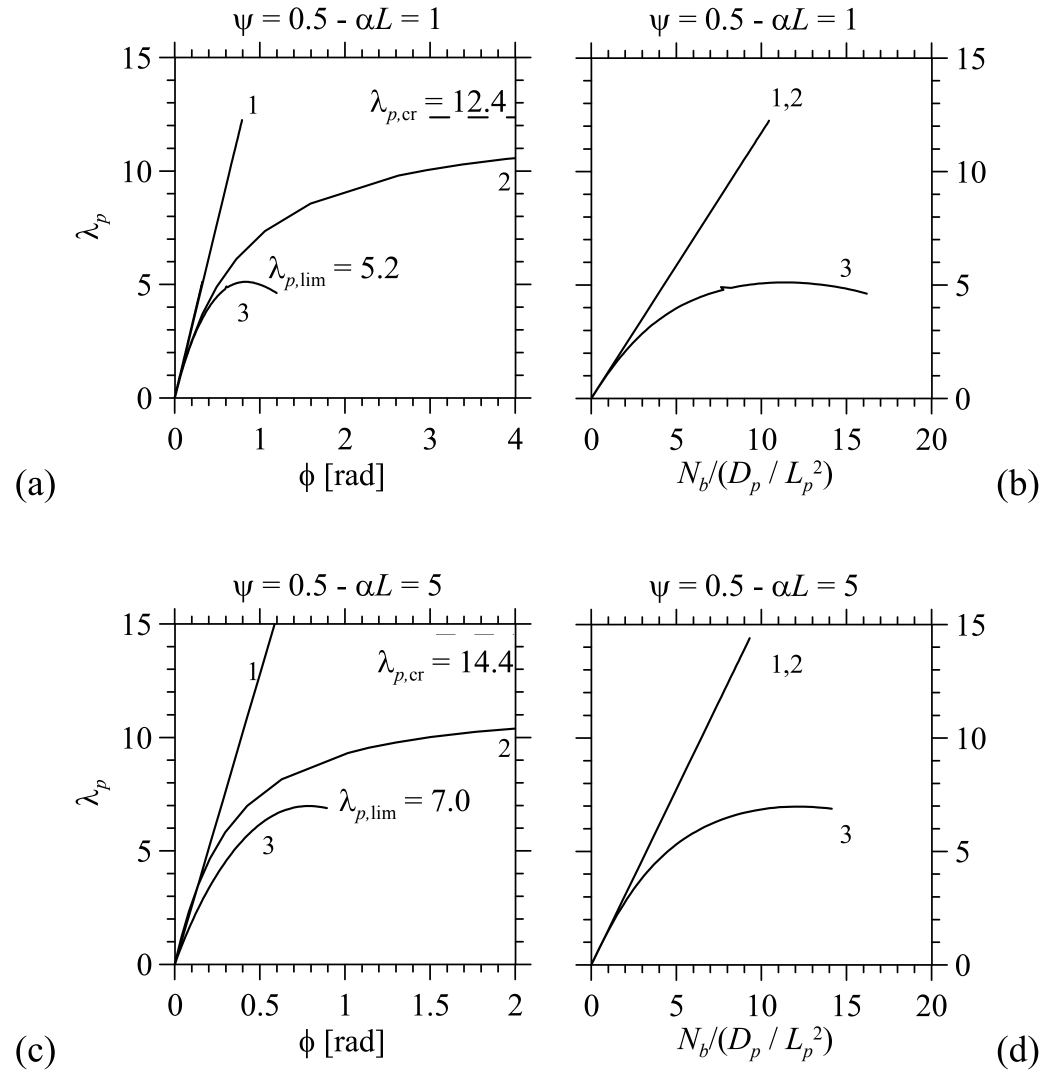

Fig. 1.54 – Rectangular pipe with $\psi = 0.5$ and $\alpha L = 1$ (a, b) and 5 (c, d). Load multiplier λ_p as a function of the rotation ϕ at the foundation beam end (a, c) and dimensionless axial force in foundation beam $N_t L_p^2/D_p$ (b, d). Linear analysis (straight line 1), incremental analysis with second order effects (curve 2), nonlinear incremental analysis that upgrades the axial forces at each load step (curve 3).

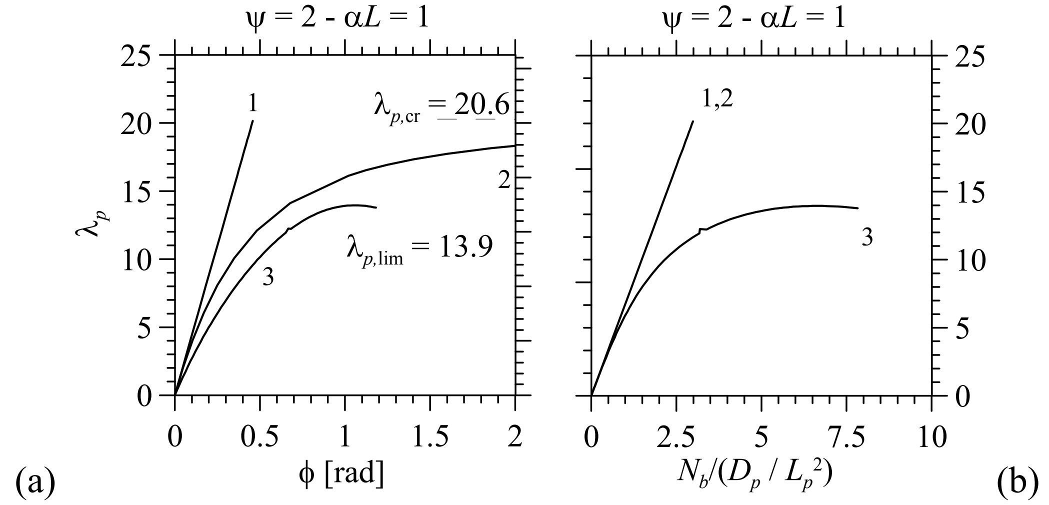

Fig. 1.55 – Rectangular pipe with $\psi = 2$ and $\alpha L = 1$. Load multiplier λ_p as a function of the rotation ϕ at the foundation beam end (a) and dimensionless axial force in foundation beam $N_t L_p^2/D_p$ (b). Linear analysis (straight line 1), incremental analysis with second order effects (curve 2), nonlinear incremental analysis that upgrades the axial forces at each load step (curve 3).

For other values of αL, load multipliers $\lambda_{p,\mathrm{lim}}$ at limit point are determined and presented in Figs. 1. 1.56a and b using cross symbols, whereas continuous lines and dots represents buckling loads. The differences between buckling analysis and nonlinear incremental analysis are larger up to $\alpha L = 10$ for the pipe having $\psi = 0.5$ (Fig. 1. 1.56a); whereas for stiffer soil, load multipliers $\lambda_{p,\mathrm{lim}}$ are quite close to buckling loads $\lambda_{p,\mathrm{cr}}$. For pipe with $\rho = 4$, $\eta = 2$ ($\psi = 2.0$), Fig. 1. 1.56b shows that the differences between buckling and nonlinear incremental analysis are larger up to $\alpha L = 5$.

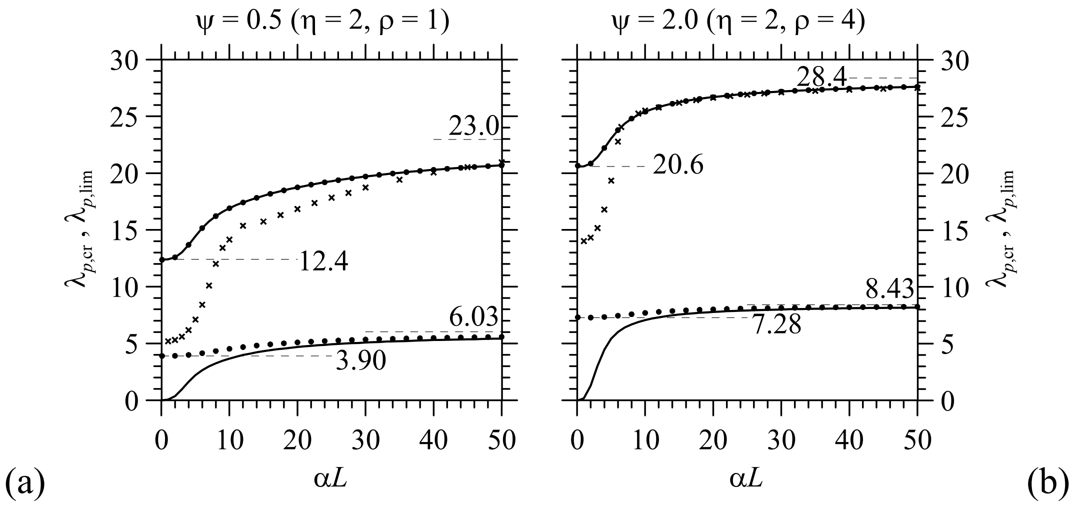

Fig. 1.56 – First and second dimensionless critical loads of rectangular pipes vs. αL for ψ = 0.5 (a) and 2.0 (b). Continuous lines and dots describe pipe with free and pinned foundation ends, respectively. The cross symbols represent load multipliers at limit points.

$\alpha L = 1$		$\eta = L/L_p$			
$\lambda_{p,\mathrm{lim}}/\lambda_{p,\mathrm{cr}}$		0.5	1	2	4
$\rho = D_b/D_p$	0.5	1.00	0.80	0.52	0.27
	1	1.00	1.00	0.42	0.27
	2	1.00	0.99	0.53	0.29
	4	1.00	1.00	0.68	0.32

Tab. 1.7 – Ratio $\lambda_{p,\mathrm{lim}}/\lambda_{p,\mathrm{cr}}$ for rectangular pipes on elastic half plane with $\alpha L = 1$.

$\alpha L = 5$		$\eta = L/L_p$			
$\lambda_{p,\mathrm{lim}}/\lambda_{p,\mathrm{cr}}$		0.5	1	2	4
$\rho = D_b/D_p$	0.5	1.00	0.96	0.65	0.25
	1	1.00	1.00	0.49	0.25
	2	1.00	0.96	0.65	0.26
	4	1.00	1.00	0.84	0.31

Tab. 1.8 – Ratio $\lambda_{p,\mathrm{lim}}/\lambda_{p,\mathrm{cr}}$ for rectangular pipes on elastic half plane with $\alpha L = 5$.

Finally, for $\alpha L = 1$ and 5, Tabs. 7 and 8 show the ratio $\lambda_{p,\mathrm{lim}}/\lambda_{p,\mathrm{cr}}$ for some values of pipe parameters ρ and η. Each diagonal in Tabs. 7 and 8 exhibits the same value of ψ, which provides the same $\lambda_{p,\mathrm{cr}}$ regardless of the chosen parameters ρ and η. Conversely, small limit load multiplier $\lambda_{p,\mathrm{lim}}$ occurs with low values of ρ and if $L > 2\, L_p$. However, Figs 1.54a and c and Fig. 1.55a show that the limit load multiplier $\lambda_{p,\mathrm{lim}}$ requires significant rotation. Consequently, ordinary structures collapse due to reached strength limit rather than elastic instability.

2 Stability of Timoshenko beams resting on elastic half-plane

2.1 Introduction

The effect of parameters associated with shear deformations on the buckling capacity is significant for sandwich panels, for built-up columns and for short beams, and that is why the buckling of Timoshenko beams has been widely studied in the past (Timoshenko and Gere 1961, Bazant and Cedolin 1991, Wang et al. 2005). However, a comprehensive study of the shear deformation effects on the buckling of beams resting on elastic media has never been thoroughly developed. Nonetheless, numerous studies assume various alternative substrate models, from the simplest Winkler model (Hetenyi 1946) to the more complex soil model suggested by Wieghardt (1922). For instance, Abbas and Thomas (1978), Yokoyama (1988), Cheng and Pantelides (1988), Wang et al. (1991) proposed numerical solutions to study the elastic stability of Timoshenko beams on Winkler soil. Moreover, Hlaváček (2003) presented a thorough mathematical analysis of the buckling problem of a simply supported Timoshenko beam on Winkler soil. Recently, Timoshenko beam-column resting on a two- or three-parameter elastic foundation has received increasing attention, e.g. see Arboleda-Monsalve et al. (2008), Sapountzakis and Kampitsis (2010, 2011, 2012) and references cited therein. Finally, Smith (1969), Ruta and Elishakoff (2006) studied a simply supported beam on a Wieghardt-type elastic foundation and derived an analytical solution for the buckling loads.

It is worth noting that, to the author's knowledge, the analytical or numerical analyses concerning the buckling of Timoshenko beams in frictionless contact with an elastic half-plane are not available. To this aim, the present chapter generalizes the finite element model proposed in Tullini and Tralli (2010). Results have recently been published and discussed in Tullini et al. (2012b). In particular, the soil is represented as an elastic half-space in plane state conditions. The present finite element method makes use of a mixed variational formulation based on a proper Green function of the half-plane, which describes the relation between beam deflections and contact pressure. The corresponding finite element model for the soil-beam system adopts “modified” Hermitian shape functions (Naraynaswami and Adelman 1974; Kosmatka 1995; Reddy 1997; Minghini et al. 2007) and constant soil reactions for each foundation element. Therefore, the present finite element model represents a one-dimensional theory that makes use of a boundary integral equation to reduce the two-dimensional half-plane to its one-dimensional boundary. Unlike what is claimed in Tullini and Tralli (2010), possible constraints cannot be directly applied to global stiffness and geometric matrices. In fact, the adopted Green function of the soil holds for a half-plane loaded by a point force normal to its boundary and requires a free boundary elsewhere. Therefore, constraint equations are added to the mixed variational formulation of the foundation-soil system by means of a penalty approach.

Numerical examples refer to beams, with pinned or free ends, characterized by two slenderness values. Buckling loads and the corresponding mode shapes are determined for various values of the mechanical and geometrical characteristics of the soil-beam system. Moreover, a classical two-dimensional finite element model is used as reference solution, which allows to asses the validity range of Euler-Bernoulli and Timoshenko beam models. Finally, the results reported in the present chapter are intended to give reference solutions to future works adopting multi-parameter substrate models.

2.2 Basic relationships

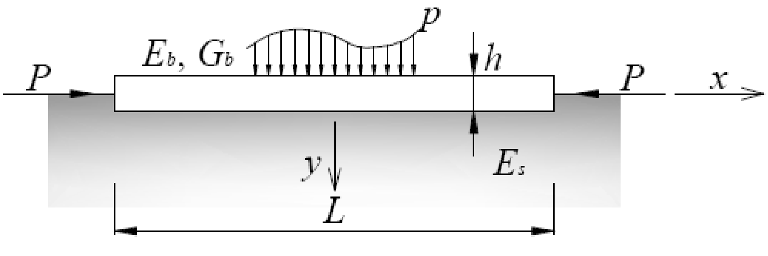

Fig. 2.1 – Beam on elastic half plane subject to external load $p(x)$ and compressive force P.

An elastic beam of length L, cross-section height h and width b, resting on a semi-infinite linearly elastic substrate, is referred to a Cartesian coordinate system (0; x, y), where x coincides with both the centroidal axis and the boundary of the half-plane and y is directed downward. The beam is made of homogeneous linearly elastic material, with longitudinal and transverse elastic moduli E_b, G_b, and Poisson coefficient ν_b. The isotropic material of the soil is characterized by the modulus E_s and Poisson's ratio ν_s. Generalized plane stress or plane strain regime is considered; in the latter case, both beam and half-plane have a unitary values of the width b. A concentrated compressive force P acts at each beam end as shown in Fig. 2.1. A distributed vertical external load $p(x)$ and couple $m(x)$ can also be applied along the beam axis x. Frictionless and bilateral conditions characterize the interface between beam and soil. Consequently, a vertical soil reaction $r(x)$ is enforced to both beam and substrate and the vertical displacement $v(x)$ of the beam coincides with those of the half-plane boundary.

Assuming positive cross-section rotation φ in counterclockwise direction, axial and transverse displacements of Timoshenko beam model can be written as:

$$u(x, y) = \varphi\, y, \quad v(x, y) = v(x), \tag{2.1}$$

and the corresponding nonzero axial and shear strains become:

$$\varepsilon = \varphi' y, \quad \gamma = v' + \varphi, \tag{2.2}$$

where prime represents differentiation with respect to x. Plane strain assumption yields the following stress-strain relations:

$$\sigma = E_b/(1-\nu_b^2)\ \varepsilon, \quad \tau = G_b\, \gamma. \tag{2.3}$$

Using strain components (Eq. 2.2) and constitutive laws (Eq. 2.3), the potential energy Π_e of the Timoshenko beam can be written as (Reddy 2006):

$$\Pi_e = \frac{1}{2}\int_L [D_b(\phi'(x))^2 + k_b G_b A(v'(x)+\phi(x))^2]\,\mathrm{d}x - L_e \tag{2.4a}$$

$$L_e = b\int_L \Big[\big(p(x)-r(x)\big)\,v(x) + m(x)\,\phi(x)\Big]\mathrm{d}x \tag{2.4b}$$

where $A = bh$ is the beam cross-sectional area and $D_b = E_0\, bh^3/12$ is the flexural rigidity, with $E_0 = E_b$ or $E_0 = E_b/(1-\nu_b^2)$ for a generalized plane stress or plane strain state, respectively, and k_b is the shear factor (Cowper 1966; Tullini and Savoia 1999):

$$k_b = \frac{5}{(6-\nu_b G_b/E_b)} \quad \text{or} \quad k_b = \frac{5}{\left[6-\nu_b(1+\nu_b)\,G_b/E_b\right]} \tag{2.5a, b}$$

for a generalized plane stress or plane strain state, respectively.

Renewed interest in the derivation of the second order work terms of the Timoshenko beam has recently arisen (Aristizábal-Ochoa 2008, Blaauwendraad 2008). However, for the purposes of the present work, the classical Engesser approach is considered (Timoshenko and Gere 1961); thus, the total potential energy Π_b of the beam, including second order effects, can be written as

$$\Pi_b = \Pi_e - \frac{P}{2}\int_L [v'(x)]^2\,dx\,. \tag{2.6}$$

Making use of Clapeyron’s theorem, the total potential energy of the soil is equal to half the potential energy of the contact stresses at the beam soil interface (Tullini and Tralli 2010):

$$\Pi_s = -\frac{b}{2}\int_L r(x)\,v(x)\,\mathrm{d}x = -\frac{b}{2}\int_L r(x)\,\mathrm{d}x\int_L g(x,\hat{x})\,r(\hat{x})\,\mathrm{d}\hat{x}, \tag{2.7}$$

where the vertical displacement $v(x)$ is replaced by the boundary integral equation commonly referred to as Flamant’s solution (Johnson 1985) already defined for the Euler-Bernoulli beam case:

$$g(x,\hat{x}) = -\frac{2}{\pi\,E}\ln|x-\hat{x}| \tag{2.8}$$

with $E = E_s$ or $E = E_s/(1-\nu_s^2)$ for a generalized plane stress or plane strain state, respectively.

Constraint equations $R_i(v, \varphi) = 0$ among displacements or rotations can be included in the total potential energy Π of the beam-substrate system by means of a penalty approach (Reddy 2006),

$$\Pi(v,r) = \Pi_b(v,r) + \Pi_s(r) + \frac{1}{2}\sum_i k_i\ [R_i(v,\varphi)]^2, \tag{2.9}$$

where k_i is the penalty parameter, whose value should be large enough to accurately satisfy the constraint equations. For beams with free ends, rigid-body displacement related to Flamant's solution can be removed by choosing an arbitrary abscissa $\bar{x}$ where a null value of $v(\bar{x})$ is forced. It is worth noting that Flamant's solution (Eq. 5) holds for a half-plane loaded by a point force normal to its boundary, which must be free to deform everywhere. The penalty approach allows to reformulate a problem with constraints as one without constraints.

2.3 Discrete model

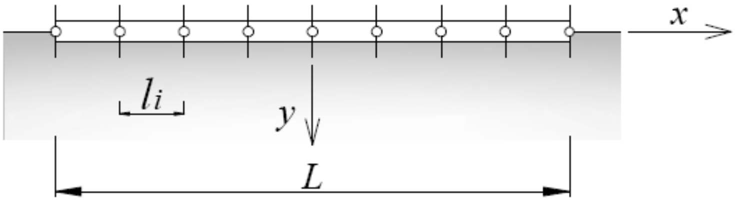

Fig. 2.2 – Beam on elastic half plane subdivided into 8 equal FEs

The discretization of the beam-substrate system is the same one described in the first chapter for the Euler-Bernoulli beam case, which can be created by subdividing the beam into finite elements of length l_i (Fig. 2.2) and by considering a piecewise constant soil reaction inside each element (Tullini and Tralli 2010): $r(\xi) = [\boldsymbol{\rho}(\xi)]^T \mathbf{r}_i$, where $\mathbf{r}_i$ denotes the vector components of nodal soil reaction and $\boldsymbol{\rho}$ assembles constant shape functions. Beam displacements and rotations are discretized in the usual form as follows:

$$\mathbf{d}(\xi) = \mathbf{N}(\xi)\ \mathbf{q}_i \tag{2.10}$$

where $\xi = x/l_i$, $\mathbf{d} = [v, \varphi]^{\mathrm{T}}$ collects the unknown displacement function, $\mathbf{q}_i = [v_1, \varphi_1, v_2, \varphi_2]^{\mathrm{T}}$. As for the beam shape functions, collected in matrix $\mathbf{N}(\xi)$, the "modified" Hermitian polynomials that follow from the solution of the homogeneous Timoshenko beam problem are assumed (Naraynaswami and Adelman 1974; Kosmatka 1995; Reddy 1997; Minghini et al. 2007):

$$\begin{aligned}
N_{11} &= \left[1 - 3\xi^2 + 2\xi^3 + \phi_i(1-\xi)\right]/(1+\phi_i); & N_{21} &= 6\xi(1-\xi)/\left[l_i(1+\phi_i)\right]; \\
N_{12} &= -l_i\,\xi\left[(1-\xi)^2 + \phi_i(1-\xi)/2\right]/(1+\phi_i); & N_{22} &= \left[1 - 4\xi + 3\xi^2 + \phi_i(1-\xi)\right]/(1+\phi_i); \\
N_{13} &= \left[3\xi^2 - 2\xi^3 + \phi_i\xi\right]/(1+\phi_i); & N_{23} &= -6\xi(1-\xi)/\left[l_i(1+\phi_i)\right]; \\
N_{14} &= -l_i\,\xi\left[-\xi + \xi^2 - \phi_i(1-\xi)/2\right]/(1+\phi_i); & N_{24} &= \left(-2\xi + 3\xi^2 + \phi_i\xi\right)/(1+\phi_i).
\end{aligned} \tag{2.11}$$

Such shape functions contain the shear parameter:

$$\phi = \frac{12D_b}{k_b G_b A L^2} = \frac{E_0}{k_b G_b}\left(\frac{h}{L}\right)^2, \tag{2.12}$$

which tends to zero when the influence of shear deformations becomes negligible, resulting in a locking-free formulation with shape functions that reduce to those of the classical Euler-Bernoulli beam model. For a prismatic beam, the stationarity condition of the total potential energy Π written in discrete form provides the following system:

$$\begin{bmatrix} \dfrac{D_b}{L^3}\left(\tilde{\mathbf{K}}_b - \dfrac{PL^2}{D_b}\tilde{\mathbf{K}}_g\right) & b\mathbf{H} \\ b\mathbf{H}^{\mathrm{T}} & -\dfrac{b}{E}\tilde{\mathbf{G}} \end{bmatrix} \begin{Bmatrix} \mathbf{q} \\ \mathbf{r} \end{Bmatrix} = \begin{Bmatrix} b\mathbf{F} \\ \mathbf{0} \end{Bmatrix}. \tag{2.13}$$

where the vector $\mathbf{q}$ collects nodal displacements, $\mathbf{r}$ denotes the vector of constant soil reactions underlying the beam finite element, $\mathbf{F}$ is the external load vector, $D_b/L^3\tilde{\mathbf{K}}_b$ is the elastic stiffness matrix of the beam, with element matrices $\tilde{\mathbf{K}}_{bi}$ reported in Przemieniecki (1968), $P/L\tilde{\mathbf{K}}_g$ is the geometric (or incremental) matrix (Kosmatka 1995) and the element of matrices $\mathbf{H}$ and $\breve{\mathbf{G}}$ together with the element matrices $\tilde{\mathbf{K}}_{bi}$ and $\tilde{\mathbf{K}}_{gi}$ are reported in the appendix A1. System in Eq. 2.13 yields the following solution:

$$\frac{D_b}{L^3}\left[\widetilde{\mathbf{K}}_b - \frac{PL^2}{D_b}\widetilde{\mathbf{K}}_g + \widetilde{\mathbf{K}}_{\text{soil}}\right]\mathbf{q} = b\mathbf{F}, \tag{2.14}$$

$$\mathbf{r} = E\,\widetilde{\mathbf{G}}^{-1}\mathbf{H}^{\mathrm{T}}\mathbf{q}, \tag{2.15}$$

where $\widetilde{\mathbf{K}}_{\text{soil}} = (\alpha L)^3\,\mathbf{H}\widetilde{\mathbf{G}}^{-1}\mathbf{H}^{\mathrm{T}}$ is the stiffness matrix of the soil and the parameter $(\alpha L)^3 = EbL^3/D_b$ characterises the beam-substrate system (Biot 1937; Vesic 1961; Tullini and Tralli 2010).

Finally, the buckling loads are given by the roots P_{cr} of the equation $\det[\widetilde{\mathbf{K}}_b - P_{\text{cr}}L^2/D_b\,\widetilde{\mathbf{K}}_g + \widetilde{\mathbf{K}}_{\text{soil}}] = 0$, which can be suitably reduced to a standard eigenvalue problem. In the following, dimensionless critical loads are referred to the Euler critical load $P_{\text{cr,E}} = \pi^2 D_b/L^2$.

2.4 Comparison of the present model with a classical FE model

The present finite element model is compared with a two-dimensional elastic model, where both beam and half-plane are modelled by quadrilateral finite elements in plane state. The mesh created for simulating the half-plane is equal to the one described for the Euler-Bernoulli beam case.

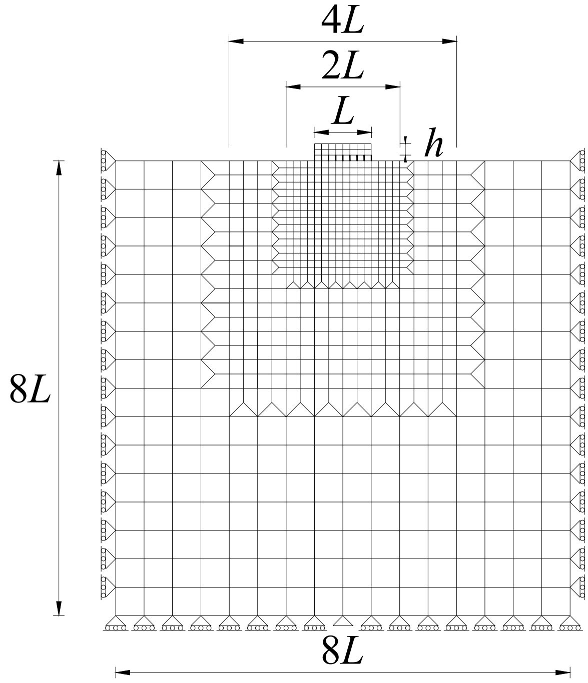

Fig. 2.3 – Mesh adopted for the two-dimensional model with foundation beam subdivided into 2 and 8 elements in vertical and horizontal direction.

Fig. 2.3 shows the simple case of the foundation beam subdivided into 2 and 8 elements in vertical and horizontal direction, respectively. Moreover, vertical master-slave links connect the nodes of each beam end section in order to avoid local deformations. It must be noted that the adopted two-dimensional code uses geometric matrix also for half-space finite elements.

2.4.1 Convergence test for a beam with free ends

Tab. 2.1 collects the number of equations of the 2D model and the presented model, varying the number of beam elements. By comparing this table with the corresponding one for the Euler-Bernoulli beam case, it is clear that the 2D mesh adopted to represent the beam does not significantly affect the total number of equations as, in fact, the large number of equations is due to the mesh adopted for the half-plane. Then, the number of equations of the 2D model n_{eq}^{2D} is related to the number of equations of the present analysis n_{eq}^{PA} by means of the relation defined for the Euler-Bernoulli beam case:

$$n_{eq}^{2D} \cong 2\,(n_{eq}^{PA})^2 . \tag{2.16}$$

where $n_{eq}^{PA} = 2\,n_{el} + 2$ as usual.

n_{el}	n_{eq}	
	2D model	Presented Analysis
2^3	1527	18
2^4	5615	34
2^5	21727	66
2^6	85439	130
2^7	338815	258
2^8	1349375	514

Tab. 2.1 – Number of equations for the two models considered, with respect to the number of beam FEs

Tables 2.2a and b shows the first dimensionless critical load $P_{cr}/P_{cr,E}$ for a beam with free ends evaluated with both the present model and the two-dimensional model as a function of foundation beam subdivision n_{el}^{2D} for $\alpha L = 5$ and 25, respectively, and $L/h = 5, 15$.
To solve the eigenvalue problem, the CPU time t^{2D} of the two-dimensional model is equal to 165 t^{PA}, where t^{PA} is the CPU time of the present analysis. Therefore, while the present model can be considered effective to determine buckling loads and critical modes, the 2D model will however be taken into account in order to evaluate critical load differences increasing αL.

n_{el}^{PA}	n_{el}^{2D}	$\alpha L = 5$			
		$L/h = 5$		$L/h = 15$	
		PA	2D	PA	2D
8	2×8	1.794	2.064	1.870	2.184
16	4×16	1.863	1.955	1.939	2.080
32	8×32	1.892	1.903	1.967	2.032
64	16×64	1.905	1.877	1.980	2.008
128	32×128	1.912	1.864	1.987	1.997
256	64×256	1.915	1.857	1.990	1.991
2^{11}	-	1.917	-	1.992	-

(a)

n_{el}^{PA}	n_{el}^{2D}	$\alpha L = 25$			
		$L/h = 5$		$L/h = 15$	
		PA	2D	PA	2D
8	2×8	9.519	14.537	21.608	71.424
16	4×16	11.653	12.651	35.278	57.725
32	8×32	12.280	11.975	41.550	50.490
64	16×64	12.490	11.735	44.132	46.734
128	32×128	12.577	11.652	45.286	44.680
256	64×256	12.619	11.626	45.837	43.518
2^{11}	-	12.651	-	46.343	-

(b)

Tab. 2.2 – First dimensionless critical loads $P_{\text{cr}}/P_{\text{cr,E}}$ for a beam with free ends corresponding to the present analysis (PA) or 2D models as a function of n_{el} for $L/h = 5, 15$, $\alpha L = 5$ (a) and $\alpha L = 25$ (b)

2.5 Buckling analysis of beams with different end restraints

For the cases reported in this section, equal finite elements are used in beam length subdivision and n_{el} = 256 is adopted, giving rise to sufficiently accurate solutions. Moreover, for the two beam slenderness cases considered, i.e. L/h equal to 5 and 15 and assuming a Poisson's ratio $\nu_b = 0$, the corresponding shear parameters ϕ are equal to 0.096 and 0.0107, respectively. In order to obtain sufficiently accurate buckling loads $P_{\mathrm{cr},m}^{\mathrm{2D}}$, the two-dimensional model of the beam utilizes a rectangular mesh having 32 and 128 subdivisions in vertical and horizontal directions, respectively.

2.5.1 Beam of finite length with pinned ends

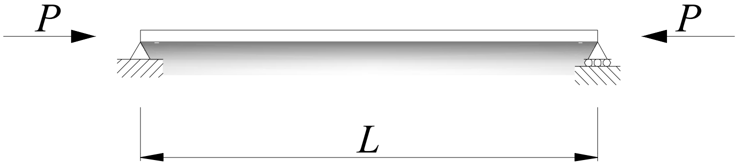

Fig. 2.4 – Beam with free ends on elastic half-plane subject to axial load.

The case of a simply supported beam is considered first (Fig. 2.16). This case may refer to a rigid portal frame whose columns are hinged to the foundation beam ends; thus, the structure enforces zero relative displacement between beam ends, but allows independent rotations. The constraint equation that must be applied to Eq. 6 is $R_1 = v(L/2) - v(-L/2) = 0$, assuming k equal to $10^4\, D_b/L^3$.

Considering the first slenderness case (L/h = 5), Figs. 2.5a and b show all dimensionless critical loads $P_{\mathrm{cr}}/P_{\mathrm{cr,E}}$ versus the parameter αL^3 and αL, respectively. Fig. 2.5c represents the ratio $P_{\mathrm{cr}}/[P_{\mathrm{cr,E}}\,(\alpha L)^2]$ versus the parameter αL. The corresponding results obtained for the second slenderness case (L/h = 15) are shown in Figs. 2.6a, b and c.

For $\alpha L = 0$, i.e. for a simply supported beam without supporting soil, numerical results are in excellent agreement with exact solutions (Timoshenko and Gere 1961) for both slenderness cases:

$$P_{\mathrm{cr},m} = m^2 P_{\mathrm{cr,E}} \left[1 + \frac{m^2 \pi^2 \phi}{12} \right]^{-1} \quad \text{for } m = 1, 2, 3, \ldots \tag{2.17}$$

The effect of shear strain is to decrease critical loads with respect to the classical Euler solution and the influence of shear deformation increases for increasing the mode number m. Relations similar to Eq. 2.17 hold for several end restraints, especially for fixed-fixed, fixed-free, fixed-sliding restraint columns (Bazant and Cedolin 1991; Wang et al. 2005). The Timoshenko critical load $P_{\mathrm{cr}}^{\mathrm{T}}$ and the corresponding Euler critical load $P_{\mathrm{cr}}^{\mathrm{E}}$ are related by $P_{\mathrm{cr}}^{\mathrm{T}} = P_{\mathrm{cr}}^{\mathrm{E}}/[1 + P_{\mathrm{cr}}^{\mathrm{E}}/(k_b\, G_b\, A)]$. For increasing m, the value given by Eq. 2.17 converges to

$$P_{\mathrm{cr},\infty} = P_{\mathrm{cr,E}} \frac{12}{\pi^2\, \phi} = \frac{12\, D_b}{L^2\, \phi} = k_b G_b A \tag{2.18}$$

and the corresponding wavelength of the buckling mode tends to zero. The ratio $P_{\mathrm{cr},\infty}/P_{\mathrm{cr,E}}$ is equal to 12.7 and 114.0 for $L/h = 5$ ($\phi = 0.096$) and $L/h = 15$ ($\phi = 0.0107$). For low values of αL and increasing mode number, Figs. 2.5a and b and Figs. 2.6a and b show that the present finite element solutions are very close to the corresponding values of $P_{\mathrm{cr},\infty}$.

Increasing αL, the curves in Figs. 2.6a, b and c exhibit many curve veering and crossing points, and interchange themselves, whereas the curves in Figs. 2.5a, b and c are characterized by few crossing points. The behaviour of the longer beam ($L/h = 15$) is quite similar to the one obtained with the Euler-Bernoulli beam, whereas in that case critical loads do not present an upper limit. Moreover, for increasing αL, Figs. 2.5a and b and Figs. 2.6a and b show that several critical loads converge to the value given in Eq. 2.18. In particular, for $L/h = 5$, Figs. 2.5a and b show that the first and second buckling loads converge to $P_{\mathrm{cr},\infty} = 12.7$ with an error less than 1% for αL greater than 21 and 13, respectively; whereas for the longer beam ($L/h = 15$), Figs. 2.6a and b shows that convergence ($P_{\mathrm{cr},\infty} = 114.0$) is achieved for $\alpha L > 50$. Furthermore, Figs. 2.5a and b show that the third and fourth critical loads converge to $P_{\mathrm{cr},\infty}$ for αL approximately equal to 11, whereas in Figs. 2.6a and b the third and fourth critical loads converge to $P_{\mathrm{cr},\infty}$ for αL approximately equal to 34, then in this case critical loads after the second one converge to $P_{\mathrm{cr},\infty}$ rapidly with respect to the first and second critical loads. For both slenderness cases, the ratio $P_{\mathrm{cr}}/[P_{\mathrm{cr,E}}\, (\alpha L)^2]$ tends obviously to zero and the corresponding representation adopted in Figs. 2.5c and 6c is not as important as for the Euler-Bernoulli beam case.

$L/h = 5$

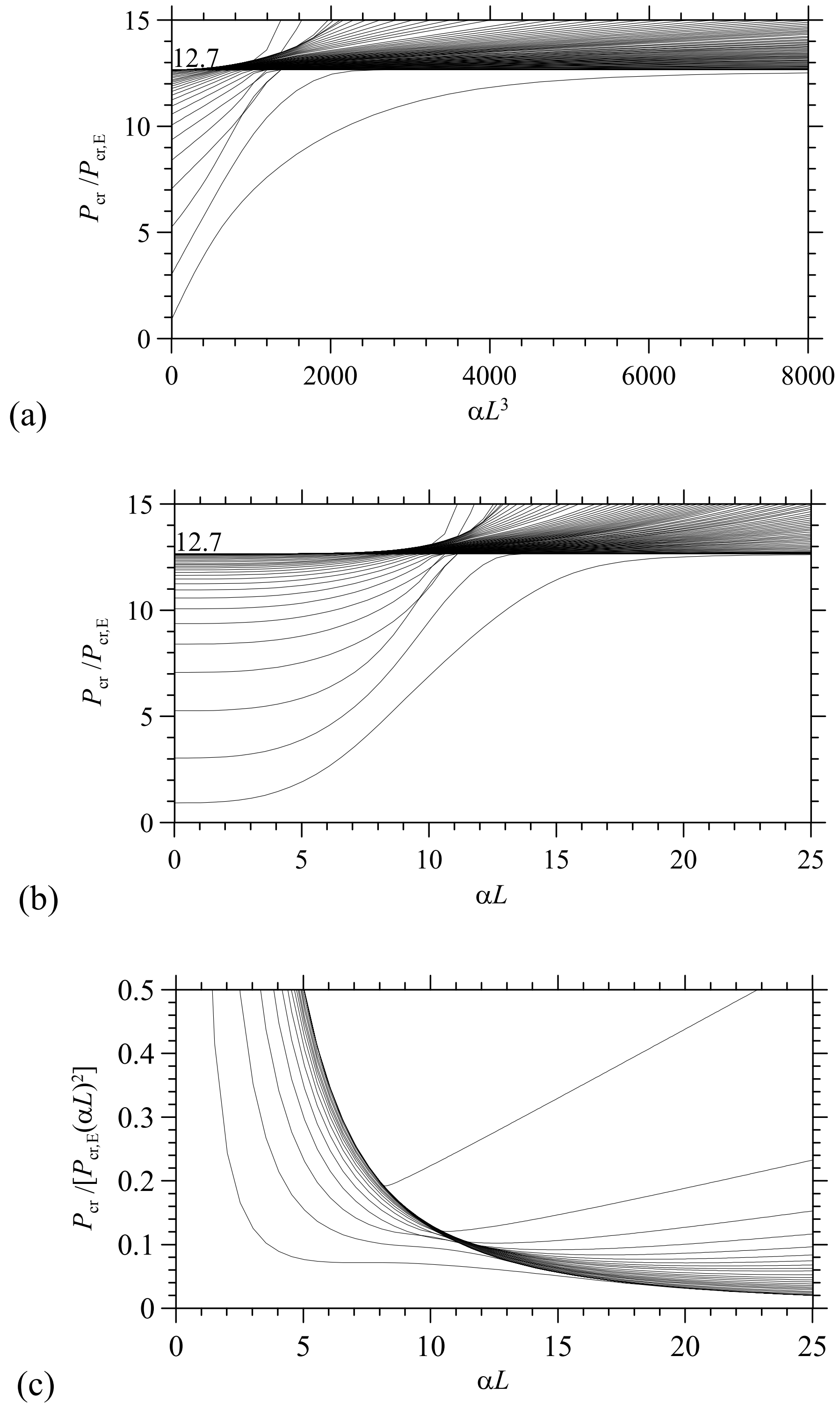

Fig. 2.5 – Dimensionless critical loads $P_{cr}/P_{cr,E}$ versus αL for a Timoshenko beam with pinned ends having $L/h = 5$.

$L/h = 15$

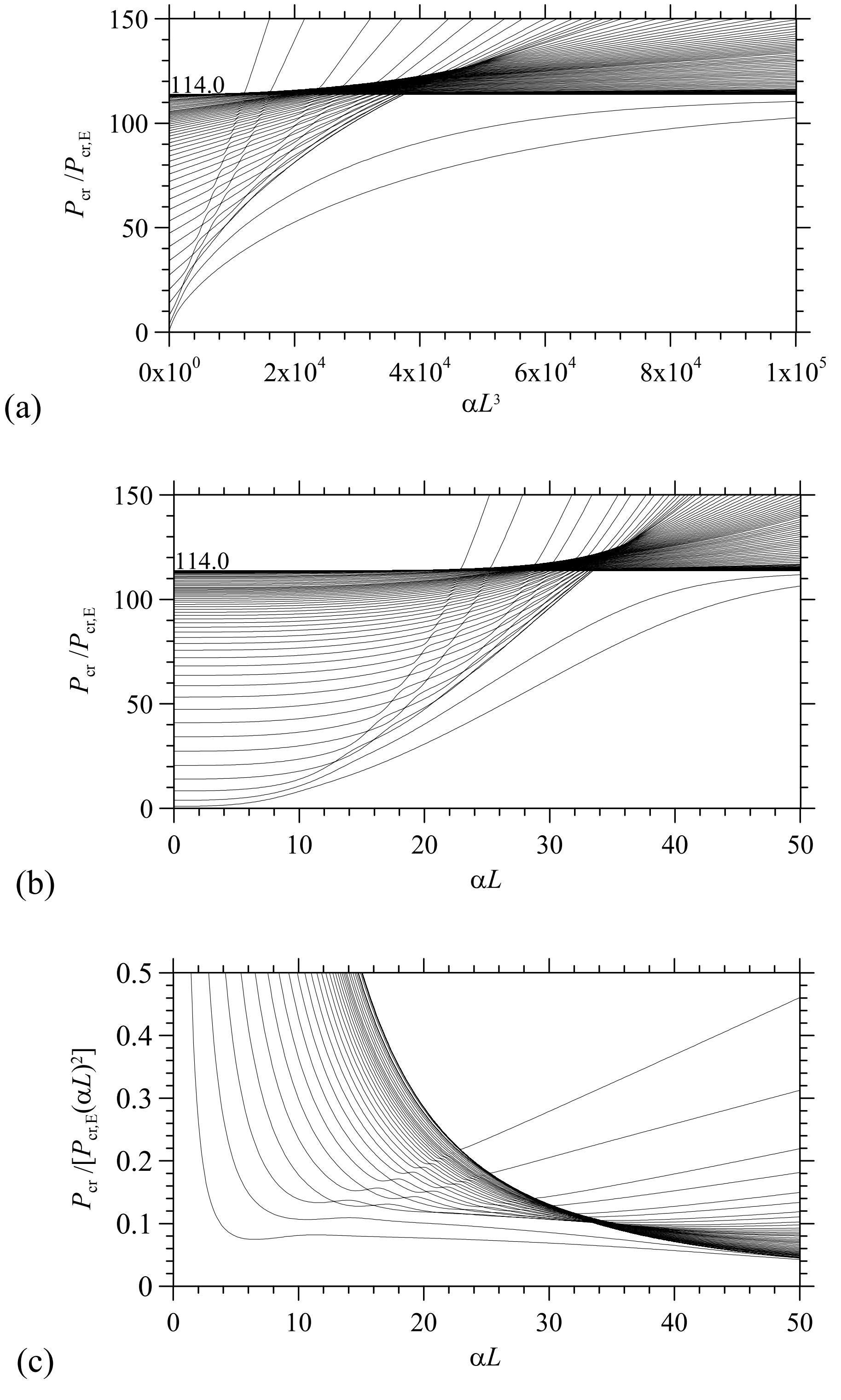

Fig. 2.6 – Dimensionless critical loads $P_{\mathrm{cr}}/P_{\mathrm{cr,E}}$ versus αL for a Timoshenko beam with pinned ends having $L/h = 15$.

The buckling loads obtained for the simply supported Timoshenko beam resting on an elastic half-plane appear to be quite similar to those related to beams on Winkler or Wieghardt soils (Smith 1969). For instance, Cheng and Pantelides (1988), Hlaváček (2003) provide the following analytical solution for a simply supported Timoshenko beam resting on Winkler soil with subgrade coefficient *c*:

$$P_{\mathrm{cr,W}} = P_{\mathrm{cr,E}} \left[m^2 \left(1 + \frac{m^2 \pi^2 \phi}{12} \right)^{-1} + \frac{1}{m^2 \pi^4} \frac{cL^4}{D_b} \right] \quad \text{for } m = 1, 2, 3, \ldots \tag{2.19}$$

For sufficiently high values of Winkler soil coefficient c, the critical load $P_{\mathrm{cr,W}}$ converges to $P_{\mathrm{cr},\infty}$ and the buckling mode presents a wavelength that tends to zero. However, in § 2.5.1.3, results obtained for a beam with pinned ends on Winkler soil are discussed.

2.5.1.1 Modal shapes

Considering the short beam case for first (L/h = 5), for αL = 5 Fig. 2.7a shows the first and second mode shapes that are characterized by one and two half-waves, respectively, whereas for αL = 10, the first and second mode shapes can not be described by sinusoidal functions. For αL = 15 it must be noted that the second critical load already achieves limit value $P_{\mathrm{cr},\infty}$ (Figs. 2.5a and b), then Fig. 2.7c shows the first mode shape characterized by great deflections at beam ends whereas the second mode shape presents short wavelength depending on mesh size n_{el}, i.e. increasing values of n_{el} yields smaller and smaller wavelength. For simplicity, in the critical modes depicted in Fig. 2.7c, n_{el} is reduced to 32. For $\alpha L \geq 20$, first eigenvalue reaches $P_{\mathrm{cr},\infty}$ (Figs. 2.5a and b), then, both first and second mode shapes need to be represented considering n_{el} reduced to 32, in order to appreciate the small wavelength.

Considering the long beam case (L/h = 15), for αL = 5 Fig. 2.8a shows sinusoidal buckling modes, which are quite similar irrespective of the ratio L/h to the short beam case. Increasing αL, the first and second mode shapes are quite similar to the ones obtained for the Euler-Bernoulli beam case, with deformations localized near beam ends (Figs. 2.8b, c, d and e). However, for the case of long beam on very stiff soil (αL = 50), Fig. 2.8f shows that the buckling modes are characterized by very short wavelengths and n_{el} is reduced to 32.

Buckling modes are characterized by very short wavelength even if the corresponding critical loads is far from $P_{\mathrm{cr},\infty}$ (Figs. 2.6a and b).

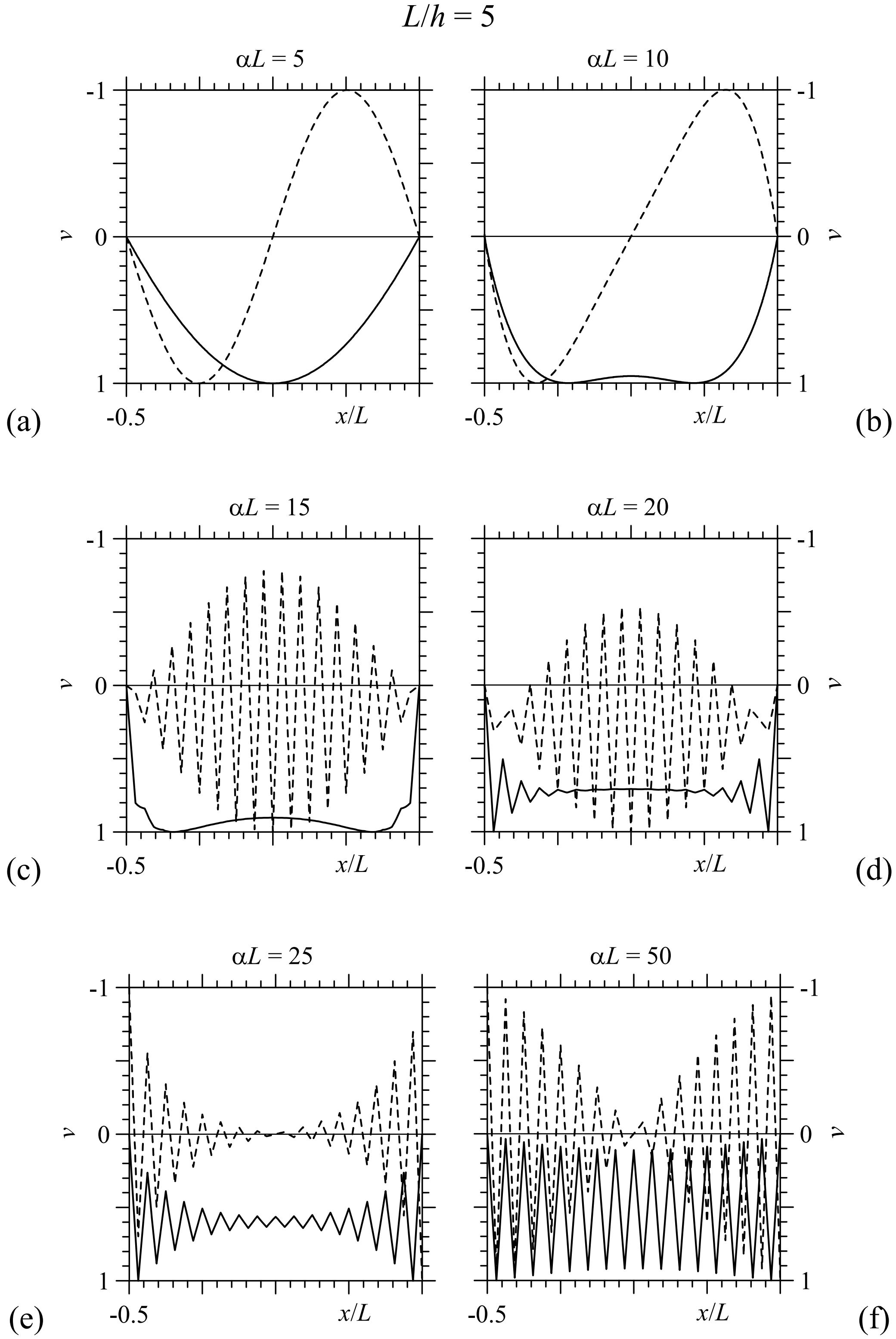

Fig. 2.7 – First (continuous line) and second (dashed line) buckling modes for a Timoshenko beam with pinned ends and $L/h = 5$, varying αL.

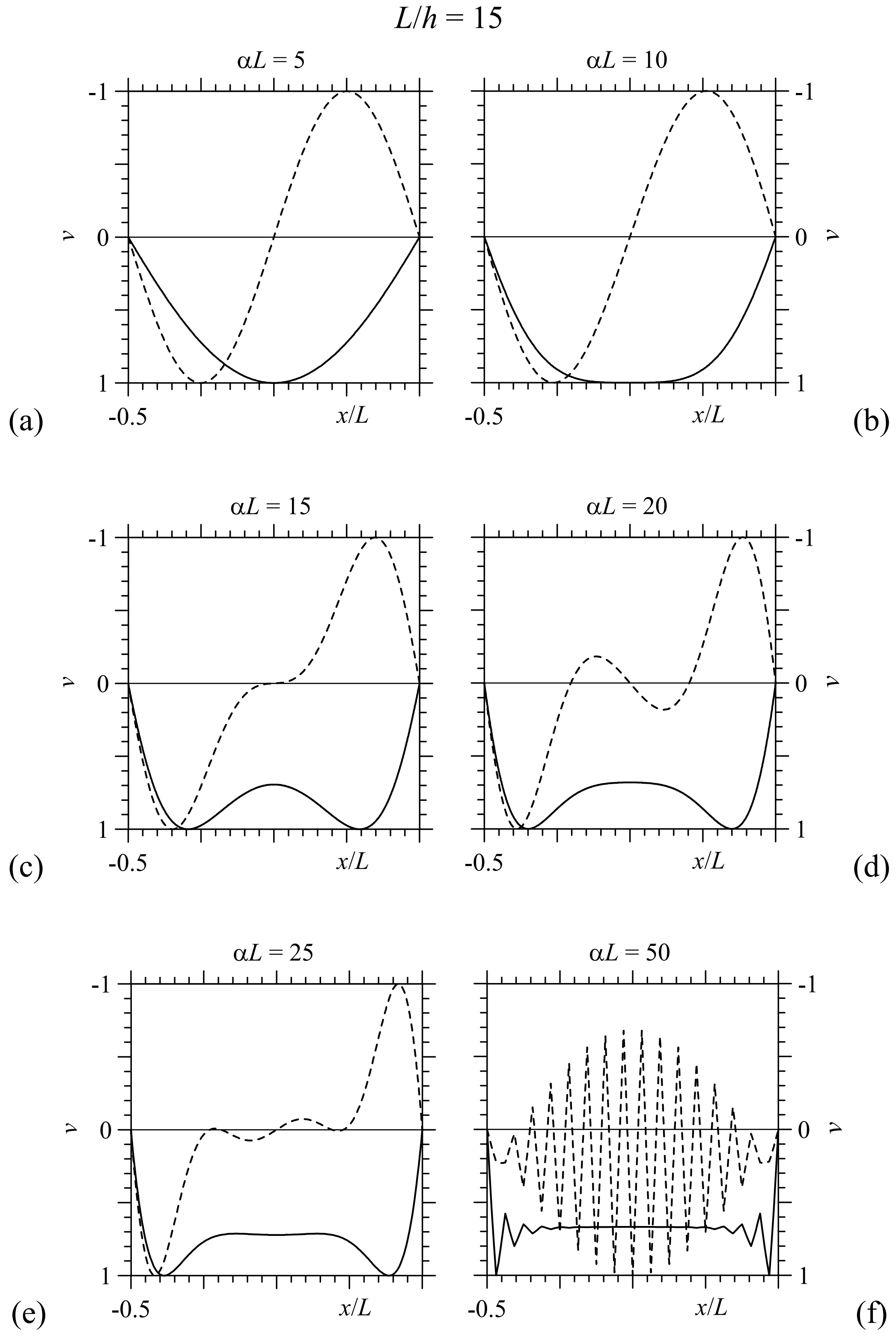

Fig.8 – First (continuous line) and second (dashed line) buckling modes for a Timoshenko beam with pinned ends and $L/h = 15$, varying αL.

2.5.1.2 Two-dimensional FE model results

The beam with pinned ends is then modelled by a 2D traditional FE model. A horizontal master-slave link that connects the nodes at half height of the beam end sections is introduced in order to simulate the restraint condition.

The first four critical loads $P_{\mathrm{cr},m}^{\mathrm{2D}}$, with $m = 1, 2, 3, 4$, obtained with the classical 2D FE model are compared with the values obtained with the presented model, by adopting dot symbols in Figs. 2.9a and b, for L/h equal to 5 and 15, respectively. For low αL values, the first two critical loads $P_{\mathrm{cr},1}^{\mathrm{2D}}$, $P_{\mathrm{cr},2}^{\mathrm{2D}}$ are quite close to those obtained with the presented model; whereas the third and fourth buckling loads $P_{\mathrm{cr},3}^{\mathrm{2D}}$, $P_{\mathrm{cr},4}^{\mathrm{2D}}$ are lower than those of the presented model and these differences appear more evident in the short beam case (Fig. 2.9a).

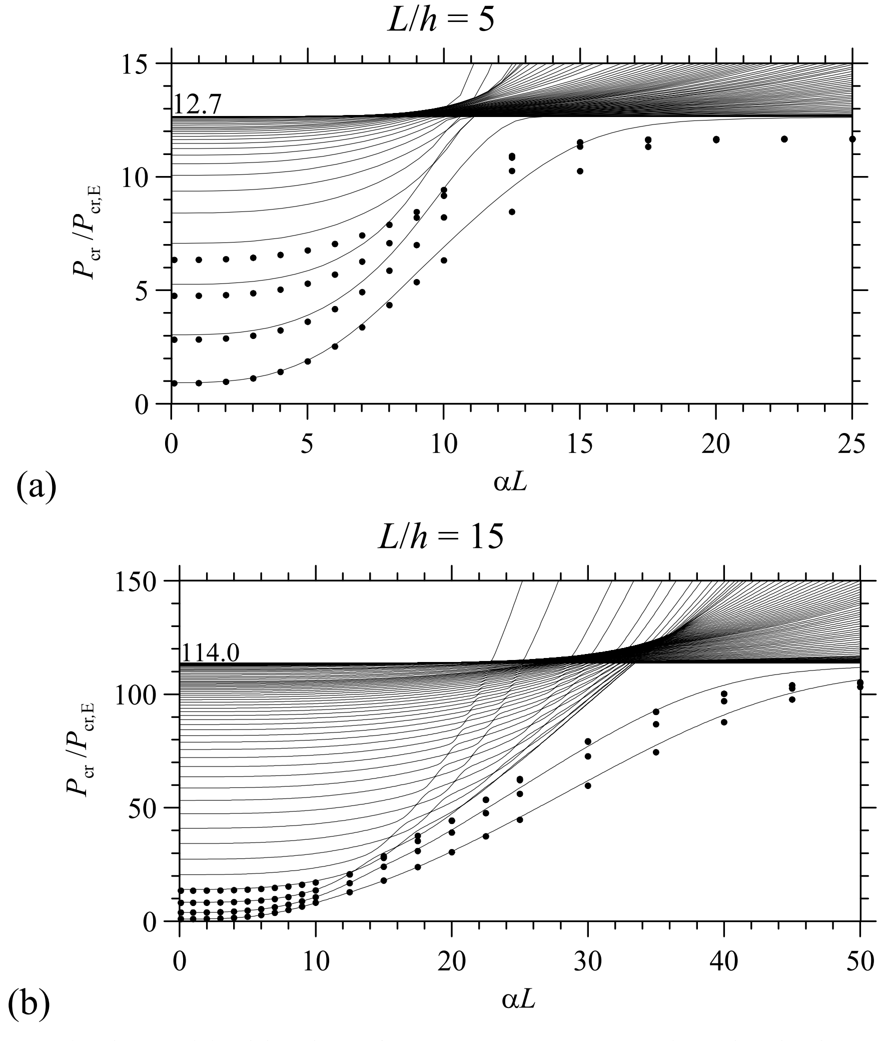

Fig. 2.9 – Dimensionless critical loads $P_{\mathrm{cr}}/P_{\mathrm{cr,E}}$ versus αL for a Timoshenko beam with pinned ends having $L/h = 5$ (a) and 15 (b). Continuous lines for the presented model, dots for the 2D model.

For increasing values of the parameter αL, the first four buckling loads $P_{\mathrm{cr},m}^{\mathrm{2D}}$, with $m = 1, 2, 3, 4$, reach a limit characterised by a constant value lower than $P_{\mathrm{cr},\infty}$. These differences are about 7.3% for the short beam ($L/h = 5$) and 4.2% for the long one ($L/h = 15$).

Figs. 2.10a-f show first and second mode shapes obtained with the 2D model for $L/h = 5$ for increasing αL. For $\alpha L = 5$ and 10 (Figs. 2.10a-d), first and second mode shapes are sinusoidal and they do not interchange themselves, whereas for $\alpha L = 25$ mode shapes are characterized by deformations localized at the upper part of the beam (Figs. 2.10e and f), such behaviour can not be described by a one-dimensional beam model. This justifies the differences between the buckling loads evaluated with the two-dimensional model and the beam model for large values of the parameter αL.

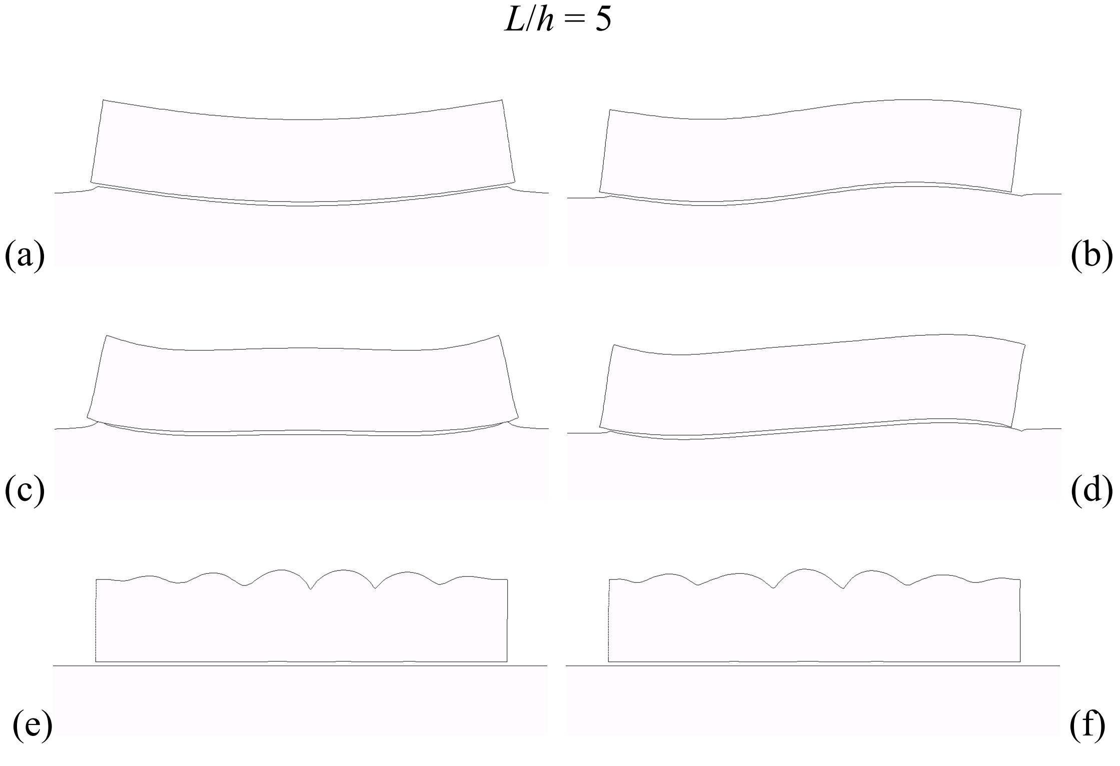

Fig. 2.10– First (a, c, e) and second (b, d, f) mode shapes for a short two-dimensional foundation beam ($L/h = 5$) with pinned ends having $\alpha L = 5$ (a, b) , $\alpha L = 10$ (c, d) and $\alpha L = 25$ (e, f).

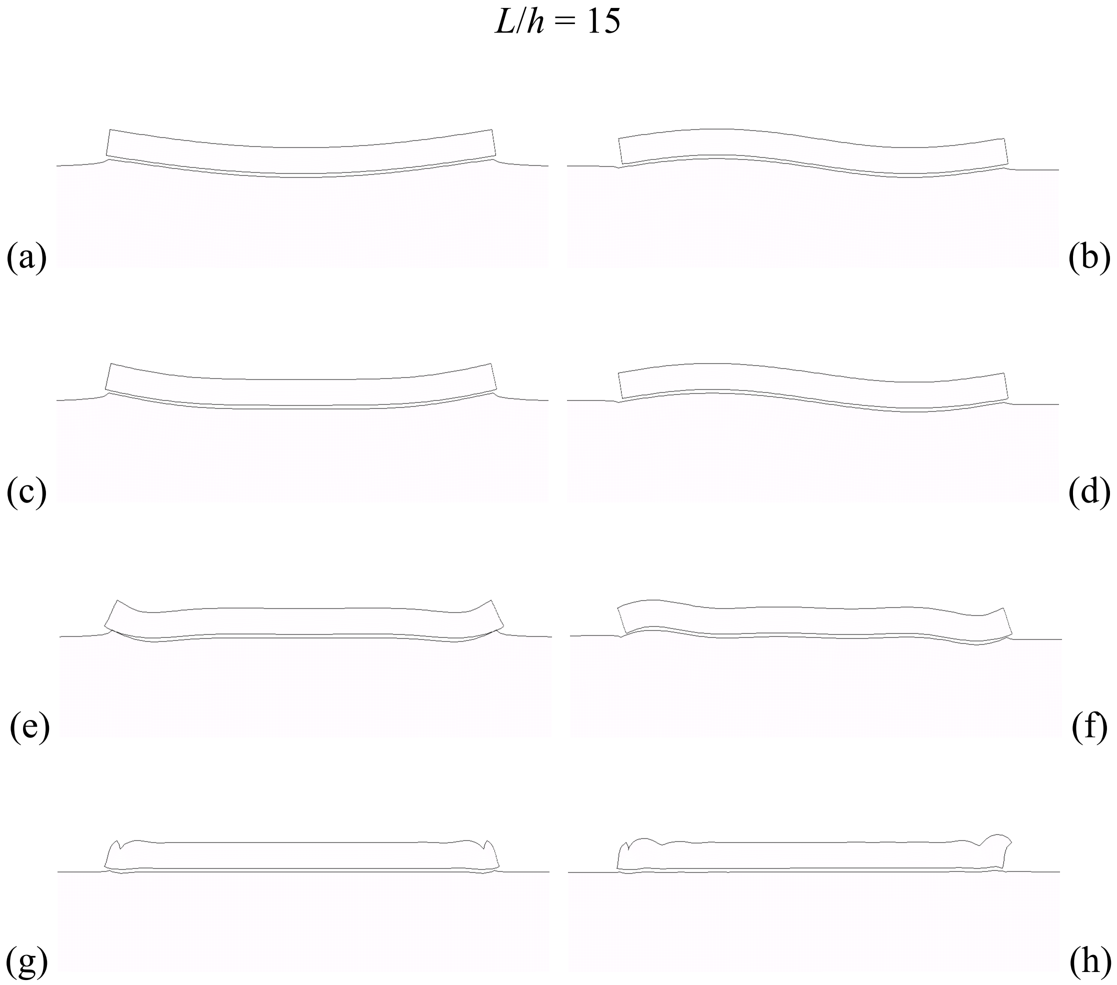

Fig. 2.11 – First (a, c, e, g) and second (b, d, f, h) mode shapes for a long two-dimensional foundation beam (*L*/*h* = 5) with pinned ends having $\alpha L = 5$ (a, b) , $\alpha L = 10$ (c, d), $\alpha L = 25$ (e, f) and $\alpha L = 50$ (g, h)

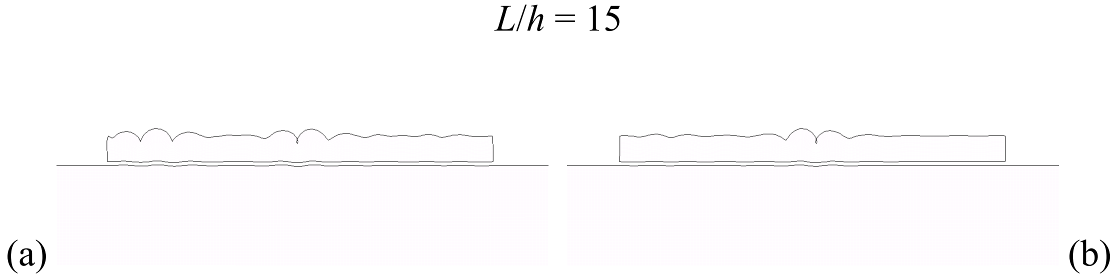

Fig. 2.12 –Third (a) and fourth (b) mode shapes for a long 2D beam (*L*/*h* = 15) with pinned ends and having $\alpha L = 50$.

For the long beam case (*L*/*h* = 15) modelled by 2D FEs, Figs. 2.11a-f show first and second mode shapes for increasing αL. For beams on soft soil, mode shapes are sinusoidal (Figs. 2.11a-d), whereas for $\alpha L = 25$ and 50 (Figs. 2.11e-h) mode shapes are characterized by deformations localized at beam ends, similarly to the results obtained with the present model (Fig.8e). In this case, the behaviour found for the short beam and $\alpha L = 25$ (Figs. 2.10e and f) can be detected if the third and fourth mode shapes are evaluated (Figs. 2.12a and b).

2.5.1.3 Buckling of a beam with pinned ends on Winkler half-space

Applying Winkler's hypothesis (1867) to the basic relationships of a Timoshenko beam on elastic half-space including second order effects, the corresponding buckling problem may be solved numerically by means of a discrete model. As shown in § 1.5.2.2, the beam-subgrade parameter for the Winkler-type half space is given by:

$$\gamma = \sqrt{\frac{c\,L^4}{D_b}} \tag{2.20}$$

where c represents the modulus of subgrade reaction or the Winkler constant.

In the following, the usual restraint condition for a beam with pinned ends ($R_1 = v(\pm L/2) = 0$) is considered for determining critical loads with the discrete model, moreover the same restraint condition adopted for the beam on half-plane with pinned ends ($R_1 = v(L/2) - v(-L/2) = 0$) is adopted for determining the first critical load. Figs. 2.13a and b show dimensionless critical loads $P_{\mathrm{cr}}/P_{\mathrm{cr,E}}$ as a function of γ for L/h equal to 5 and 15, respectively. Similarly to the case of the Timoshenko beam on half-plane, increasing mode number, the critical loads for low values of γ converge to $P_{\mathrm{cr},\infty}$ (Eq. 2.18) for both slenderness cases. For $\gamma = 0$, critical loads are coincident with the ones of a Timoshenko beam with pinned ends and without supporting soil (Eq. 2.17).

Substituting Eq. 1.34 into Eq. 2.19, Hlaváček (2003) analytic solution turns out to be

$$P_{\mathrm{cr,W}} = P_{\mathrm{cr,E}}\left[m^2\left(1+\frac{m^2\pi^2\phi}{12}\right)^{-1}+\left(\frac{\gamma}{m\,\pi^2}\right)^2\right] \quad \text{for } m = 1, 2, 3, \ldots \tag{2.21}$$

and it is added to Figs. 2.13a and b up to $m = 8$ with circles. The first critical load obtained with the discrete model and taking into account rigid body displacement is smaller than $P_{\mathrm{cr,W,1}}$ and converges to $P_{\mathrm{cr},\infty}$ for γ larger than 500 and 1000 for L/h equal to 5 and 15, respectively This difference is caused by the restraint condition adopted for determining the first critical load, which allows rigid body vertical displacements that are usually neglected in traditional solutions (Yokoyama 1988). Other critical loads determined with the discrete model turn out to be coincident with Hlaváček solution and converge to $P_{\mathrm{cr},\infty}$ for γ close to 120 and 1000 for L/h equal to 5 and 15, respectively. Differently than the case of the beam on half-plane, the second critical load is close to other results both considering and neglecting rigid body displacement for the beam.

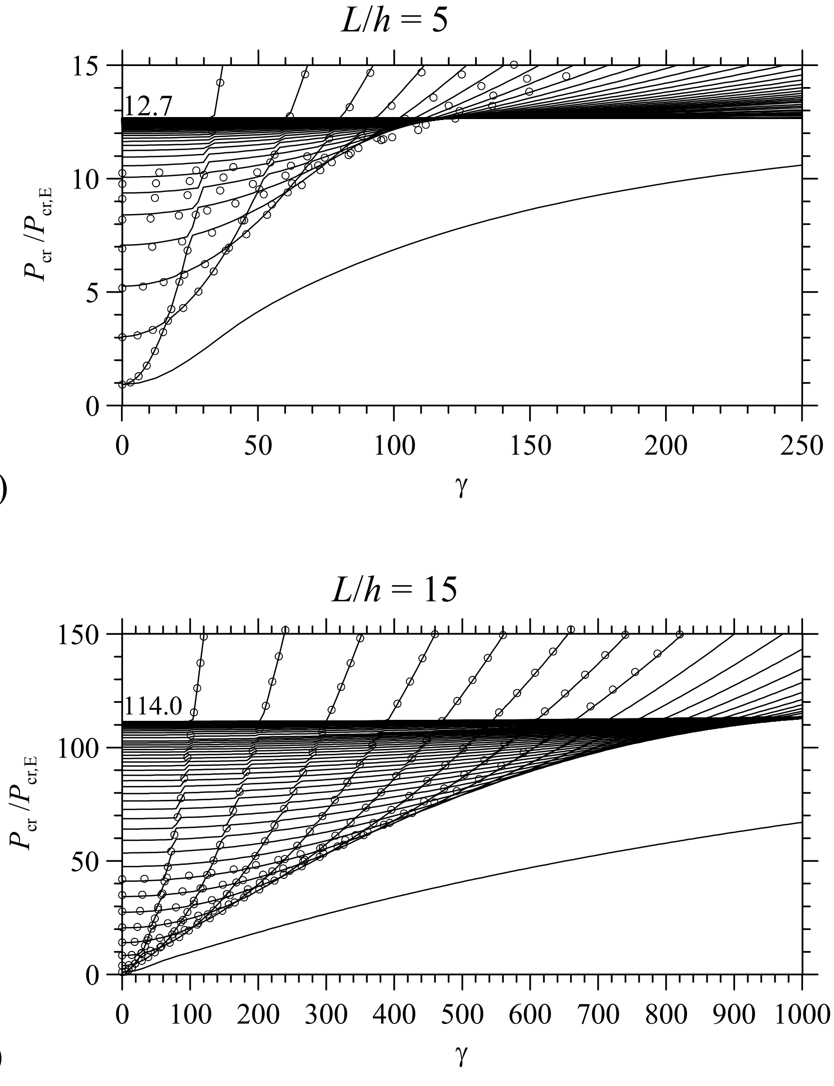

Fig. 2.13 – Dimensionless critical loads $P_{\mathrm{cr}}/P_{\mathrm{cr,E}}$ (continuous lines) and $P_{\mathrm{cr,W}}/P_{\mathrm{cr,E}}$ (circles) as function of γ for a beam with pinned ends on Winkler half space.

Figs. 2.26 a-d show first and second mode shapes for beams on soft and stiff half-space for both slenderness cases. For γ equal to 15, corresponding to αL quite close to 5, adopting Biot relation between c and elastic half-plane parameters (Eq. 1.37), first and second mode shapes are sinusoidal and are similar to the ones obtained for the case of the beam on half-plane for both slenderness cases (Figs. 2.7a and 2.8a).

$$c = \frac{0.710}{2^{4/3}}\left[\frac{E^4\, b^4}{D_b}\right]^{1/3} = 0.282\left[\frac{E^4\, b^4}{D_b}\right]^{1/3}. \tag{2.22}$$

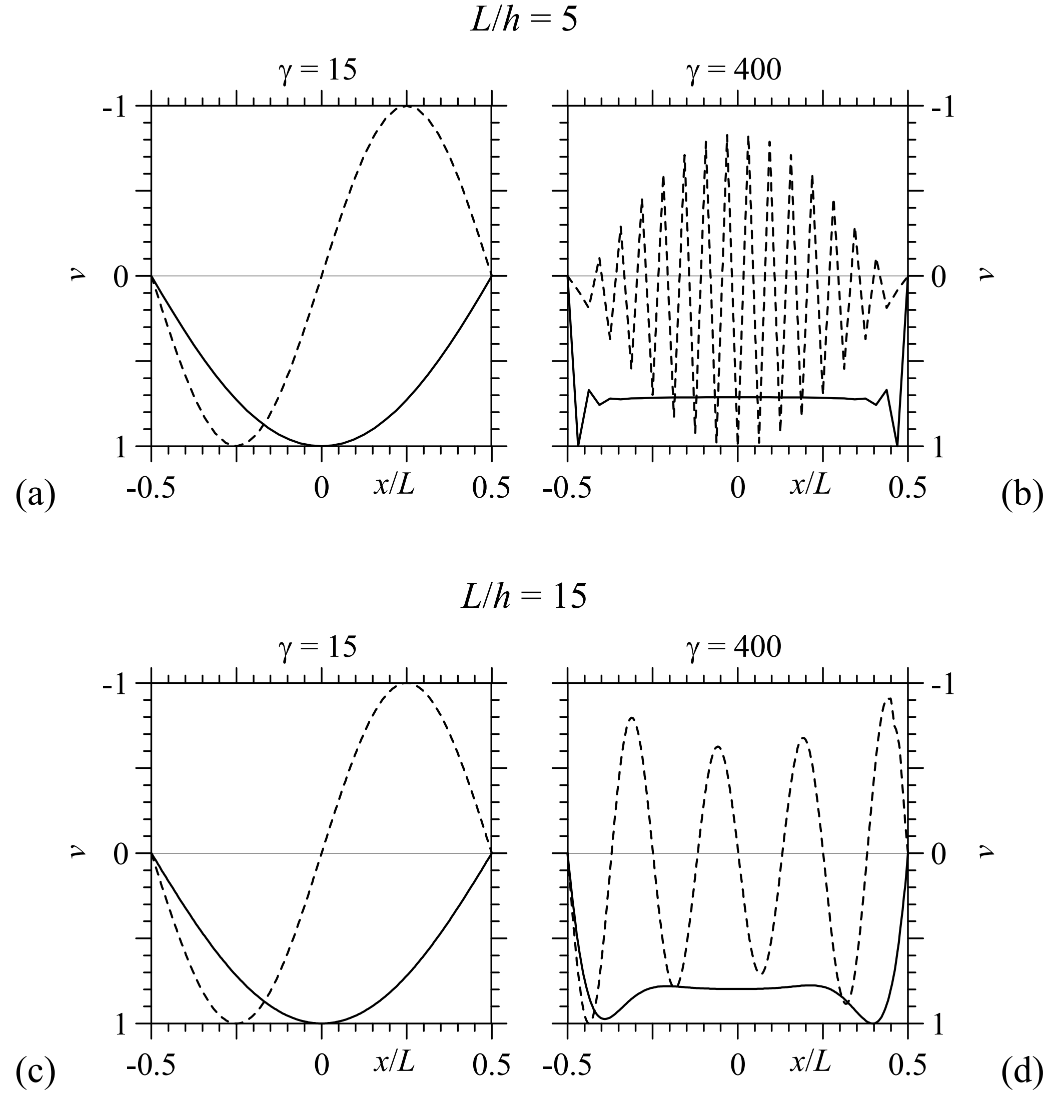

Fig. 2.14 – First (continuous line) and second (dashed line) buckling modes for a Timoshenko beam with pinned ends on Winkler half-space.

For γ equal to 400, corresponding to αL quite close to 25, the first and second mode shapes for the short beam case are characterized by very short wavelengths and 32 FEs are adopted to represent displacements. In this case, the first mode shape (Fig. 2.26 b, continuous line) is similar to the corresponding one obtained for the beam on half-plane (Fig. 2.7c, continuous line) and it is characterized by large deformations close to beam ends. The second mode shape is characterized by deformations along the entire beam length (Fig. 2.26 b, dashed line) and is similar to the corresponding one obtained for the beam on half-plane (Fig. 2.7c, dashed line).

Considering the long beam case (Fig. 2.26 d), the first mode shape is characterized by large deflections at beam ends, whereas the second mode shape is sinusoidal and different than the corresponding one obtained for the case of the beam on half-plane (Fig. 2.8d, dashed line).

2.5.2 Beam of finite length with free ends

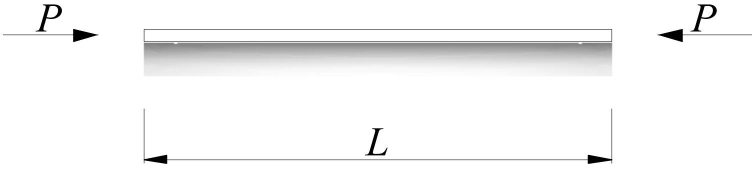

Fig. 2.15 – Beam with free ends on elastic half-plane subject to axial load.

The buckling of a Timoshenko beam with free ends on elastic half plane (Fig. 2.27) is considered. Figs. 2.16a and b show all dimensionless critical loads $P_{\mathrm{cr}}/P_{\mathrm{cr,E}}$ as a function of the parameter αL^3 and αL, respectively for slenderness L/h equal to 5; whereas Figs. 2.17a, b and c show the same data for slenderness L/h equal to 15. For $\alpha L = 0$ and for both slenderness ratios, the buckling loads are in excellent agreement with exact solutions (Timoshenko and Gere 1961) for both slenderness cases (Eq. 2.17). For increasing mode number, buckling loads converge to $P_{\mathrm{cr},\infty}$ given in Eq. 2.18. Moreover, Figs. 2.17a and b show that the first two buckling loads appear quite below the other critical loads and converge to the value $P_{\mathrm{cr},\infty}$ for increasing values of αL. In particular, for $L/h = 5$, first and second critical loads both converge to $P_{\mathrm{cr},\infty} = 12.7$ for αL greater than 21, whereas for the longer beam ($L/h = 15$), Figs. 2.17a and b show that convergence ($P_{\mathrm{cr},\infty} = 114.0$) is achieved for $\alpha L > 50$. For both slenderness cases, third and fourth critical loads have the same behaviour depicted for the beam with pinned ends and converge to $P_{\mathrm{cr},\infty}$ for αL approximately equal to 11 and 34, for $L/h = 5$ and 15, respectively.

$L/h = 5$

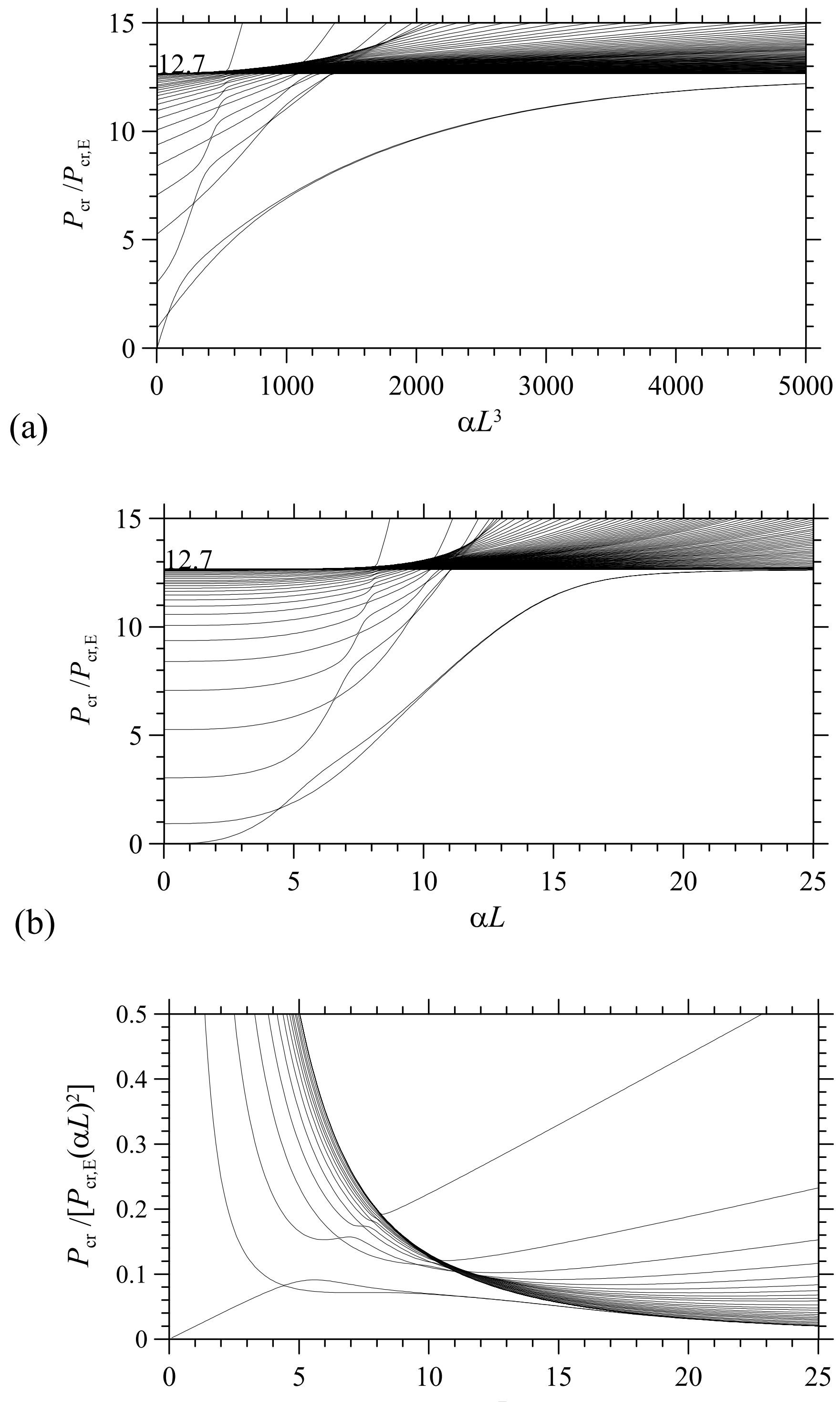

Fig. 2.16. – Dimensionless critical loads $P_{cr}/P_{cr,E}$ versus αL for a Timoshenko beam with free ends having $L/h = 5$.

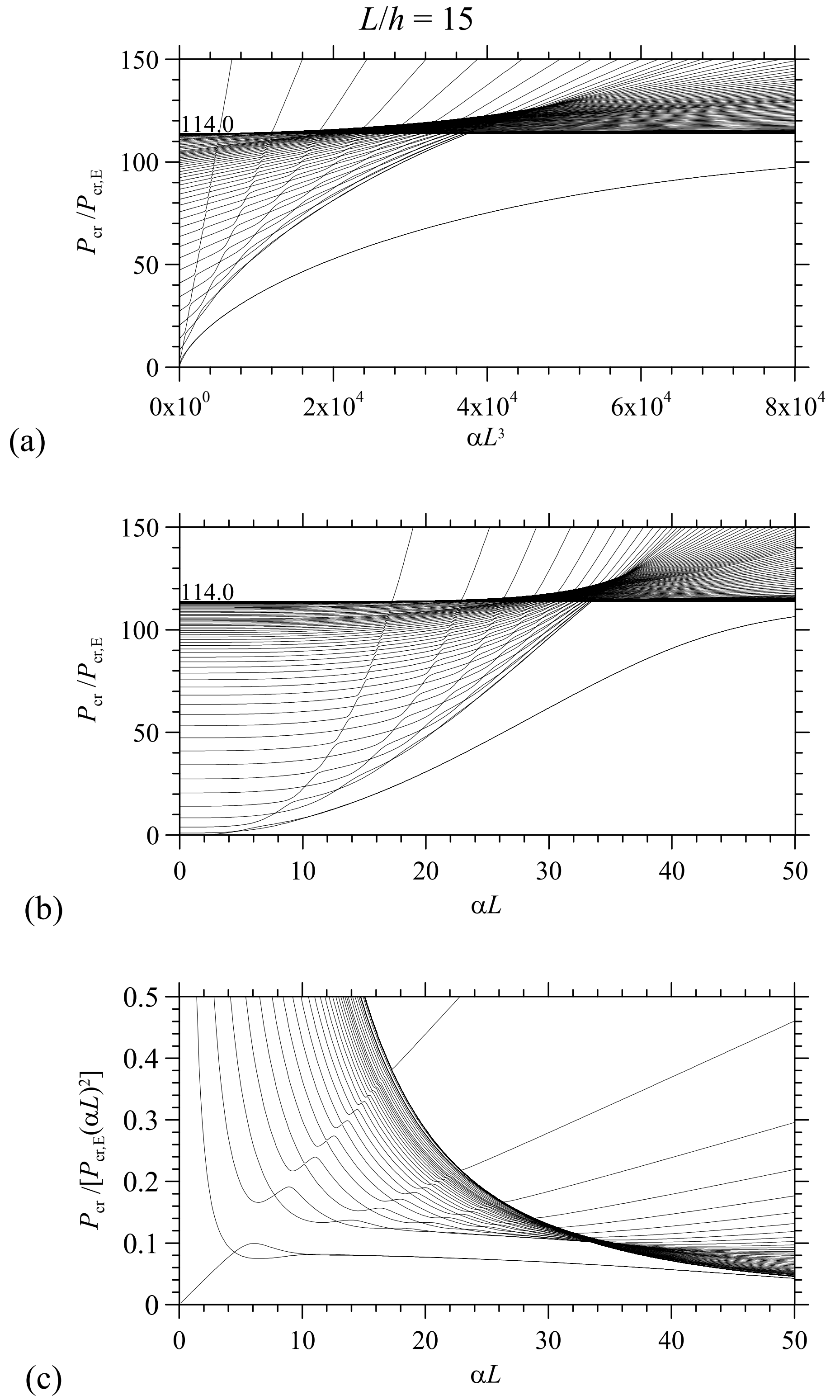

Fig. 2.17 - Dimensionless critical loads $P_{cr}/P_{cr,E}$ versus αL for a Timoshenko beam with free ends having L/h = 15.

2.5.2.1 Modal shapes

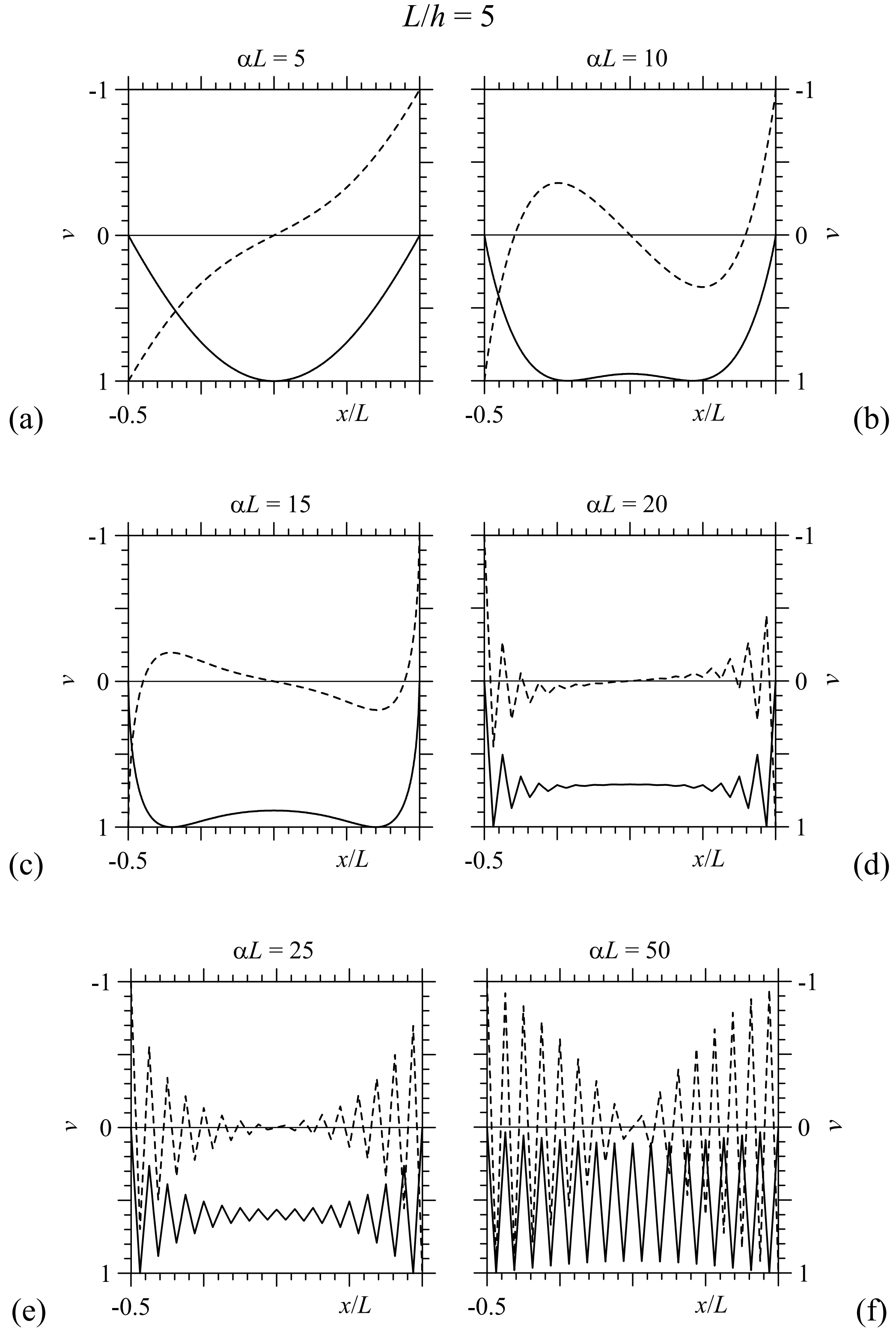

Fig. 2.18 – First (continuous line) and second (dashed line) buckling modes for a Timoshenko beam with free ends for increasing αL.

Considering the short beam case, for beams stiffer than the soil ($\alpha L = 5$), Fig. 2.18a shows buckling modes that are practically coincident with those of the Euler-Bernoulli beam case, i.e. with $\phi = 0$. Increasing αL (Figs. 2.18b and c), the first and second mode shapes are not characterized by a sinusoidal behaviour and great deformations tend to concentrate near beam ends. For beams on stiff soil ($\alpha L \geq 20$), Figs. 2.18d-f clearly show that buckling modes are characterized by very short wavelengths and the number of beam FEs is reduced as previously done for the case of the beam with pinned ends. However, differently than that case, the second mode shape starts to have short wavelengths together with the first mode shape and, in fact, the first and second critical loads converge to $P_{\mathrm{cr},\infty}$ for the same value of αL (Figs. 2.16a and b).

For the long beam case and increasing αL, the first and second mode shapes (Figs. 2.19a-e) are quite similar to the corresponding ones obtained for the Euler-Bernoulli beam. Very short wavelengths appear with very stiff soil (αL = 50, Fig. 2.19f), where n_{el} is reduced to 32.

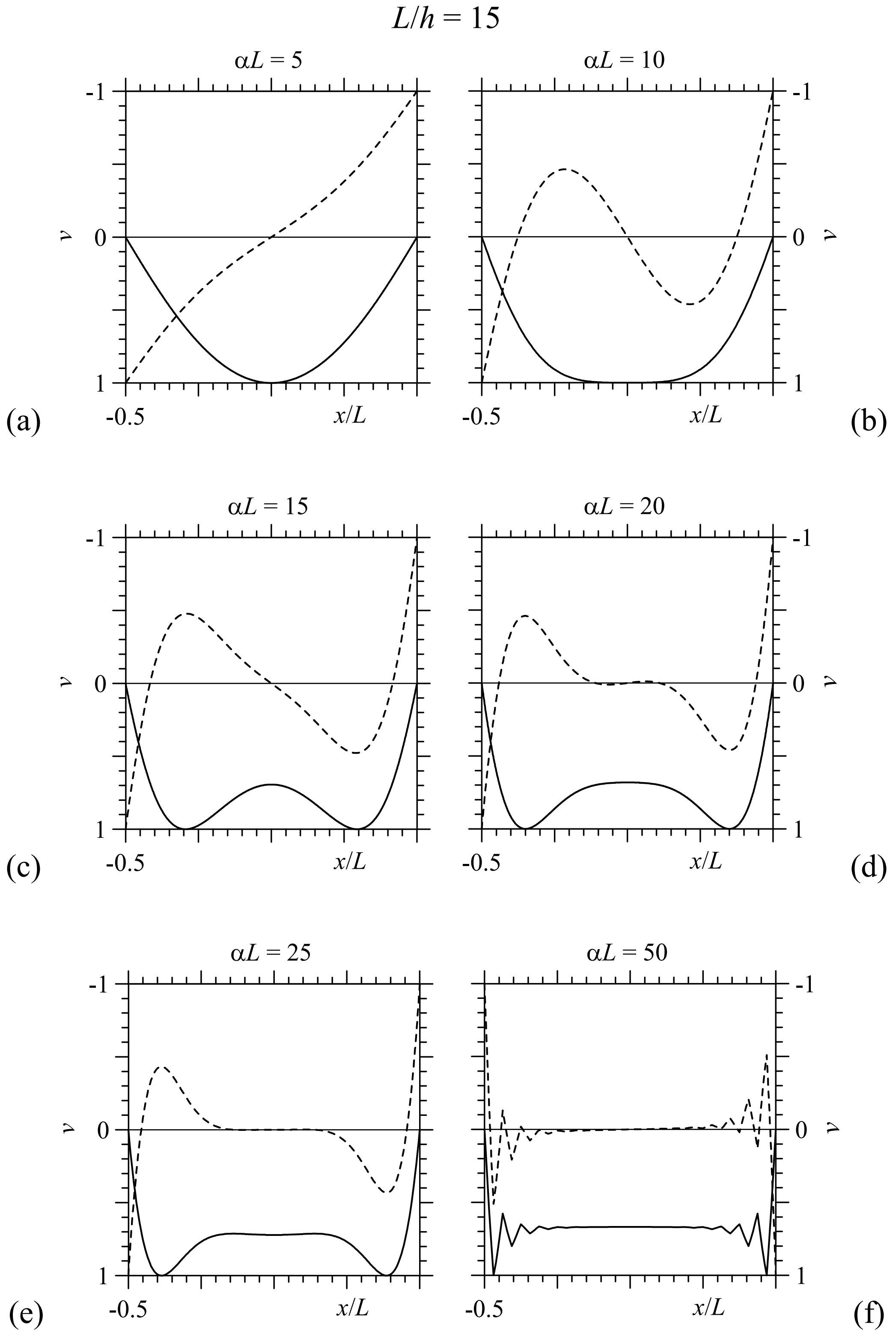

Fig. 2.19 – First (continuous line) and second (dashed line) buckling modes for a Timoshenko beam with free ends for increasing αL.

2.5.2.2 Two-dimensional FE model results

The first four critical loads $P^{2D}_{cr,m}$, with $m = 1, 2, 3, 4$, obtained with the two-dimensional finite element model are denoted by dot symbols and compared with presented results in Figs. 2.17a and b for $L/h = 5$ and 15, respectively. Fig. 2.20b shows that the first two critical loads $P^{2D}_{cr,1}$, $P^{2D}_{cr,2}$ are close to those obtained with the present model up to $\alpha L = 50$; whereas for the short beam (Fig. 2.20a), the two finite element models have close results up to $\alpha L = 10$. As for the third and fourth buckling loads, the values $P^{2D}_{cr,3}$, $P^{2D}_{cr,4}$ are lower than those of the model for the short beam case (Fig. 2.20a). For increasing values of αL, the critical loads $P^{2D}_{cr,m}$, with $m = 1, 2, 3, 4$, depicted in Figs. 2.20a and b, converge to the same limit values reported in Figs. 2.9a and b, respectively.

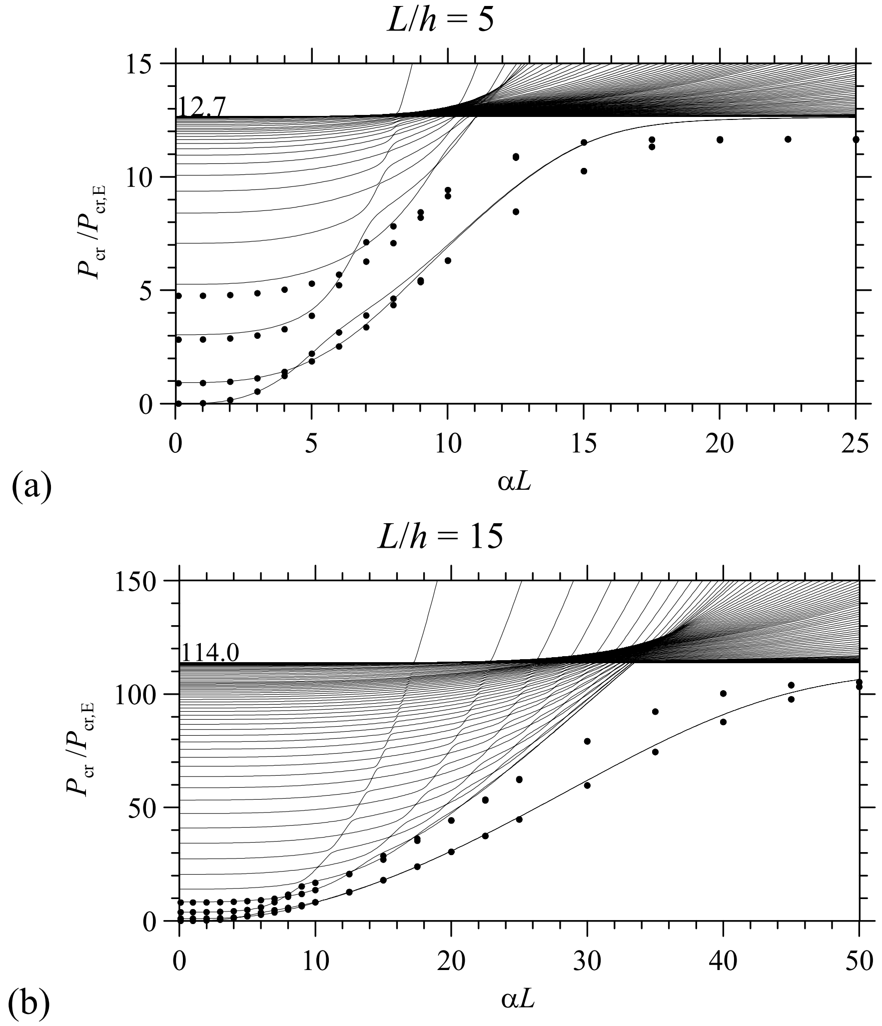

Fig. 2.20 – Dimensionless critical loads $P_{cr}/P_{cr,E}$ versus αL for a Timoshenko beam with free ends having $L/h = 5$ (a) and 15 (b). Continuous lines for the presented model, dots for the 2D model.

Figs. 2.21a-f and 22a-f show the first two buckling modes of the two-dimensional finite element model for different values of the parameter αL, for $L/h = 5$ and 15, respectively. For beams stiffer than the soil ($\alpha L = 5$), the first critical mode depicted in Figs. 2.21a and 22a are sinusoidal and the second ones (Figs. 2.21b and 2.22b) represent rigid rotations. Then, these buckling modes agree with those reported in Figs. 2.18a and b and Figs. 2.19a and b. For long beam on stiff soil ($\alpha L = 25$, $L/h = 15$), Figs. 2.22e and f show the first two buckling modes that present displacements localized at the free ends, symmetrical and antisymmetrical, respectively. These buckling modes agree with those reported in Fig. 2.19e. For short beam on stiff soil ($\alpha L = 25$, $L/h = 5$), Figs. 2.21e and f clearly show that buckling is localized in the upper part of the beam. It is evident that a beam model fails to represent this kind of surface buckling; hence, the corresponding buckling modes reported in Fig. 2.18e present an irregular behaviour depending on the mesh size. The same behaviour is obtained for long beams and $\alpha L > 50$. This justifies the differences between the buckling loads evaluated with the two-dimensional model and the beam model for large values of the parameter αL.

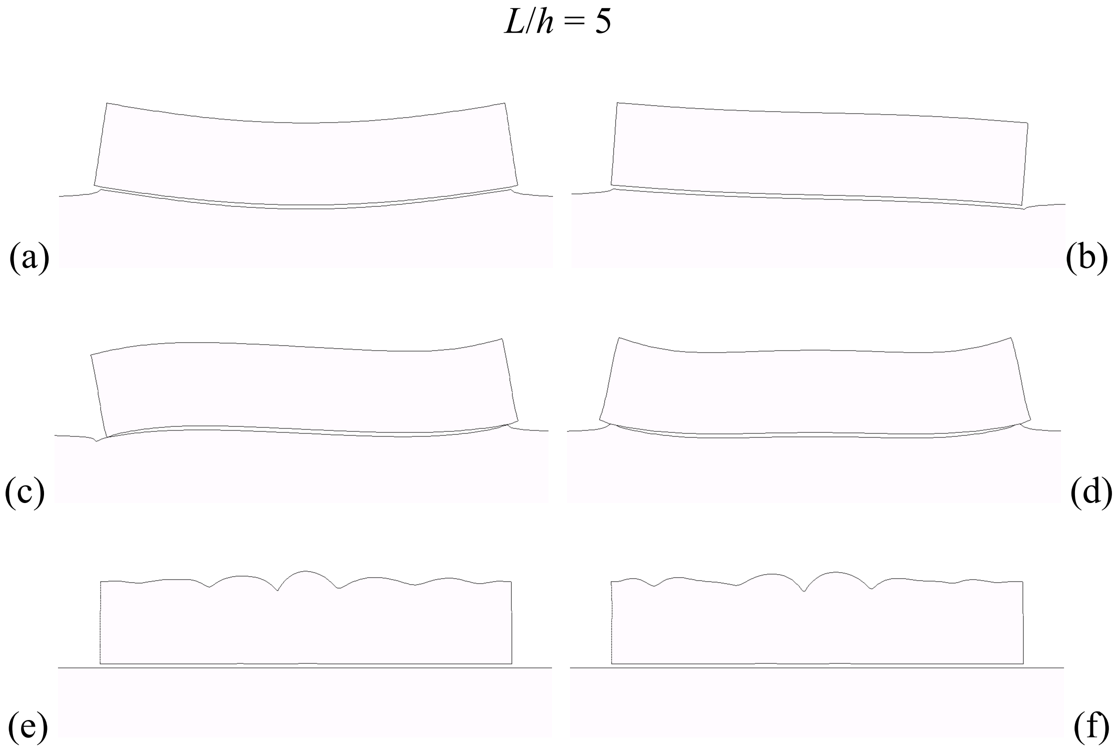

Fig. 2.21 – First (a, c, e) and second (b, d, f) buckling modes for a short two-dimensional foundation beam ($L/h = 5$) with free ends having $\alpha L = 5$ (a, b) , $\alpha L = 10$ (c, d) and $\alpha L = 25$ (e, f).

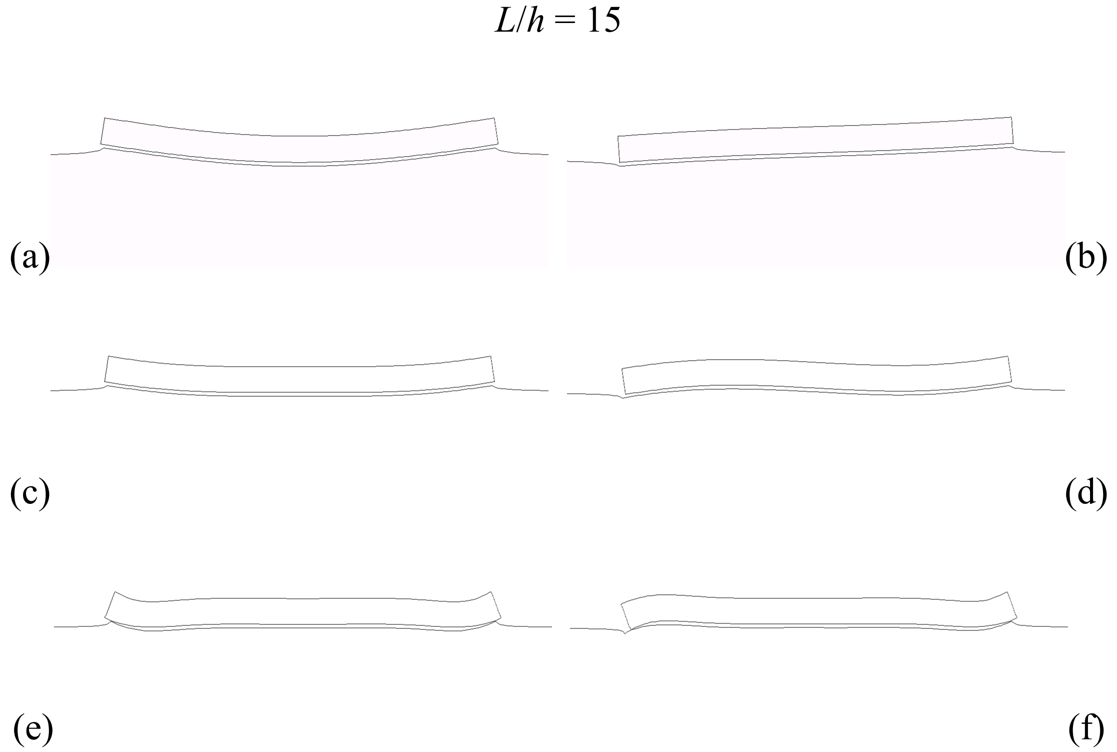

Fig. 2.22 – First (a, c, e) and second (b, d, f) buckling modes for a short two-dimensional foundation beam ($L/h = 5$) with free ends having $\alpha L = 5$ (a, b) , $\alpha L = 10$ (c, d) and $\alpha L = 25$ (e, f).

2.5.2.3 Buckling of a beam with free ends on Winkler half-space

In this section, critical loads of a beam with free ends on Winkler half-space are determined. Figs. 2.23a and b show dimensionless critical loads $P_{cr}/P_{cr,E}$ as a function of γ for L/h equal to 5 and 15, respectively. Similarly to the case of the beam on half-plane, first and second critical loads are smaller than other results and converge to $P_{cr,\infty}$ for γ greater than 500 and 1000 for L/h equal to 5 and 15, respectively.

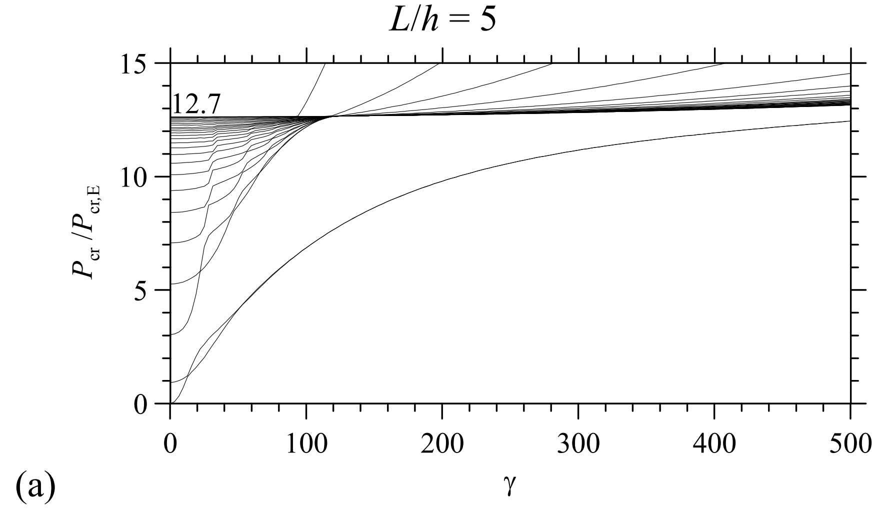

(a)

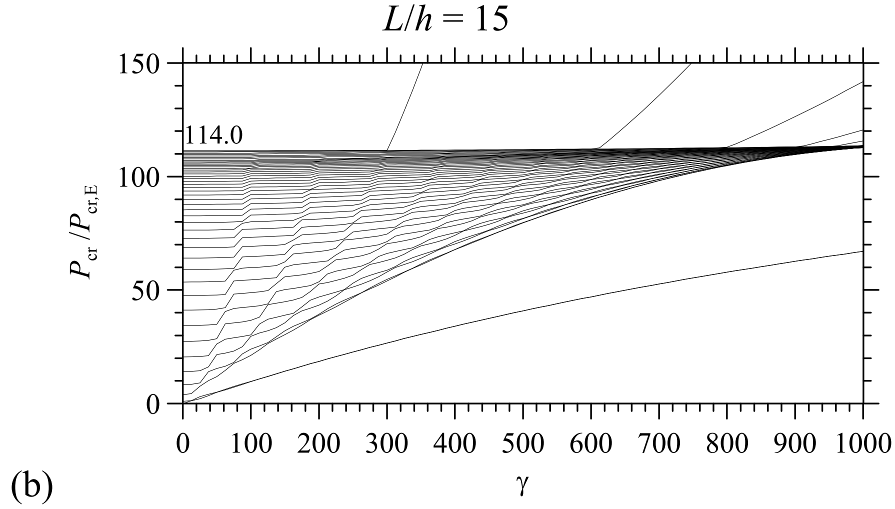

(b)

Fig. 2.23 – Dimensionless critical loads $P_{cr}/P_{cr,E}$ (continuous lines) and $P_{cr,W}/P_{cr,E}$ (circles) as function of γ for a beam with pinned ends on Winkler half space.

Figs. 2.32a-d show the first and second mode shapes for beams on soft and stiff half-space for both slenderness cases. For both slenderness cases and γ equal to 15, the first mode shape is sinusoidal (continuous lines, Figs. 2.32a and c), whereas the second mode shape is asymmetric (dashed lines in Figs. 2.32a and c). Then, mode shapes for beams on soft Winkler half-space turn out to be quite similar to the ones obtained for the case of the beam on half-plane (Figs. 2.18a and 19a). For γ equal to 400, the first and second mode shapes for the short beam case are characterized by very short wavelengths and 32 FEs are adopted to represent displacements (Fig. 2.32b). In this case, the first and second mode shapes are quite similar to the corresponding ones obtained for the beam on half-plane (Fig. 2.18d) and are characterized by large deformations close to beam ends, however few half waves are present with respect to the beam on half-plane. Considering the long beam case (Fig. 2.32d), the first and second mode shapes are characterized by large deflections at beam ends, similarly to the case of the beam on elastic half-plane (Fig. 2.19e).

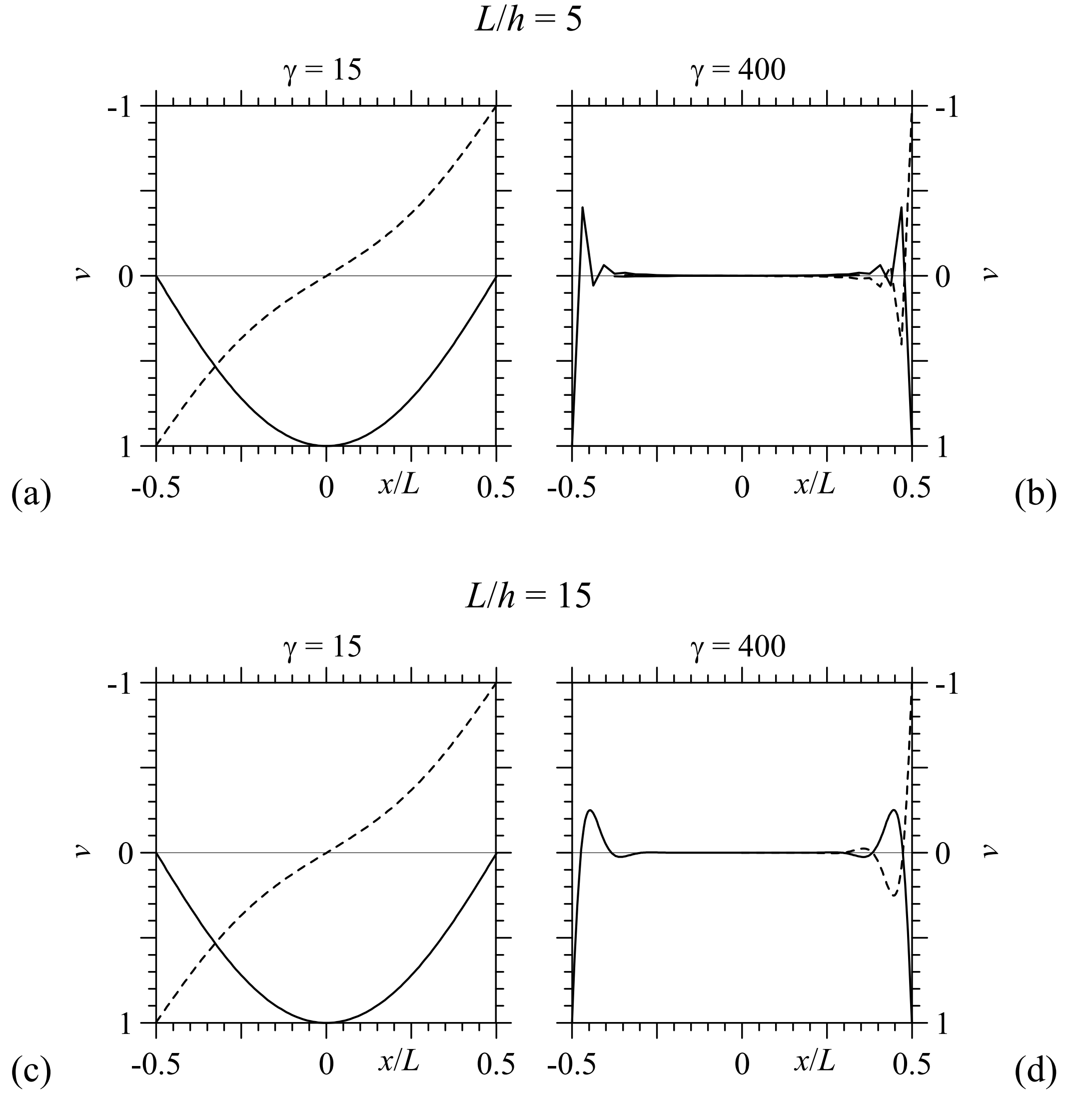

Fig. 2.24 – First (continuous line) and second (dashed line) buckling modes for a Timoshenko beam with free ends.

2.5.2.4 First critical load determined with different beam models

Finally, Fig. 2.25 shows the first critical load for a beam with free ends corresponding to the Euler-Bernoulli beam model ($\phi = 0$), the Timoshenko beam model ($\phi = 0.0107$ and 0.096) and the two-dimensional finite element models. The values determined by Timoshenko model and two-dimensional finite elements appear to be quite close, whereas the Euler-Bernoulli model gives suitable solutions for low values of αL, e.g. relative errors lower than 1% occur if $\alpha L < 0.5\, L/h$, whereas errors lower than 2% occur if $\alpha L < 0.7\, L/h$. To explain this behaviour, it is worth noting that the critical wavelength $\Lambda_{\mathrm{cr,R}}$ of the sinusoidal waveform assumed in Reissner (1937) for the Euler-Bernoulli beam of infinite length is equal to (Volynskii et al. 2000):

$$\Lambda_{\mathrm{cr,R}} = 2\pi\, h \sqrt[3]{\frac{E_0}{3E}} = \frac{2\pi \sqrt[3]{4}}{\alpha} = \frac{9.97}{\alpha} \,, \tag{2.23}$$

where direct proportionality between the wavelength $\Lambda_{\mathrm{cr,R}}$ and the thickness h of the beam is predicted. Usually, Euler-Bernoulli beam model holds for sufficiently high values of the critical half-wavelength, e.g. $\Lambda_{\mathrm{cr,R}}/2 > 10\, h$; thus, Eq. 2.23 yields $\alpha h < 1/2$, or equivalently $\alpha L < 0.5\, L/h$. For beam with $\alpha L > 0.5\, L/h$, the transverse shear deformation of the beam may become important and needs to be considered.

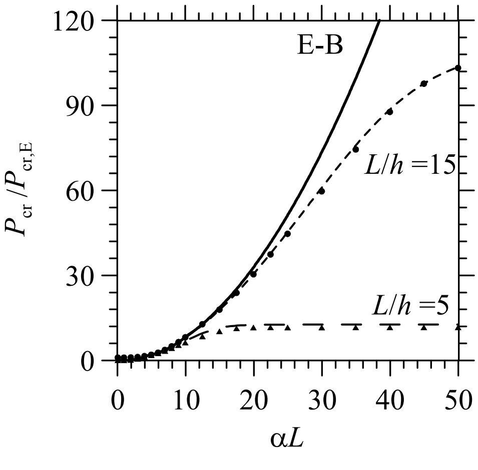

Fig. 2.25 – First dimensionless critical load versus αL for a beam with free ends and Euler-Bernoulli beam model (continuous line), Timoshenko beam models (dashed lines), two-dimensional finite element models (triangle and dot symbols for $L/h = 5$ and 15, respectively).

2.6 Coupling of 2D plane elements and boundary integral equations

In the previous paragraphs, the present model is compared to a traditional 2D FE model, where both beam and half-space are modelled by plane elements. The comparison of buckling analysis results obtained with the present model with the 2D model showed that the present model is not able to describe correctly the behaviour of a thick beam on a stiff half-space. For large values of αL, modal shapes obtained with the 2D model are characterized by displacements localised at beam surface and the corresponding critical loads are lower than the ones obtained with the present model, differences are evident for thick beams on stiff soil (i.e. for $L/h = 5$, Figs. 2.10e, f and Figs. 2.21e, f).

Therefore, the coupling of traditional plane elements with the boundary integral equation of the half-space in plane state can reduce the differences obtained by the one dimensional beam model with respect to the traditional 2D model. In the following, the basic relationships of a rectangular domain in plane state representing a thick layer are briefly described; then, traditional quadrilateral isoparametric elements in plane state are adopted and coupled with the boundary integral equation of the half-plane (Eq. 5).

2.6.1 Basic relationships

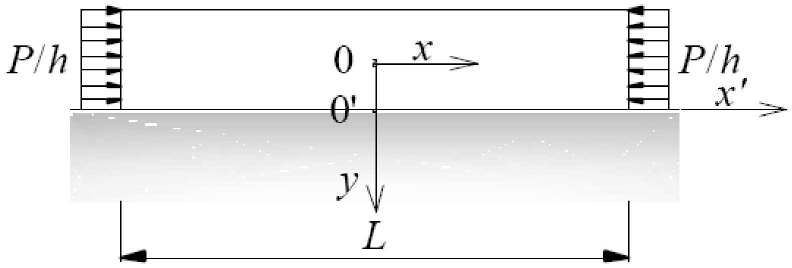

Fig. 2.26 – Layer in plane stress or plane strain state on elastic half plane subject to compressive pressure.

A layer in plane strain or plane stress state (Fig. 2.26), with length L, height h and width b, resting on a semi-infinite linearly elastic half plane is considered. A principal Cartesian coordinate system (0; x, y) is defined, where x coincides with the boundary of the half plane and y is chosen in the downward transverse direction. A secondary Cartesian coordinate system (0'; x', y) is chosen setting axis *x'* parallel to *x* and coincident with the centroidal axis of the layer, with domain defined as:

$$\Omega(x,y):\begin{cases}-L/2\le x\le L/2\\ -h/2\le y\le h/2\end{cases}\tag{2.24}$$

Elastic parameters of layer and half space have been defined in previous paragraphs; E_b and E_s indicate the Young moduli of layer and substrate, respectively; analogously, Poisson ratios of layer and substrate are denoted by ν_b and ν_s, respectively. Volume forces $m(x,y)$ such as the self-weight of the layer may be applied on the layer domain Ω, whereas surface loads $t\ (x,y)$ may be applied on layer boundary Γ. Moreover, the layer is loaded at the ends by horizontal compressive pressures p as shown in Fig. 2.26:

$$p(x,y):\begin{cases}+\sigma_p=P/(bh) & x=-L/2;-h/2\le y\le h/2\\ -\sigma_p=-P/(bh) & x=+L/2;-h/2\le y\le h/2\end{cases}\tag{2.25}$$

The interface between layer and soil is frictionless so that only a vertical soil reaction is acting along the contact surface: $r(x,0)=r(\bar{x})$

Considering the plane stress problem, layer displacements are represented by $q(x,y)=[u(x,y)\ v(x,y)]^T$ in $\Omega(x,y)$ (Timoshenko and Goodier 1951). Strains are obtained by derivation of displacements:

$$\varepsilon(x,y)=\begin{bmatrix}\varepsilon_x & \varepsilon_y & \gamma_{xy}\end{bmatrix}^T=\begin{bmatrix}\dfrac{\partial u}{\partial x} & \dfrac{\partial v}{\partial y} & \dfrac{\partial u}{\partial y}+\dfrac{\partial v}{\partial x}\end{bmatrix}^T\tag{2.26}$$

and the stress field associated with the strains is given by:

$$\sigma(x,y)=\begin{bmatrix}\sigma_x\\ \sigma_y\\ \tau_{xy}\end{bmatrix}=C\varepsilon=E_{ps}\begin{bmatrix}1 & \nu_b & 0\\ \nu_b & 1 & 0\\ 0 & 0 & G_b/E_{ps}\end{bmatrix}\begin{bmatrix}\varepsilon_x\\ \varepsilon_y\\ \gamma_{xy}\end{bmatrix}\tag{2.27}$$

where $G_b = E_b / [2\ (1 + \nu_b)]$, $E_{ps} = E_b\ (1 - \nu_b) / [(1 + \nu_b)\ (1 - 2\nu_b)]$ for a plane strain state and $E_{ps} = E_b / [2\ (1 - \nu_b)]$ for a plane stress state.
The strain energy of the layer can be written as:

$$U_b = \frac{1}{2} b \int_{\Omega} \sigma^T \varepsilon \, d\Omega = \frac{1}{2} b \int_{\Omega} \varepsilon^T C \varepsilon \, d\Omega \tag{2.28}$$

The potential energy of the layer is given by:

$$\Pi_b = U_b - b \int_{\Omega} u^T m \, d\Omega + h \int_{\Gamma} u^T t \, d\Gamma \tag{2.29}$$

The potential energy of the soil is given by Eq. 2.7, then the total potential energy of the 2D layer-substrate system is:

$$\Pi = U_b - b \int_{\Omega} u^T m \, d\Omega + b \int_{\Gamma} u^T t \, d\Gamma - \frac{1}{2} \int_L r(\bar{x}) \, \mathrm{d}x \int_L g(\bar{x}, \hat{x}) \, r(\hat{x}) \, \mathrm{d}y \tag{2.30}$$

2.6.2 Discrete model

A simple discretization of the layer can be created by subdividing the domain horizontally and vertically in $n_{el,x}$ and $n_{el,y}$ subdivisions, respectively, obtaining a mesh of $n_{el} = n_{el,x} \times n_{el,y}$ quadrilateral elements having length l_i and height h_i. For simplicity, a mesh of equal quadrilateral elements is considered (Fig. 2.27), in order to adopt isoparametric quadrilateral elements to represent layer behaviour.

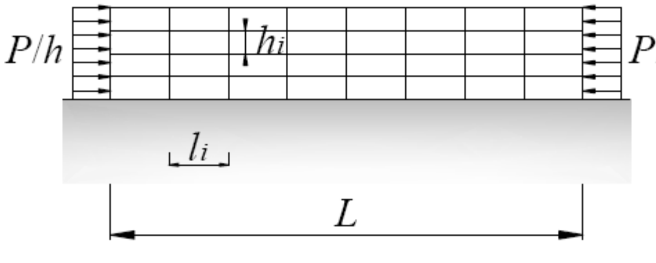

Fig. 2.27 – Layer subdivided into 4 × 8 = 32 equal quadrilateral elements.

Each quadrilateral element is defined by four nodes in natural coordinates, which are interpolated as

$$x = \sum_{i=1}^{4} N_i x_i; \quad y = \sum_{i=1}^{4} N_i y_i \tag{2.31}$$

where N_i are the Lagrange shape functions, which are also adopted for interpolating the displacement field in each element by the nodal displacements:

$$u^e = \sum_{i=1}^{4} N_i\, u_i; \quad v^e = \sum_{i=1}^{4} N_i\, v_i \, . \tag{2.32}$$

Then, the mesh is characterized by $n = (n_{el,x} + 1) \times (n_{el,y} + 1)$ nodes and considering horizontal and vertical displacements for each node, the finite element displacement vector **q** is defined by $2n$ degrees of freedom:

$$\mathbf{q} = [u_1 \quad v_1 \quad u_2 \quad v_2 \quad \dots \quad u_n \quad v_n]^T \tag{2.33}$$

In order to take into account the interaction with the half-plane, displacement vector can be partitioned as $\mathbf{q} = [\mathbf{q}_1; \mathbf{q}_2]^T$, where $\mathbf{q}_1$ collects the displacements of the nodes lying on the contact surface between the layer and the half-space, whereas $\mathbf{q}_2$ collects the remaining nodal displacements.

The displacement vector $\mathbf{q}^e$ for each element is defined by 8 degrees of freedom:

$$\mathbf{q}^e = [u_1 \quad v_1 \quad u_2 \quad v_2 \quad u_3 \quad v_3 \quad u_4 \quad v_4]^T \tag{2.34}$$

The soil surface underlying the layer is be subdivided in portions having length equal to the width of quadrilateral beam elements and one constant soil reaction is assumed. Accordingly, soil reaction for the *i*th element can be approximated as $r(\xi)= [\rho(\xi)]^T \mathbf{r}_i$, where $\mathbf{r}_i$ denotes the vector components of nodal half-plane reaction and ρ assembles constant shape functions..

Substituting Eq. 2.33 and the approximation of reactions in variational principal (Eq. 2.30) and assembling over all the elements, the total potential energy assumes the following expression:

$$\Pi(\mathbf{q},\mathbf{r}) = \frac{1}{2}\mathbf{q}^{\mathrm{T}}\mathbf{K}_b^{\mathrm{2D}}\,\mathbf{q} - b\,\mathbf{q}^{\mathrm{T}}\mathbf{F}^{\mathrm{2D}} + b\,\mathbf{q}_1^{\mathrm{T}}\mathbf{H}\,\mathbf{r} - \frac{b}{2}\mathbf{r}^{\mathrm{T}}\mathbf{G}\,\mathbf{r}\,, \tag{2.35}$$

where $\mathbf{K}_b^{\mathrm{2D}}$ is the stiffness matrix of the layer, $\mathbf{F}^{\mathrm{2D}}$ is the vector of nodal forces (see appendix A3). Matrices **H** and **G** do not vary with respect to Euler Bernoulli or Timoshenko beam cases.

The stationarity conditions of the total potential energy written in discrete form are provided by the following system:

$$\begin{bmatrix} \mathbf{K}_{b,11}^{2\mathrm{D}} & (\mathbf{K}_{b,12}^{2\mathrm{D}})^T & b\mathbf{H} \\ \mathbf{K}_{b,12}^{2\mathrm{D}} & \mathbf{K}_{b,22}^{2\mathrm{D}} & \mathbf{0} \\ b\mathbf{H}^T & \mathbf{0} & -\frac{b}{E}\mathbf{G} \end{bmatrix} \begin{Bmatrix} \mathbf{q}_1 \\ \mathbf{q}_2 \\ \mathbf{r} \end{Bmatrix} = \begin{Bmatrix} b\mathbf{F}_1^{2\mathrm{D}} \\ b\mathbf{F}_2^{2\mathrm{D}} \\ \mathbf{0} \end{Bmatrix} \tag{2.36}$$

which can be easily solved following the procedures adopted for beams and frames on elastic half plane.

2.6.3 Static analysis of a layer resting on an elastic half-plane

The simple case of a beam with free ends on elastic half-plane loaded by a uniform pressure over the side of the two element close to midpoint (Fig. 2.28) is considered. With reference to the discrete model, the resultant force P is subdivided along the nodes close to midpoint. The displacements of the 2D mesh adopted for the layer are determined increasing the number of subdivisions along x axis $n_{el,x}$ and adopting $n_{el,y} = n_{el,x}/4$. In order to avoid local deformations along height at beam ends, vertical master slave-links are introduced by applying constraint equations $R_{i,i+1} = v_i - v_{i+1} = 0$ by means of a penalty function at the nodes of each layer section end.

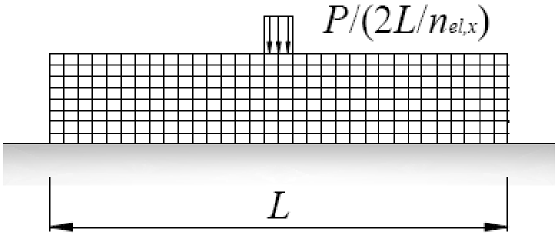

Fig. 2.28 – Beam on elastic half-space loaded by a concentrated force P at midpoint.

Figs. 2.29a,b show the deformed meshes of the layer for $n_{el,x} = 64$, $L/h = 5$, and for $\alpha L = 5$ and 25 respectively. For the soft soil case (Fig. 2.29a), the 2D mesh is characterized by almost uniform vertical displacements along the height, whereas for the stiff soil case (Fig. 2.29b), displacements are very small close to the contact surface and are large at the upper edge of the mesh. For $L/h = 15$

(Figs. 2.30a,b), the displacements of the 2D mesh are characterized by almost uniform vertical displacements along the height.

$L/h = 5$, $\alpha L = 5$

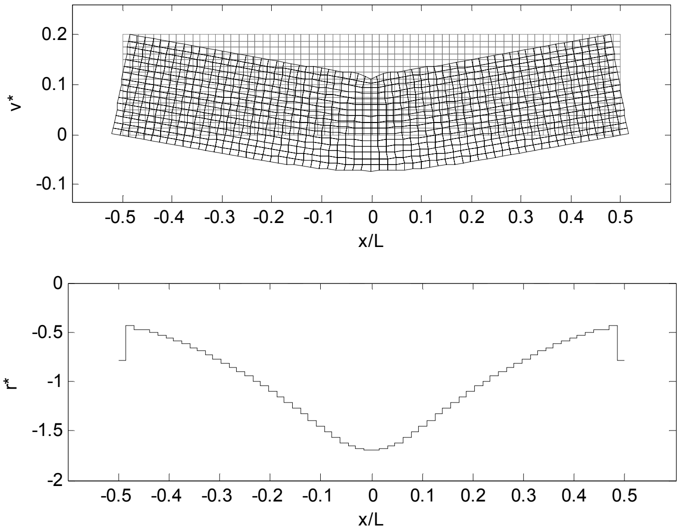

(a)

$L/h = 5$, $\alpha L = 25$

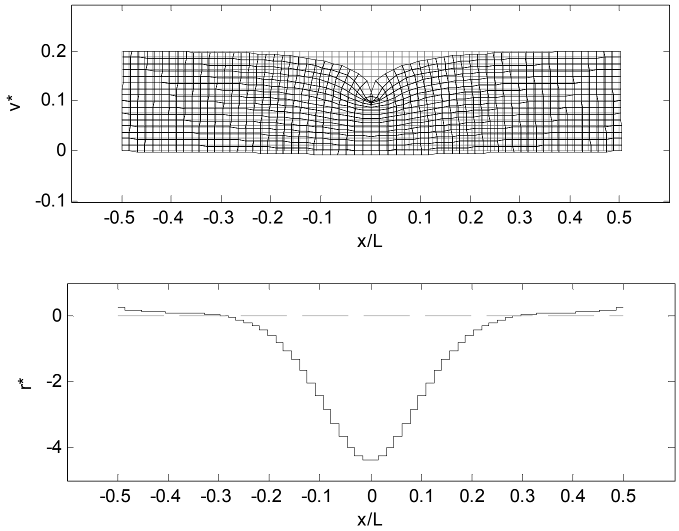

(b)

Fig. 2.29 – Displacements of the 2D mesh and half-plane pressures for a beam loaded by a concentrated force at midpoint.

$L/h = 15$, $\alpha L = 5$

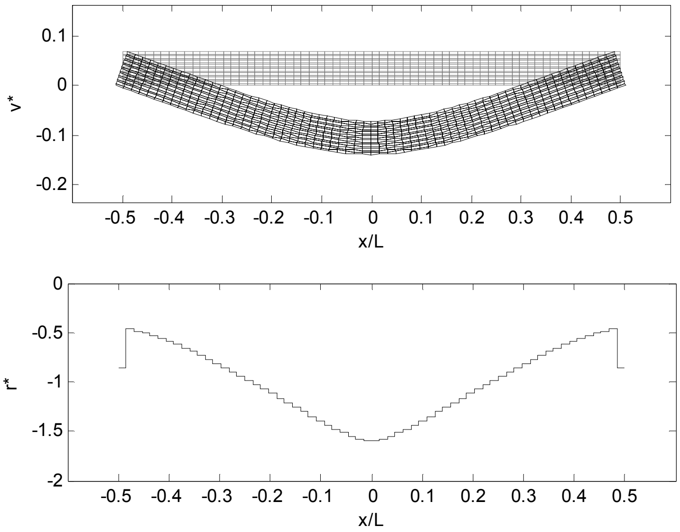

(a)

$L/h = 15$, $\alpha L = 25$

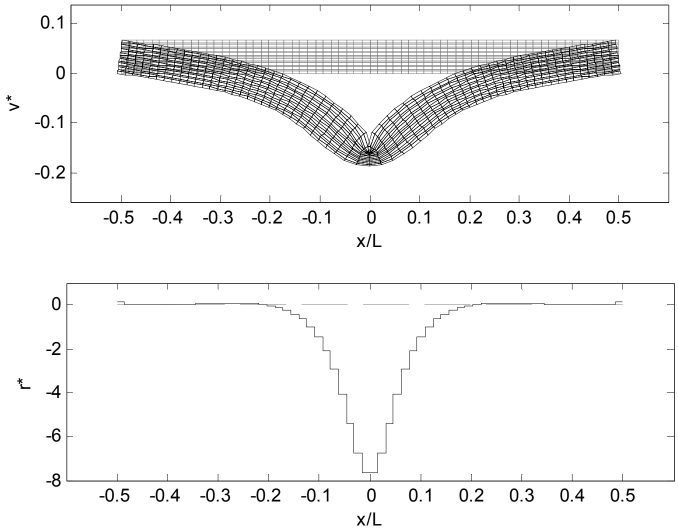

(b)

Fig. 2.30 – Displacements of the 2D mesh and half-plane pressures for a beam loaded by a concentrated force at midpoint.

Assuming as reference case the Timoshenko beam model, Figs. 2.31a,b show relative errors for vertical displacement $v(0,0)$ evaluated at the centre of the 2D mesh for increasing $n_{el,x}$ and L/h equal to 5 and 15, respectively, for different values of αL. For the short beam case, the 2D model is close to Timoshenko beam model only for the soft soil case, see plot for $\alpha L = 5$; in particular, the error $\delta v(0)$ is close to 1% for $n_{el,x} = 128$. For the long beam case, the 2D model is quite close to Timoshenko beam model for soft soil case and quite stiff soil case, see plot for $\alpha L = 5$, 10 and 15, characterized by errors $\delta v(0)$ less than 1% for $n_{el,x} = 128$, whereas for $\alpha L = 25$ error $\delta v(0)$ is close to 7%.

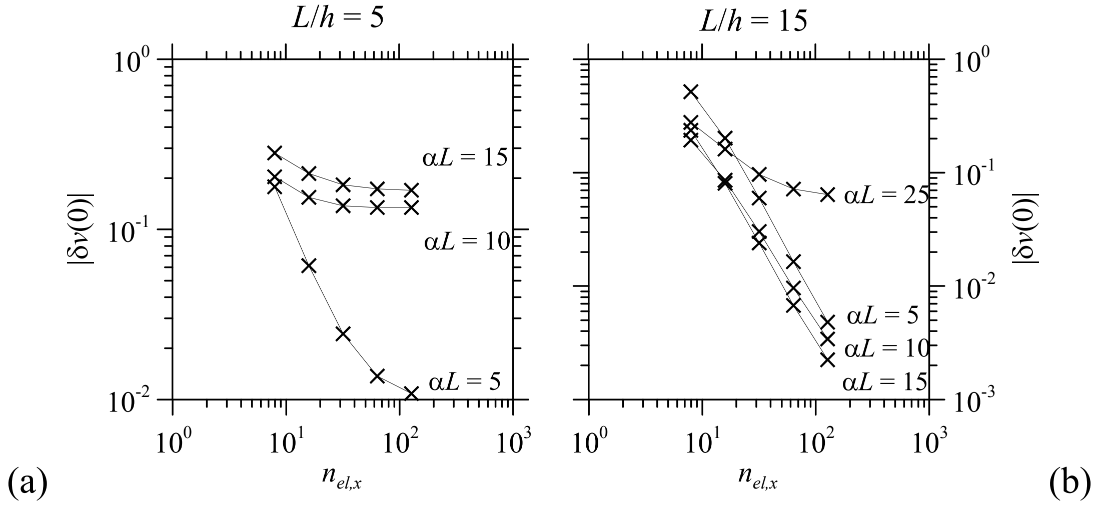

Fig. 2.31 – Relative errors for the vertical displacement at the centre of the 2D mesh with respect to the displacement at beam midpoint for the Timoshenko beam.

2.6.4 Buckling analysis of 2D beams with free ends on half-plane

In this section, a compressed layer with free ends modelled by a 2D mesh on elastic half plane is considered. Critical loads and mode shapes are determined increasing αL for L/h equal to 5 and 15. Results are compared with the corresponding ones obtained with the Timoshenko beam model and the classical 2D FE model described in section 2.4, where second order effect in the half-plane are taken into account.

For the short layer case ($L/h = 5$), first and second critical loads of the present 2D model (with 64×16 elements) are smaller than the corresponding values of the 2D FE model but they converge to a constant value $P_{\text{cr}} = 11.8\ P_{\text{cr,E}}$ which is quite close to $P_{\text{cr},\infty}$. Convergence is achieved for larger values of αL (close to 50) with respect to the Timoshenko beam case and the 2D FE model. For the long beam case ($L/h = 15$), first and second critical loads of the present 2D model are smaller than the corresponding values for the 2D FE model but they converge to a constant value $P_{\text{cr}} = 112.7\ P_{\text{cr,E}}$ which is quite close to $P_{\text{cr},\infty}$. Convergence is achieved for larger values of αL (close to 100) with respect to the Timoshenko beam case and the 2D FE model.

It must be reminded that the traditional 2D model takes into account the geometric matrix of the 2D FEs of both layer and half-plane mesh, whereas the present 2D model considers the geometric matrix only for the mesh of the layer. Then, for both layer cases on soft half-plane ($\alpha L < 10$), the stresses on the 2D half plane are small and the effect of the geometric matrix of the half-plane mesh in the traditional model is almost negligible, then, critical loads obtained with the present 2D model are very close to the corresponding values obtained with the traditional FEs. Increasing half-plane stiffness, the effect of the geometric matrix of the half plane mesh becomes important and the corresponding critical loads are smaller than the ones obtained with the present 2D model.

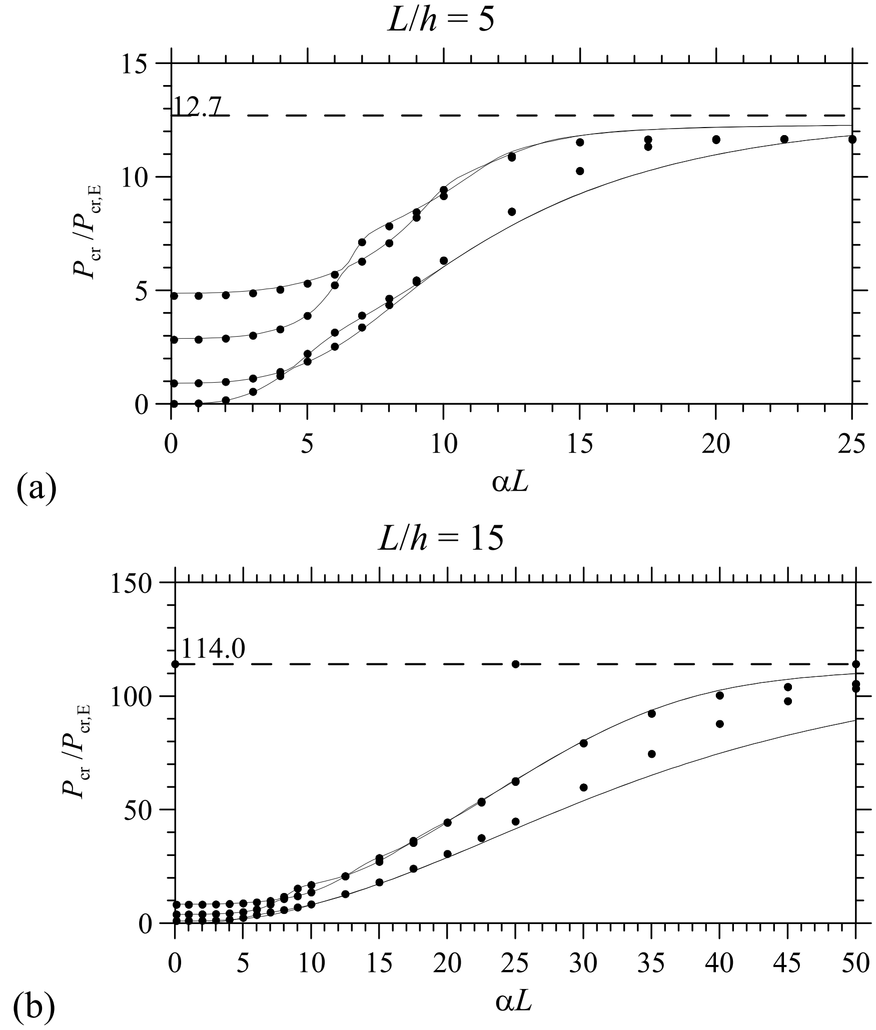

Fig. 2.32 – First four critical loads for a 2D layer on elastic half-plane (continuous lines) and for a 2D layer on traditional 2D half-plane (dots), with $L/h = 5$ (a) and 15 (b).

Considering the short layer case, for $\alpha L = 5$ (Figs. 2.33a,b), first mode shape is sinusoidal and second mode shape represents a rigid body rotation, whereas for $\alpha L = 25$ (Figs. 2.33c,d), first and second mode shapes are characterized by large deflections close to layer ends. Deformations located at the upper part of the layer are obtained with αL equal to 50 (Figs. 2.33e,f).

$L/h = 5$, $\alpha L = 5$

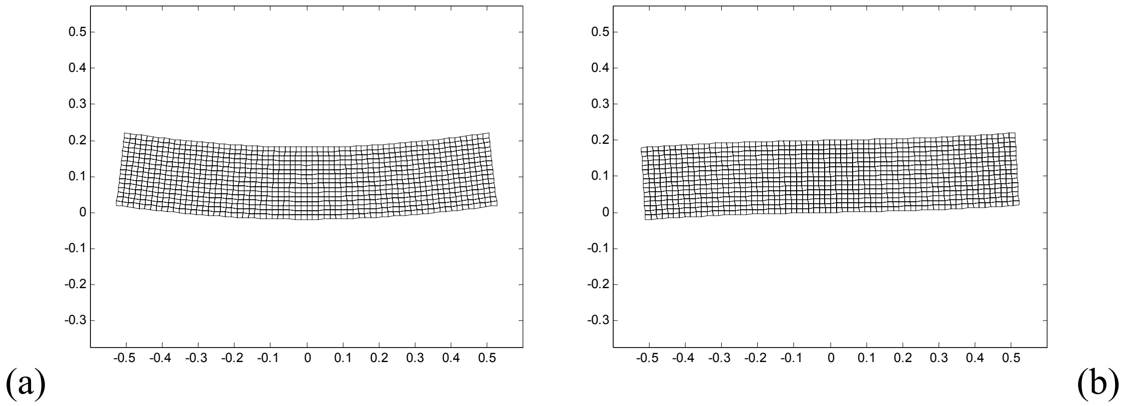

$L/h = 5$, $\alpha L = 25$

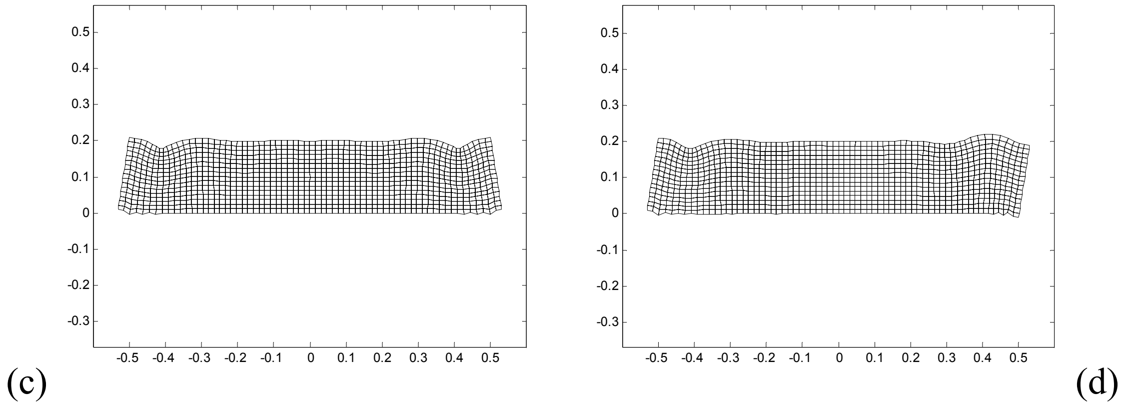

$L/h = 5$, $\alpha L = 50$

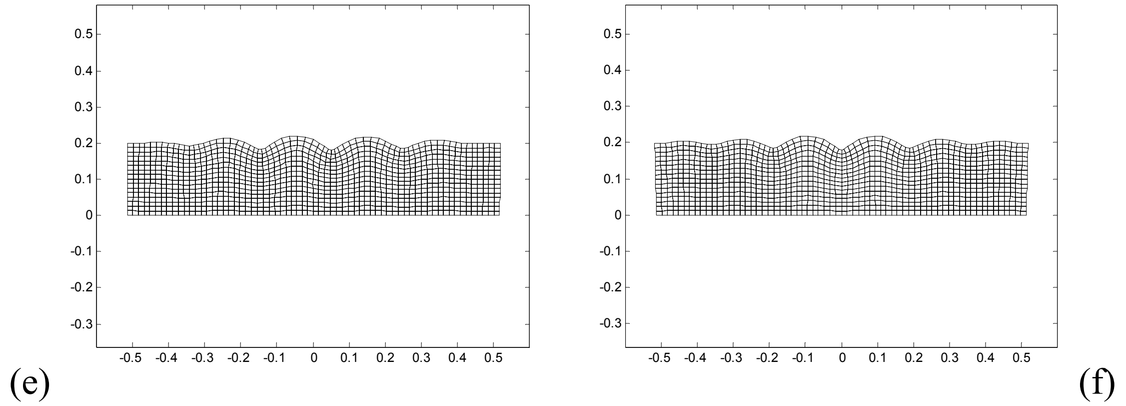

Fig. 2.33 – First (a-c-e) and second (b-d-f) mode shapes for a layer modelled by a 2D mesh on elastic half-plane with $L/h = 5$ and increasing αL.

Then, for the long layer case and α*L* = 5 (Figs. 2.34a,b), first mode shape is sinusoidal and second mode shape represents a rigid body rotation, whereas for α*L* = 25 (Figs. 2.34c,d), first and second mode shapes are characterized by large deflections close to layer ends. Deformations located at the upper part of the layer are obtained with α*L* equal to 50 and considering third and fourth mode shapes (Figs. 2.35a,b).

L/*h* = 15, α*L* = 5

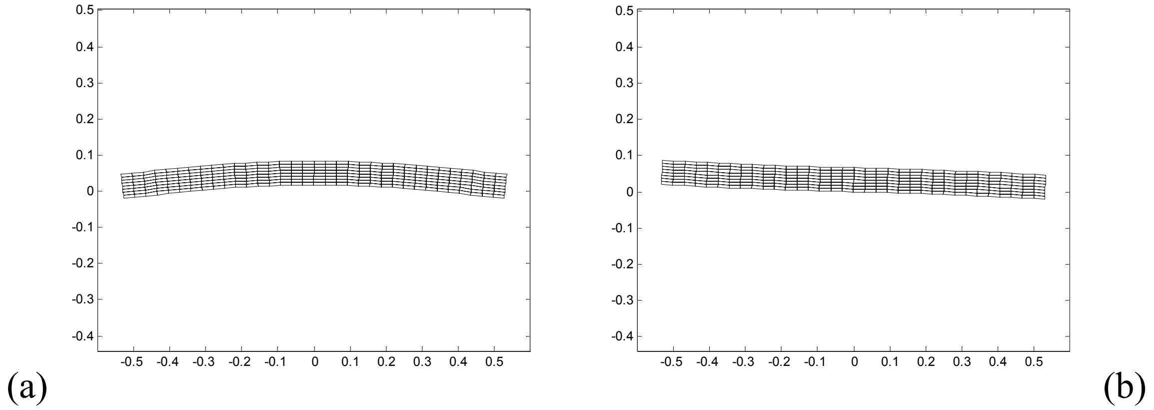

L/*h* = 15, α*L* = 25

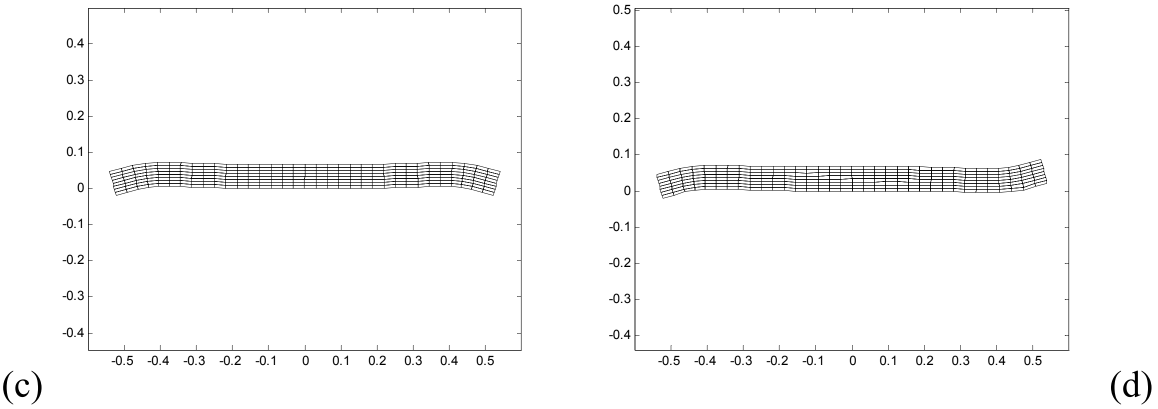

Fig. 2.34 – First (a-c) and second (b-d) mode shapes for a layer modelled by a 2D mesh on elastic half-plane with *L*/*h* = 15 and increasing α*L*.

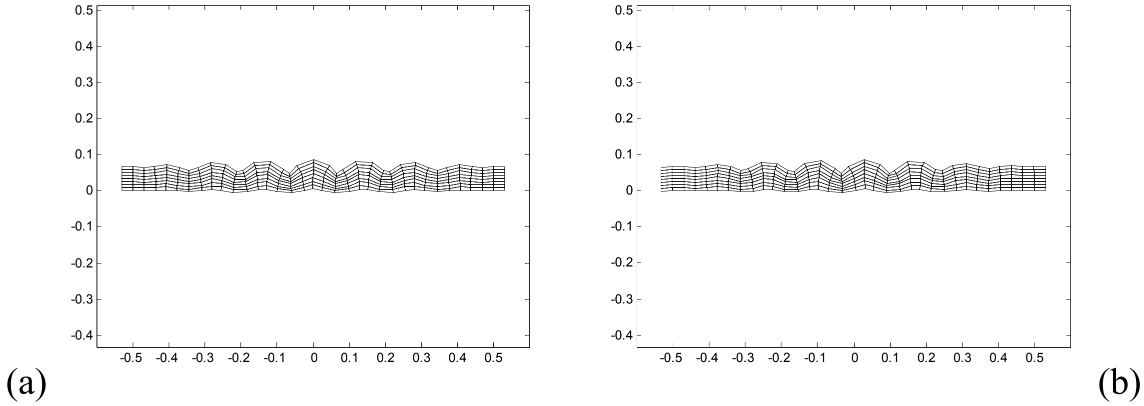

$L/h = 15$, $\alpha L = 50$

Fig. 2.35 – Third (a) and fourth (b) mode shapes for a layer modelled by a 2D mesh on elastic half-plane with $L/h = 15$, $\alpha L = 50$.

Then, the present model of a layer modelled by 2D FEs on elastic half plane turn out to be quite effective. However, the layer appears to be stiffer than the one modelled with the classical FE model due to the geometric stiffness matrix of the half plane.

Then, buckling modes with short wavelengths and deflections located in the upper part of the beam are obtained with large values of αL.

The present 2D model may be more useful for representing a 2D layer over an elastic half-plane, loaded by a plane frame modelled by one dimensional FEs, with the possibility to apply nonlinear properties to the material of the layer and to study the nonlinear behaviour of upper part of the support.

3 Analysis of slender beams and frames resting on elastic half-plane including material nonlinearity

3.1 Introduction

In computer-based nonlinear analysis of building frameworks, the inelastic behaviour of frames under vertical and seismic loads is often concentred at the ends of beams and columns. An early approach to model the inelastic behaviour of beam-column elements consists in the use of zero length plastic located at the member ends. Plastic hinges were taken into account into a beam-column element for the first time by Clough and Johnston (1967). The authors defined a 'parallel' component element characterized by elastic-perfectly plastic and elastic sub-elements. The stiffness matrix of the member was defined by the sum of the stiffnesses of the components. Giberson (1967) defined the first 'series model', which consisted of a linear elastic element with one equivalent nonlinear rotational spring attached to each end. Then, the inelastic deformations of the member were lumped into the end springs and it was possible to select the appropriate moment-rotation relation for the end springs. Several lumped plasticity constitutive models have been proposed in the following years (Takeda et al. 1970; Otani 1974; Lai et al. 1984). The series model increase the number of elements and degrees of freedom needed for the discretization of a frame structure. Moreover, in usual push-over analyses, plastic hinges need to be added to the initial model whenever a section experiences inelastic deformations.

Hasan et al. (2002) proposed a simple and efficient model for the push-over analysis of frames. The model was adapted from a procedure originally conceived for the elastic analysis of frame structures having linear elastic semi-rigid moment connections (Monforton and Wu 1963). Moreover, second order effects due to axial loads were taken into account by Xu (1992). A potential plastic hinge section of a frame member was treated as a semi-rigid connection with predefined load-deformation characteristics; then, the stiffness matrix of the member was modified without adding further finite elements and degrees of freedom to the discrete model of the structure. Shakourzadeh et al. (1999) defined a procedure for taking into account the semi-rigid behaviour of connections of thin-walled space frames, which may be adapted to represent potential plastic sections, taking into account membrane, shear, bending, torsion and warping effects. Then, a plastic hinge section can be introduced into the initial discrete model of a frame structure by simply modifying the matrices of the corresponding element.

Plastic analysis of beams and plates on elastic support were performed in the past for determining collapse loads of floating beams and concrete pavements adopting the Winkler model to represent the half-space behaviour (Meyerhoff 1962, Augusti 1970, Bhat 1986, Rao and Singh 1986). Collapse mechanisms were characterized by three plastic hinges for the case of a beam loaded by a concentrated force at midpoint. Recently, the same problem has been studied by Belenkiy (2007).

In the following, plastic analysis of beams on elastic half-plane are performed. For this purpose, two similar and efficient models able to study beams with semi-rigid connections are presented and extended to the present model of an Euler-Bernoulli beam on elastic half-plane. This procedure is also extended to the analysis of pipes on elastic half-plane, in order to perform incremental analyses and evaluate the stiffness degradation of the structure. Several examples of beams loaded by concentrated forces and pipes subject to distributed loads are dealt with. For simplicity, a rigid-perfectly plastic curve is adopted to describe the moment-rotation relation for the plastic hinges.

3.2 Semi-rigid analysis for a beam-column element

Analysis and design of frames in practice is generally based on simplified assumptions related to beam-column connection behaviour. The ‘fully rigid’ model and the ‘ideally pinned’ model represent two idealized models adopted frequently for describing the behaviour of beam-column connections. This aspect is typically considered in the design of steel frames, where beam-to-column connections need particular attention. However, semi-rigid properties of reinforced concrete beam-column joints may also be considered (Filippou et al. 1983; Amanat and Enam 1999, Basaga et al. 2012).

The fully rigid model is characterized by rotation continuity between the column and the beam, together with the full transfer of bending moments. On the other hand, the ideally pinned model is not characterized by rotation continuity between beam and column and, consequently, no bending moment is transmitted to the column by the beam. These idealized models allow designers to work with simplified structural analyses; however, they may not represent the actual behaviour of the connections. Many experimental investigations demonstrated that rigid connections may be characterized by a small rotational flexibility, whereas pinned connections may have a small rotational stiffness. Then, beam-column connections commonly used in steel buildings exhibit a semi-rigid behaviour characterized by a moment-rotation relationship depending on connection type. For example a single-web angle connection has behaviour quite close to an idealized pinned connection, whereas a connection with a welded flange plate with web-angle has behaviour quite close to a fully rigid connection (Chen and Lui 2005).

3.2.1 Monforton-Wu-Xu model for a beam with semi-rigid ends

In many studies concerning semi-rigid frame analysis (Monforton and Wu 1963), the moment-rotation relation at each end of a planar beam-column element may be modelled as a linear spring, introducing the non-dimensional ‘rigidity factor’ r_i or ‘fixity factor’ (Chen and Lui 2005):

$$r_i = \frac{\varphi_i}{\theta_i} = \frac{1}{1 + (3D_b / R_i\, L)}, \tag{3.1}$$

where R_i is the rotational stiffness of the generic *i*th connection, D_b and L are beam stiffness and length, respectively.

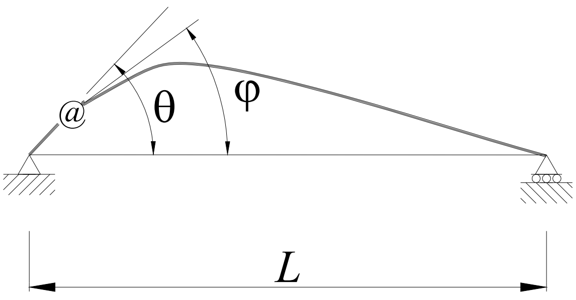

Fig. 3.1 – Semi-rigid moment-connection.

The rigidity factor defines the rotational stiffness of a generic connection relative to the stiffness of the attached member. Considering Fig. 3.1, the r_i represents the ratio between the beam end-rotation φ_i and the total rotation θ_i of the beam and the connection. The rigidity factor is defined in the range between 1 and 0 as the connection stiffness varies between $R = \infty$ and $R = 0$, respectively. The case $R = \infty$ corresponds to a perfectly rigid connection, whereas $R = 0$ represents a perfectly 'pinned' connection.

Considering an Euler-Bernoulli beam with semi-rigid moment connections at each end, the corresponding elastic stiffness matrix $\overline{\mathbf{K}}_b^e$ is given by the product of the standard stiffness matrix $\mathbf{K}_b^e$ and a correction matrix $\mathbf{C}_b$ which depends on the rigidity factors r_i of the two end connections (Monforton and Wu 1963):

$$\overline{\mathbf{K}}_b^e = \mathbf{K}_b^e \, \mathbf{C}_b \tag{3.2}$$

External loads such as distributed loads are modified similarly to the stiffness matrix ($\overline{\mathbf{F}}_e = \mathbf{F}_e \, \mathbf{C}_b$). Moreover, Xu (1992) applied the rigidity-factor concept to second-order analysis of semi-rigid frames. In this case, the standard geometric stiffness matrix $\mathbf{K}_g^e$ is modified by a correction matrix $\mathbf{C}_g$ depending on the rigidity factors r_i of the two end connections:

$$\overline{\mathbf{K}}_g^e = \mathbf{K}_g^e \, \mathbf{C}_g \, . \tag{3.3}$$

Correction matrices $\mathbf{C}_b$ and $\mathbf{C}_g$ are reported in appendix A4.

Considering a generic frame structure modelled by traditional Euler-Bernoulli beam elements, semi-rigid connections are located at the intersections between beams and columns and along beam elements. Each connection is characterized by a nonlinear moment-rotation relation, which describes the variation of the rotational stiffness R_i under increasing moment. Then, stiffness matrices corresponding to beam elements having one or two semi-rigid ends are modified by Eqs. 3.2 and 3.3. The behaviour of the frame under increasing loads or displacements can be finally determined by upgrading the rotational stiffness of each connection and the stiffness matrices at each increment of the analysis.

3.2.2 Shakourzadeh model for a beam with semi-rigid ends

Shakourzadeh, Guo and Batoz (1999) proposed an efficient model able to introduce the effect of semi-rigid connections in linear and nonlinear analysis of three-dimensional frames. The model was applied to beam FEs having seven degrees of freedom per node and it was characterized by a rigidity parameter for each degree of freedom, in order to represent the rigidity of the end connection for membrane, shear, bending, torsion and warping effects.

In the following, the model proposed by Shakourzedeh is applied to a beam FE having three degrees of freedom at each node and only flexural rigidity parameters of the end connections are considered. Then, only beam end rotations need to be modified in order to take into account of the semi-rigid ends (Fig. 3.2b).

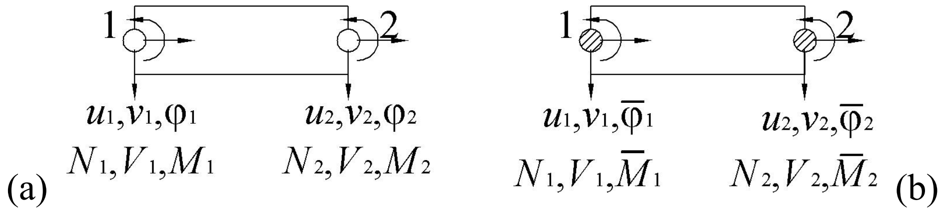

Fig. 3.2 – Beam finite element having three degrees of freedom per end (a). Equivalent beam finite element including semi-rigid moment connections (b).

The equilibrium of a generic beam element (Fig. 3.2a) can be represented by:

$$\mathbf{n}_e = \mathbf{K}_b^e \, \mathbf{q}_e - \mathbf{F}_e , \qquad (3.4)$$

where $\mathbf{q}_e = \{u_1, v_1, \varphi_1, u_2, v_2, \varphi_2\}$ is the vector of nodal displacements of generic element, $\mathbf{n}_e = \{N_1, V_1, M_1, N_2, V_2, M_2\}$ is the vector of nodal forces applied on the element, $\mathbf{K}_b^e$ is the elastic stiffness matrix and $\mathbf{F}_e$ is the equivalent load vector. The equilibrium of the equivalent element which includes semi-rigid moment connections (Fig. 3.2b) is given by:

$$\mathbf{n}_e = \overline{\mathbf{K}}_b^e\, \overline{\mathbf{q}}_e - \overline{\mathbf{F}}_e, \tag{3.5}$$

where $\overline{\mathbf{K}}_b^e$ is the modified stiffness matrix of the element, $\overline{\mathbf{q}}_e = \{u_1, v_1, \overline{\varphi}_1, u_2, v_2, \overline{\varphi}_2\}$ is the vector of equivalent nodal displacements and $\overline{\mathbf{F}}_e$ is the modified equivalent load vector. The equivalent nodal displacements can be subdivided as follows:

$$\overline{\mathbf{q}}_e = \mathbf{q}_e + \mathbf{q}_j, \tag{3.6}$$

where $\mathbf{q}_\mathrm{j} = \{0, 0, \phi_1, 0, 0, \phi_2\}$ is the vector of end-connection rotations. Considering a linear behaviour for the connection, rotations and nodal forces are defined by

$$\mathbf{K}_j = \mathrm{diag}\{0, 0, R_1, 0, 0, R_2\}, \tag{3.7}$$

where R_1 and R_2 represent the rotational stiffness of the end connections. However, $\mathbf{K}_j$ matrix elements outside the main diagonal may be introduced in order to take into account shear, torsion and warping coupled effects.
Substituting Eq. 3.6 in Eq. 3.4 and considering Eq. 3.7, the modified stiffness matrix and the equivalent load vector are defined by:

$$\overline{\mathbf{K}}_b^e = \mathbf{C}\,\mathbf{K}_b^e, \quad \overline{\mathbf{F}}_e = \mathbf{C}\,\mathbf{F}_e \tag{3.8a, b}$$

with

$$\mathbf{C} = \mathbf{K}_j(\mathbf{K}_j + \mathbf{K}_b^e)^{-1} = (\mathbf{I} + \mathbf{K}_b^e\,\mathbf{K}_j)^{-1} \tag{3.9}$$

It must be noted that **C** turn out to be obviously different than the correction matrix $\mathbf{C}_e$ matrix defined by Monforton and Wu (1963), but the corresponding modified stiffness matrices $\overline{\mathbf{K}}_b^e$ turn out to be coincident. The model proposed by Shakourzadeh may be also applied to nonlinear geometric analyses, adopting the correction matrix of the static case:

$$\overline{\mathbf{K}}_g^e = \mathbf{C}\,\mathbf{K}_g^e \tag{3.10}$$

In this case, the resulting modified geometric matrix turns out to be quite different with respect the one obtained by Monforton and Wu (Eq. 3.3). However, solving a typical stability problem det$[\overline{\mathbf{K}}_b - \overline{\mathbf{K}}_g] = 0$, the resulting critical loads show negligible differences adopting the models described. For example, a portal frame with compressed columns and with semi-rigid beam-column connections is considered (Fig. 3.3). Column height is equal to one half of top beam length, whereas beam and column elastic stiffness are equal. Beam-column connections are characterized by a rigidity factor $r = 0.5$.

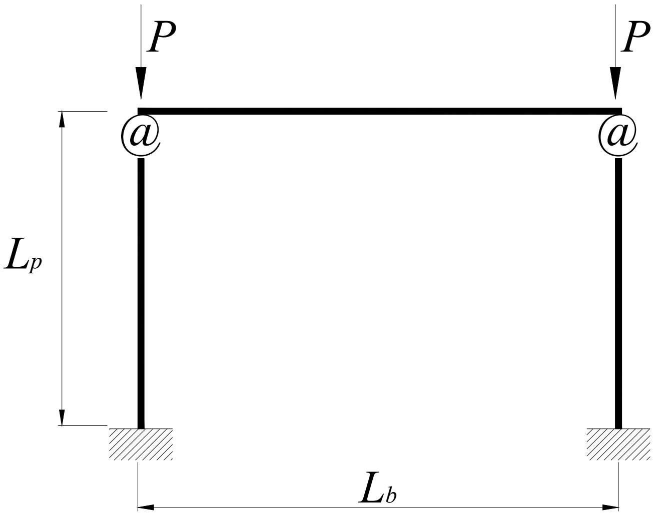

Fig. 3.3 – Portal frame with compressed columns and semi-rigid beam-column connections.

The frame is discretized by subdividing beam and columns with the same number n_{el} of equal FEs. In order to evaluate the influence of the modified geometric matrix, semi-rigid connections are placed at the end of each column.

The first four critical loads are determined for increasing n_{el}. The results determined adopting Monforton-Wu-Xu semi-rigid model with n_{el} = 256 are taken as reference $P_{\mathrm{cr}}^{\mathrm{REF}}$. Figs. 3.4a, b shows relative errors $\delta P_{\mathrm{cr}} = (P_{\mathrm{cr}}^{\mathrm{FEM}} - P_{\mathrm{cr}}^{\mathrm{REF}}) / P_{\mathrm{cr}}^{\mathrm{REF}}$ as a function of n_{el}.

Critical loads determined adopting the semi-rigid connection model defined by Shakourzadeh (Fig. 3.4a) converge to reference results. First and second critical loads converge with a ratio close to n_{el}^{-2} and errors are close to $2 \cdot 10^{-5}$ for n_{el} = 64. Adopting the semi-rigid connection model defined by Monforton, Wu and Xu, however, the first critical load do not converge to reference result but errors are less than $2 \cdot 10^{-5}$. Second, third and fourth critical loads converge to reference results with a ratio close to n_{el}^{-4}.

Hence, critical loads show negligible differences adopting the models described, then both models may be adopted for studying frame structures having semi-rigid connections; however the model proposed by Shakourzadeh is able to take into account further end connection effects (shear, torsion and warping effects) by simply adding the corresponding stiffness into $\mathbf{K}_j$. The model proposed by

Shakourzadeh is not characterized by a 'rigidity factor', but it directly makes use of the connection stiffness R_i ; however, Eq. 3.1 clearly shows the relation between Shakourzadeh and Monforton-Wu-Xu models, then, both models may be extended to nonlinear elastic analyses.

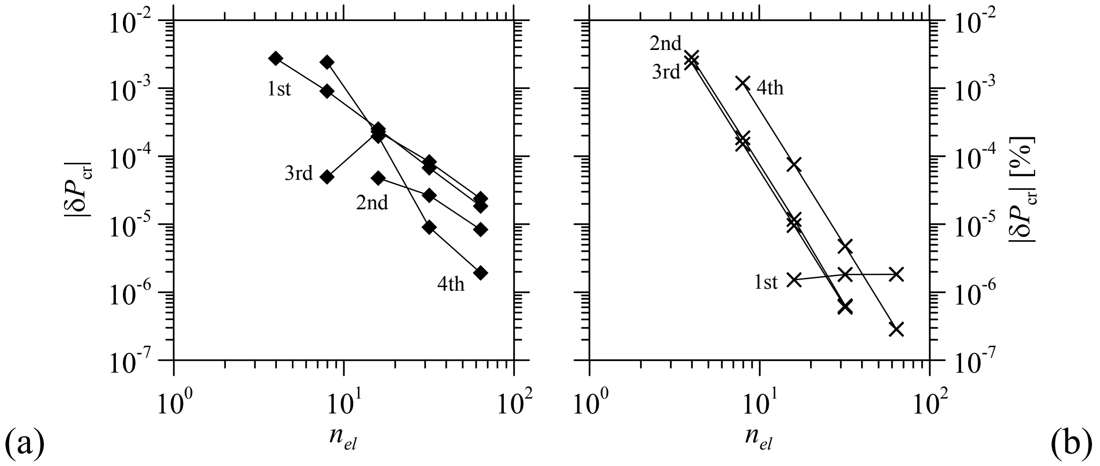

Fig. 3.4 – Relative errors δP_{cr} for the first four buckling loads as a function of n_{el} for a portal having semi-rigid beam-column connections. Shakourzadeh model (a), Monforton-Wu-Xu model (b)

3.3 Plasticity model for a beam-column element

The plastic hinge theory is a straightforward way to establish the incremental stiffness of beam elements, adopting the following assumptions:

- the plastic deformation is concentrated on one or both ends of the beam element;
- plastic hinge forms at a section once the moment applied at the section equals the plastic moment of the element.

The first assumption is often defined as the 'concentrated plasticity assumption', which is commonly accepted in the elasto-plastic analysis of frame structures, whereas the second assumption is based on an ideal elasto-plastic $M - \varphi$ relationship (Fig 5).

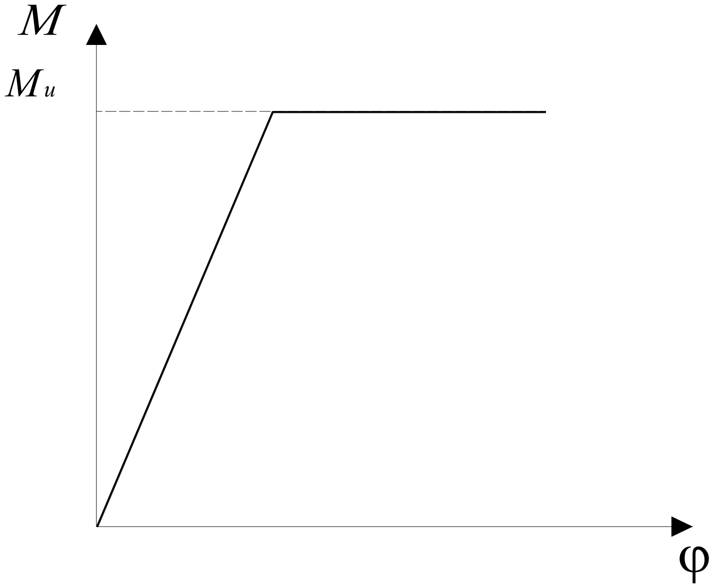

Fig. 3.5 – Ideal moment-rotation curve of the beam element.

A nonlinear elastic analysis such as a pushover analysis is able to evaluate the stiffness degradation of a frame structure if the elastic limit is reached and exceeded. The degradation of the flexural stiffness of a frame member cross-section starts when the material fibres farthest from the neutral axis of the cross-section experience initial yielding. The yielding moment M_y characterizes the beginning of the stiffness degradation. Then, increasing bending moment, plasticity spreads through section depth and along the member length to form a fully-developed plastic hinge, at which point the flexural stiffness of the beam cross-section is exhausted. The ultimate moment M_u and the ultimate rotation φ_u characterize the plastic hinge completely developed. The stiffness degradation is described by a moment-rotation ($M - \varphi$) curve which depends on cross-section shape and material.

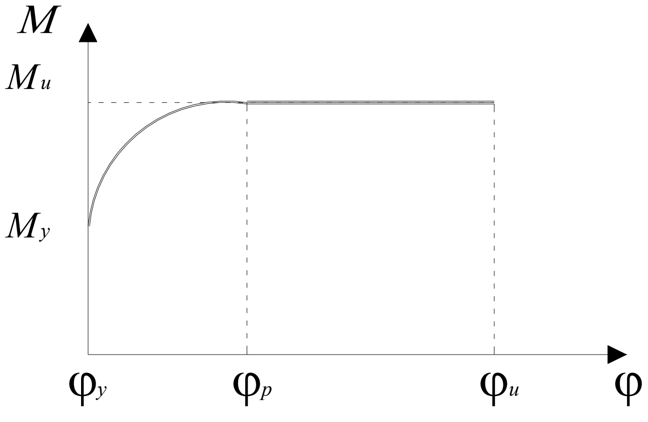

Fig. 3.6 – Post-elastic moment-rotation relation adopted by Hasan et al. (2002).

Following the work of Hasan, Xu and Grierson (2002), Fig. 3.6 shows a post-elastic moment-rotation relationship, which represents the behaviour of most section shapes used in steel building frameworks. It is clear that the model of post-elastic behaviour of a plastic hinge section is similar to the model of a semi-rigid connection. Then, the rotational stiffness R_i of a semi-rigid connection can be replaced by the flexural stiffness of the section:

$$R_{p,i} = \mathrm{d}M / \mathrm{d}\varphi \tag{3.11}$$

For moment levels less than M_y, the variation of post-elastic rotation $\mathrm{d}\varphi = 0$ and the corresponding flexural stiffness $R_{p,i} = \infty$. When the moment reaches M_u, the variation of post-elastic moment $\mathrm{d}M = 0$ and the corresponding flexural stiffness $R_{p,i} = 0$. For $M_y < M < M_u$, the flexural stiffness of the member section is determined by differentiating the equation adopted to describe the curve $M - \varphi$ with respect to φ.

Introducing $R_{p,i}$ in Eq. 3.1, the degradation of the flexural stiffness of a member section experiencing a post-elastic behaviour can be characterized by the 'plasticity factor':

$$p_i = \frac{1}{1 + (3D_b / R_{p,i}\, L)} \tag{3.12}$$

Which varies between 1 and 0 as the flexural stiffness varies between an ideal elastic value ($R_{p,i} = \infty$) and a fully plastic value ($R_{p,i} = 0$).

In the following examples, for simplicity, a rigid-perfectly plastic curve (Fig. 3.7) is adopted to describe the moment-rotation relation for the potential plastic hinges. Then, flexural stiffness of the member section assumes the value $R_{p,i} = \infty$ when the section is in the elastic range and it changes to $R_{p,i} = 0$ when the corresponding bending moment reaches M_u.

Fig. 3.7 – Post-elastic rigid-perfectly plastic moment-rotation relationship.

The application of Monforton-Wu-Xu or Shakourzadeh model to pushover analysis of frames requires to define a-priori the position of potential plastic hinges into the discrete model of the structure. For example, plastic hinges may be placed at beam-column connections and along beam length. In this case, the total number of FEs and degrees of freedom do not vary with respect to a simple elastic analysis, in particular it is not necessary to modify the discrete model during pushover analysis. It is clear that the results of the analysis turn out to depend strictly on the initial positions of the plastic hinges. However, at the end of the pushover analysis, it is obviously possible to verify if bending moments at each finite element end respect the plasticity condition $M_i \leq M_{u,i}$, then, further potential plastic hinges may be added to the initial discrete model in order to perform a more accurate pushover analysis.

3.4 Analysis of beams on elastic half-plane including material nonlinearity

A beam on elastic half-plane may represent the behaviour of a thin film on an elastic substrate, a sandwich panel, or it may represent the foundation of a more complex plane structure such as a pipe. In the following, starting from the discrete model of an Euler-Bernoulli beam on elastic half-plane (§ 1.3), material nonlinearity of beam cross-section is taken into account applying the simple and effective model proposed by Shakourzadeh et al. (1999) for the pushover analysis of frames. In this case, plastic hinges are located at several points along beam length (Fig. 3.8). A plastic hinge may be placed at foundation beam ends, in order to take into account the degradation of cross-section stiffness due to the increasing bending moment at the column-foundation intersection. Furthermore, one or more plastic hinges may be placed along the beam length, under concentrated or distributed loads, in order to take into account the degradation of stiffness due to increasing bending moments along beam length.

3.4.1 Beam with plastic hinges on elastic half-plane

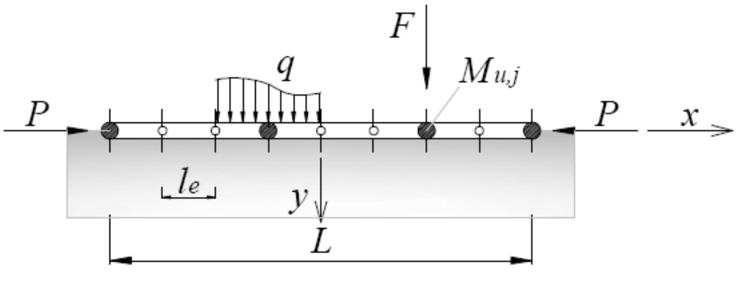

Fig. 3.8 – Beam on elastic half-plane subdivided into equal FEs, with plastic hinges at its ends and along its length.

Considering an Euler-Bernoulli beam on elastic half-plane, subdivided into equal FEs, a generic element e is characterized by the equilibrium equation:

$$\mathbf{n}_e = \mathbf{K}_b^e\,\mathbf{q}_e - \mathbf{F}_e + \mathbf{H}_e\,\mathbf{r}_e, \qquad (3.13)$$

where $\mathbf{H}\,\mathbf{r}_e$ represents the equivalent load vector generated by the half space reaction under the beam element. Considering an element with a plastic hinge at one or both ends (Fig. 3.8) and applying the procedure adopted by Shakourzadeh et al. (1999), Eq. 3.13 becomes

$$\mathbf{n}_e = \overline{\mathbf{K}}_b^e \, \overline{\mathbf{q}}_e - \overline{\mathbf{F}}_e + \overline{\mathbf{H}}_e \, \mathbf{r}_e , \tag{3.14}$$

where $\mathbf{n}_e = \{N_1, V_1, M_1, N_2, V_2, M_2\}$ is the vector of nodal forces applied on the element. Hence, the matrix $\overline{\mathbf{H}}_e = \mathbf{C}\,\mathbf{H}_e$ is modified similarly to the stiffness matrix and the equivalent load vector (Eqs. 3.8a, b).

3.4.2 Incremental analysis of beams on half-plane including material nonlinearity

In the following, a beam with free ends on elastic half plane loaded by a concentrated force F at midpoint is considered. The beam has a length $L = 10$ m, cross-section height $h = 0.5$ m and it is characterized by a ultimate moment $M_u = 100$ kNm, determined following Eurocode 2 material design rules for a reinforced concrete rectangular section (concrete C25/30 and steel B450C), having width equal to 1 m, reinforced with 10 bars with diameter 10 mm.

The first potential plastic hinge is placed a-priori obviously at beam midpoint, where the largest bending moment along beam length is expected. Then, further plastic hinges are placed close to midpoint, where bending moment assumes large values after the first plastic hinge formation. Plastic hinge positions are defined by the following coordinate (Fig. 3.9):

$$x_{pl} = \{0, \pm L/8, \pm L/4\} . \tag{3.15}$$

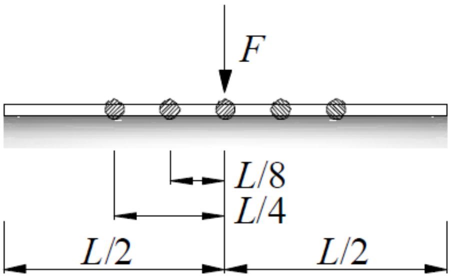

Fig. 3.9 – Beam with free ends on elastic half plane loaded at midpoint, having 5 potential plastic hinges along its length.

The discrete model adopted for the beam is characterized by 32 FEs, then plastic hinge positions correspond to the 9th, 13th, 17th, 21st and 25th node. Analyses are performed evaluating the vertical displacement at midpoint d due to the increasing applied force F and displacement control method is adopted. Analyses are stopped when the second (and third, symmetric) plastic hinge is formed. It is worth noting that increasing beam displacements and consequently increasing half-plane displacements, the hypothesis of linear half-plane may not be respected, then analyses may be performed up to the development of the second and fourth plastic hinges.

In the following figures, load displacement curves $F-d$ are presented for increasing αL values, which correspond to increasing half-plane stiffness. Small dashed lines represent linear static analyses, whereas continuous lines represent nonlinear incremental analyses. Moreover, beam displacement, soil reactions and bending moments are presented. For each case, the beam characterized by an elastic behaviour is represented by a dot on $F-d$ curve and by large dashed lines in displacement, reaction and bending moment diagrams, whereas the first plastic hinge is represented by a triangle on $F-d$ curve and by continuous lines in other diagrams. Finally a cross on $F-d$ curve and short dashed lines in other diagrams represent the behaviour of the beam when the second plastic hinge is developed, except for the beam on very soft soil cases (i.e. for αL = 1 and 2), which are not characterized by the development of a second plastic hinge. Further values in $F-d$ curves, except for beams on very soft soil, are characterized by the violation of the plasticity condition ($M > M_u$) in the nodes adjacent to the second and third plastic hinge. For αL = 1 and 2 (Figs. 3.10a-h), the 1st plastic hinge is obviously obtained at beam midpoint, however, increasing displacement at midpoint d, a very small slope of $F-d$ curve is observed. Beam displacements in plastic range are obviously characterized by the loss of slope continuity at beam midpoint. Moreover, soil reactions and bending moments for the beam in plastic range remain quite coincident to the values reached when the first plastic hinge is formed. For αL = 3 (Figs. 3.11a-d), the 1st plastic hinge is obviously obtained at beam midpoint, in this case the slope of $F-d$ curve after the first plastic hinge is larger than the previous cases; however, a large displacement at midpoint is necessary to obtain the second plastic hinge. The behaviour of the beam in plastic range is characterized by large soil reactions close to beam midpoint and negative bending moment far from beam midpoint. For αL = 5 (Figs. 3.11e-h), the 1st plastic hinge is obtained at beam midpoint and the second and third plastic hinges are obtained at $x = \pm L/4$. After the formation of the second and third plastic hinges, the slope of $F-d$ curve does not change significantly. The behaviour of the beam in plastic range is characterized by large soil reactions close to beam midpoint and negative bending moment along beam length, except close to beam midpoint. For αL = 10 and 20 (Figs. 3.12e-h), the 1st plastic hinge is obtained at beam midpoint and the second and third plastic hinges are obtained at $x = \pm L/8$.

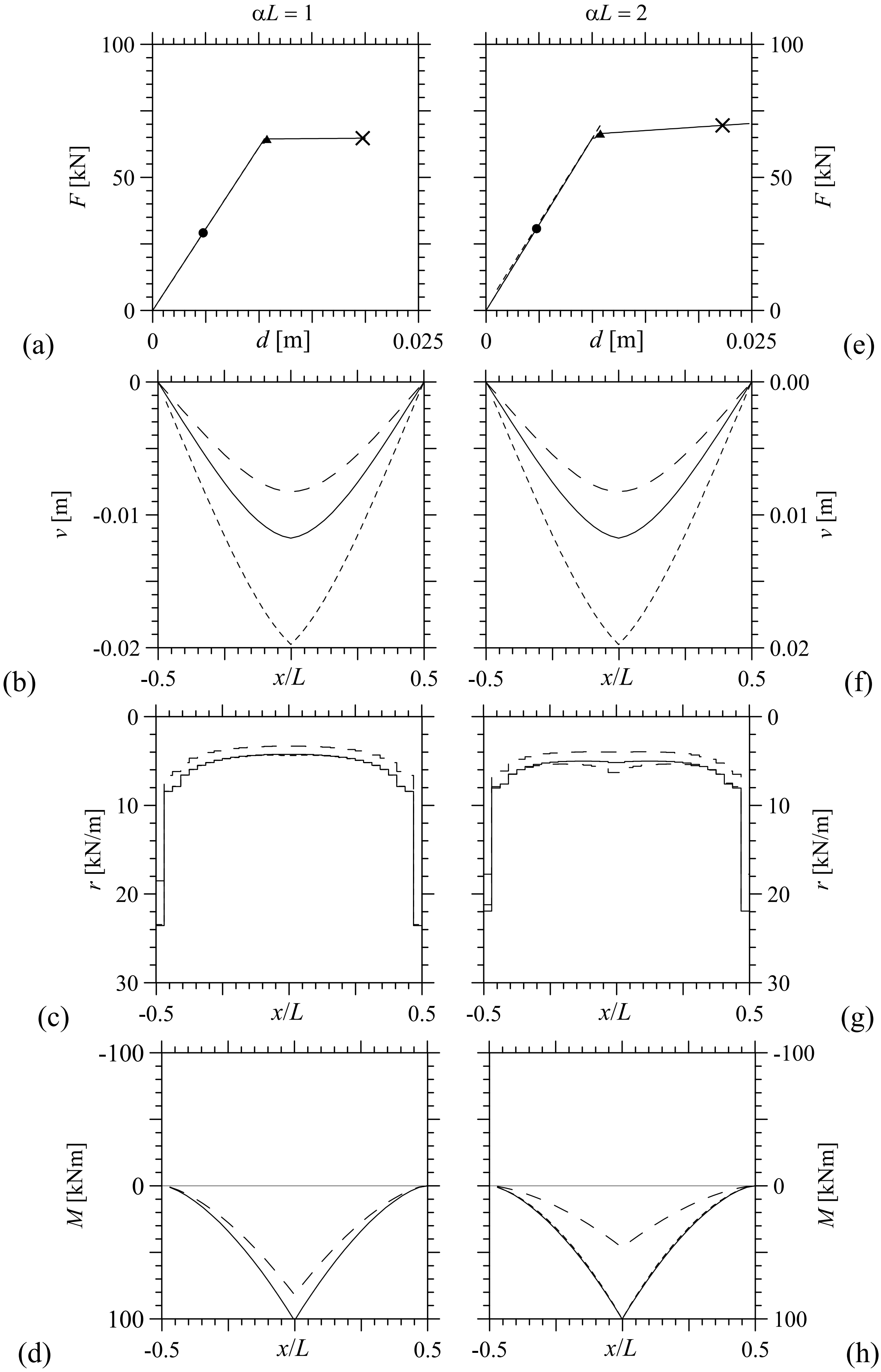

Fig. 3.10 – Beam on elastic half plane loaded at midpoint including material nonlinearity. Load-deflection curve (a,e), vertical displacement (b, f), soil reactions (c, g) and bending moment (d, h). Beam in elastic state (dot, large dashed lines), first hinge (triangle, continuous lines), and beam in plastic state (short dashed lines).

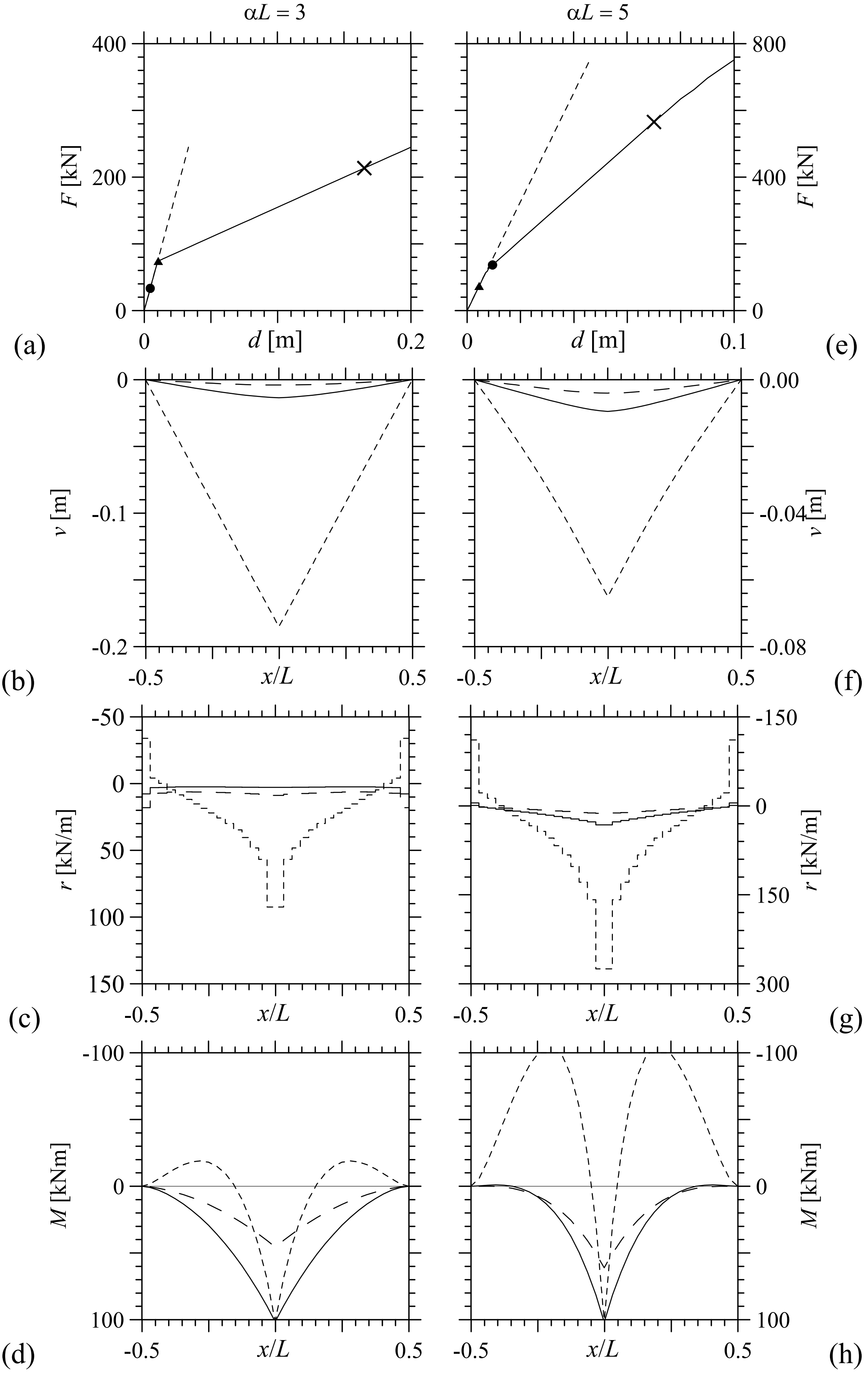

Fig. 3.11 – Beam on elastic half plane loaded at midpoint including material nonlinearity. Load-deflection curve (a,e), vertical displacement (b, f), soil reactions (c, g) and bending moment (d, h). Beam in elastic state (dot, large dashed lines), first plastic hinge (triangle, continuous lines), and second plastic hinge (cross, short dashed lines).

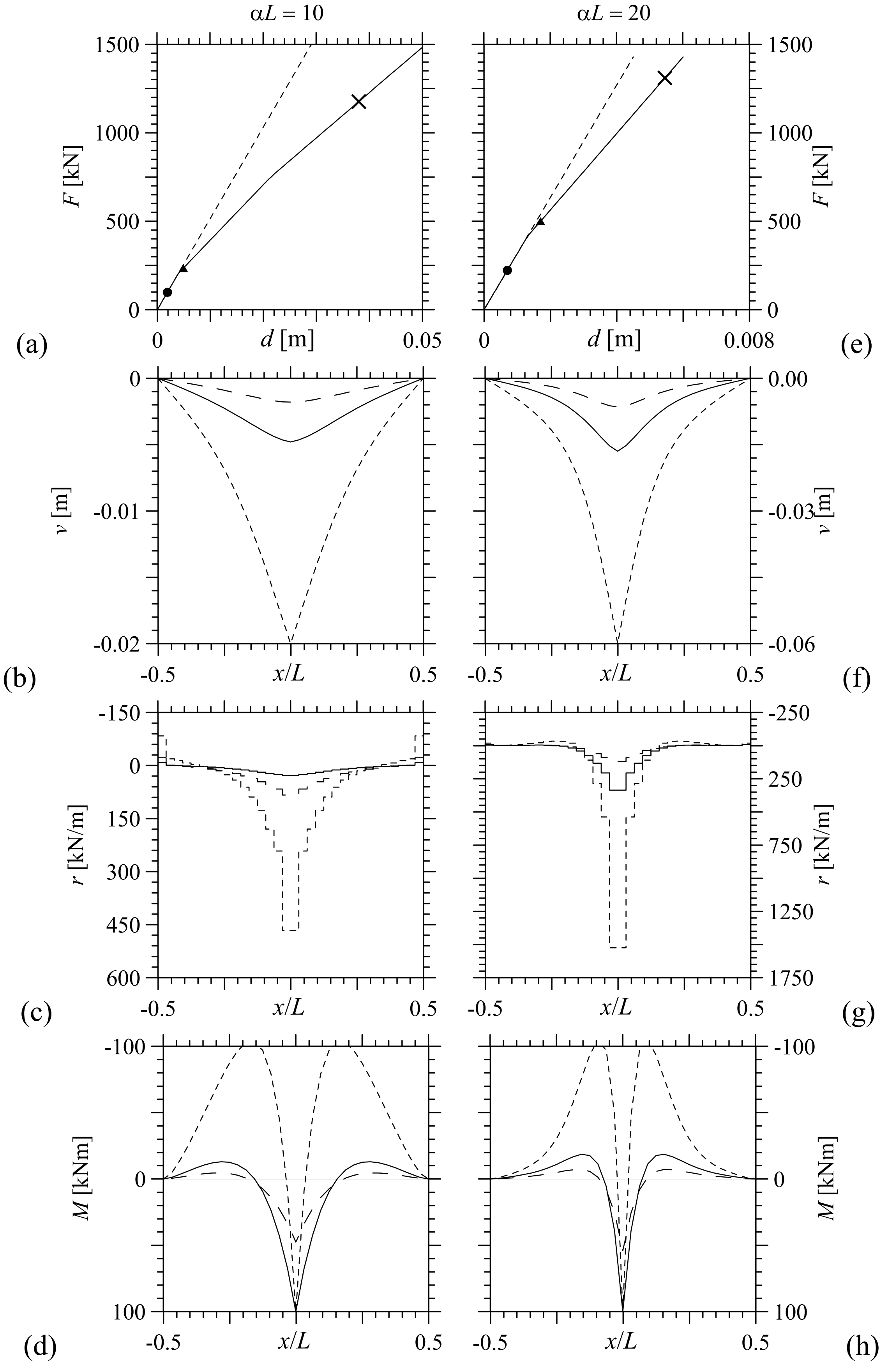

Fig. 3.12 – Beam on elastic half plane loaded at midpoint including material nonlinearity. Load-deflection curve (a,e), vertical displacement (b, f), soil reactions (c, g) and bending moment (d, h). Beam in elastic state (dot, large dashed lines), first plastic hinge (triangle, continuous lines), and second plastic hinge (cross, short dashed lines).

Observing the load-deflection curves of the six examples, it is clear that the slope after the first hinge increases for increasing α*L*, moreover, the concentrated force *F* necessary to obtain the first hinge increases for increasing α*L*. Beam displacement at midpoint corresponding to the first hinge is close to 0.01m for α*L* up to 5, whereas it is smaller for the beam on quite stiff and stiff soil (close to 0.005 m for α*L* = 10 and 0.002 m for α*L* =20).

Since further plastic hinges are obtained close to second and third plastic hinge positions, analyses turn out to depend strictly on beam discretization. In the following, the case of a beam subdivided into 32 equal FEs, with potential plastic hinges at each beam end is considered and an incremental analysis is performed up to the development of further plastic hinges. Considering the case with α*L* = 10, already showed in Fig. 3.12a, Fig. 3.13 shows load-displacement curve of linear static analysis with large dashed lines, whereas the nonlinear incremental analysis with three potential plastic hinges is represented by a continuous line. The nonlinear incremental analysis which takes into account potential plastic hinges along the entire beam length is represented by a small dashed line. In this case, the second and third plastic hinges are obtained at $x = \pm 3/16L$, similarly to the position set a-priori in the previous examples, then the corresponding point in the load-displacement curve (cross in Fig. 3.13) do not vary significantly. Then, further plastic hinges are obtained at beam FE ends close to beam midpoint and the vertical displacement turn out to be larger than the one obtained with three plastic hinges.

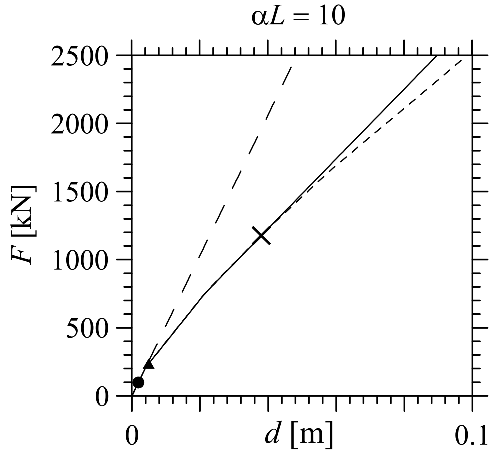

Fig. 3.13 – Beam on elastic half plane loaded at midpoint including material nonlinearity. Load-deflection curve for linear elastic analysis (large dashed line), nonlinear incremental analysis with 3 potential plastic hinges (continuous line), nonlinear incremental analysis with potential plastic hinges located at each beam end (small dashed line).

Analysis performed with a finite number of potential plastic hinge represents an upper limit for the analysis that allows potential plastic hinges over the entire beam length.

Considering potential plastic hinges along the entire beam length, it is found that further plastic hinges after the second and the third one are obtained close to beam midpoint, as it is shown in Fig 14, where continuous line represents the bending moment corresponding to the development of the second and third plastic hinge ($x = \pm 3/16L$). The dashed line and the line with dots represent the bending moments corresponding to further hinges close to beam midpoint ($x = \pm L/8$ and $x = \pm L/16$, respectively). Then, the plastic hinge closest to beam midpoint moves from $x = \pm 3/16L$ to $x = \pm L/16$. This behaviour is quite similar to the one of beams and plates on Winkler-type half-space, which were analyzed for studying the plastic behaviour of floating ice sheets or concrete pavements subject to concentrated loads (Meyerof 1962, Kerr 1986, Rao and Singh 1986). In this case, the position of the maximum negative bending moment tends to move towards the load (Augusti 1970).

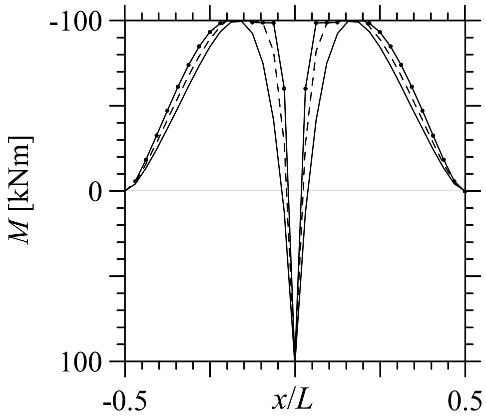

Fig. 3.14 – Bending moments for a beam with potential plastic hinges along its entire length.

3.4.3 Incremental analysis of beams on half-plane including material and geometric nonlinearity

A beam with free ends on elastic half plane is considered. The beam has the same geometric and material characteristics of the one described in the previous paragraph. However in this case, the beam is characterized by a potential plastic hinge at midpoint (Fig. 3.15), having a ultimate bending moment M_u = 100 kN and it is subject to an increasing axial load P. In this case, for simplicity, the ultimate bending moment does not depend on axial stress level P.

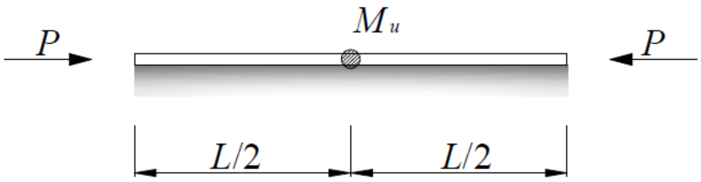

Fig. 3.15 – Compressed beam with free ends with a potential plastic hinge at midpoint.

In the following, incremental analyses of the beam including second order effects due to axial load are carried out for increasing αL values. Vertical displacement at midpoint is taken as reference parameter to evaluate the behaviour of the beam and determine the curve $P-v(0)$. Each analysis is stopped when further plastic hinges may be obtained if the plasticity condition $M_i \leq M_u$ is not respected at beam FE ends. Figs. 3.16a-d show dimensionless axial load $P/P_{\mathrm{cr,E}}$ for increasing $v(0)$ for αL equal to 5, 10, 15 and 20. Each figure is characterized by a continuous line representing the behaviour of the beam without the potential plastic hinge. It is clear that in this case, axial load P converge to the first critical load corresponding to a symmetric mode shape of a beam with free ends (§ 1.5.5). In Figs. 3.16a-d, continuous lines with dots represent the behaviour of the beam with the potential plastic hinge at midpoint. Before reaching $M = M_u$ at midpoint, $P-v(0)$ curve is coincident with the curve for the beam without potential plastic hinge. When $M = M_u$, each curve moves to the one of a beam with a weak section at midpoint and axial load P converge to the first critical load of a beam on elastic half-plane with a weakened section at midpoint (§ 1.5.6) if the plasticity condition $M \leq M_u$ is respected along beam length Considering the cases of a beam on soft soil (Figs. 3.16a and b), analyses are stopped before converging to the first critical load of a beam with a weak section at midpoint. Considering the cases of a beam on stiff half-plane (Figs. 3.16 c and d), further plastic hinges are not obtained along beam length and it can be found easily that axial loads converge to values quite close to $0.069(\alpha L)^2$.

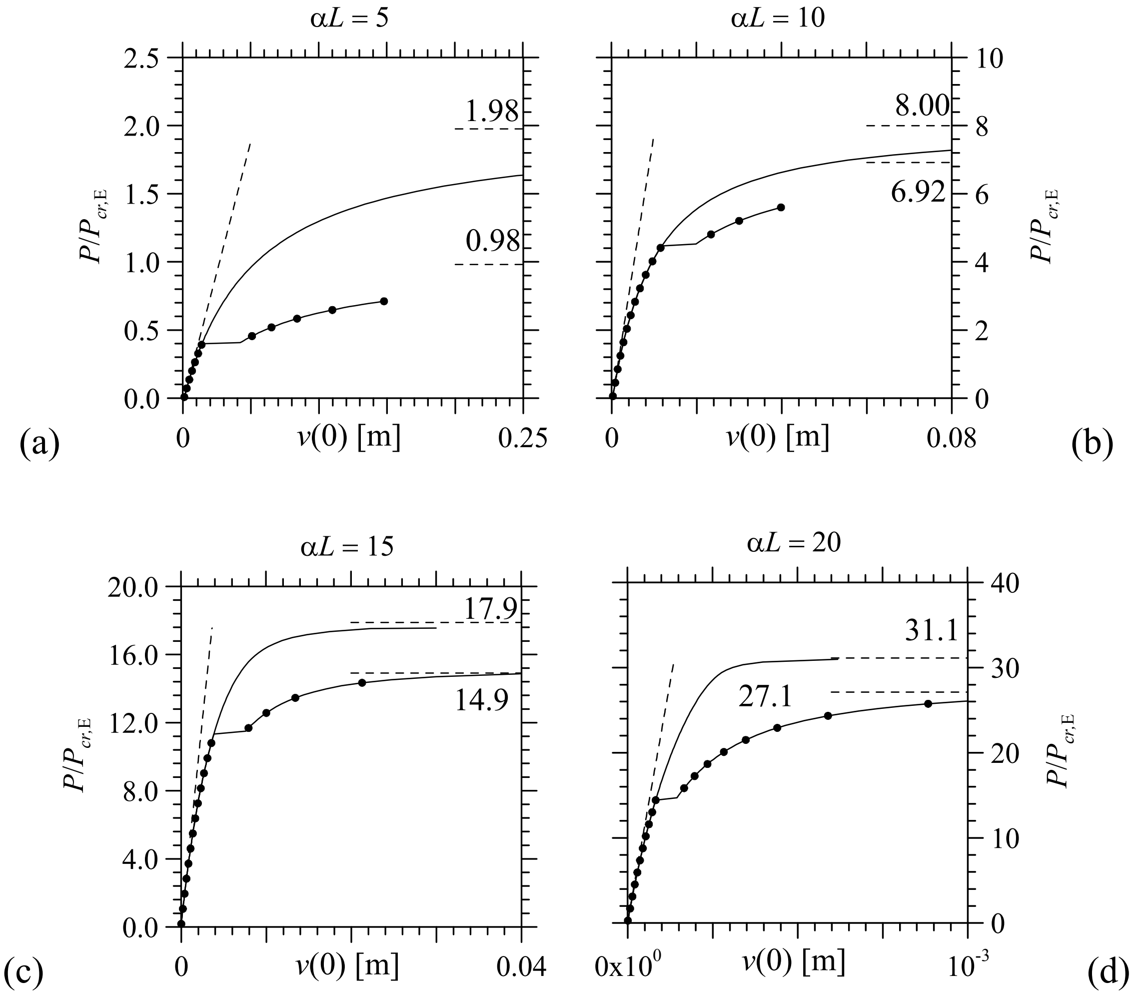

Fig. 3.16 – Axial load for increasing vertical displacement at mid point for a beam with free ends (continuous lines) and a beam with free ends and a potential plastic hinge at midpoint (lines with dots), for αL = 5 (a), 10 (b), 15 (c), 20 (d).

3.5 Incremental analysis of frames on half-plane including material nonlinearity

In paragraph § 1.7, buckling and incremental analyses of pipes including second order effects were performed and the present model turned out to be simple and effective, especially with respect to analyses done adopting a traditional FE model.

In this paragraph, a pipe on elastic half-plane is studied taking into account material nonlinearity by placing potential plastic hinges where large bending moment values are expected. A reinforced-concrete structure is considered and each potential plastic hinge section has an ultimate moment M_u depending on axial load N.

3.5.1 Description and design of the structure

The analysed structure consists of a pipe or concrete box-culvert 22.10 m long, built to grant the free flow of a stream under a railway line (FIB 1999). Pipe width is equal to 7.7 m and its height is equal to 5.8 m as shown in Fig. 3.17, where the cross-section height of each pipe element is highlighted. The top beam is covered by a bed of soil having height equal to 2.5 m and ballast with a height equal to 0.8 m. Lateral slabs are obviously subject to the lateral earth pressure. Then, a service load due to a train acts on the upper beam.

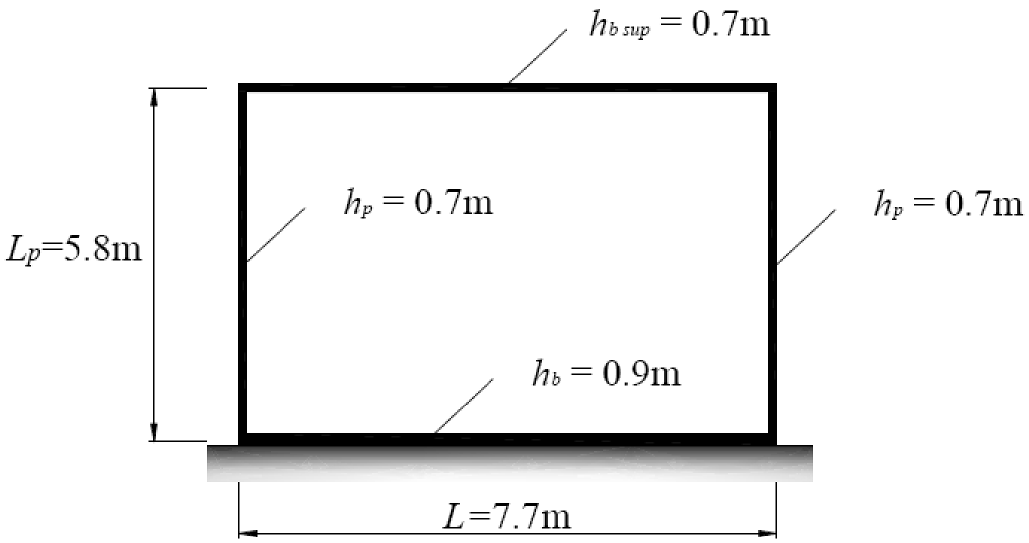

Fig. 3.17 – Cross-section of the pipe studied.

The following material properties are considered for the structure (Eurocode 2):

- Concrete grade 30	$f_{ck} = 30.0$	MPa
compressive design strength	$f_{cd} = 20.0$	MPa
compressive resistance for cracked zones	$f_{cd1} = 15.0$	MPa
compressive resistance for uncracked zones	$f_{cd2} = 10.6$	MPa
mean value of tensile strength	$f_{ctm} = 2.9$	MPa
modulus of elasticity	$E_{cm} = 29.0$	GPa
- Reinforcing steel, grade 500	$f_{yk} = 500$	MPa
design strength	$f_{yd} = 435$	MPa
modulus of elasticity	$E_{st} = 200$	GPa

Authors (FIB 1999) defined soil parameters in order to adopt a Winkler-type model, assuming a vertical modulus of subgrade reaction $c = 20\ N/cm^3$. Adopting Biot (1937) relation between the modulus c and the elastic properties of the corresponding half-plane:

$$c = \frac{0.710}{2^{4/3}} \left[\frac{E_S^4\, b^4}{D_b} \right]^{1/3} = 0.282 \left[\frac{E_S^4\, b^4}{D_b} \right]^{1/3} . \tag{3.16}$$

The soil under the structure turns out to have the parameters of a soft clay (Bowles 1997):

modulus of elasticity	$E_S = 16$	MPa
unit weight	$\gamma_S = 19$	kN/m^3

The real loads acting on the pipe are defined as follows, assuming a transverse strip having width equal to 1 m:

- self-weight, considered adopting a unit weight value $\gamma_{cls} = 25$ kN/m^3;
- gravity load on the upper beam due to soil and ballast:

$$q_{soil} = 19 \cdot 2.5 \cdot 1.0 = 47.5 \text{ kN/m}$$

$$q_{ballast} = 18 \cdot 0.8 \cdot 1.0 = 14.4 \text{ kN/m}$$

- train load:

$$q_{train} = 74.5 \text{ kN/m}$$

- lateral soil pressure at rest (adopting a k_0 coefficient equal to 0.5), the top and bottom values of the trapezoidal distributed load are:

$$q_{top} = 0.5\,(47.5 + 14.4) = 30.95 \text{ kN/m}$$

$$q_{bottom} = 0.5\,(19 \cdot 6.6 \cdot 1.0) + 30.95 = 93.65 \text{ kN/m}$$

- lateral earth pressure due to a uniform surcharge of 40 kN/m^2 on the left side of the earth adjacent to the pipe:

$$p_{earth} = 0.5 \cdot 40 \cdot 1 = 20 \text{ kN/m}.$$

The following figure resumes the loads applied to the structure.

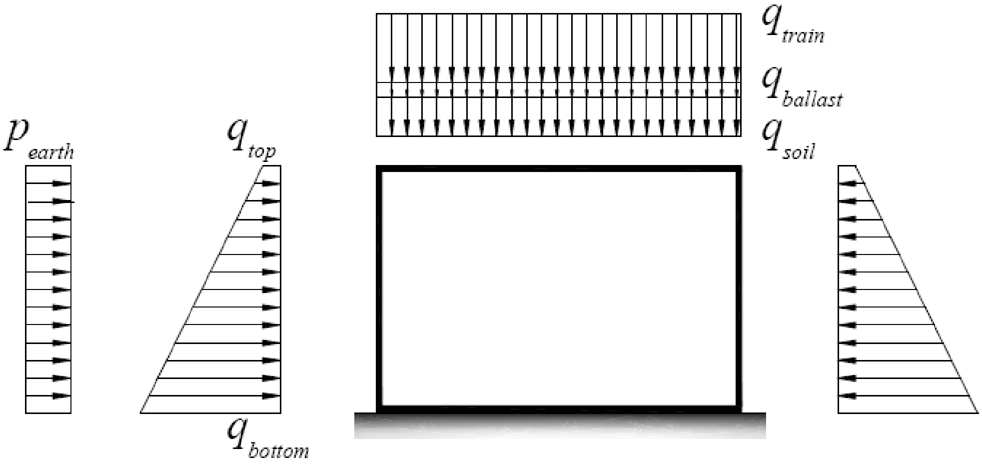

Fig. 3.18 – Applied loads on structure (self-weight is not represented for simplicity).

Structural elements have been designed in FIP (1999) adopting Eurocode 2 design rules. The following combination of actions has been used:

$$S_d = S\,\{\gamma_G G_k + \gamma_Q Q_k\}, \tag{3.17}$$

where G_K represents permanent loads (self-weight, soil and ballast weight, lateral earth pressure at rest), Q_K represents variable loads (trail load, lateral earth pressure grom trail load) and $\gamma_G = 1.35$, $\gamma_Q = 1.5$.

Tab. 3.1 resumes axial forces and bending moments at several cross-section of the pipe (beam-column nodes and beam midpoints). Moreover, minimum steel reinforcement is determined for each section, adopting the following simplified expressions and without consideration for the compression reinforcement:

$A_s = M_{Sd} / (0.9\, d f_{yd})$ for beams (neglecting axial forces); (3.18a)

$A_s = [M_{Sd} + N_{Sd}\,(d - h/2)] / (0.9\, d f_{yd}) - N_{Sd} / f_{yd}$ for columns (3.18b)

Tab. 3.2 shows the actual reinforcements adopted by the designer. $A_{s,eff}$ and $A'_{s,eff}$ represent designed steel reinforcements. Each section is characterized by a nominal concrete cover value equal to 35 mm.

Element	Section	M_{Sd} [kNm]	N_{Sd} [kN]	A_s [cm^2]
Foundation	left corner	930	-368	26.4
	midspan	-1199	-368	34.6
	right corner	557	-368	15.4
Upper beam	left corner	-719	-283	27.1
	midspan	805	-283	30.5
	right corner	-911	-283	34.6
Column (left)	Top	-719	-890	17.5
	bottom	-930	-1032	24.7

Tab. 3.1 – Bending moments, axial forces and minimum steel reinforcements for beam and column cross-sections of the pipe.

Element	Section	A_s [cm^2]	$A_{s,eff}$ [cm^2]		$A'_{s,eff}$ [cm^2]	
Foundation	left corner	26.4	53.1	10∅26	38.0	10∅22
	midspan	34.6	38.0	10∅14	15.4	10∅14
	right corner	15.4	53.1	10∅26	38.0	10∅22
Upper beam	left corner	27.1	53.1	10∅26	38.0	10∅22
	midspan	30.5	38.0	10∅22	15.4	10∅14
	right corner	34.6	53.1	10∅22	38.0	10∅22
Columns		24.7	38.0	10∅22	15.4	10∅14

Tab. 3.2 – Steel reinforcements for beam and column cross-sections of the pipe.

3.5.2 Description of the discrete model

Calculations are referred to a transverse strip having width equal to 1.0 m, then a plane frame is adopted for modelling the structure. The pipe is discretized by adopting traditional beam FEs and discretizing the soil pressure with a piecewise constant function. Beam FEs parameters are resumed in the following table.

Member	Area	Inertia
	$[m^2]$	$[m^4]$
upper beam	0.7	0.0286
columns	0.7	0.0286
foundation	0.9	0.0608

Tab. 3.3 – Area and inertia of beam elements

The soil-structure interaction parameter of the foundation of the pipe turn out to be:

$$\alpha L = \sqrt[3]{\frac{E_S\, b\, L^3}{(1-\nu_S^2)\, D_b}} \cong 1.55 \text{ m.} \tag{3.19}$$

Beam-column connections are modelled as infinitely rigid links having length equal to one half of the corresponding cross-section height; then, the remaining parts of columns and top beam are discretized by 4 equal beam FEs and foundation is discretized by 8 equal beam FEs. Fig. 3.19 shows the FE discretization of the pipe together with FEs number, moreover, dots represent potential plastic hinge positions.

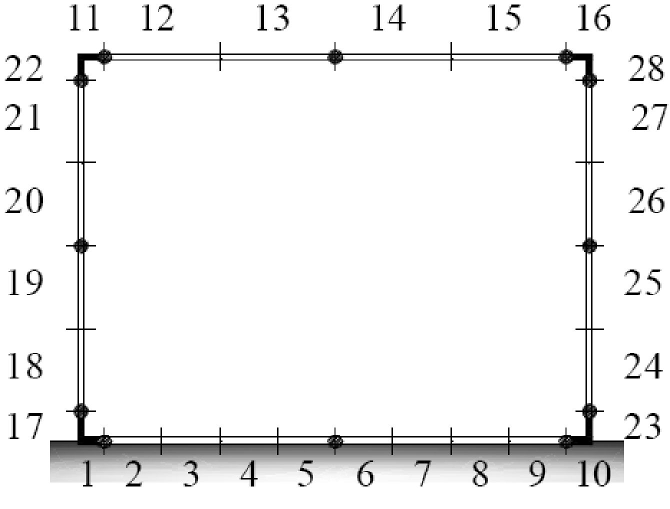

Fig. 3.19 – FE model for the pipe with beam FEs number. Dots represent potential plastic hinge positions.

Potential plastic hinges are placed at FE ends near beam-column connections, at foundation midpoint, at top beam and column midpoint, where maximum bending moment values are expected. Assuming a local Cartesian coordinate system for each element having x axis directed from left to right for foundation and top beam FEs and directed upward for column FEs, Tab 4 lists beam FE ends having a plastic hinge. Each plastic hinge is characterized by a diagram $N - M_u$, which furnishes the ultimate bending moment of the section as a function of axial load. Diagrams are obviously determined taking into account the steel reinforcements adopted by the designer (Tab. 3.2).

element	node 1	node 2
#2	•	
#5		•
#6	•	
#9		•
#12	•	
#13		•
#14	•	
#15		•
#18	•	
#19		•
#20	•	
#21		•
#24	•	
#25		•
#26	•	
#27		•

Tab. 3.4 – Plastic hinge positions.

3.5.3 Numerical examples: pipe loaded by increasing service loads

In the following, a incremental analyses of the pipe subject to various loads are carried out taking into account material nonlinearity. The behaviour of plastic hinge sections is monitored by *N-M* curves, which have to follow the corresponding $N\text{-}M_u$ diagrams depending on section geometry and steel reinforcements adopted. Each incremental analysis is stopped when a local or global collapse mechanism is achieved; then, ultimate load is compared with an upper bound represented by the limit load which may be obtained by applying the collapse mechanism of the pipe to a portal with fixed column bases.

3.5.3.1 Example 1: pipe loaded by a distributed force along the upper beam

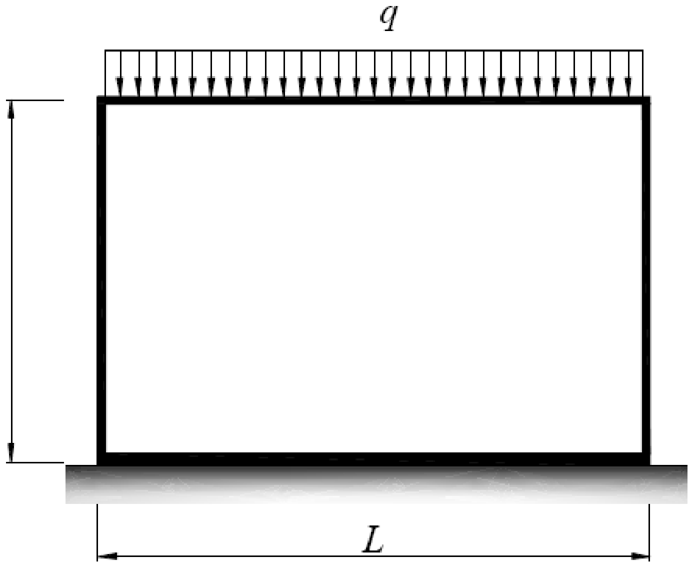

Fig. 3.20 – Pipe loaded by a distributed force at top beam.

The first example is characterized by an increasing distributed load q on the top beam of the pipe. The vertical displacement at beam midpoint is taken as a reference parameter to determine the curve $q-d$. The formation of the first plastic hinge is localized at top beam midpoint (end 2 of element #13, end 1 of element #14). The formation of second and third plastic hinges is localized at column tops (end 2 of elements #21 and #27). Then, a local collapse mechanism for the top beam is obtained (Fig. 3.21). The ultimate load of the structure turns out to be equal to:

$$q_{u,1} = 513\,\text{kN/m}, \tag{3.20}$$

which is quite close (96%) to the limit load that may be determined for a portal frame with clamped column bases with the same collapse mechanism:

$$q_{\text{lim},1} = 536\ \text{kN/m}. \tag{3.21}$$

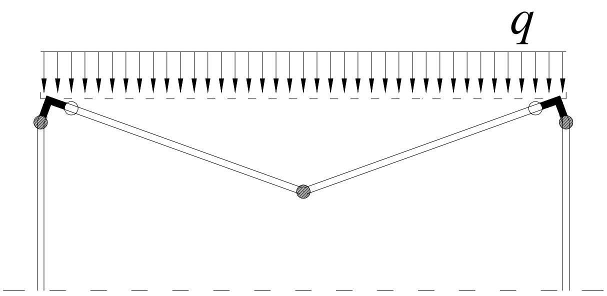

Fig. 3.21 – Collapse mechanism.

The first plastic hinge formation is characterized by q = 386 kN/m and d = 0.0094 m, whereas the second and third ones are formed with q = 513 kN/m and d = 0.0175 m (Fig. 3.22). Figs. 3.23a and b show the bending moment variation as function of axial force for the two potential plastic hinge sections activated during the incremental analysis. The *N-M* curve for the first plastic hinge section is characterized by a very small axial force before intersecting *N-*M_u diagram (Fig. 3.23a). The diagram of bending moment with respect to the axial force for the second and third plastic hinge sections is characterized by increasing compressive force and increasing bending moment. When the first plastic hinge is formed, the slope of *N-M* curve changes due to the stiffness reduction of the structure.

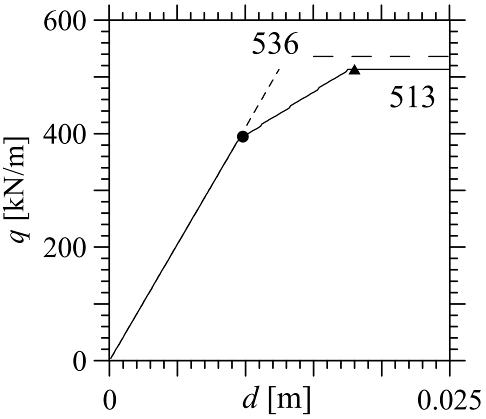

Fig. 3.22 – Load-deflection curve representing the incremental analysis of a pipe loaded by a distributed force at top beam.

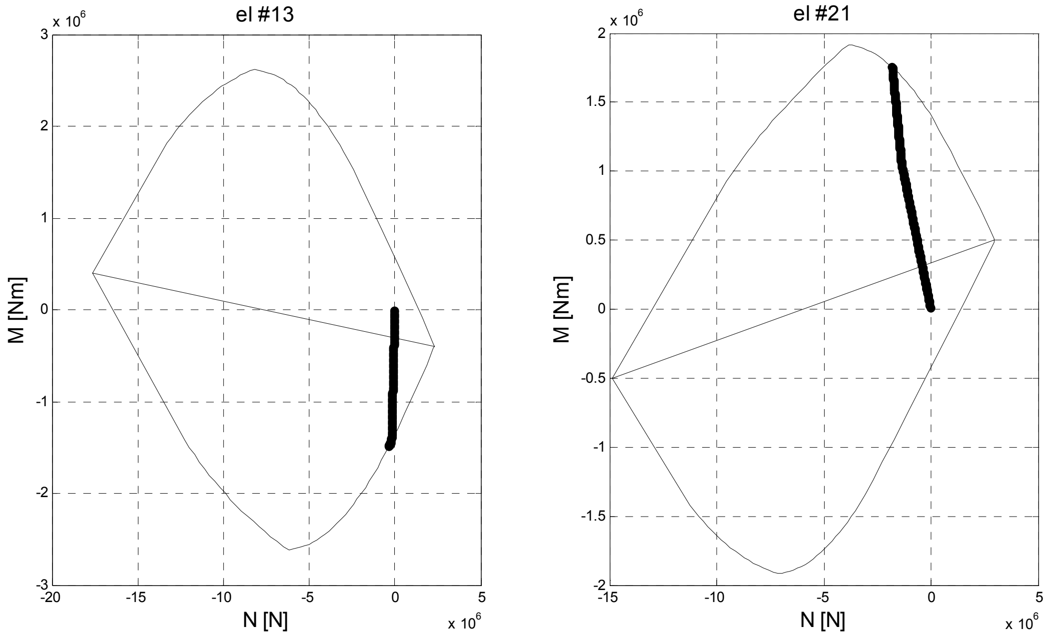

(a) (b)

Fig. 3.23 – *N*-*M* values assumed during the incremental analysis by potential plastic hinge sections with respect to N-M_u diagram.

3.5.3.2 Example 2: pipe loaded by self-weight and service load along the upper beam

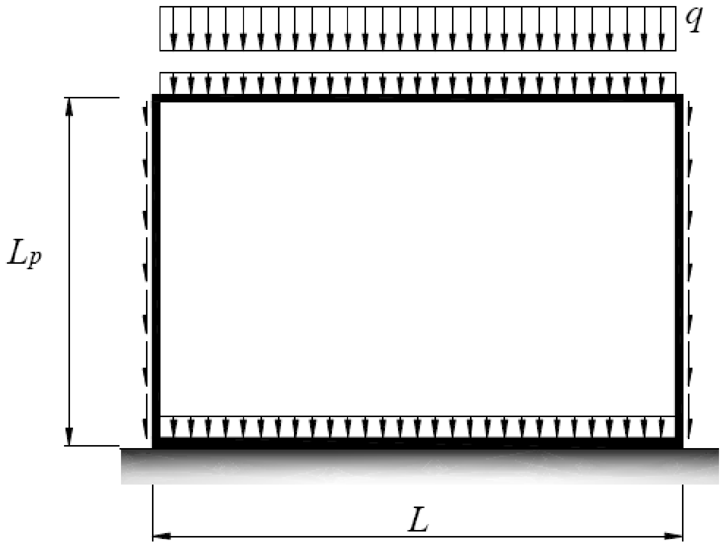

Fig. 3.24 – Pipe loaded by self-weight along and a distributed service load at top beam.

The second example takes into account the self-weight of the pipe elements and considers an increasing distributed load q on the top beam. In this case, the effect of self-weight is to increase the axial force of column elements, then, ultimate bending moments may be quite different with respect to the previous example. However, similarly to the previous example, a local collapse mechanism for the top beam is obtained (Fig. 3.21). The ultimate load of the structure turns out to be equal to:

$$q_{u,2} = 359 \text{ kN/m}, \tag{3.22}$$

which is smaller (68%) with respect to the limit load that may be determined for a portal frame with clamped column bases with the same collapse mechanism:

$$q_{\lim,2} = 528 \text{ kN/m}. \tag{3.23}$$

In this case, for $q = 0$, displacement at top beam midpoint is nonzero due to the effect of the self-weight (Fig. 3.28), then the first plastic hinge formation is characterized by $q = 234$ kN/m and $d = 0.012$ m. The second and third plastic hinge are formed with $q = 359$ kN/m and $d = 0.027$ m.

Figs. 3.30a and b show the bending moment variation as function of axial force for the two potential plastic hinge sections activated by the incremental analysis. *N-M* diagrams are quite similar to the ones obtained for the previous example; then, self-weight does not influence significantly the behaviour of the plastic hinges, but it reduces the ultimate load of the structure with respect to the previous example.

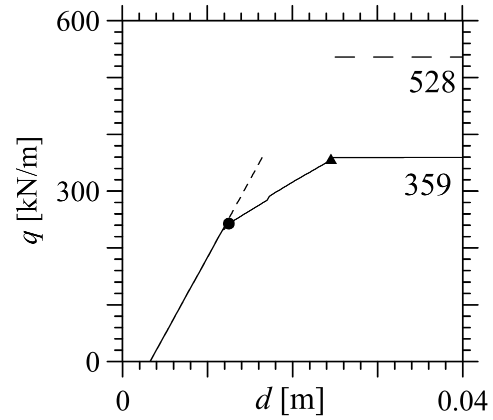

Fig. 3.25 – Load-deflection curve representing the incremental analysis of a pipe loaded by self-weight and by an increasing distributed force at top beam.

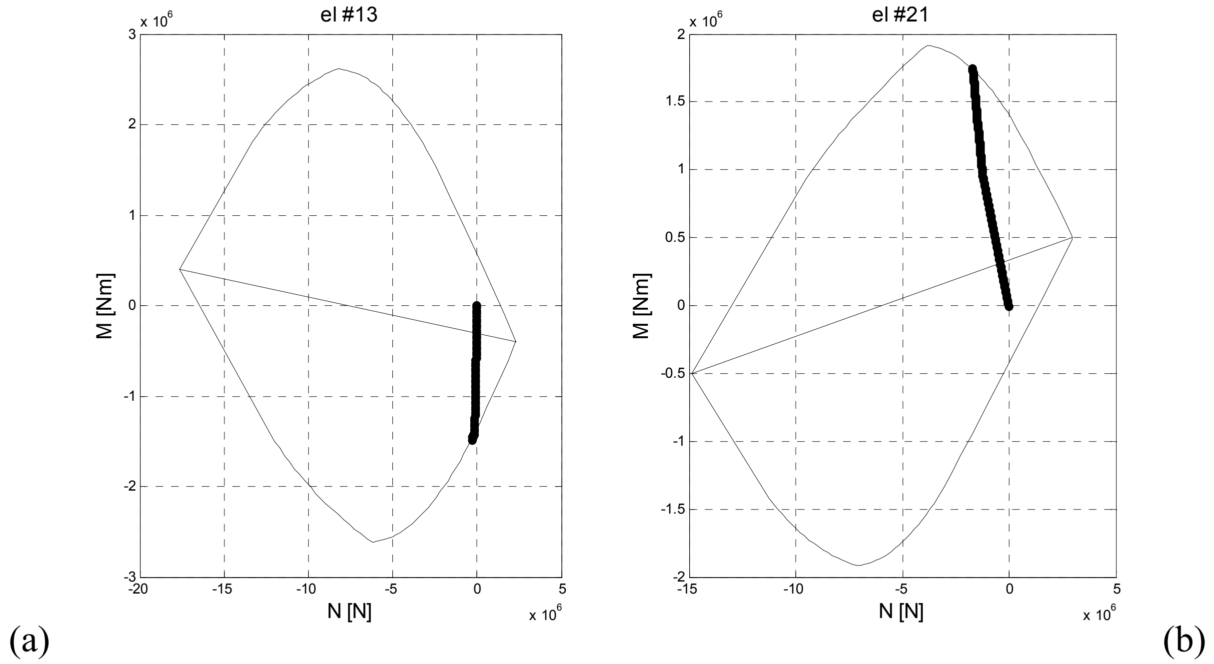

Fig. 3.26 – *N*-*M* values assumed during the incremental analysis by potential plastic hinge sections with respect to *N*-M_u diagram.

3.5.3.3 Example 3: pipe loaded by dead loads and increasing service loads

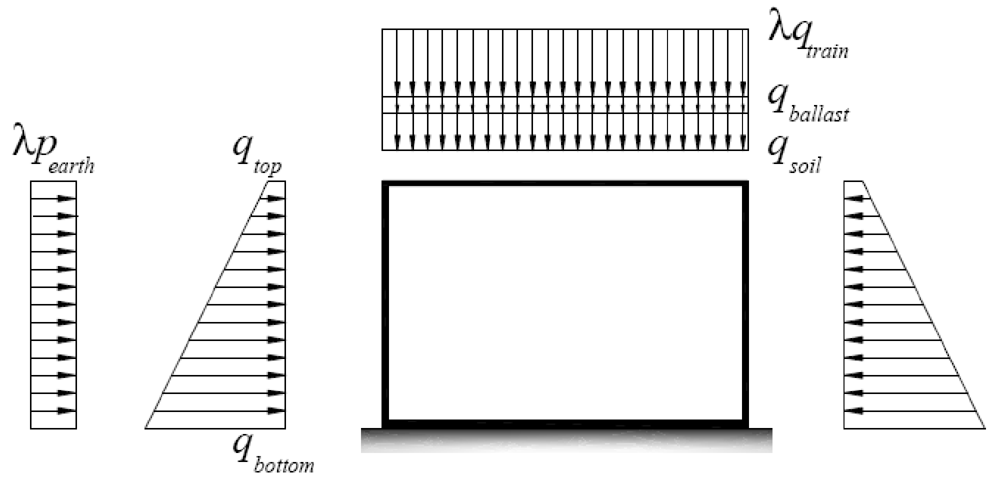

Fig. 3.27 – Pipe loaded by design loads along and a distributed service load at top beam.

This example takes into account the self-weight of pipe elements, the vertical distributed loads on the upper beam due to soil and ballast and the corresponding lateral earth pressures acting on both columns. Then, the example considers an increasing distributed load λ q_{train} on the top beam and the corresponding increasing lateral load λ p_{earth} along the left column. With reference to the FE discretization of the pipe (Fig. 3.19), the trapezoidal lateral load due to earth pressure is discretized by a piecewise constant load.

For $\lambda = 0$, displacement at top beam midpoint is nonzero ($d = 0.013$ m) due to the effect of the dead weights G_k and the corresponding soil pressures, then the first plastic hinge is obtained at the top of the right column (element #27, end 2) with $\lambda = 3.18$ and $d = 0.077$ m (triangle in Fig. 3.28). However, after the formation of the first plastic hinge, the slope of load-displacement curve does not change significantly. The second plastic hinge is localised at the top beam midpoint (element #13, end 2 and element #14, end 1) with $\lambda = 3.45$ and $d = 0.082$ m (dot in Fig. 3.28). After the formation of the second plastic hinge, the slope of load-deflection curve is quite lower than before. The third and fourth plastic hinges are triggered almost at the same step of the analysis, at foundation midpoint and at the top of the left column. Then, a collapse mechanism for the top beam is obtained and the ultimate load multiplier is $\lambda_u = 3.99$, with $d = 0.102$ m (cross in Fig. 3.28).

The collapse mechanism is characterized by three aligned plastic hinges along top beam (Fig. 3.21), even if plastic hinges are obtained at the top of the columns. This mechanism allows to determine an upper bound for the ultimate load, considering a portal frame with fixed column bases. The upper bound turn out to be $\lambda_{lim} = 5.70$, which is larger than λ_u due to the soft soil support.

Fig. 3.29 shows the deformed mesh of the discrete model of the pipe during incremental analysis.

Figs. 3.30a-d show the bending moment variation as function of axial force for the potential plastic hinge sections activated by the incremental analysis.

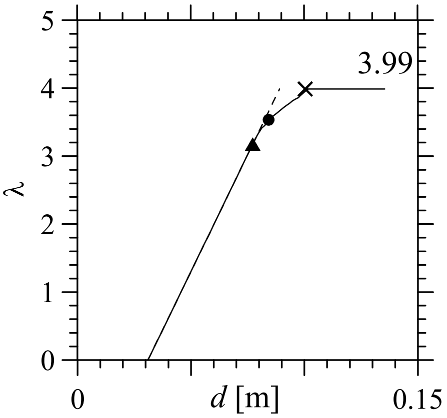

Fig. 3.28 – Load-deflection curve representing the incremental analysis of a pipe loaded by self-weight and by an increasing distributed force at top beam.

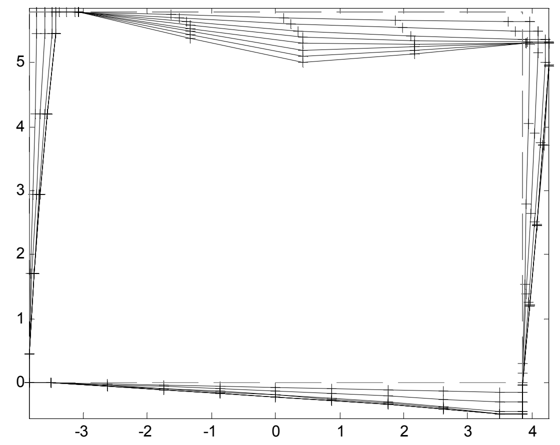

Fig. 3.29 – Pipe deformation during incremental analysis.

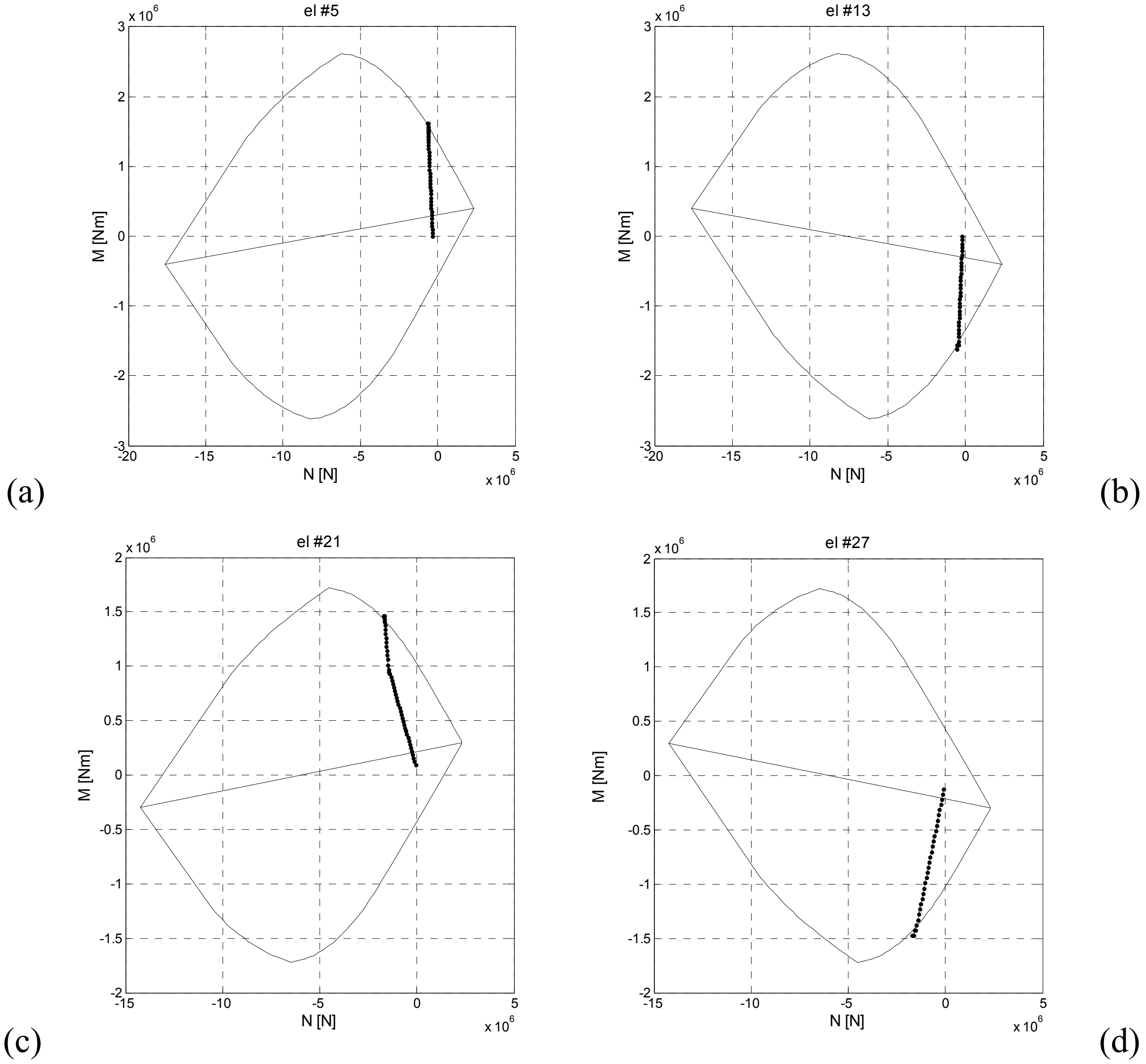

Fig. 3.30 – *N*-*M* values assumed during the incremental analysis by potential plastic hinge sections with respect to N-M_u diagram.

Axial forces turn out to be very small for the plastic hinge sections at top beam and foundation midpoint (Figs. 3.30a,b), whereas plastic hinge sections at the top of the columns (Figs. 3.30c,d) are characterized by increasing compressive forces. Moreover, a slope variation in *N-M* curve due to the first and second plastic hinges development is clearly shown in Fig. 3.30c for the last plastic hinge section.

4 Static and buckling analysis of beams resting on 3D elastic half-space

4.1 Introduction

In this chapter, static and buckling analyses of beams on a three dimensional (3D) half-space are considered. Analysis of beams on three dimensional half space is particularly important in the civil engineering field. Shallow foundations in the form of beams are usually adopted in ordinary structures.

The early studies of Boussinesq (1885) and Cerruti (1882) defined the potential of an elastic and isotropic 3D half-space. Starting from such potential, the expressions of stresses and displacements generated by a concentrated force on half-space surface can be determined (Johnson 1985). Analyses related to the determination of displacements generated by various force distributions on the surface of the half space have been carried out by many researchers. Love (1929) determined surface displacements due to a uniform pressure over a rectangular area. The indentation of a rigid punch on the half-space represents another problem which involves Boussinesq's solution. This problem is strictly related to the determination of the dynamic stiffness of a rectangular foundation and it is also a classical problem in physics, since its solution represents the charge density of a thin electrified plate. Many researchers determined the solution of this problem by adopting different approaches such as power series or the boundary element method (Rvachev 1959; Gorbunov-Posadov and Serebrjanyi 1961; Borodachev 1976; Brothers 1977; Mullan et al. 1980; Dempsey and Li 1989; Bosakov 2003).

The static analysis of beams on 3D half space was considered for the first time by Biot (1937), who studied a Euler-Bernoulli (E-B) beam of infinite length resting on an elastic half-space adopting Fourier integrals. Gorbuonov-Possadov (1961), together with the indentation problem, studied E-B beams of infinite and finite length on elastic half space adopting the power series method. Barden (1965) studied E-B beams of finite length on elastic half-space adopting power series and compared results with experimental data. Then, Vesic (1961) solved the same problem introduced by Biot and considered the case of an infinite beam loaded by a concentrated load and a couple, determining a relation between half-space elastic parameters and Winkler subgrade constant.

In this chapter, the Galerkin boundary element method is adopted for the determination of surface displacements and/or pressures generated by different loads/imposed displacement. Moreover, a mixed formulation which assumes as independent fields both surface pressures and displacements is considered and a piecewise constant function is adopted for discretizing surface pressures and displacements. Then, the case of a foundation beam on elastic half-space is considered by assuming as independent fields both foundation displacement and surface pressure. A Finite Element (FE) model is derived for the static and buckling analysis of a foundation beam resting on elastic half-space. Numerical results are obtained by using “modified” Hermitian shape functions (Minghini et al. 2007) for the beam and constant pressures for the soil. The parameter αL introduced for the beam on half-plane, which takes into account both beam slenderness and half-space stiffness, is modified to describe the problem at hand taking into account the ratio between beam length and cross-section width. Static analysis results are compared with analytic solutions and buckling analysis results turn out to be quite similar to the ones obtained for the beam on half-plane and Winkler half-space.

4.2 Half space model

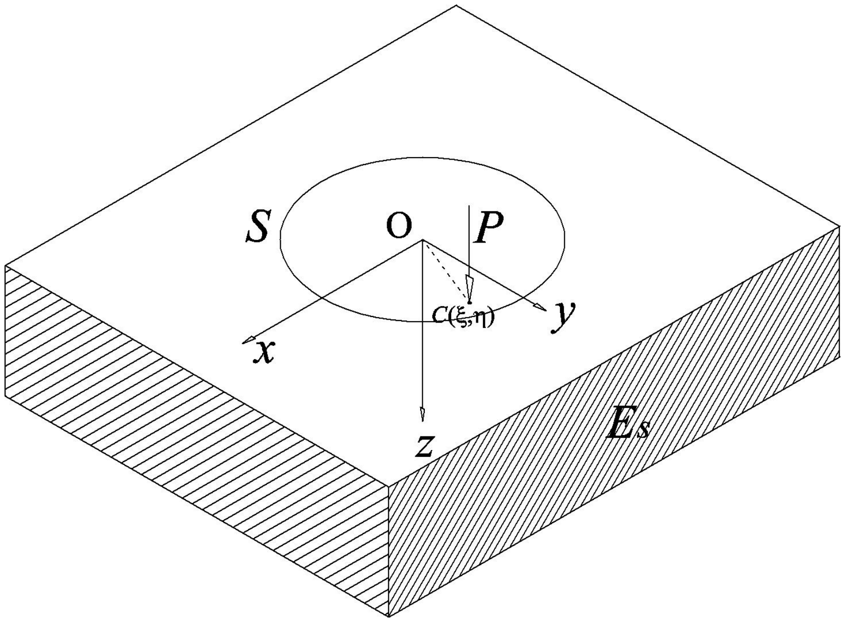

Fig. 4.1 – Half space subject to a concentrated vertical force.

A three-dimensional half space characterized by elastic modulus E_s and Poisson's ratio ν_s is considered. The half-space (Fig. 4.1) is referred to a Cartesian coordinate system (O; x, y, z), where z is directed downward; then $z = 0$ represents the surface of the half-space. A generic area S is considered on the surface $z = 0$, which can be loaded by various kinds of pressure distributions; in the following, only a (vertical) normal pressure $r(x, y)$ is considered.

The classic approach for finding stresses and displacements in an elastic half-space due to surface forces was studied by Boussinesq (1885) and Cerruti (1882) by adopting the theory of potential. In the following expression is presented the vertical displacement $v(x, y)$ of the surface, under the action of a normal pressure $r(\xi, \eta)$.

$$v = \int_S g(x,y,\xi,\eta)\; r(\xi,\eta)\, dA \tag{4.1}$$

S is the loaded area and $g(x, y;\ \xi, \eta)$ is the solution for the vertical displacements due to a unitary normal force applied in a generic point C(ξ, η) (Johnson 1985):

$$g(x,y;\xi,\eta) = \frac{1-\nu_s^2}{\pi E_s} \frac{1}{d(x,y,\xi,\eta)}, \tag{4.2}$$

where $d = [(x - \xi)^2 + (y - \eta)^2]^{1/2}$ represents the distance of point C from the origin.

The deformed surface generated by a unitary normal force is a hyperboloid, which is infinite at the origin and it is asymptotic to the undeformed surface $z = 0$ at a large distance from the origin.

The solutions of simple problems such as the determination of the displacements due to constant pressures applied to regular areas (rectangular), or vice-versa the determination of the surface pressures generated by known displacements, may be determined analytically starting from the expression of the displacement generated by a unitary normal force (Eq. 4.1). In the following examples, a rectangular area S is considered, $L1$ and $L2$ are the area length and width in x and y direction, respectively:

$$S = \{(\mathrm{x}, \mathrm{y}, \mathrm{z}): -L1/2 \leq x \leq L1/2, -L2/2 \leq y \leq L2/2, z = 0\} \tag{4.3}$$

4.3 Galerkin boundary element method

Many problems starting from Eq. 4.1 can not be solved analytically and, thus, numerical procedures may be adopted. To obtain a numerical solution of (Eq. 4.1), a Galerkin approach should be considered by introducing the bilinear form

$$B(r,\bar{r}) = B(\bar{r},r) = \int_S \int_S g(x,y,\xi,\eta)\ r(\xi,\eta)\bar{r}(x,y)\, dA\, dA \tag{4.4}$$

and the inner product

$$(v,\bar{r}) = \int_S v(x,y)\ \bar{r}(x,y) dA\,. \tag{4.5}$$

The weak form of Eq. 4.1 can be written as

$$(v,\bar{r}) = B(r,\bar{r}) \tag{4.6}$$

The simplest Galerkin discretization is adopted, the soil area S may be divided into elements of generic shape (triangles, rectangles); in the following, the rectangles with length h_{xi} and height h_{yi} are assumed together with the piecewise constant base function:

$$\rho_i(x,y) = \begin{cases} 1 & \text{on the } i\text{th element} \\ 0 & \text{elsewhere on } S \end{cases} \tag{4.7}$$

Hence, the soil reaction and the vertical displacement for each ith element can be approximated as

$$r(x,y) = [\rho(x,y)]^{\mathrm{T}}\mathbf{r}_i \tag{4.8}$$

$$v(x,y) = [\rho(x,y)]^{\mathrm{T}}\mathbf{q}_i\,, \tag{4.9}$$

where $\mathbf{r}_i$ and $\mathbf{q}_i$ denote the vector components of soil reaction and vertical displacements. Each component $\mathbf{q}_i$ is lumped at the centre of the corresponding ith surface element.

Substituting Eqs. 4.8 and 4.9 into Eq. 4.6, the weak problem written in discrete form takes the following expression:

$$\mathbf{H}\mathbf{q} = \mathbf{G}\mathbf{r}\,, \tag{4.10}$$

which describes a mixed problem, where displacements **q** can be prescribed and pressures **r** have to be determined, or vice-versa. The components of matrices **H** and **G** are:

$$h_{ij} = \int_{y_i}^{y_{i+1}}\int_{x_i}^{x_{i+1}} \rho_i\,\rho_j\,\mathrm{d}x\,\mathrm{d}y = \begin{cases} (x_{i+1}-x_i)(y_{i+1}-y_i) & i=j \\ 0 & i\neq j \end{cases} \tag{4.11}$$

$$g_{ij} = -\frac{(1-\nu_s^2)}{\pi E_s}\int_{y_i}^{y_{i+1}}\int_{x_i}^{x_{i+1}} \rho_i\,\mathrm{d}x\,\mathrm{d}y \int_{\eta_j}^{\eta_{j+1}}\int_{\xi_j}^{\xi_{j+1}} \frac{\rho_j}{d(x,y;\xi,\eta)}\mathrm{d}\xi\,\mathrm{d}\eta\,. \tag{4.12}$$

Where $(x_i, x_{i+1}; y_i, y_{i+1})$ are the (global) coordinates of the i_{th} surface element and $(\xi_i, \xi_{i+1}; \eta_i, \eta_{i+1})$ are the coordinates of the j_{th} surface element. It is obvious that **H** matrix turns out to be equal to a diagonal matrix, whose elements represent the area of each surface sub-element, whereas the elements of matrix **G** are reported in appendix A5.

4.3.1 Surface discretization

The surface S is subdivided into quadrilateral elements and the simplest subdivision is obviously the regular mesh. Setting the number of elements n_x and

n_y in plane directions, each element length is $h_{xi} = L1/n_x$ and the corresponding width is $h_{yi} = L2/n_y$. However, it is well known that the solution of Eqs. 4.1, 4.4 and 4.5 in general exibit singular behaviour near the edges and corners of the rectangular surface S (Dauge 1988), then, a regular mesh may not be able to describe correctly surface displacements and/or reactions at surface edges and corners. In order to obtain accurate results, it is common to use power graded meshes (Erwin and Stephan 1992; Ainsworth et al. 2000; Graham and McLean 2006), which are characterized by a grading exponent $\beta \geq 1$. A generic dimensionless coordinate t, on the interval (0,1) is described by the following expression:

$$t_j = \begin{cases} \dfrac{1}{2}\left[\left(\dfrac{2j}{n}\right)^{\beta} - 1\right] & \text{for} \quad 0 \leq j \leq n/2 \\ -t_{n-j} & \text{for} \quad n/2 < j \leq n \end{cases} \tag{4.13}$$

where n is the number of points on the interval. For $\beta = 1$ the mesh turns out to be uniform, but as β increases, the points are more concentrated at the end of the interval. In the following table, some examples of power-graded meshes are shown. For simplicity, a square area having $L1 = L2 = 1$ is considered and the same number of subdivisions is adopted along x and y axes ($n_x = n_y = n$).

Considering the figures in Tab. 4.1, it is worth noting that for increasing β, the elements near surface edges and corners tend to be smaller and smaller, however, elements close to the origin tend to be bigger. Then, the exponent β in Eq. 4.13 has to be chosen in order to obtain accurate results both near surface edges and close to the origin.

N	4	8	16
$\beta = 1$	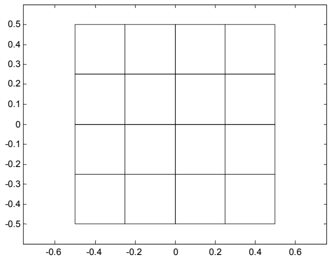	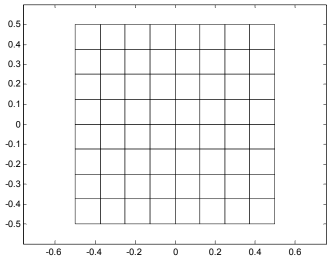	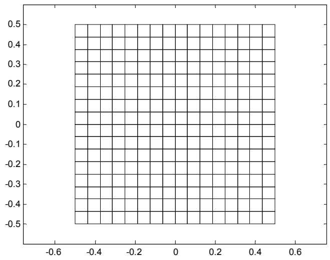
$\beta = 2$	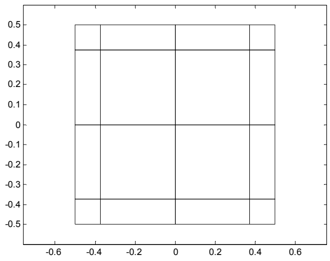	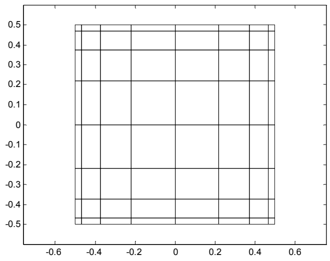	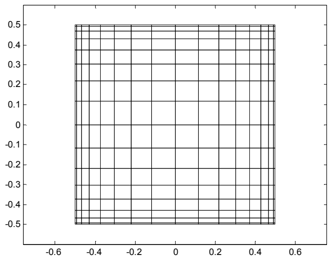
$\beta = 3$	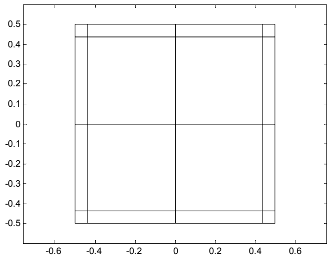	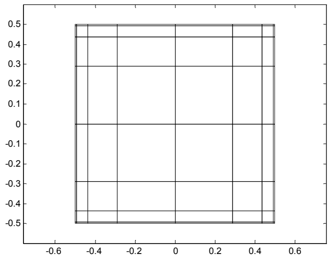	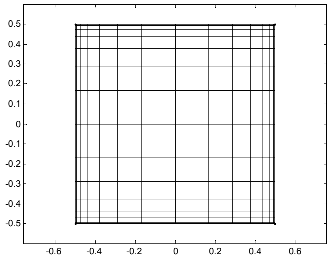
$\beta = 4$	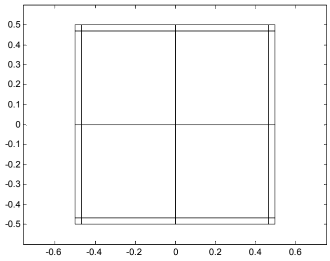	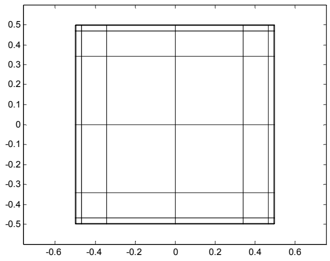	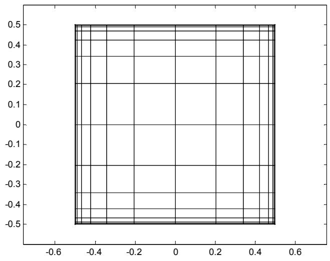

Tab. 4.1 – Examples of power-graded meshes applied to a square unitary area, varying *n* and β.

4.3.2 Rigid rectangular punch on elastic half-space

A typical problem which starts from Eq. 4.1 is related to the determination of the surface pressure generated by a well-defined displacement; in this case, a uniform vertical displacement is considered (Fig. 4.2). This problem is frequently studied in soil-structure interaction analysis and it can be also defined as the uniform indentation of an elastic half-space by a smooth rigid rectangular footing.

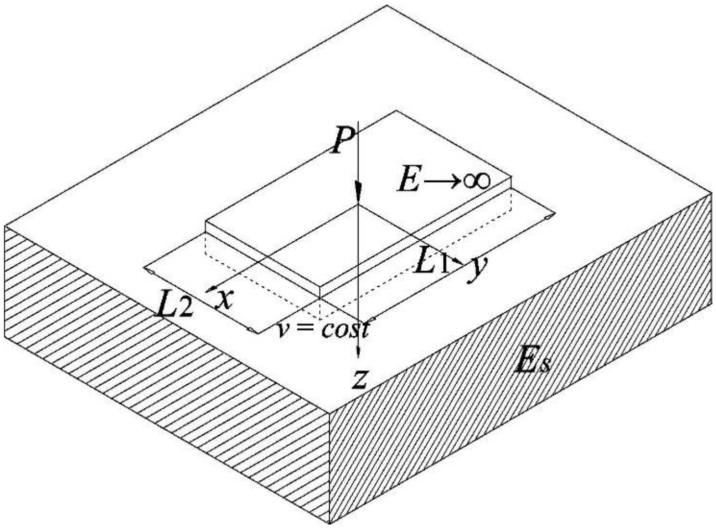

Fig. 4.2 – Rigid rectangular indenter on elastic half-space subject to a vertical uniform displacement.

Many researchers had already studied this problem by adopting different solution methods (Rvachev 1959; Noble 1960; Gorbunov-Posadov and Serebrjanyi 1961; Borodachev 1976; Brothers 1977; Mullan et al. 1980; Dempsey and Li 1989; Bosakov 2003). The determination of the solution of the integral equation considered (Eq. 4.1) is also a classical problem in physics and it represents the charge density of a thin, electrified plate *S* loaded by a given potential (Ervin et al. 1990; Ervin and Stephan 1992). This problem is also related to the determination of the dynamic stiffness of rigid foundations on elastic half-space (Pais and Kausel 1988; Dempsey and Li 1989; Guzina et al. 2006).

In the following, the problem of the indentation of a rigid punch is solved starting from Eq. 4.10 and considering different soil surface discretizations (varying β and increasing subdivision number along each side of the square).

Results in terms of surface pressures are presented and the resulting translational stiffness is evaluated.

Setting a uniform displacement value v_0, the corresponding vector $\mathbf{q}_v$ is defined by putting each vector element equal to v_0, then, from Eq. 4.10, the soil reaction vector is obtained:

$$\mathbf{r} = \mathbf{G}^{-1}\,\mathbf{H}\mathbf{q}_v \qquad (4.14)$$

Considering for simplicity the case of a square surface ($L1 = L2 = L$), Figs. 4.3a and b show dimensionless soil pressures $r/(E\ L)$ along x axis, obtained with n = 16 elements for each surface side and varying β ($E = E_s/(1-\nu_s^2)$). In Figs. 4.4a, b and c, dimensionless soil surface pressures $r/(E\ L)$ are shown by adopting a three-dimensional representation. It is clear that surface pressures assume a constant value quite close to the origin, whereas they increase rapidly in proximity of surface edges and corners. Results obtained with the uniform mesh are not able to represent correctly the behaviour at surface edges and corners, whereas increasing β, the values near surface corners increase rapidly.

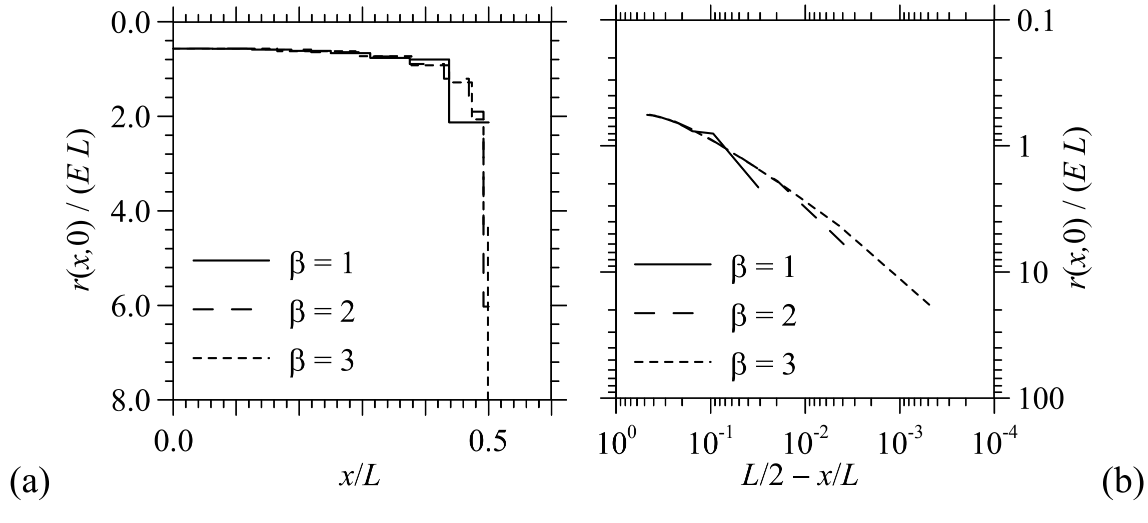

Fig. 4.3 – Dimensionless soil surface pressures along x axis.

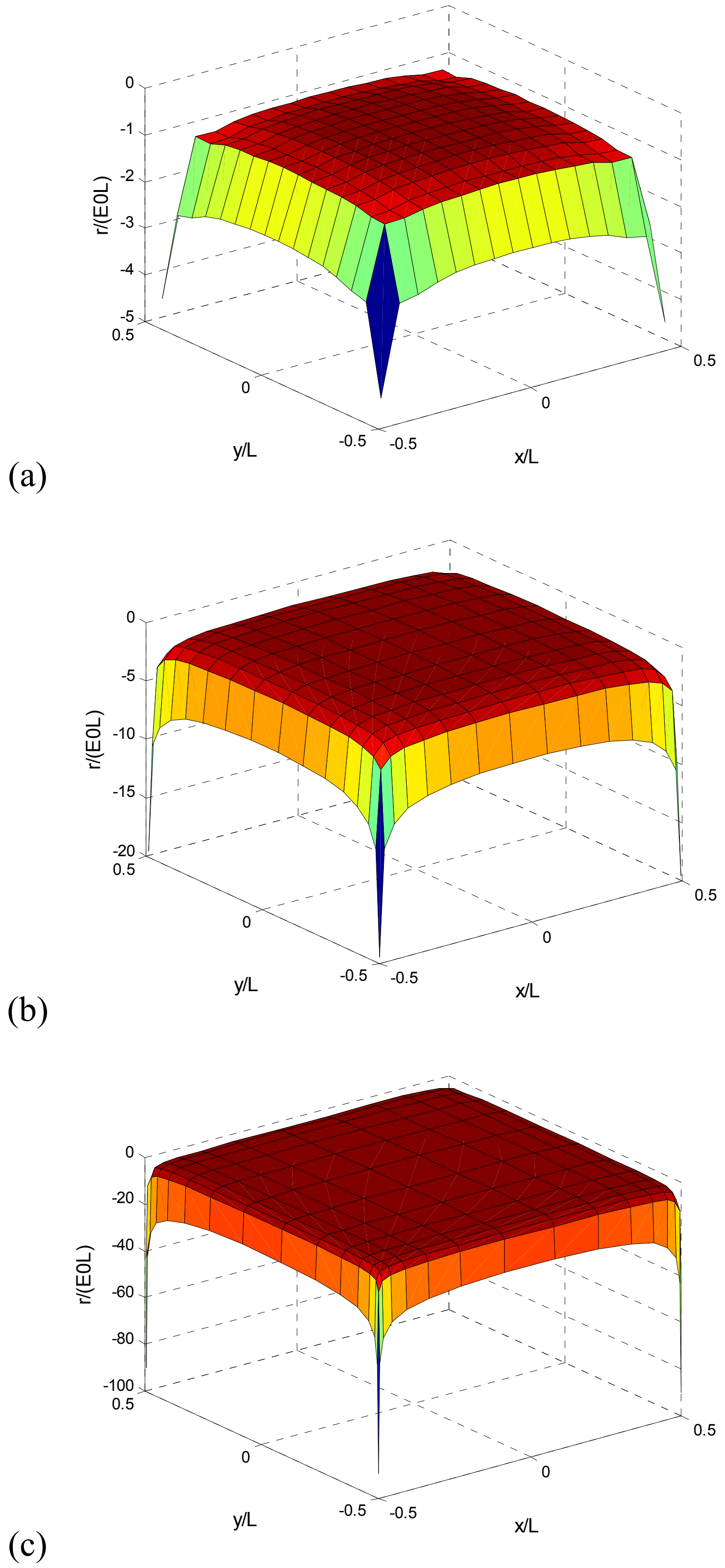

Fig. 4.4 – Dimensionless soil surface pressures due to a unitary vertical displacement of a square surface subdivided with a power graded mesh having 16 elements for each side and β = 1 (a), 2 (b) and 3 (c).

The forces F_i corresponding to soil pressures on each element are obtained by multiplying pressures and areas collected in the diagonal of **H**. The total force F generated by the uniform displacement v_0 is obtained by adding together the forces F_i and the soil stiffness k_v is obtained dividing the total force with respect to the uniform displacement.

$$\mathbf{H}\,\mathbf{r} = \mathbf{F} \tag{4.15a}$$

$$F = \sum_{i=1}^{n_{TOT}} F_i \tag{4.15b}$$

$$k_v = \frac{F}{v_0} \tag{4.15c}$$

Where $n_{TOT} = n_x \cdot n_y = n^2$ is the total number of soil surface elements.

The soil stiffness obtained for the square surface with $\beta = 4$ and $n_x = n_y = 2^7$ is considered as reference solution:

$$k_v^{REF} = 1.1523 \frac{E_s}{1-\nu_s^2} L\,, \tag{4.16}$$

Then, errors $\delta k_v = (k_v^{REF} - k_v)/k_v^{REF}$ are evaluated varying β and increasing the number of subdivisions along each side of the surface. Relative errors are shown in Figs. 4.5a and b varying $n_x = n_y$ and n_{TOT}, respectively.

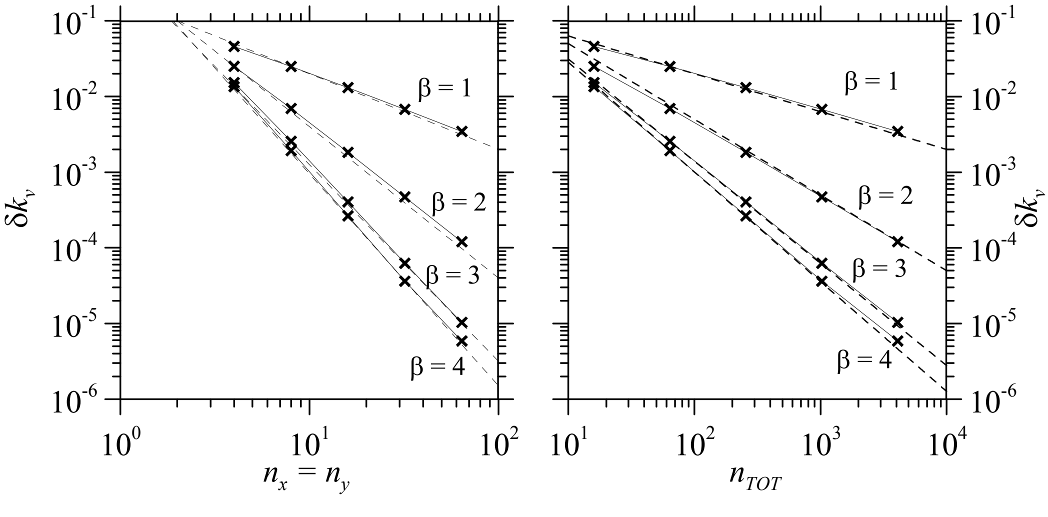

Fig. 4.5 – Relative errors for k_v, varying the number of subdivisions along each surface side (a) and varying the total number of sub-elements of the surface mesh (b).

Fig. 4.5b clearly shows that vertical stiffness converge with different converge rates varying β, in particular the results obtained with the uniform mesh converge to the reference solution with rates close to n^{-1} and $n_{TOT}^{-0.5}$, whereas rates are close to n^{-2} and $n_{TOT}^{-1.0}$ for β equal to 2. Convergence rates obtained with β equal to 3 ($n^{-2.7}$ and $n_{TOT}^{-1.35}$) turn out to be quite close to those obtained with β equal to 4 ($n^{-2.7}$ and $n_{TOT}^{-1.45}$). Moreover, for β = 3 and $n_x = n_x = 2^6$, relative error is less than 10^{-4} (10^{-2} %). Considering convergence tests shown in Figs. 4.5a and b, the soil surface discretization obtained with β = 3 can be considered the most effective with respect to other cases; in particular the case β = 4 does not increase significantly the results accuracy, but generates big sub-elements close to the origin of the surface.

Author	Method	$k_v/(E\,L)$
Present analysis	BEM	1.152
Guzina et al. 2006	BEM	1.152
Bosakov 2003	Orthogonal polynomials	1.146
Erwin, Stephan, Abou El-Seoud 1990	BEM	1.152
Dempsey and Li 1989	Numerical integration	1.152
Pais and Kausel 1988	-	1.175
Whitman and Richart 1967	-	1.080
Gorbunov and Posadov 1961	Power series	1.095

Tab. 4.2 – Stiffness values for square foundation $E = E_s / (1-\nu_s^2)$.

Soil stiffness due to a uniform vertical displacement of a rigid square punch (Eq. 4.16) is compared with similar results that can be found in literature. Tab. 4.2

shows values of k_v obtained by different researchers and by adopting various methods of solution. The soil stiffness obtained with the present model is close to the results proposed by Dempsey and Li (1989), Ervin et al. (1990) and Guzina et altri (2006). Dempsey and Li (1988) used numerical integration with Gauss quadrature adopting an adaptive discretization of the surface, whereas Ervin et al (1990) and Guzina et al. (2006) adopted the boundary element method (BEM).

Applying Rayleigh (1926) considerations, it is worth noting that the vertical stiffness value may be delimited by an upper and lower bound:

$$\frac{2}{\sqrt{\pi}} < k_v \frac{1-\nu_s^2}{E_s\, L} < \sqrt{2} \quad \rightarrow \quad 1.1284 < 1.1523 < 1.4142. \tag{4.17}$$

Where the lower bound represents the stiffness of a circle having the same area of the square and the upper bound is the stiffness of the circle circumscribed to the square area.

Then, the present model can be considered effective and can be applied to other examples and, in particular, it can be coupled with traditional finite elements representing a foundation beam and/or plate.

Another problem, similar to the one described in the previous paragraph, consists in the evaluation of the rotational stiffness with respect to the *x* axis of a rigid square punch on elastic half-space.

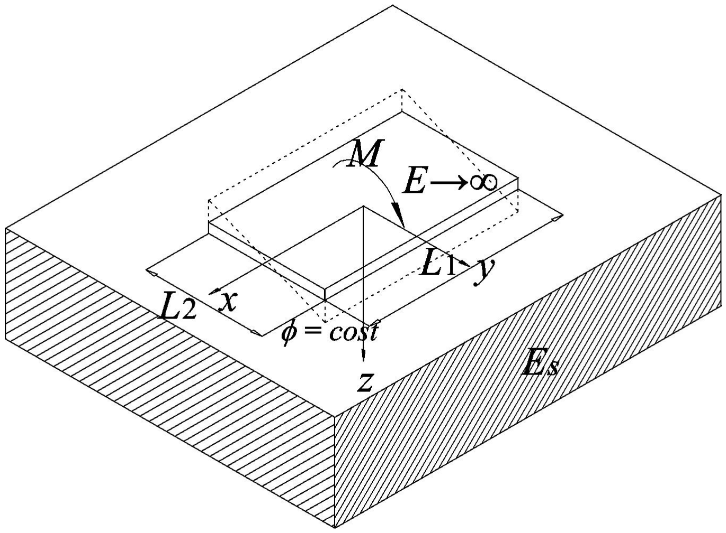

Fig. 4.6 – Rigid rectangular indenter on elastic half-space subject to a rotation along *x* axis.

In this case, a rotation value ϕ_x is defined and the corresponding displacement vector $\mathbf{q}_{\phi x}$ is created. The components of $\mathbf{q}_{\phi x}$ are obviously defined by $q_{\phi xi} = \phi_x \cdot y_i$. Eq. 4.15a gives surface pressures again; in this case the total moment with respect to *x* axis needs to be evaluated and the rotational stiffness can be easily obtained:

$$M_x = \sum_{i=1}^{n_{TOT}} F_i \, y_i \tag{4.18a}$$

$$k_{\phi x} = \frac{M_x}{\phi_x} \tag{4.18b}$$

Similarly to the previous example, considering for simplicity *L*1 = *L*2 = *L*, the rotational stiffness obtained adopting β = 4 and $n_x = n_y = 2^7$ is considered as the reference solution:

$$k_{\phi x}^{REF} = 0.2601 \frac{Es}{1-\nu_s^2} L^2 , \tag{4.19}$$

then, errors $\delta k_{\phi x} = (k_{\phi x}^{REF} - k_{\phi x}) / k_{\phi x}^{REF}$ are evaluated varying β and increasing the number of subdivisions along each side of the surface. Relative errors are shown in Fig. 4.6a and b varying $n_x = n_y$ and n_{TOT}, respectively.

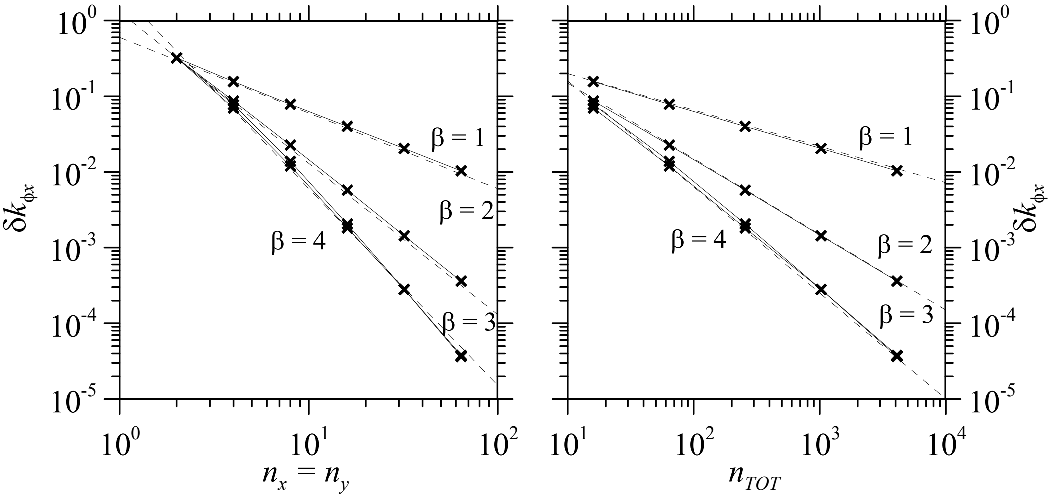

Fig. 4.7 – Relative errors for $k_{\phi x}$, varying the number of subdivisions along each surface side (a) and varying the total number of sub-elements of the surface mesh (b).

Fig. 4.6b clearly shows that vertical stiffness converge with different rates varying β and in particular that the results obtained with the uniform mesh converge to the reference solution with rates close to n^{-1} and $n_{TOT}^{-0.5}$ for β equal to 1, whereas rates are close to n^{-1} and $n_{TOT}^{-1.0}$, for β equal to 2. Convergence ratios obtained with β equal to 3 ($n^{-2.8}$ and $n_{TOT}^{-1.4}$,) turn out to be coincident with the one obtained with β equal to 4. Moreover, for β = 3 and $n_x = n_x = 2^6$, relative error is less than $5 \cdot 10^{-5}$. Then in this case, similarly to the previous example, the power graded mesh with β = 3 represents the best choice for the surface discretization.

Finally, varying $L1/L2$ ratio, the rectangular contact surfaces are considered and by applying Eqs. 4.14 and 4.15, the vertical soil stiffness and rotational soil stiffness can be evaluated. The results obtained with a power graded mesh characterized by β = 3 and $n_x = n_y = 2^6$ are shown in Fig. 4.8 with crosses, adopting the parameters defined in Eq. 4.20a, b, in order to compare results with the data determined by Lee (1963) and Whitman and Richart (1967). Similar results adopting power series were obtained also by Gorbunov and Posadov (1961). The present model turns out to be effective also for rectangular surfaces and the power graded mesh with β = 3 is sufficient to obtain accurate values.

$$\beta_v = \frac{F}{v_0}\frac{1-\nu_s^2}{E_s}\frac{1}{\sqrt{L1\,L2}}; \quad \beta_\varphi = \frac{M}{\varphi}\frac{1-\nu_s^2}{E_s}\frac{1}{L1\,L2^2} \qquad (4.20a, b)$$

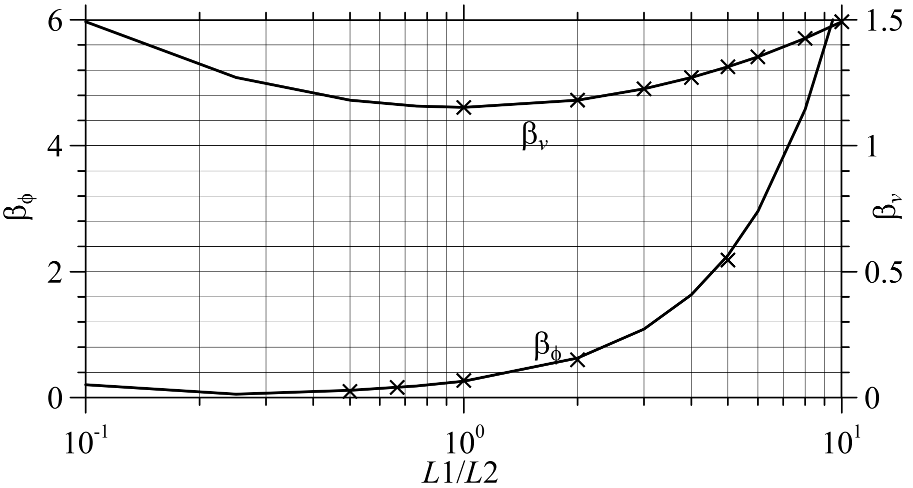

Fig. 4.8 – Vertical translational stiffness β_v and rotational stiffness β_ϕ of a rigid rectangular indenter on an elastic half space, varying $L1/L2$ ratio. Crosses for the present analysis, continuous lines for Whitman and Richart (1967) data.

4.3.3 Uniform pressure

Another problem which starts from Eq. 4.1 consists in the determination of the displacement generated by a uniform pressure *p* applied to a generic rectangular area (Fig. 4.9) having length 2*a* and width 2*b*.

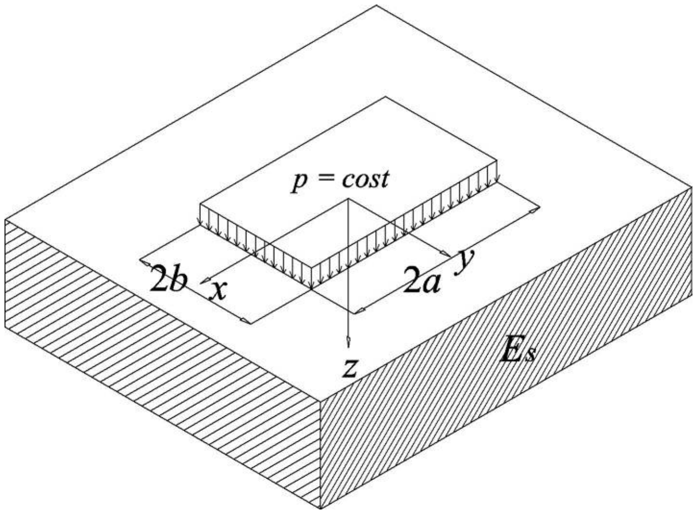

Fig. 4.9 – Elastic half-space loaded by a constant pressure *p* over a generic rectangular area.

The analytic solution was determined by Love (1929) and is given by the following expression, whereas Fig. 4.10 shows the dimensionless surface displacement for the case of a square loaded area ($a = b = 1$):

$$\begin{aligned} v^*(x,y) = \frac{v(x,y)}{p}\frac{\pi E_s}{1-\nu_s^2} = (x+a)\ln&\left\{\frac{(y+b)+[(y+b)^2+(x+a)^2]^{1/2}}{(y-b)+[(y-b)^2+(x+a)^2]^{1/2}}\right\}+ \\ +(y+b)\ln&\left\{\frac{(x+a)+[(y+b)^2+(x+a)^2]^{1/2}}{(x-a)+[(y+b)^2+(x-a)^2]^{1/2}}\right\}+ \\ +(x-a)\ln&\left\{\frac{(y-b)+[(y-b)^2+(x-a)^2]^{1/2}}{(y+b)+[(y+b)^2+(x-a)^2]^{1/2}}\right\}+ \\ +(y-b)\ln&\left\{\frac{(x-a)+[(y-b)^2+(x-a)^2]^{1/2}}{(x+a)+[(y-b)^2+(x+a)^2]^{1/2}}\right\} \end{aligned} \quad (4.21)$$

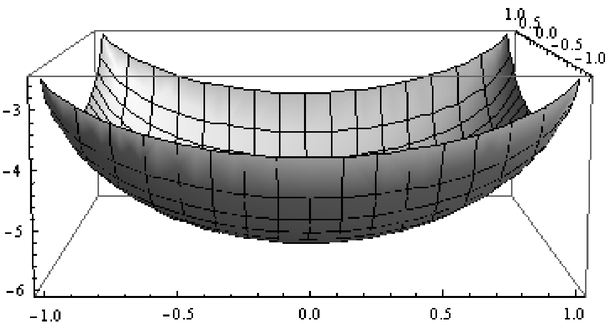

Fig. 4.10 – Surface deflection generated by a uniform unitary pressure on a square area with side equal to 2.

The solution can be determined numerically using Eq. 4.14. A surface pressure vector **p** is defined by setting each element equal to *p*, and from Eq. 4.14 the displacement vector can be easily determined:

$$\mathbf{q} = (\mathbf{H}^T)^{-1}\mathbf{G}\,\mathbf{p} \tag{4.22}$$

The matrix **H** of the present model is a diagonal matrix without null values along the diagonal, then $\mathbf{H}^T = \mathbf{H}$ and the $\mathbf{H}^{-1}$ is simple to calculate.

For simplicity, the case of a square loaded area is considered ($a = b$). Figs. 4.11a and b show the dimensionless displacement $v^*=v/(2a)$ along x axis and along the diagonal of the surface $\rho = (x^2 + y^2)^{0.5}$ for increasing β and assuming $n_x = n_y = 16$. Figs. 4.11a and b show that in this example the exponent β does not influence results significantly.

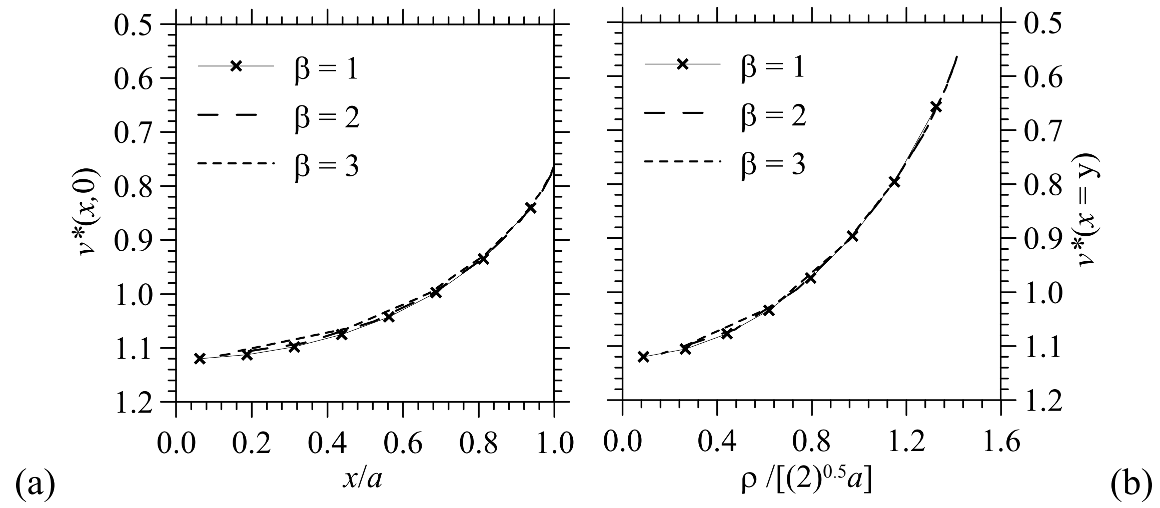

Fig. 4.11 – Dimensionless surface displacement along *x* axis (a) and along surface diagonal (b) due to a uniform pressure over a square area.

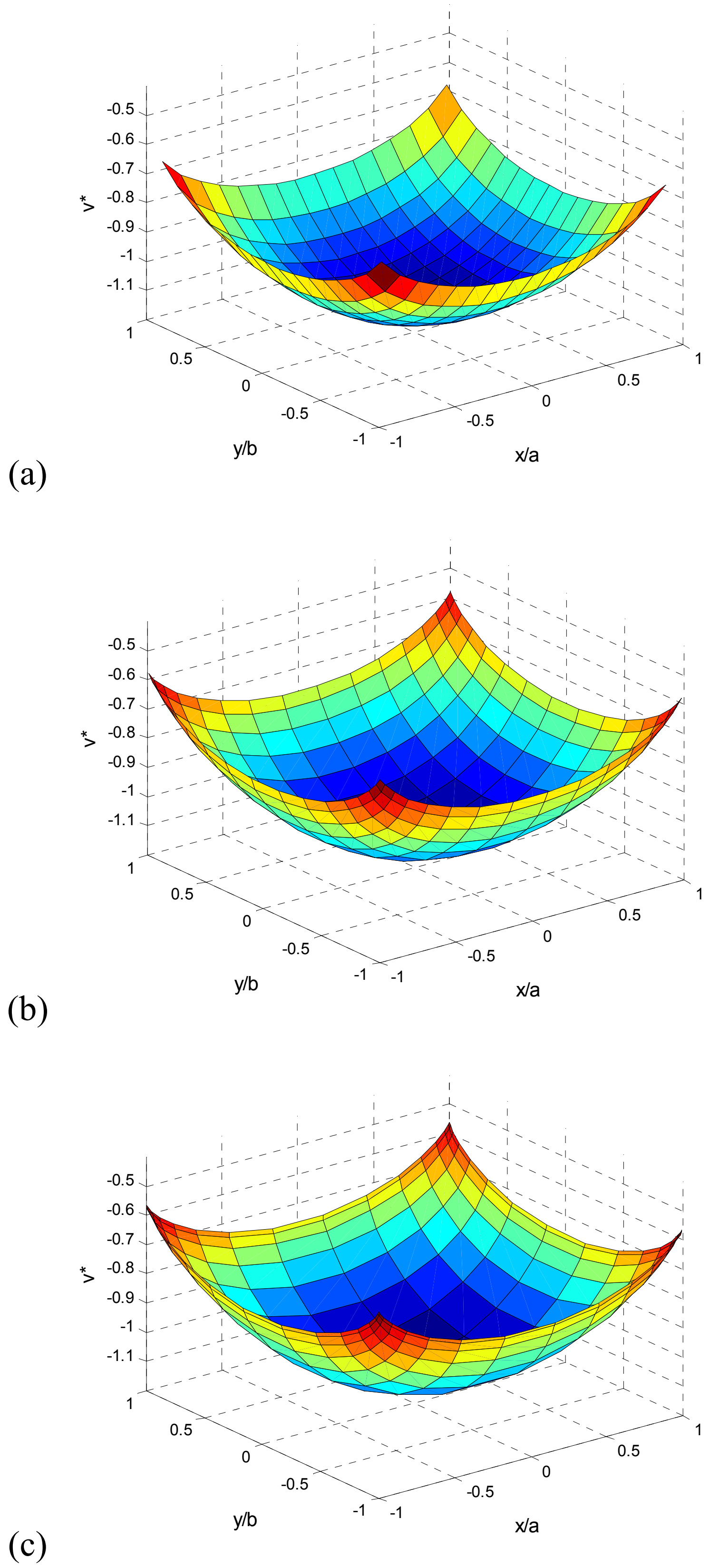

Fig. 4.12 – Dimensionless displacements generated by a uniform pressure over a square surface subdivided with a power graded mesh having 16 elements for each side and $\beta = 1$ (a), 2 (b) and 3 (c).

Figs. 4.12a, b and c show the dimensionless displacement adopting a three-dimensional representation and varying the grading exponent β. Then, dimensionless displacements are evaluated by adopting the present model at four points on the surface of the half-space. Results are compared with exact solution (Eq. 4.21) varying exponent β and increasing the number of subdivisions along each surface side. The first point O coincides with the origin of the coordinate system; the second one, M, is at the midpoint of the surface edge parallel to x axis; the third one, N, is at the midpoint of the surface edge parallel to y axis; and the last one, C, is at the upper-right corner of the surface. The four points are shown in Fig. 4.13. Considering a square surface, the displacements at points M and N are obviously coincident.

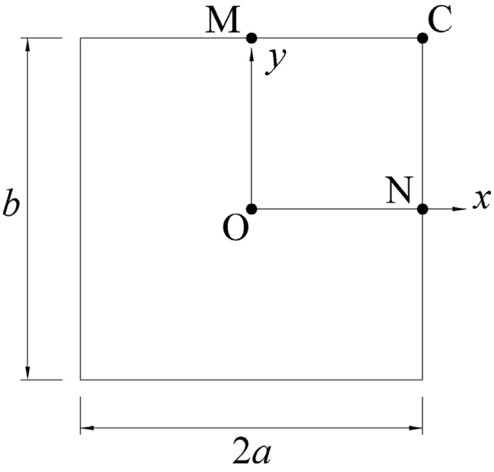

Fig. 4.13 – Points considered for the evaluation of surface displacements

Reference values (Eq. 4.21) are shown in the following expressions. It is worth noting that the adopted surface discretizations do not allow to evaluate displacements at the exact points described above since each displacement value is applied in the centre of the corresponding surface sub-element.

$$v^*(0,0) = v_{\mathrm{O}}^L = 1.122\,(2a) \tag{4.23a}$$

$$v^*(0,a) = v_M^L = 0.7659\,(2a) \tag{4.23b}$$

$$v^*(a,0) = v_N^L = 0.7659\,(2a) \tag{4.23c}$$

$$v^*(a,a) = v_C^L = 0.5611\,(2a) \tag{4.23d}$$

Relative errors $\delta v = (v^L - v^{PA}) / v^L$ for the four displacements in Eqs. 4.23 are calculated and shown in the following figures.

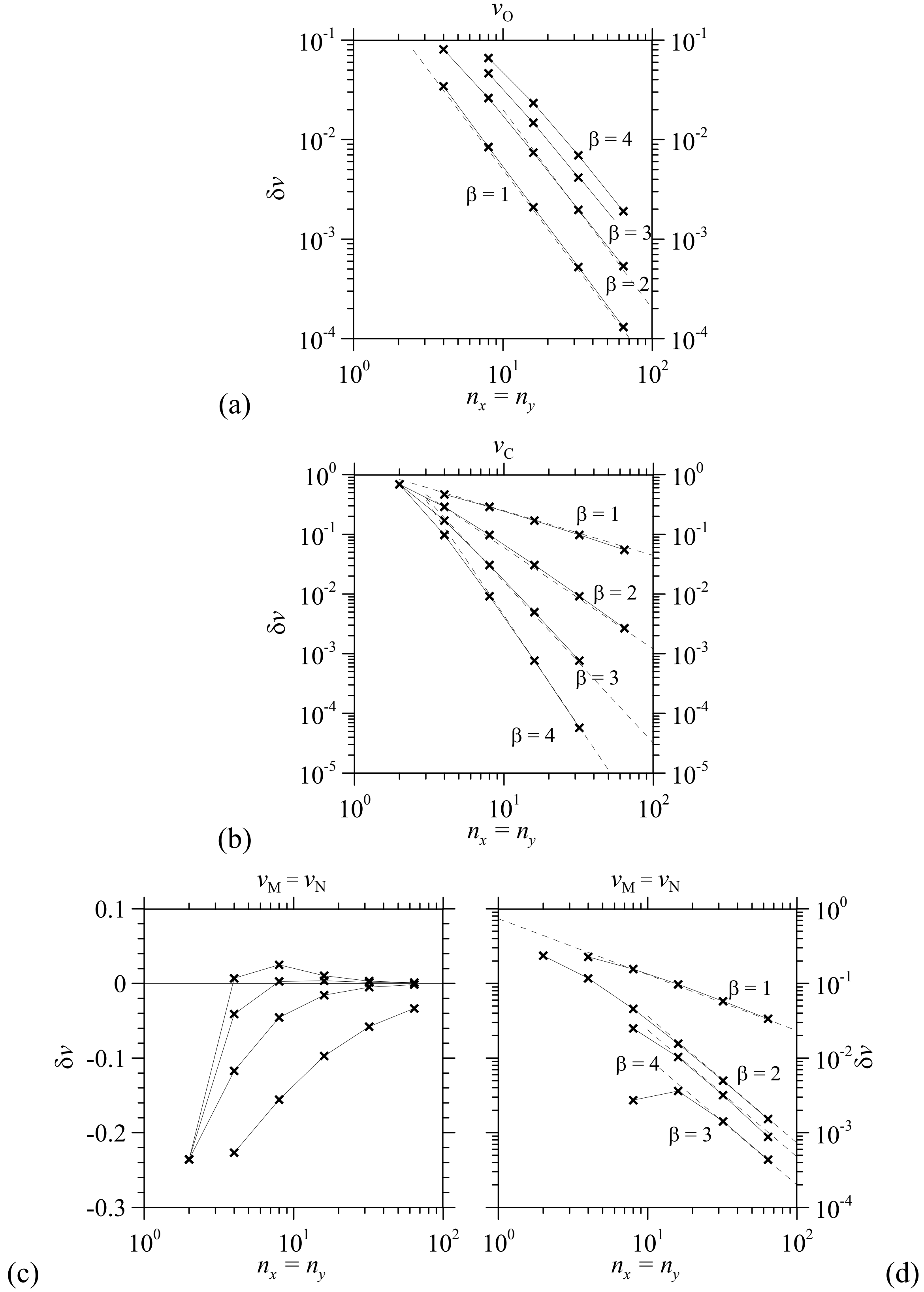

Fig. 4.14 – Relative errors for dimensionless displacements evaluated at points O (a), C (b) and M, N (c, d).

Fig. 4.14a show the relative errors for the displacement at surface origin. For all surface discretization cases considered, convergence ratios are coincident and close to n^{-2}, however relative errors are small for the uniform discretization case: for $n = 32$ and $\beta = 1$, relative error is close to 0.5%, whereas for $n = 16$ and $\beta = 3$, relative error is close to 4%. Considering the displacement at surface corner (Fig. 4.14b), relative errors follow a behaviour similar to the one found in the examples of the previous paragraph. Convergence ratios are small for $\beta = 1$ and 2 ($n^{-0.75}$ and $n^{-1.7}$, respectively), whereas for $\beta = 3$ and 4 convergence ratios are close to $n^{-2.7}$ and $n^{-3.7}$, respectively. For $n = 32$ and $\beta = 1$, relative error is close to 10%, whereas for $n = 16$ and $\beta = 3$, relative error is close to 0.8%. Figs. 4.14c and d show relative errors related to the displacement at surface edge midpoint M or N. In this case, errors for $\beta = 3$ and 4 do not have a monotonic behaviour, however, neglecting values for $n = 4$, errors can be represented in bi-logarithmic scale. Convergence ratio for $\beta = 1$ is close to $n^{-0.75}$, whereas for β equal to 2, 3 and 4 ratios are almost coincident and close to n^{-1}. For $\beta = 3$ errors are lower with respect to other discretization cases, then, the power graded mesh with $\beta = 3$ turns out to be quite effective also for this example.

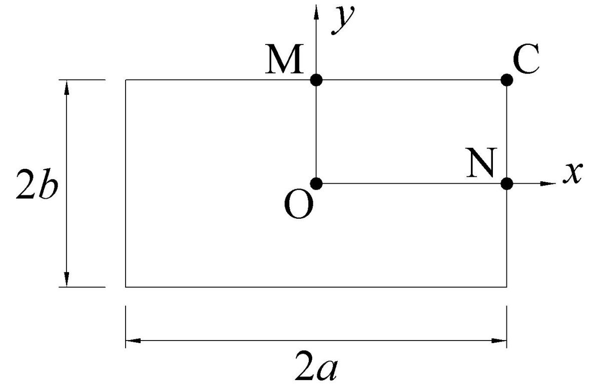

Fig. 4.15 – Rectangular surface.

Finally, adopting a surface discretization characterized by a power graded mesh with $\beta = 3$ and assuming $n_x = n_y = 64$, the rectangular surfaces loaded by a uniform pressure are considered and the results in terms of displacements at points O, M, N and C (Fig. 4.15) are shown in Fig. 4.16, varying a/b ratio. Moreover, results are compared following the representation defined by Giroud (1968) and show good agreement with respect to Love's solution (1929).

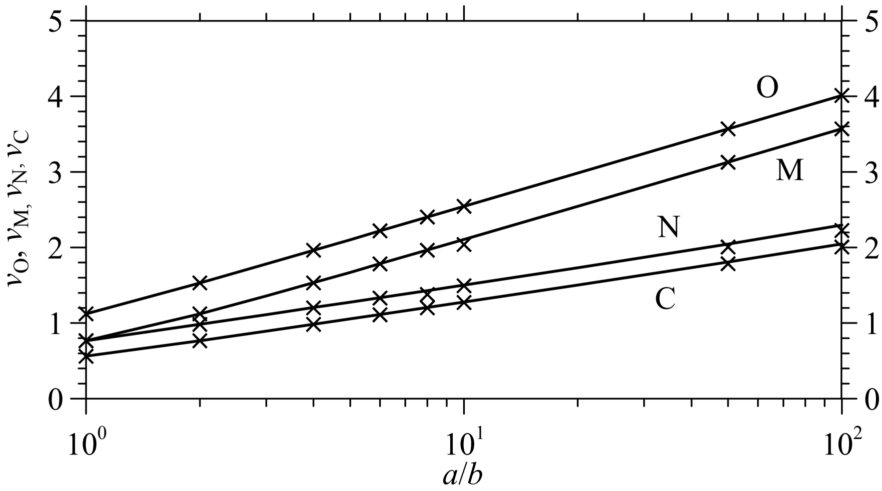

Fig. 4.16 – Vertical surface displacements beneath a rectangular area due to a uniform pressure, continuous lines for present analysis, crosses for Love’s solution.

4.4 Beam model

In the previous paragraph a boundary element method for studying problems related to vertical loads and forces applied to the surface of an elastic half-space has been presented. As it has been shown by Tullini and Tralli (2010) for a beam on elastic half-plane (2D), the most promising aspect of the present model relative to the half-space (3D) is the coupling of traditional FEs with the boundary integral equation representing the vertical displacement generated by a concentrated force acting on the surface of an elastic half-space.

The present model may be suitable to study 3D frames on elastic half-space, then, foundation beams may be subject to more complex deformations with respect to the case of the beam on elastic half-plane, where only Euler-Bernoulli and Timoshenko beams have been considered (Tullini and Tralli 2010). In order to take into account shear deformations due to both non-uniform bending and torsion, the kinematical model based on Timoshenko (1921) bending theory and Reissner (1952) torsion theory are adopted, following the model described by Minghini et al. (2008). The warping function is represented by the well known sectorial coordinate ω deriving from De Saint Venànt solution. Assuming linear elastic behaviour, the relationships between strain fields and stress resultants are obtained for beams with any given cross-section, showing that coupling terms between shear forces acting along the principal directions or between shear and non-uniform torsion may arise due to shear deformations. Then, local governing equations and relevant boundary conditions are deduced variationally from the elastic strain energy expression.

4.4.1 Analytical formulation

An ideal prismatic beam is shown in Fig. 4.1. An orthogonal, counter-clockwise, reference system C(x, y, z) is assumed, with the origin coinciding with the cross-section centroid. Axes x and y correspond to the principal axes of inertia where S stands for the cross-section (bending deformation) shear centre; hereinafter (b.d.) shear centre.

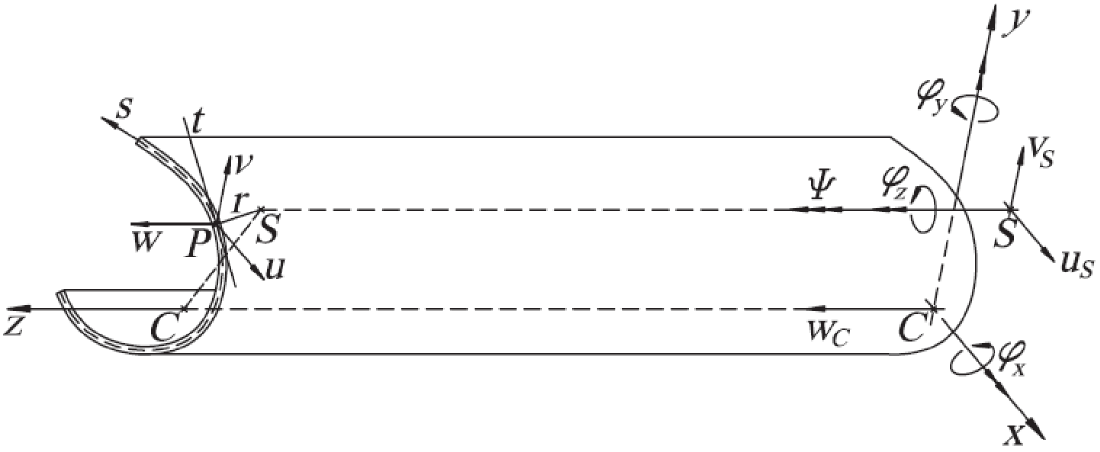

Fig. 4.17 – Global reference system for the beam.

4.4.1.1 Kinematical model

Assuming that cross-section in-plane deformations are negligible and reducing the beam to its middle surface, the geometrically-exact displacement field (Simo and Vu-Quoc 1991; Ibrahimbegovic 1993) may be determined by introducing the well-known matrix of finite rotations (Argyris 1982; Cristfield 1991). By developing a series expansion of the rotation matrix and retaining up to second-order terms, the displacement field can be approximated in the form:

$$\begin{aligned} u &= u^{(1)} + u^{(2)} \\ v &= v^{(1)} + v^{(2)} \\ w &= w^{(1)} + w^{(2)} \end{aligned} \tag{4.24}$$

where u, v, w are the displacement components at point P of the generic cross-section in x, y, and z directions, respectively. Moreover, apexes “(1)” and “(2)” indicate the first- and second-order components of the displacement field, respectively. As for the linear part of the kinematical model, Timoshenko-Reissner’s beam theory was adopted, having resorted to a single warping function. Shear deformations due to both non-uniform torsion and bending were considered. Moreover, following the proposal of Kim et al (1996) in order to analyze beams with asymmetric cross-sections, the coordinates of the (b.d.) shear centre with respect to the centroid were introduced into the displacement field by means of a proper coordinate transformation. Making the displacement field explicit, the first-order components may be written in the form:

$$\begin{aligned}
u^{(1)}(z,s) &= u_S(z) - \varphi_z(z)(y - y_S) \\
v^{(1)}(z,s) &= v_S(z) + \varphi_z(z)(x - x_S) \\
w^{(1)}(z,s) &= w_C(z) - x\varphi_y(z) + y\varphi_x(z) + \omega(s)\Psi(z)
\end{aligned} \tag{4.25}$$

whereas the second-order components are expressed by (Chang et al. 1996; Cortinez and Piovan 2006; Piovan and Cortinez 2007; Laudiero and Zaccaria 1988):

$$\begin{aligned}
u^{(2)}(z,s) &= \frac{1}{2}\left[-\left(\varphi_y^2(z) + \varphi_z^2(z)\right)x + \varphi_x(z)\varphi_y(z)y + \varphi_z^2(z)x_S\right] \\
v^{(2)}(z,s) &= \frac{1}{2}\left[\varphi_x(z)\varphi_y(z)x - \left(\varphi_x^2(z) + \varphi_z^2(z)\right)y + \varphi_z^2(z)y_S\right] \\
w^{(2)}(z,s) &= \frac{1}{2}\left[\varphi_x(z)\varphi_z(z)(x - x_S) + \varphi_y(z)\varphi_z(z)(y - y_S)\right]
\end{aligned} \tag{4.26}$$

where x_S and y_S are the (b.d.) shear centre co-ordinates; u_S and v_S are the (b.d.) shear centre displacements in x and y directions; w_C is the axial cross-section translation; φ_x and φ_y are the flexural rotations about x and y axes and, finally, φ_z represents the torsional rotation. Function $\Psi(z)$ in Eq. 4.25 defines the cross-section warping amplitude, whereas $\omega(s)$ represents the sectorial area defined by the relation (Vlasov 1961):

$$\frac{d\omega}{ds} - r = 0 \tag{4.27}$$

where r is the distance between the shear centre S (Fig. 4.1) and the tangent t to the middle line at point P.

By adopting the usual Lagrangian formulation, the strain components may be expressed in terms of Green's strain tensor, i.e.:

$$\varepsilon_{ij} = \varepsilon_{ij}^{(1)} + \varepsilon_{ij}^{(2)} \tag{4.28}$$

where $(i, j = x, y, z)$

$$\varepsilon_{ij}^{(1)} = \frac{1}{2}\left(u_{i,j}^{(1)} + u_{j,i}^{(1)}\right), \qquad \varepsilon_{ij}^{(2)} = \frac{1}{2}\left(u_{k,i}^{(1)}u_{k,j}^{(1)} + u_{i,j}^{(2)} + u_{j,i}^{(2)}\right) \tag{4.29a,b}$$

and the comma indicates partial differentiation with respect to Lagrangian coordinates (x, y, z).

Due to the assumption of cross-section in-plane undeformability, the non-vanishing strain components reduce to the axial strain ε_z and the shear strains γ_{zx} and γ_{zy}. By using Eq. 4.29 and neglecting third- and higher-order terms, the linear and non-linear parts of the strain field can respectively be written as:

$$\varepsilon_z^{(1)} = w'_C - x\varphi'_y + y\varphi'_x + \omega\Psi' \tag{4.30}$$

$$\gamma_{zx}^{(1)} = \left(u'_S - \varphi_y\right) + \frac{\partial\omega}{\partial x}\Psi - \varphi'_z\left(y - y_S\right) \tag{4.31}$$

$$\gamma_{zy}^{(1)} = \left(v'_S + \varphi_x\right) + \frac{\partial\omega}{\partial y}\Psi + \varphi'_z\left(x - x_S\right) \tag{4.32}$$

$$\begin{aligned}\varepsilon_z^{(2)} = {} & \frac{1}{2}\left[u'_S - \varphi'_z\left(y - y_S\right)\right]^2 + \frac{1}{2}\left[v'_S + \varphi'_z\left(x - x_S\right)\right]^2 \\ & + \frac{1}{2}\left[\left(x - x_S\right)\left(\varphi'_x\varphi_z + \varphi_x\varphi'_z\right) + \left(y - y_S\right)\left(\varphi'_y\varphi_z + \varphi_y\varphi'_z\right)\right]^2\end{aligned} \tag{4.33}$$

$$\begin{aligned}\gamma_{zx}^{(2)} = {} & \varphi_z\left[v'_S + \varphi'_z\left(x - x_S\right)\right] + \frac{1}{2}\varphi_x\varphi_z - \left(\varphi_y\varphi'_y + \varphi_z\varphi'_z\right)x + \\ & + \frac{1}{2}\left(\varphi'_x\varphi_y + \varphi_x\varphi'_y\right)y + \varphi_z\varphi'_z x_S\end{aligned} \tag{4.34}$$

$$\begin{aligned}\gamma_{zy}^{(2)} = {} & -\varphi_z\left[u'_S - \varphi'_z\left(y - y_S\right)\right] + \frac{1}{2}\varphi_y\varphi_z + \\ & + \frac{1}{2}\left(\varphi'_x\varphi_y + \varphi_x\varphi'_y\right)x - \left(\varphi_x\varphi'_x + \varphi_z\varphi'_z\right)y + \varphi_z\varphi'_z y_S\end{aligned} \tag{4.35}$$

where prime denotes derivative with respect to z. Due to the assumption of small strains involving derivative of axial displacement w, terms $\frac{\partial w}{\partial x}\frac{\partial w}{\partial z}$, $\frac{\partial w}{\partial y}\frac{\partial w}{\partial z}$ and $\left(\frac{\partial w}{\partial z}\right)^2$ provided by Eq. 4.29-b were ignored in evaluating the non-linear components (Eqs. 4.33, 4.34 and 4.35) of the strain field.

The first-order nonzero components of the stress tensor are the normal stress σ_z and the tangential stresses τ_{zx} and τ_{zy} giving the internal stress resultants:

$$N=\int_A \sigma_z dA\,,\quad V_x=\int_A \tau_{xz} dA\,,\quad V_y=\int_A \tau_{yz} dA \tag{4.36}$$

$$M_x=\int_A \sigma_z y dA\,,\quad M_y=-\int_A \sigma_z x dA\,,\quad M_\omega=\int_A \sigma_z \omega dA \tag{4.37}$$

$$M_z=\int_A \left(\tau_{yz} x-\tau_{xz} y\right) dA - V_x y_S + V_y x_S\,,\quad M_z^\omega=\int_A \left(\tau_{xz}\frac{\partial\omega}{\partial x}+\tau_{yz}\frac{\partial\omega}{\partial y}\right) dA \tag{4.38}$$

where A represents the cross-section area; N is the axial force; V_x and V_y are the shear forces acting at the (b.d.) shear centre; M_x and M_y are the bending moments with respect to the principal axes x and y and, finally, M_ω, M_z and M_z^ω are the bimoment, the total twisting moment and the twisting moment due to non-uniform torsion, respectively.

4.4.1.2 Constitutive laws

Indicating with E_b and G the longitudinal and transverse elastic moduli of the beam, the first-order components of the stress tensor can be expressed as:

$$\sigma_z = E_b \varepsilon_z^{(1)} \tag{4.39}$$

$$\tau_{zx} = G\gamma_{zx}^{(1)}\,,\qquad \tau_{zy} = G\gamma_{zy}^{(1)} \tag{4.40}$$

Inserting Eqs. 4.39 and 4.40 into Eqs.4.36, 4.37 and 4.38b and making use of Eqs 4.30-4.32 of linear strains, yield:

$$\begin{Bmatrix} N \\ M_x \\ M_y \\ M_\omega \end{Bmatrix} = E_b \begin{bmatrix} A & 0 & 0 & 0 \\ & J_x & 0 & 0 \\ & & J_y & 0 \\ Sym & & & J_\omega \end{bmatrix} \begin{Bmatrix} w_C{}' \\ \varphi_x{}' \\ \varphi_y{}' \\ \Psi' \end{Bmatrix}, \tag{4.41a}$$

$$\begin{Bmatrix} V_x \\ V_y \\ M_z^\omega \end{Bmatrix} = G \begin{bmatrix} D_x & D_{xy} & D_{x\omega} \\ & D_y & D_{y\omega} \\ Sym & & D_\omega \end{bmatrix} \begin{Bmatrix} \left(u_S{}'-\varphi_y\right) \\ \left(v_S{}'+\varphi_x\right) \\ \left(\varphi_z{}'+\Psi\right) \end{Bmatrix}, \tag{4.42b}$$

where J_x, J_y and J_ω are the second area and sectorial moments, respectively. In evaluating the shear rigidities D_{ij} in Eq. 4.42b, the effective shear stress distribution over the cross-section is to be considered. The shear rigidity matrix takes the form:

$$\begin{bmatrix} D_x & D_{xy} & D_{x\omega} \\ & D_y & D_{y\omega} \\ Sym & & D_\omega \end{bmatrix} = \begin{bmatrix} \frac{1}{J_y^2}\int_a S_y^{*2}\frac{ds}{t} & \frac{1}{J_xJ_y}\int_a S_x^*S_y^*\frac{ds}{t} & \frac{1}{J_yJ_\omega}\int_a S_y^*S_\omega^*\frac{ds}{t} \\ & \frac{1}{J_x^2}\int_a S_x^{*2}\frac{ds}{t} & \frac{1}{J_xJ_\omega}\int_a S_x^*S_\omega^*\frac{ds}{t} \\ Sym & & \frac{1}{J_\omega^2}\int_a S_\omega^{*2}\frac{ds}{t} \end{bmatrix}^{-1} \tag{4.43}$$

where:

$$S_x^*(s)=\int_0^s ytds' \quad S_y^*(s)=\int_0^s xtds' \quad S_\omega^*(s)=\int_0^s \omega tds' \tag{4.44}$$

The off-diagonal terms D_{ij} refer to coupling between shear forces acting in the two principal planes (D_{xy}) and between shear resultants and non-uniform torsion ($D_{x\omega}$, $D_{y\omega}$), and they vanish only in the case of doubly-symmetric cross-sections.

4.4.1.3 Formulation of the linearized stability problem

The stability conditions are defined by making use of the classical energy criterion which, for practical purposes, reduces to imposing the positive definiteness of the second variation of the total potential energy:

$$\frac{1}{2}\delta^2\Pi=\frac{1}{2}\int_V E_{ijhk}\delta\varepsilon_{ij}^{(1)}\delta\varepsilon_{hk}^{(1)}dV+\frac{1}{2}\int_V S_{ij}^0\delta^2\varepsilon_{ij}^{(2)}dV-\frac{1}{2}\int_S p_i\delta^2u_idS \tag{4.45}$$

where $E_{ijhk}\delta\varepsilon_{ij}^{(1)}$ is the first variation of the Cauchy stress tensor (i.e. the linear part of the Kirchhoff tensor), S_{ij}^0 is the Kirchhoff stress tensor referred to the pre-buckling state and p_i represents the components of the conservative surface loads. Consequently, any critical load makes the functional expressed by the Eq. 4.45 stationary. The first term on the right-hand side of Eq. 4.45 represents the elastic strain energy Π_E, whereas the second and third terms represent the potential energy Π_G due to the second-order effects of pre-critical stresses and external forces. With the assumption of infinitesimal displacements, the Kirchhoff tensor reduces to the Cauchy stress tensor σ_{ij}^0 and, by dropping the symbol δ, the variations $\delta\varepsilon_{ij}^{(1)}$ and $\delta^2\varepsilon_{ij}^{(2)}$ can be expressed by Eqs. 4.30-4.35. Bearing in mind the expressions of the internal stress resultants (Eqs. 4.13-15), the first-order strains (Eqs. 4.30-4.32) and the constitutive relations (Eq. 4.18), the strain energy for a beam of length *L* may be written as follows (Kim and Kim 2005; Minghini et al. 2007):

$$
\begin{aligned}
\Pi_E &= \frac{1}{2}\int_V E_{ijhk}\varepsilon_{ij}^{(1)}\varepsilon_{hk}^{(1)} dV \\
&= \frac{1}{2}\int_L \left[N w_C{}' + M_y \varphi_y{}' + M_x \varphi_x{}' + M_\omega \Psi{}' + V_x\left(u_S{}' - \varphi_y\right) + V_y\left(v_S{}' + \varphi_x\right) + M_z^\omega\left(\varphi_z{}' + \Psi\right)\right] dz \\
&= \frac{1}{2}\int_L E\left(A w_C{}'^2 + J_x \varphi'^2_x + J_y \varphi'^2_y + J_\omega \Psi'^2\right) dz \\
&+ \frac{1}{2}\int_L G\Big[J_t \varphi'^2_z + D_x\left(u_S{}' - \varphi_y\right)^2 + D_y\left(v_S{}' + \varphi_x\right)^2 + D_\omega\left(\varphi'_z + \Psi\right)^2 \\
&+ 2D_{xy}\left(u_S{}' - \varphi_y\right)\left(v_S{}' + \varphi_x\right) + 2D_{x\omega}\left(u_S{}' - \varphi_y\right)\left(\varphi'_z + \Psi\right) + 2D_{y\omega}\left(v_S{}' + \varphi_x\right)\left(\varphi'_z + \Psi\right)\Big] dz
\end{aligned}
\tag{4.46}
$$

where, as it is usual (Laudiero and Zaccaria 1988), the functional was supplemented with the term $\frac{1}{2}\int_L G J_t \varphi'^2_z\, dz$, taking the contribution of De Saint Venànt torsion into account. Remembering the expressions in Eqs. 4.33-4.35 of second-order strains and rewriting the pre-critical normal stress in the form:

$$
\sigma_z^0 = \frac{N^0}{A} + \frac{M_x^0}{J_x} y - \frac{M_y^0}{J_y} x + \frac{M_\omega^0}{J_\omega}\omega \tag{4.47}
$$

yield:

$$
\begin{aligned}
\Pi_G &= \frac{1}{2}\int_V \sigma_{ij}^0 \varepsilon_{ij}^{(2)} dV - \frac{1}{2}\int_S p_i u_i dS \\
&= \frac{1}{2}\int_L \Big\{ N^0 \left[u_S'^2 + v_S'^2 - x_S \left(2v_S'\varphi_z' + \varphi_x\varphi_z' + \varphi_x'\varphi_z \right) + y_S \left(2u_S'\varphi_z' - \varphi_y\varphi_z' - \varphi_y'\varphi_z \right) + C_N \varphi_z'^2 \right] \\
&+ M_x^0 \left(\varphi_y'\varphi_z + \varphi_y\varphi_z' - 2u_S'\varphi_z' + C_x\varphi_z'^2 \right) - M_y^0 \left(\varphi_x'\varphi_z + \varphi_x\varphi_z' + 2v_S'\varphi_z' + C_y\varphi_z'^2 \right) \\
&- T_y^0 \left[2u_S'\varphi_z - \varphi_y\varphi_z - x_S \left(\varphi_x'\varphi_y - \varphi_x\varphi_y' \right) \right] + T_x^0 \left[2v_S'\varphi_z + \varphi_x\varphi_z - y_S \left(\varphi_x'\varphi_y - \varphi_x\varphi_y' \right) \right] \\
&+ M_z^0 \left(\varphi_x'\varphi_y - \varphi_x\varphi_y' \right) + M_\omega^0 C_\omega \varphi_z'^2 + \left[\int_0^{\bar{s}} p_x x ds \right] \varphi_y^2 + \left[\int_0^{\bar{s}} p_y y ds \right] \varphi_x^2 \\
&- \left[\int_0^{\bar{s}} \left(p_x y + p_y x \right) ds \right] \varphi_x\varphi_y + \left[\int_0^{\bar{s}} \left(p_x \left(x - x_S \right) + p_y \left(y - y_S \right) \right) ds \right] \varphi_z^2 \\
&+ 2\left[\int_0^{\bar{s}} p_z \left(x - x_S \right) ds \right] \varphi_x\varphi_z - 2\left[\int_0^{\bar{s}} p_z \left(y - y_S \right) ds \right] \varphi_y\varphi_z \Big\} dz
\end{aligned}
\tag{4.48}
$$

where $\bar{s}$ is the middle line length and coefficients C_i ($i = N, x, y, \omega$), given in (Cortinez and Piovan 2002; Kim et al. 1996; Laudiero and Zaccaria 1988):

$$
\begin{aligned}
C_N &= \frac{1}{A}\int_A \left(x^2 + y^2 \right) dA + x_S^2 + y_S^2, \quad & C_x &= \frac{1}{J_x}\int_A y\left(x^2 + y^2 \right) dA - 2y_S \\
C_y &= -\frac{1}{J_y}\int_A x\left(x^2 + y^2 \right) dA + 2x_S, \quad & C_\omega &= \frac{1}{J_\omega}\int_A \omega\left(x^2 + y^2 \right) dA
\end{aligned}
\tag{4.49}
$$

represent the so called “Wagner effect”.

4.4.2 Beam discrete model

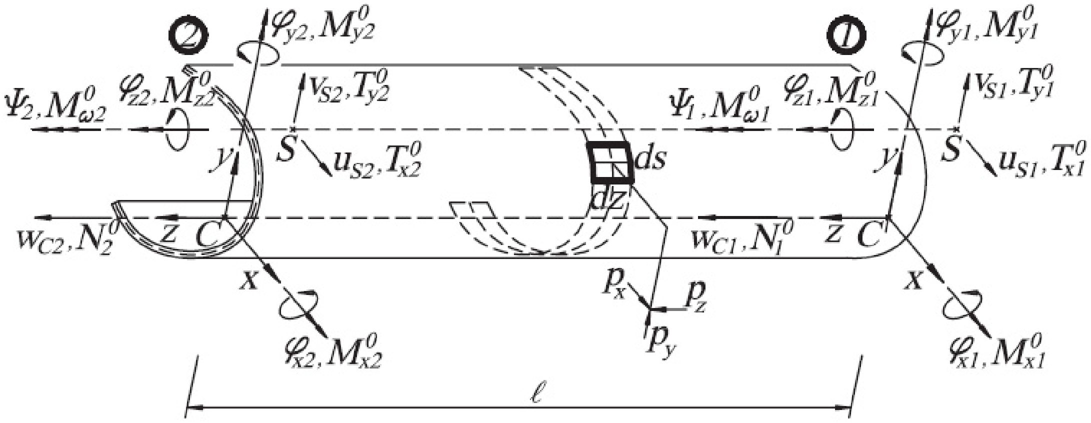

Fig. 4.18 – Free-body force distribution and nodal displacements of the element.

Fig. 4.18 shows a typical two-node beam element, nodal displacements and forces, and external (distributed) loads possibly connected by a rigid lever arm. Collecting the seven displacement functions introduced in the previous paragraph by vector:

$$\mathbf{d}^T = \left[w_C(z), u_S(z), \varphi_y(z), v_S(z), \varphi_x(z), \varphi_z(z), \Psi(z) \right] \tag{4.50}$$

and the nodal displacements by:

$$\mathbf{q}^T = \left[w_{C1}, w_{C2}, u_{S1}, \varphi_{y1}, u_{S2}, \varphi_{y2}, v_{S1}, \varphi_{x1}, v_{S2}, \varphi_{x2}, \varphi_{z1}, \Psi_1, \varphi_{z2}, \Psi_2 \right] \tag{4.51}$$

the displacement field can be written as **d** = **N** **q**, where matrix **N** collects a proper set of shape functions in the form:

$$\mathbf{N} = diag\left\{ \mathbf{N}^z, \mathbf{N}^x, \mathbf{N}^y, \mathbf{N}^\omega \right\}. \tag{4.52}$$

Substituting **d** = **N** **q** into the second variation of the total potential energy (Eq. 4.45) yields the element stiffness matrix. It should be recognized that, before assembling the global matrix of a structure, the nodal displacements $\mathbf{q}^T$ should be referred to a single reference point, as for instance the cross-section centroid. Then, the usual assemblage technique yields:

$$\frac{1}{2}\delta^2\Pi\Big|_{structure} = \frac{1}{2}\mathbf{q}^T\mathbf{K}\mathbf{q} \tag{4.53}$$

where $\mathbf{K}$ represents the global stiffness matrix. In linearized stability problems, the effects of pre-buckling deformations are ignored and the internal forces are assumed to be linear functions of the external loads. Hence, $\mathbf{K}$ can be written in the form:

$$\mathbf{K} = \mathbf{K}_E + \mathbf{K}_G \tag{4.54}$$

where $\mathbf{K}_E$ and $\mathbf{K}_G$ are the elastic and geometric stiffness matrix, respectively. Then, the critical loads are given by the roots of the equation $\det(\mathbf{K}) = 0$ which can be suitably reduced to a standard eigenvalue problem.

4.4.2.1 Interpolating shape functions

With the exception of w_C, described by linear shape functions, the unknown displacements (Eq. 4.50) were interpolated using Hermitian polynomials "modified" by parameters which take the influence of shear deformations into account. These shape functions follow from the solutions of the (homogeneous) governing equations for doubly-symmetric cross-section beams (Minghini et al. 2007; Kosmatka 1995). In fact, for Kosmatka (1995) the natural frequencies of symmetrical Timoshenko beams subjected to axial load were calculated by using these polynomials. Moreover, it was noted (Reddy 1997; Mukherjee et al. 2001) that in the case of a Timoshenko beam bent into a symmetry plane, these functions yield a super-convergent, *locking-free* finite element. For Chang et al. (1996) the same functions were adopted for flexural-torsional buckling analyses of shear-deformable thin-walled beams with a generic cross-section, even though the non-uniform torsion-shear coupling terms (D_{ij}, $i, j = x, y, \omega, i \neq j$) appearing in Eqs. 4.42b and 4.46 were ignored. This finite element (Minghini et al. 2007), including the mentioned coupling terms, gave accurate results in the static analysis of orthotropic FRP beams with non-symmetric cross-section.

With reference to bending in y-z plane and torsion, the adopted polynomials take the form:

$$
\begin{aligned}
N_{11}^{i} &= \frac{1}{1+\phi_i}\left[1-3\xi^2+2\xi^3+\phi_i\left(1-\xi\right)\right] & N_{12}^{i} &= -\frac{l}{1+\phi_i}\xi\left[\left(1-\xi\right)^2+\phi_i\left(1-\xi\right)/2\right] \\
N_{13}^{i} &= \frac{1}{1+\phi_i}\left(3\xi^2-2\xi^3+\phi_i\xi\right) & N_{14}^{i} &= -\frac{l}{1+\phi_i}\xi\left[\xi^2-\xi-\phi_i\left(1-\xi\right)/2\right] \\
N_{21}^{i} &= \frac{6\xi}{l\left(1+\phi_i\right)}\left(1-\xi\right) & N_{22}^{i} &= \frac{1}{1+\phi_i}\left[1-4\xi+3\xi^2+\phi_i\left(1-\xi\right)\right] \\
N_{23}^{i} &= -\frac{6\xi}{l\left(1+\phi_i\right)}\left(1-\xi\right) & N_{24}^{i} &= \frac{1}{1+\phi_i}\left(-2\xi+3\xi^2+\phi_i\xi\right)
\end{aligned}
\tag{4.55}
$$

whereas, for flexure in *x*-*z* plane, N_{12}^{x}, N_{14}^{x}, N_{21}^{x} and N_{23}^{x} take opposite signs. In Eqs. 4.55, *l* stands for the finite element length, $\xi = z/l$, and coefficients ϕ_i (i = x, y, ω) take the expressions:

$$
\phi_x = \frac{12EJ_y}{GD_x l^2}, \quad \phi_y = \frac{12EJ_x}{GD_y l^2}, \quad \phi_\omega = \frac{12EJ_\omega}{GD_\omega l^2} \tag{4.56}
$$

It can be observed that, when shear deformations tend to vanish, $\phi_i = 0$ ($i = x, y, \omega$) and the polynomials $N_{1j}^{\ i}$ and $N_{2j}^{\ i}$ (j = 1,…,4) appearing in Eqs. 4.55, reduce to the classical Hermitian polynomials and to their first derivatives. Consequently, the stiffness matrix $\mathbf{K}_E$ reduces to the elastic matrix for symmetric cross-sections reported by Barsoum and Gallagher (1970). Moreover, if displacement components in Eq. 4.26a,b are neglected and constant distributed loads are considered, the stiffness matrix $\mathbf{K}_G$ reduces to the geometric matrix reported by Barsoum and Gallagher (1970) as well.

4.5 Beam on 3D half space

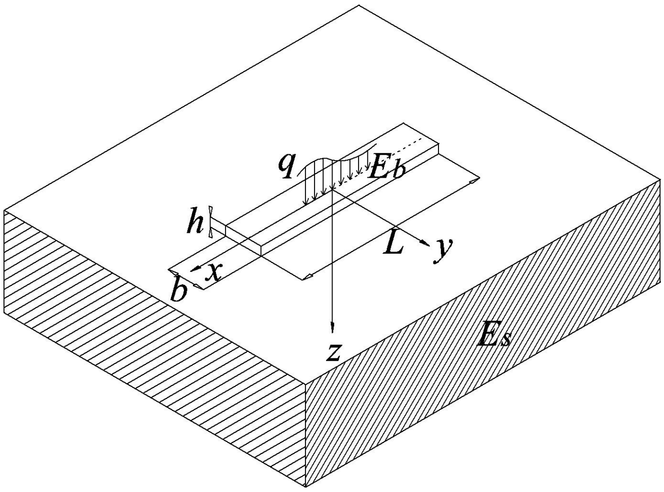

Fig. 4.19 – Beam with rectangular cross-section on elastic half-space.

The beam model described in the previous paragraph, is for simplicity reduced to the model of a Timoshenko beam on elastic half-space having a rectangular cross-section (Fig. 4.19) or a symmetric cross-section with respect to z axis. A different Cartesian coordinate system (0; x, y, z), where the plane x-y coincides with the boundary of the half-space and z is directed downward, x coincides with the centroidal axis of the beam and y is the secondary axis of inertia of beam cross-section. Beam transverse displacement in y direction is neglected, then axial and vertical displacements are given by:

$$u(x, z) = \varphi\, z, \quad v(x, z) = v(x), \tag{4.57}$$

and the corresponding nonzero axial and shear strains become:

$$\varepsilon = \varphi' z, \quad \gamma = v' + \varphi, \tag{4.58}$$

A distributed vertical external load $p(x)$ can be applied along the beam axis x as shown in Fig. 4.19. In the interface between beam and soil, frictionless and bilateral conditions are assumed. Consequently, a vertical soil reaction $r(x,y)$ is enforced to both beam and substrate. For simplicity, the vertical displacement $v(x)$ of the beam is assumed coincident with that of the half-plane boundary, then, following Selvadurai (1979) it is assumed that the beam is infinitely rigid with respect to the half-space along y direction and deflection takes place only in the *x-z* plane. This is an approximate method of taking into account the three-dimensional effects of the elastic half-space. The distribution of contact stress in the transverse direction is assumed to be equal to the contact stress generated by a rigid foundation of width *b* in a plane strain problem (Sadowsky 1928). The contact stress distribution $r(\bar{x}, y)$ is given by (Fig. 4.20b):

$$r(\bar{x}, y) = \frac{2\, r(\bar{x})}{\pi(b^2 - y^2)} \tag{4.59}$$

The simple case of constant pressure distribution along beam width (Fig.20a) is related to a foundation weak in transversal direction with respect to the half-space, then a transversal deformation of the foundation is expected. However, a beam model is not able do describe such behaviour, then the hypothesis described by Eq. 4.59 and Fig. 4.20b is considered. It is worth noting that the discretization of the problem will not be able to follow exactly that hypothesis.

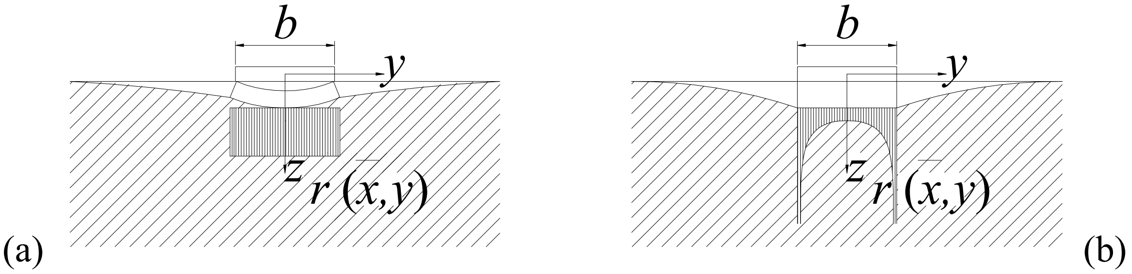

Fig. 4.20 – Limit cases for the contact stress distribution in transverse direction.

4.5.1 Variational formulation

The potential energy of the Timoshenko beam is given by:

$$\Pi_e = \frac{1}{2}\int_L [D_b(\varphi'(x))^2 + k_b G_b A(v'(x) + \varphi(x))^2]\, \mathrm{d}x - L_e \tag{4.60a}$$

$$L_e = b\int_L \left[\left(p(x) - r(x)\right) v(x) + m(x)\, \varphi(x)\right] \mathrm{d}x \tag{4.4.60b}$$

whereas the potential Π_s of the half space, similarly to the plane state case, can be written as

$$\Pi_s = U_S - \int_S r(x,y)\, v(x,y)\, \mathrm{d}A \ , \tag{4.61}$$

where U_s is the strain energy of the soil and S is the contact surface. Due to Clapeyron's theorem, the strain energy of the soil is equal to one half of the external work, therefore, the potential energy Π_s can be rewritten as

$$\Pi_s = -\frac{1}{2}\int_S r(x,y)\, v(x,y)\, \mathrm{d}A \ . \tag{4.62}$$

The expressions above are similar to the ones defined in the first and second chapter, however, in this case, surface displacement and half-space pressures are defined on a two-dimensional domain. Considering the three-dimensional half-space, the displacement of soil points underneath the foundation is given by Eq. 4.1. Substituting it into Eq. 4.62 yields

$$\Pi_s = -\frac{1}{2}\int_S r(x,y)\, \mathrm{d}A \int_S g(x,y,\xi,\eta)\, r(\xi,\eta)\, \mathrm{d}A \ , \tag{4.63}$$

where g is the expression known as Boussinesq's solution of the surface vertical displacement generated by a unitary force (Eq. 4.2).

Hence, the total potential energy $\Pi = \Pi_b + \Pi_s$ turns out to be

$$\Pi(v,r) = \Pi_e - \frac{1}{2}\int_L r(x)\, \mathrm{d}x \int_L g(x,y)\ r(y)\, \mathrm{d}y, \tag{4.64}$$

Variational formulation analogous to Eq. 4.64 was obtained by Kikuchi (1980), Bjelak and Stephan (1983) for beams resting on a Pasternak soil and by Tullini and Trallli (2010) for beams resting on elastic half-plane.

4.5.2 Discrete model

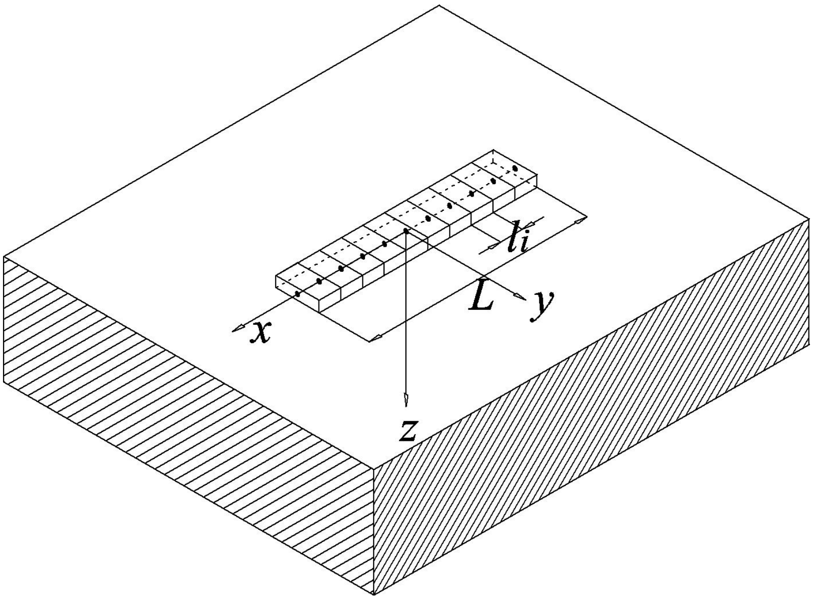

Fig. 4.21 – Beam on elastic half-space subdivided into equal FEs

The discrete model for the beam was described in the previous paragraph. The beam may be subdivided into equal FEs having length l_i along x direction, as shown in Fig. 4.21. The rectangular contact surface may be discretized in x and y directions following different methods, as it has been shown for the Galerkin boundary element method. The discretization along beam length (x direction) can follow the beam subdivision into FEs, then, the length dx_i of a generic soil surface sub-element is equal to l_i. However, in order to evaluate correctly the soil pressure singularities near beam ends, it is possible to further subdivide the FEs at beam ends by defining a number of subdivisions $n_{x,end}$ and adopting a local coordinate which follow a power-graded expression (Eq. 4.13).

An important choice is the number of surface subdivisions along beam width (y direction). One soil element along beam width (Fig. 4.22a) leads to solutions characterized by constant soil pressures along y direction. A constant soil pressure in transverse direction corresponds to a foundation beam with a transverse section deformable with respect to the half-space (Fig. 4.22a), this behaviour is completely different than the hypothesis of the problem. Vice-versa, more soil elements along beam width (Fig. 4.22b) allow to represent surface pressure singularities close to beam edges, however, the behaviour of a beam with an infinite transversal stiffness with respect to the half space can be achieved only with an infinite number of subdivisions.

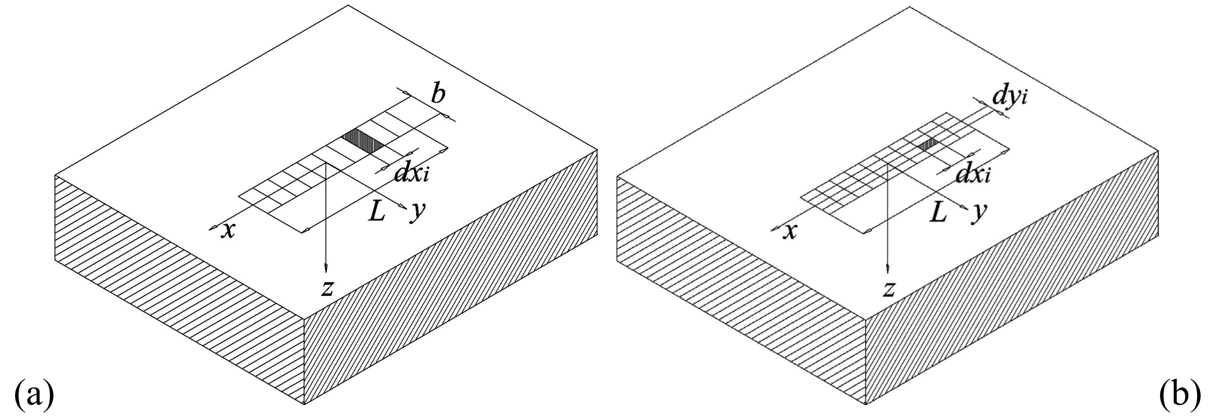

Fig. 4.22 – Discretization of the contact surface between beam and half-space. One element along beam width (a), four equal elements along beam width (b).

Tab. 4.3 shows some examples of contact surface discretizations. Starting from the simple case of a beam with $n_x = 8$ and $n_y = 1$, $n_{x,end} = 1$, the second and third row show discretizations characterized by $n_y = 3$ and 5, respectively. Such discretizations are obtained by defining a power graded function (Eq. 4.13) along y axis with $\beta = 3$ and $n = 4$ and 6, respectively, and joining the subdivisions near the midpoint. Second and third column show discretizations characterized by $n_{x,end} = 2$ and 3, respectively.

In the following, analyses are carried out by increasing the number of subdivisions n_x along longitudinal direction and considering the nine combinations presented in Tab. 4.3.

The soil reaction is approximated as done for the Galerkin boundary element method, adopting a piecewise constant function inside each element (Eq. 4.8).

Then, considering beam discretization and contact surface discretization, the total potential energy Π written in discrete form takes the expression:

$$\Pi(\mathbf{q},\mathbf{r}) = \frac{1}{2}\mathbf{q}^T\mathbf{K}_b\,\mathbf{q} - \mathbf{q}^T\mathbf{F} + \mathbf{q}^T\mathbf{H}\mathbf{r} - \frac{1}{2}\mathbf{r}^T\mathbf{G}\mathbf{r} \tag{4.65}$$

	$n_{x\,\mathrm{end}} = 1$	$n_{x\,\mathrm{end}} = 2$	$n_{x\,\mathrm{end}} = 3$
$n_y = 1$	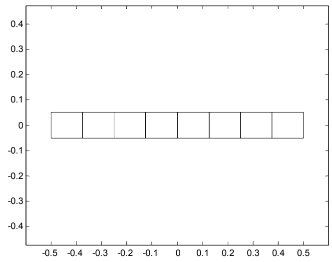	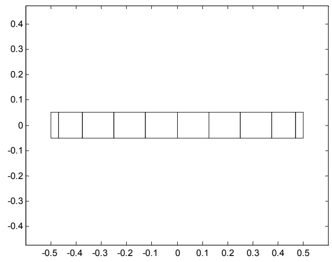	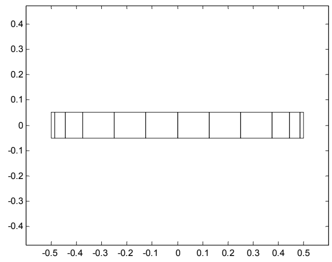
$n_y = 3$	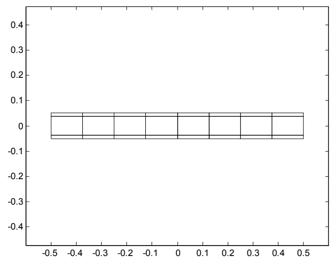	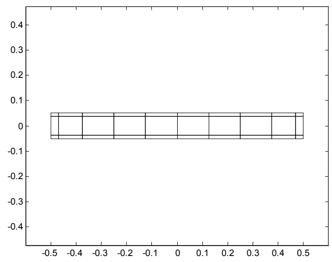	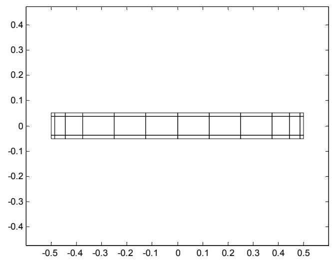
$n_y = 5$	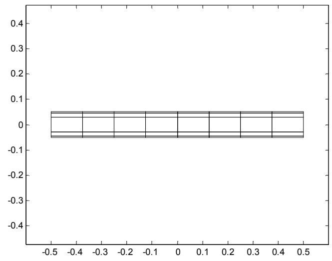	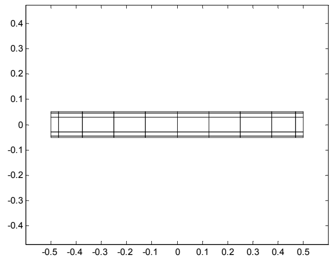	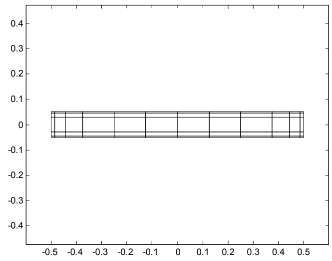

Tab. 4.3 – Examples of contact surface discretizations, varying n_y and $n_{x,end}$.

Which is similar to the corresponding one obtained for the beam on half-plane. The stationarity condition of the total potential energy Π written in discrete form provides the following system:

$$\begin{bmatrix} \dfrac{D_b}{L^3}\left(\tilde{\mathbf{K}}_b - \dfrac{PL^2}{D_b}\tilde{\mathbf{K}}_g\right) & \mathbf{H} \\ \mathbf{H}^{\mathrm{T}} & -\dfrac{1}{E}\breve{\mathbf{G}} \end{bmatrix} \begin{Bmatrix} \mathbf{q} \\ \mathbf{r} \end{Bmatrix} = \begin{Bmatrix} b\mathbf{F} \\ \mathbf{0} \end{Bmatrix} \tag{4.66}$$

where the vector **q** collects nodal displacements, **r** denotes the vector of constant soil reactions, **F** is the external load vector, $D_b/L^3\tilde{\mathbf{K}}_b$ is the elastic stiffness matrix of the beam, $P/L\tilde{\mathbf{K}}_g$ is the geometric (or incremental) matrix. Element matrices $\tilde{\mathbf{K}}_{bi}$ and $\tilde{\mathbf{K}}_{gi}$ are equal to those introduced in the second chapter.

Moreover, the matrix $\breve{\mathbf{G}}$ turns out to be coincident with the one introduced in the Galerkin boundary element method (Eq. 4.10). The matrix **H** turns out to be coincident to the corresponding matrix obtained for the plane state case if one subdivision along beam width is considered, whereas for $n_y = 3$ and 5, **H** is reported in appendix A5.
System in Eq. 4.66 yields the following solution:

$$\mathbf{r} = \frac{E_s}{1-\nu_s^2}\breve{\mathbf{G}}^{-1}\mathbf{H}^{\mathrm{T}}\mathbf{q}\,. \tag{4.67}$$

$$\left[\tilde{\mathbf{K}}_b - \lambda\tilde{\mathbf{K}}_g + \breve{\mathbf{K}}_{\mathrm{soil}}\right]\mathbf{q} = \mathbf{F}\frac{bL^3}{D_b} \tag{4.68}$$

where $\breve{\mathbf{K}}_{\mathrm{soil}}$ is the stiffness matrix of the half-space:

$$\breve{\mathbf{K}}_{\mathrm{soil}} = (\alpha L)^3\,\mathbf{H}\breve{\mathbf{G}}^{-1}\mathbf{H}^{\mathrm{T}}\,. \tag{4.69}$$

The load multiplier λ and parameter αL are defined as follows;

$$\lambda = \frac{PL^2}{D_b}, \qquad \alpha L = \sqrt[3]{\frac{E_s\, b\, L^3}{(1-\nu_s^2)\, D_b}}\,. \tag{4.70a, b}$$

The parameter αL in Eq. 15b describes the beam-substrate system and it is coincident with the one obtained in the plane state case, according to references (Biot 1937; Vesic 1961; Tullini and Tralli 2010). Low values of αL characterise short beams stiffer than the soil, whereas higher values of αL describe beams on stiff soil. In this case, however, b is not set equal to 1, but it can assume any value and another parameter needs to be defined in order to describe the problem:

$$\chi = L/b \tag{4.71}$$

Then, long beams on stiff soil are characterized by large values of αL and χ.
Parameters αL and χ are typically adopted for studying beam resting on a three-dimensional elastic half space (Gorbunov-Posadov and Serebrjanyi 1961; Barden 1962).

4.6 Static analysis of beams on 3D elastic half-space

In the following, static analyses of beams with free ends and finite length resting on a three-dimensional elastic half-space are presented. Three simple load cases are considered: concentrated vertical load at beam midpoint, uniform vertical load distribution along beam length and concentrated moment at beam midpoint. It is worth noting that the half-space behaviour is linear and bilateral; then, in the following examples, pressures along contact surface may result both tractions (negative values) and compressions (positive values). However, considering more complex load conditions and, in particular, adding the effects of the self-weight of the foundation, surface pressures turn out to be compressive.

The following examples show beam deflections, surface reactions and beam bending moment varying αL. For simplicity, beams with rectangular cross-sections are considered. For an isotropic beam with $\nu_b = 0.2$ and slenderness ratios L/h equal to 3 and 5, the coefficient ϕ_x is approximately equal to 0.3 and 0.1, respectively. The Euler-Bernoulli beam case ($\phi_x = 0$) is also considered.

4.6.1 Foundation beam loaded by a concentrated force at midpoint

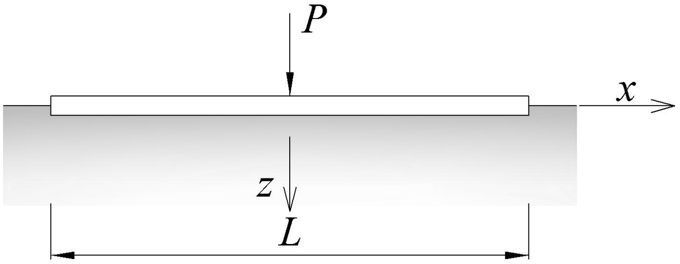

Fig. 4.23 – Beam on elastic half-space loaded by a concentrated force *P* at midpoint.

A foundation beam on elastic half-space loaded by a concentrated force *P* at midpoint is considered. The first example is related to an Euler-Bernoulli beam having $\chi = 10$, with results determined by assuming $n_x = 2^8$, $n_{x,end} = 1$ and by considering three cases of subdivision along *y* direction; $n_y = 1$ represents the simplest case, then $n_y = 3$ and 5 adopting a power-graded mesh are considered. Figs. 4.25a and b show dimensionless beam displacement generated by the concentrated force for $\alpha L = 5$ and 25, respectively. Displacement obtained with

n_y = 3 and n_y = 5 appears almost coincident, whereas with n_y = 1, beam displacement is greater with respect to other results, in particular close to beam midpoint. Similar considerations can be done about surface pressures along beam length (Figs. 4.25c and d). Pressures obtained with one subdivision along y direction are greater with respect to the other cases, whereas pressures obtained with n_y = 3 and n_y = 5 are quite close to each other. Moreover, Figs. 4.25e and f show transversal surface pressures at beam midpoint for αL = 5 and 25, respectively. Adopting 3 or 5 elements along beam width, pressure singularities near surface edges can be determined, then pressures close to y = 0 are smaller with respect to the case with n_y = 1.

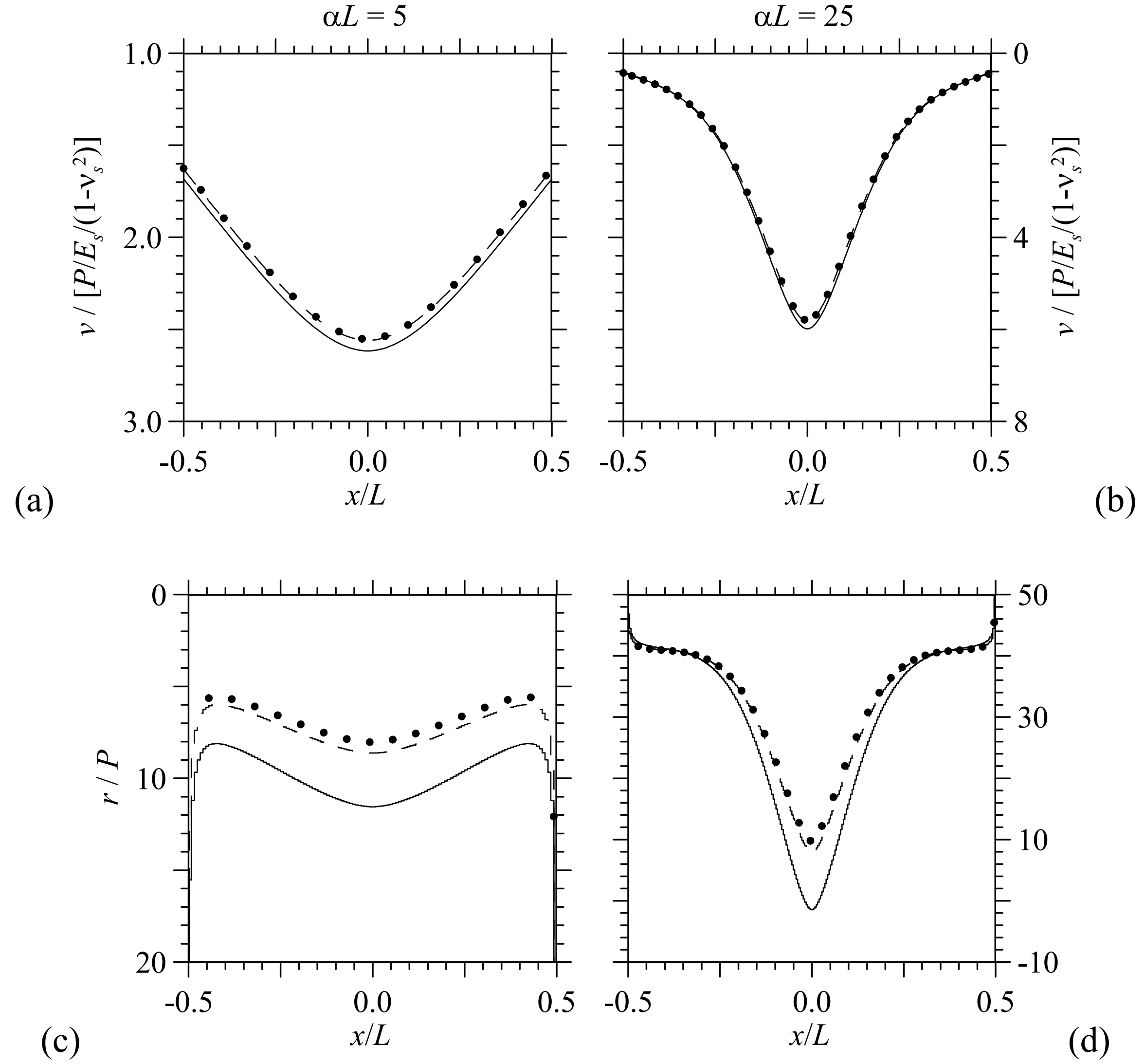

Fig. 4.24 – Vertical displacement (a, b) and surface pressures (c, d) along beam length of a beam loaded by a concentrated force at midpoint. Continuous lines for n_y = 1, dashed line for n_y = 3, dots for n_y = 5.

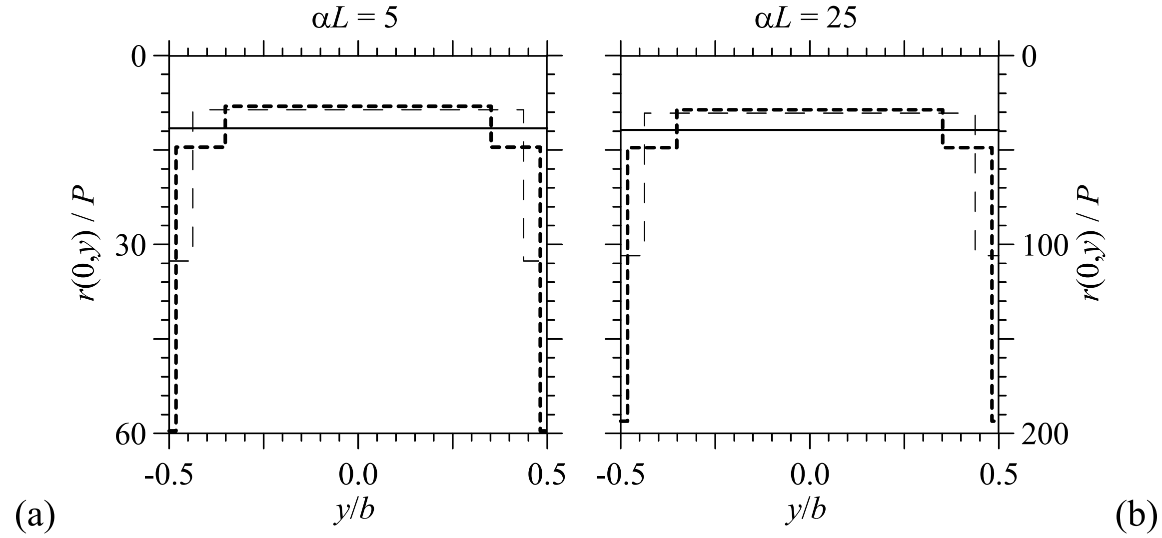

Fig. 4.25 –Surface pressures at midpoint along beam width (a, b) for a beam loaded by a concentrated force at midpoint. Continuous lines for $n_y = 1$, dashed line for $n_y = 3$, dashed bold line for $n_y = 5$.

It is worth noting that $n_y = 1$ corresponds to the case of a flexible beam along transverse direction with respect to the half-space, whereas $n_y > 1$ allows to consider pressure singularities near surface edges. However, only a large number of subvidisions along y direction should be able to fit correctly the expression determined by Sadowskyi (Eq. 4.59).

Prior to present further results for different values of αL, a convergence test is performed in order to evaluate errors committed varying the number of subdivisions along beam width. Considering a beam with $\chi = 10$, the results obtained with $n_x = 2^{10}$, $n_{x,end} = 1$ and $n_y = 7$ are taken as reference solution, adopting a power-graded subdivision along y direction. Then, varying n_x and n_y, relative errors are evaluated for beam displacement and surface pressure at midpoint for αL = 5 and 25. Figs. 4.26a-d show that the number of subdivisions along y direction influences significantly the results, for increasing n_x, and, indeed, relative errors tend to be constant and do not converge for each case considered. If only one subdivision is adopted along beam width, errors are obviously greater with respect to reference results, in particular errors for beam displacement at midpoint are close to 4% for αL = 5 and 25, whereas errors for surface pressure at midpoint are close to 40% for αL = 5. Adopting 3 power graded subdivisions along beam width, relative errors are smaller with respect to the previous case, in particular relative errors for beam displacement at midpoint are less than 1%. However surface pressure at midpoint for αL = 5 is characterized by a relative error close to 10% (Fig. 4.26), which becomes less than 1% for αL = 25.

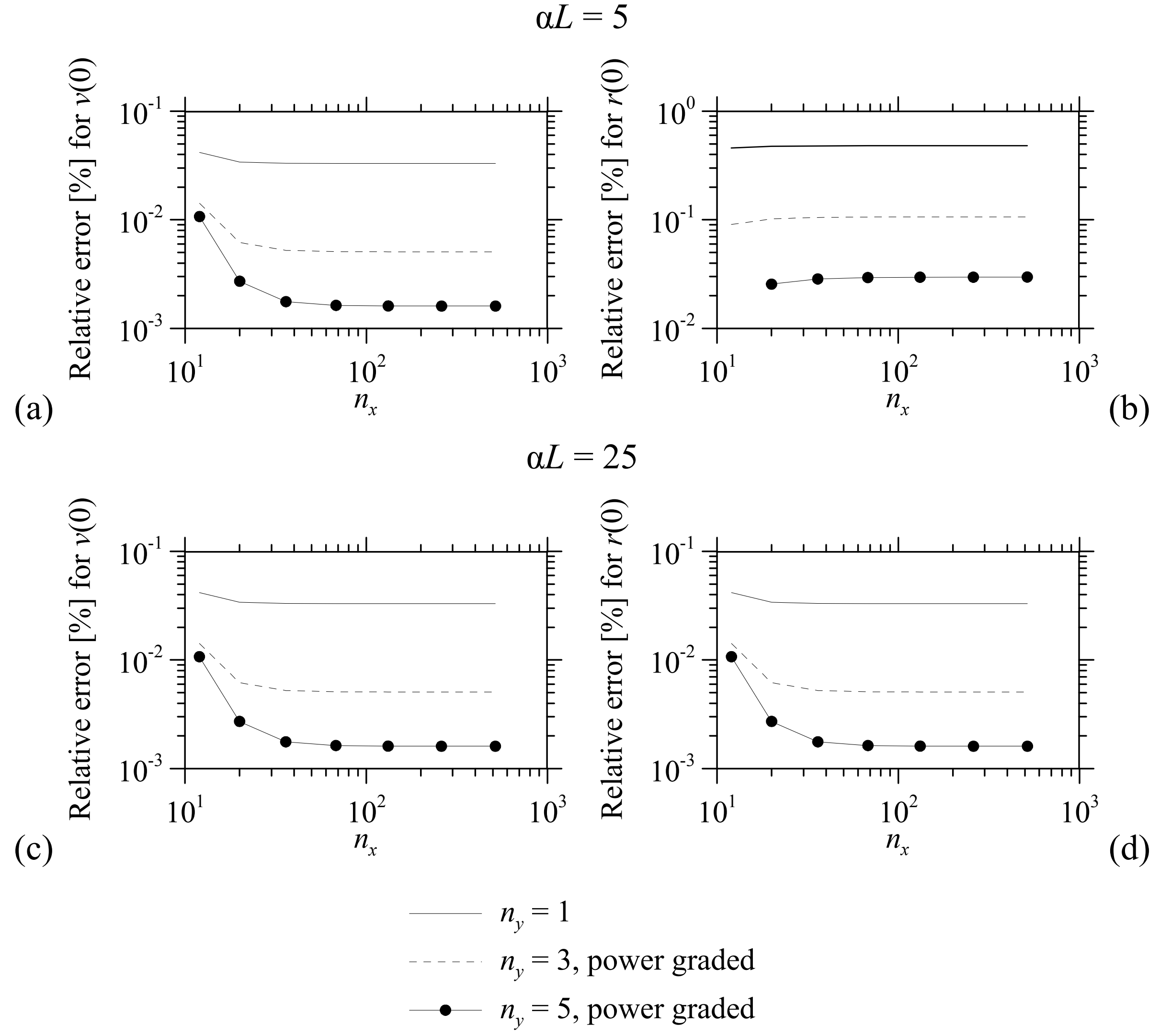

Fig. 4.26 – Relative errors for a beam loaded at midpoint with $\chi = 10$, varying mesh discretization.

In the following examples, $n_x = 2^8$, $n_{x,end} = 1$ and $n_y = 3$ are adopted for determining beam displacements, surface pressures and bending moments along beam length.

Figs. 4.27 and 4.28 show dimensionless displacement v / $[P/(E\ b)]$, dimensionless half-space reaction r / $[P(Lb)]$ and dimensionless bending moment $M/(PL)$ with respect to the dimensionless abscissa x/L, for values of αL equal to 1, 5, 10, 50, which correspond to the decreasing beam stiffness with respect to the half-space. Each figure show results for three different values of ϕ. For simplicity E is used instead of $E_s/(1-\nu_s^2)$.

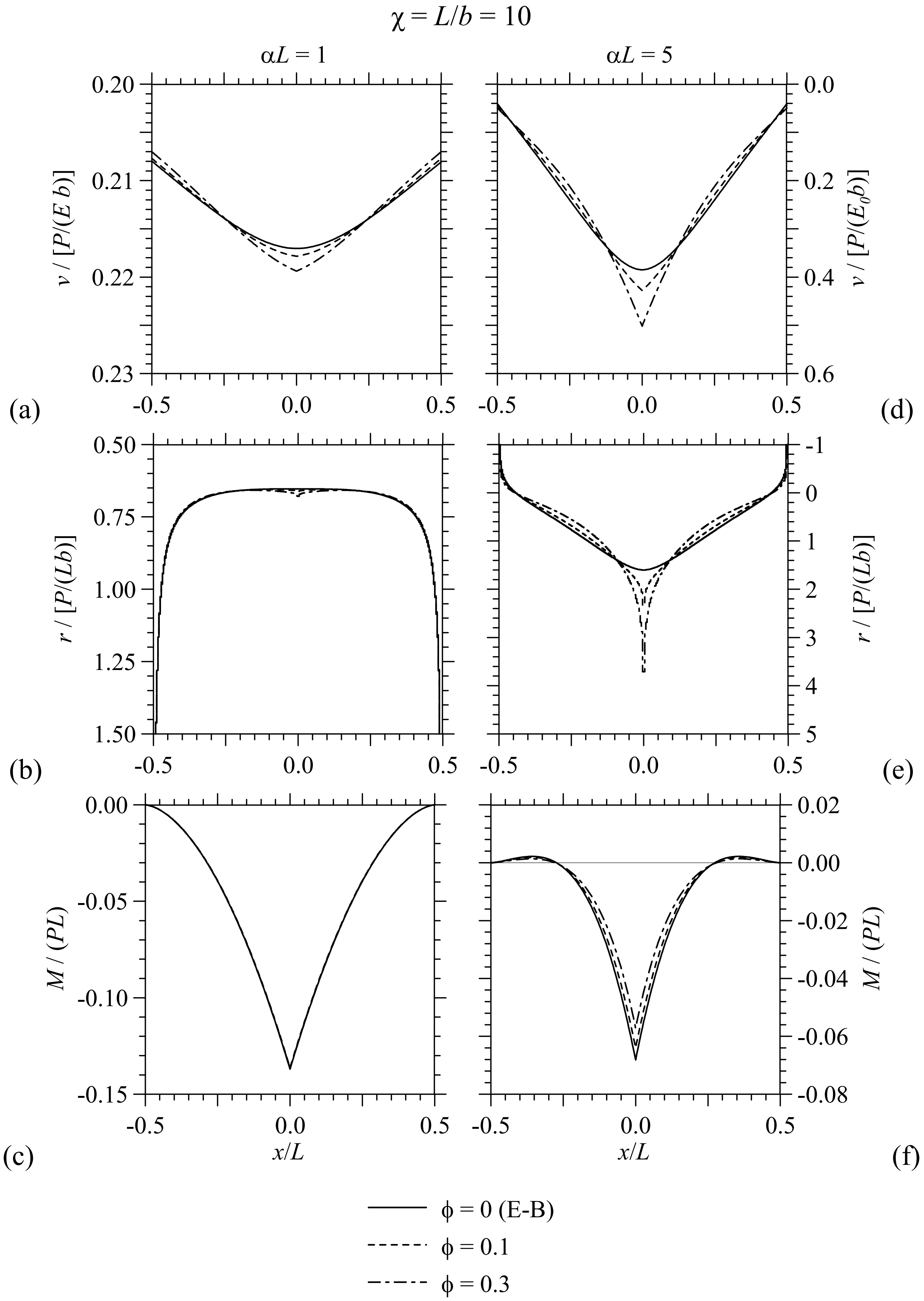

Fig. 4.27 – Foundation beam loaded by a concentrated force at midpoint. Vertical displacement (a, d), half-space reactions (b, e) and bending moment (c, f) along the beam for $\alpha L = 1$ (a, b, c) and $\alpha L = 5$ (d, e, f).

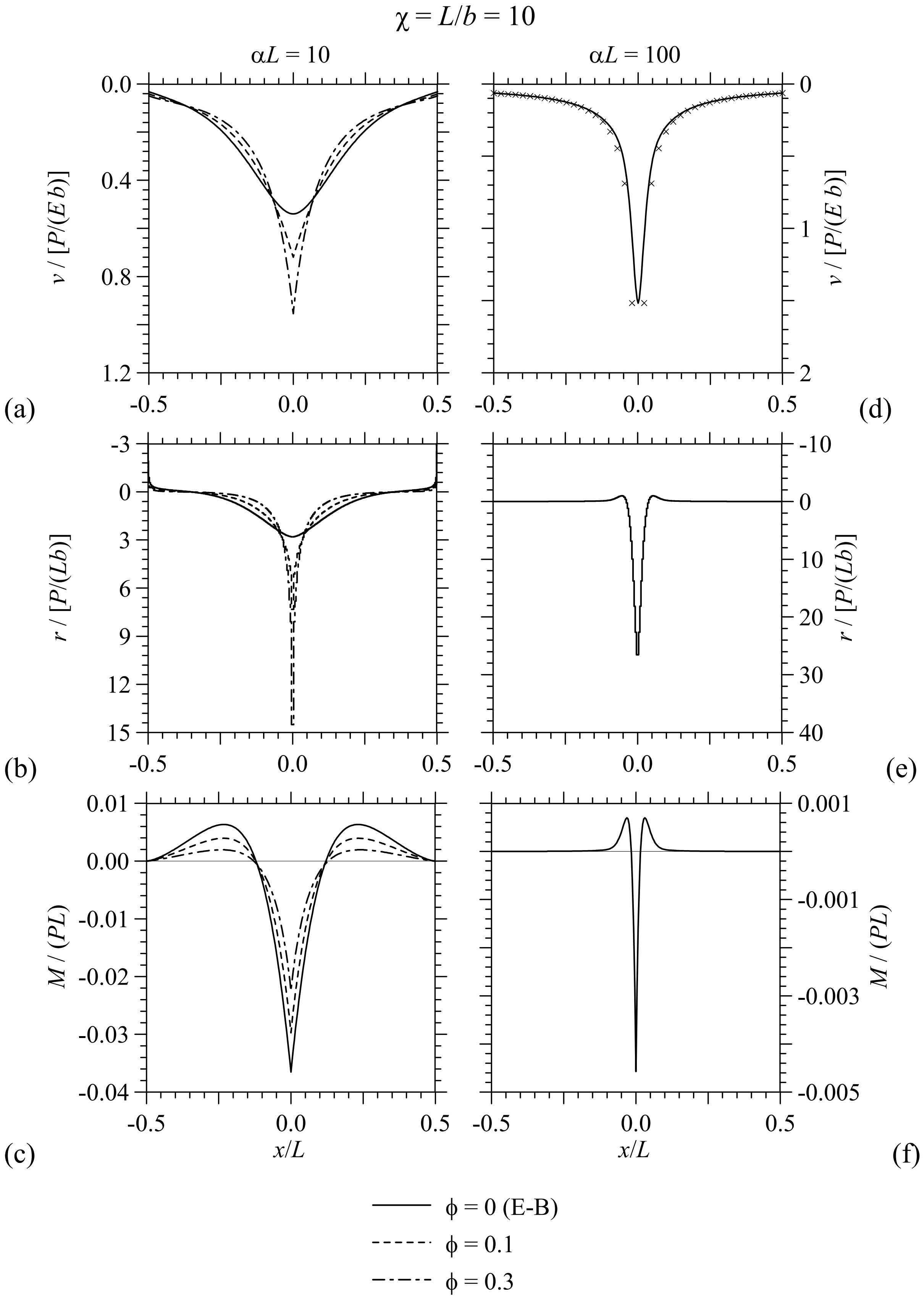

Fig. 4.28 – Foundation beam loaded by a concentrated force at midpoint. Vertical displacement (a, d), half-space reactions (b, e) and bending moment (c, f) along the beam for $\alpha L = 10$ (a, b, c) and $\alpha L = 50$ (d, e, f).

Fig. 4.27a shows beam displacements referred to $\alpha L = 1$, in this case it is clear that the rigid displacement value is larger with respect to the relative displacement of beam midpoint, then beam behaviour is quite close to a rigid rectangular indenter. For nonzero values of ϕ, wedge-shaped beam deflection are obtained.

Figs. 4.27b and c show that half-space reaction and bending moment obtained with $\alpha L = 1$ do not depend significantly on ϕ and are characterized by a singular behaviour at beam ends. Results obtained with $\alpha L = 5$ are shown in Figs. 4.27d-f. In this case beam rigid displacement is smaller with respect to beam deflection at midpoint (Fig. 4.27d) and for nonzero values of ϕ, wedge-shaped beam deflection generates singular half-space reactions at midpoint (Fig. 4.27e). Bending moment values decrease for increasing the value of ϕ (Fig. 4.27f).

Figs. 4.28a-c show results related to $\alpha L = 10$, which turn out to be quite analogous to the corresponding results obtained with $\alpha L = 5$. Then Figs. 4.28d-f are referred to $\alpha L = 100$. Considering one surface subdivision for each beam element along x axis, the matrix in Eq. 4.66 tends to be singular for $\phi \neq 0$, then the corresponding results are not shown. Apart from the neighbourhood of the point load, the vertical displacement shown in Fig. 4.28d is in good agreement with the following expression:

$$v(x) = \frac{P}{\pi E} \frac{1}{|x|}, \tag{4.72}$$

which corresponds to the surface displacement due to a concentrated normal force (Eq. 4.1) on x-z plane, as shown with crosses in Fig. 4.28d.

Fig. 4.29a shows dimensionless displacement at beam midpoint and beam end for increasing αL. For very low αL values, both displacements tend to be coincident with those corresponding to a rigid-punch. Increasing αL, displacement at midpoint obviously increases, whereas displacement close to beam ends tend to converge to a constant value defined by

$$v(L/2) = \frac{P}{\pi E} \frac{1}{L/2} \rightarrow v/[P/(Eb)] = \frac{2}{\pi \chi} \tag{4.73}$$

which is quite close to 0.06 for $L/b = 10$.

It is worth noting that, differently from the case of the beam on elastic half-plane considered in the previous chapters, in this case a large value of αL does not necessarily correspond to a long beam, then, for increasing αL, displacements at beam ends do not tend to zero.

Fig. 4.29b shows dimensionless half-space pressure close to beam end for increasing αL. For a beam on stiff soil, pressure assumes large values due to the singular behaviour showed in Fig. 4.27b, then, increasing αL, pressure tends obviously to zero.

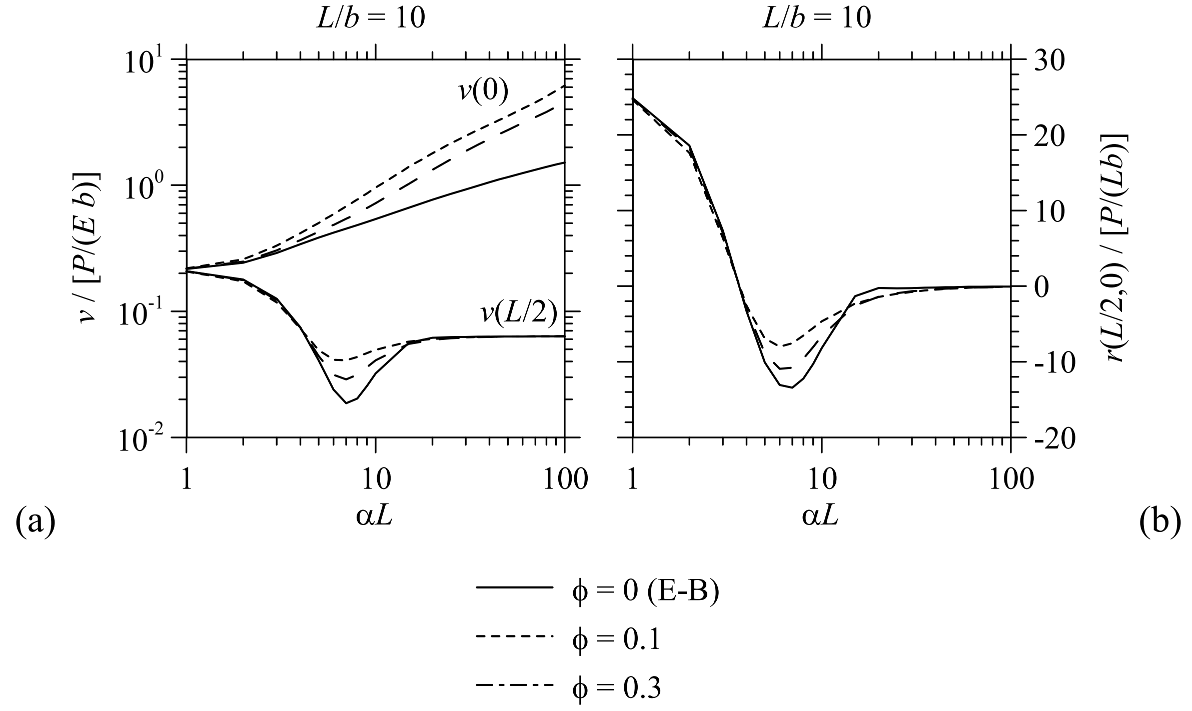

Fig. 4.29 – Foundation beam loaded by a concentrated force at midpoint. Displacement at midpoint $v(0)$ and beam end $v(L/2)$ (a), half-space reaction close to beam end (b).

Biot (1937) studied the behaviour of an infinite Euler-Bernoulli beam on an elastic foundation, loaded by a concentrated force P, considering both the case of a two-dimensional foundation and of a three-dimensional foundation. In the latter case, the maximum bending moment is expressed by:

$$M_{\max} = M(0) = 0.166\, Pb\, [16\, \bar{k}\, D_b / (E\, b^4)]^{0.277}, \tag{4.74}$$

where $\bar{k}$ is a parameter set equal to 1 in case of uniform pressure distribution along beam width and equal to 1.13 in case of uniform deflection along beam width. The present model, characterized by pressures varying both in x and y direction ($n_y = 3$), is quite close to the hypothesis of uniform deflection along beam width. Then, setting χ equal to 10, 30 and 100, bending moments at beam midpoint are evaluated for increasing αL and compared to Eq. 1.37 with $\bar{k}$ = 1.13 (Fig. 4.30). Eq. 1.37 is in good agreement with the results of the present analysis for αL greater than 3.

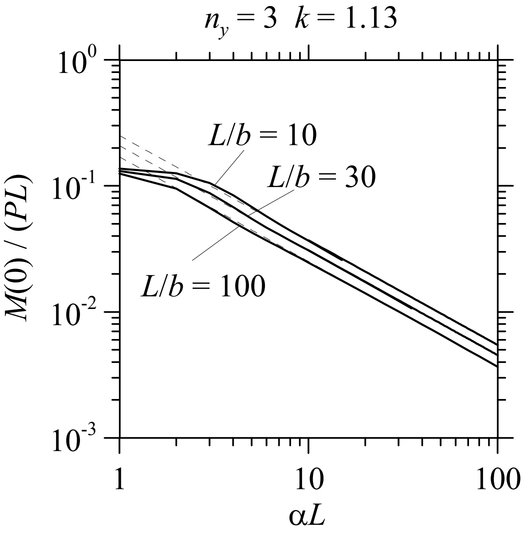

Fig. 4.30 – Foundation beam loaded by a concentrated force P at midpoint. Bending moment at midpoint for three values of *L*/*b* and increasing αL. Continuous lines for the present mode, dashed line for Biot solution (Eq. 1.37).

4.6.2 Foundation beam loaded by a uniform force distribution

The case of a beam on elastic half-space loaded by a uniform force distribution q along its entire length (Fig. 4.31) is now considered.

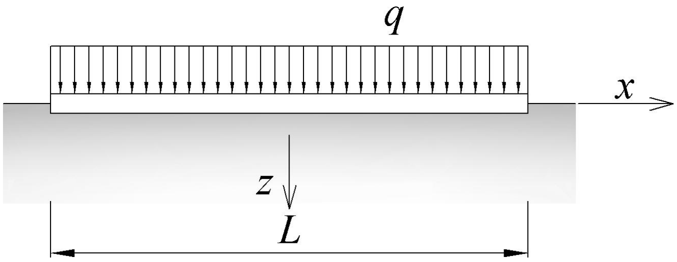

Fig. 4.31 – Beam on elastic half-space loaded by a uniform force distribution.

Adopting $n_x = 2^8$, $n_{x,end} = 1$ and $n_y = 3$, beam displacements, surface pressures and bending moments along beam length are determined for $\chi = 10$ and different αL values.

For $\alpha L = 1$, Fig. 4.32a shows that beam displacement is characterized by a rigid body vertical translation and a small deflection. Half-space pressures presented in Fig. 4.32b are typical of a rigid indenter and, moreover, reaction and bending moment are in this case not influenced by ϕ. For $\alpha L = 5$, reaction (Fig. 4.32e) is characterized by singularities at beam ends but soil reaction close to beam midpoint are larger than those of the previous case. Both displacement (Fig. 4.32d) and reaction are not influenced by ϕ, whereas bending moment (Fig. 4.32c) decreases as ϕ increases. Displacement and reaction obtained with αL = 10 (Figs. 4.33a and b) are quite similar to those obtained with $\alpha L = 5$, whereas bending moment (Fig. 4.33c) is quite different and characterized by large values close to $L/4$. For $\alpha L = 100$, the results are presented only for the Euler-Bernoulli beam case (Figs. 4.33d-f) due to the singular behaviour of matrix in Eq. 4.66. Beam displacements (Fig. 4.33d) are quite different to those determined with Love analytic solution (Eq. 4.21 for $y = 0$), which are shown with crosses in the figure. Half-space reaction (Fig. 4.33e) is nearly constant along beam length excluding singularities at beam ends, whereas bending moment (Fig. 4.33f) is characterized by two peaks close to beam ends.

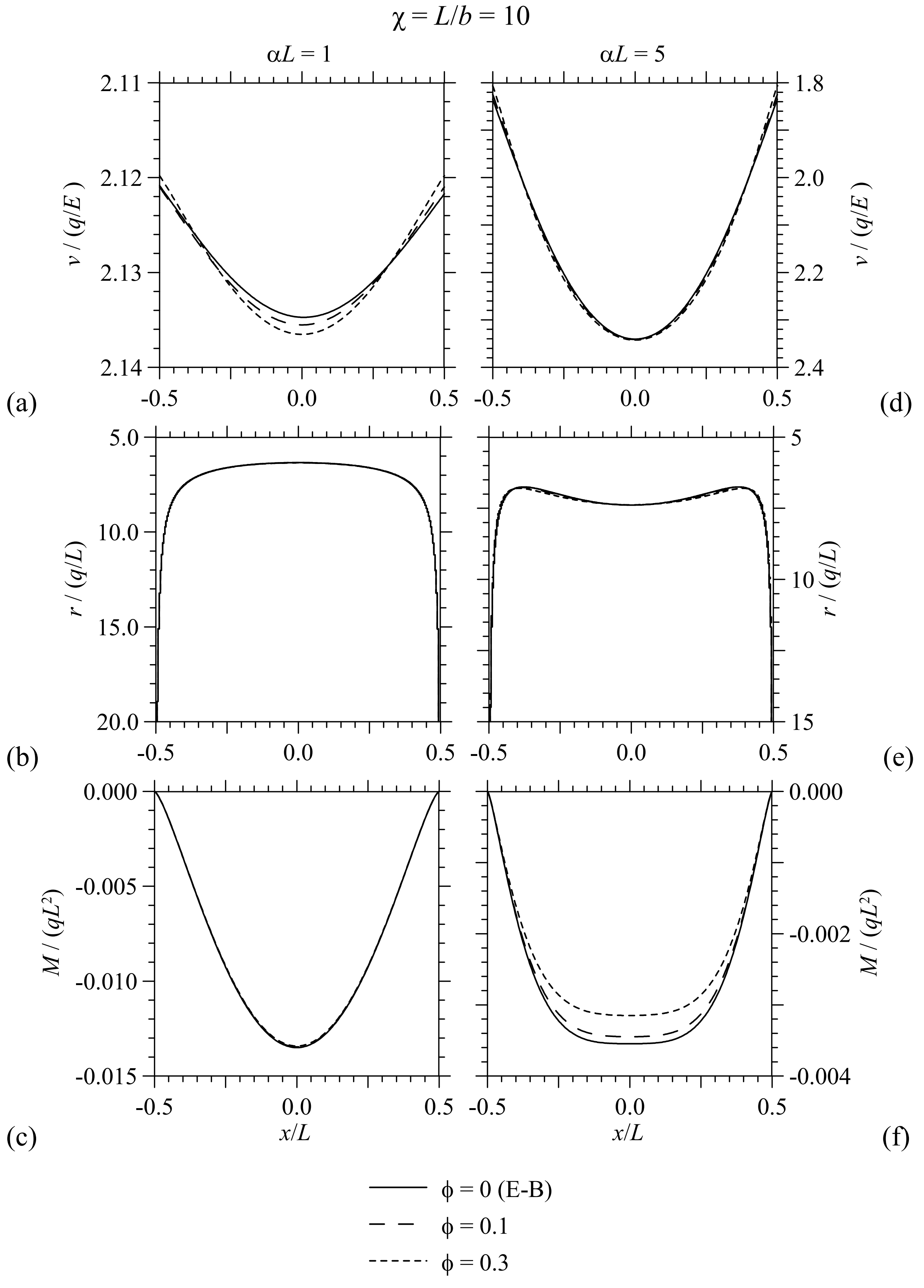

Fig. 4.32 – Foundation beam loaded by a uniform force distribution. Vertical displacement (a, d), half-space reactions (b, e) and bending moment (c, f) along the beam for $\alpha L = 1$ (a, b, c) and $\alpha L = 5$ (d, e, f).

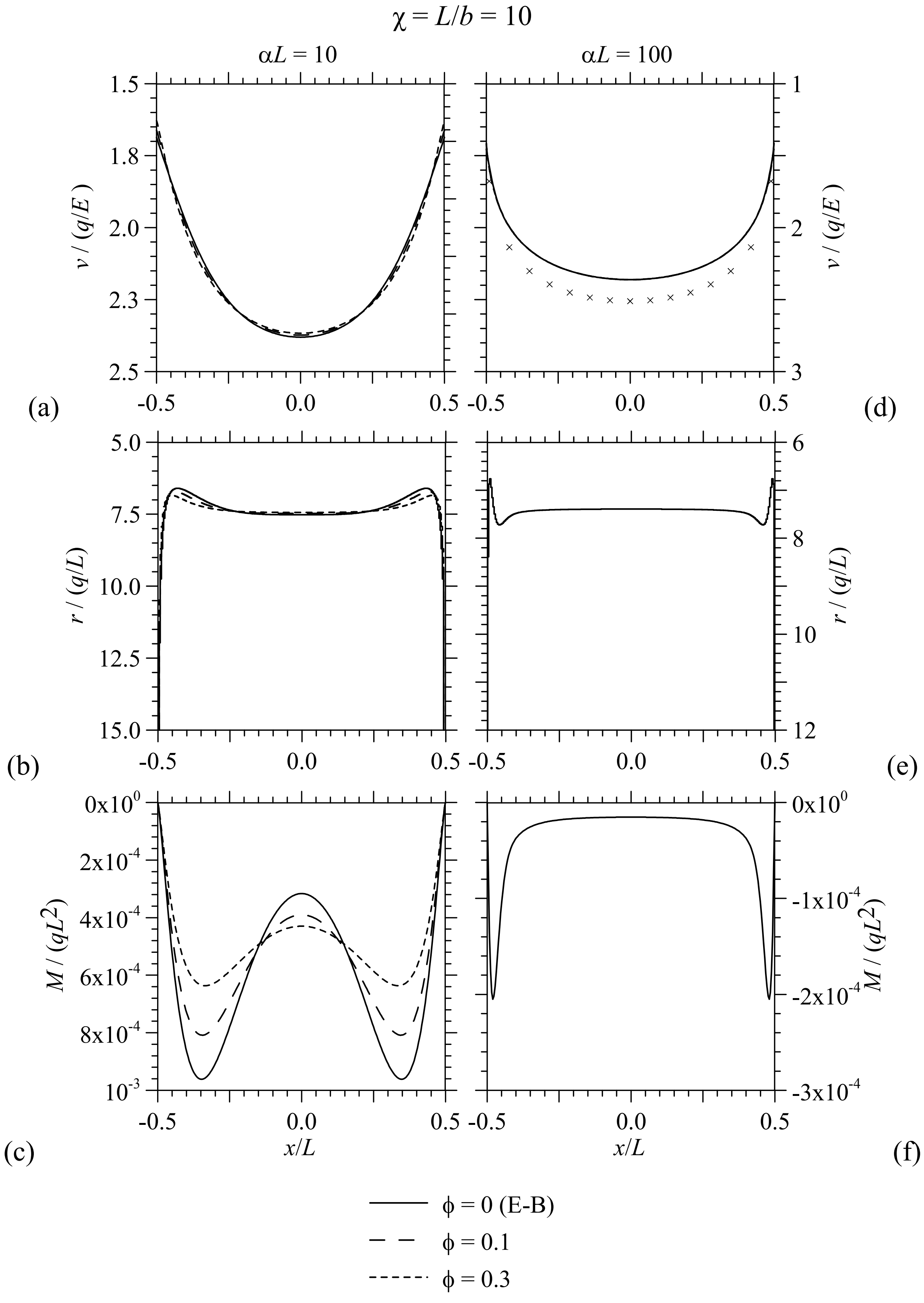

Fig. 4.33 – Foundation beam loaded by a uniform force distribution. Vertical displacement (a, d), half-space reactions (b, e) and bending moment (c, f) along the beam for $\alpha L = 10$ (a, b, c) and $\alpha L = 50$ (d, e, f).

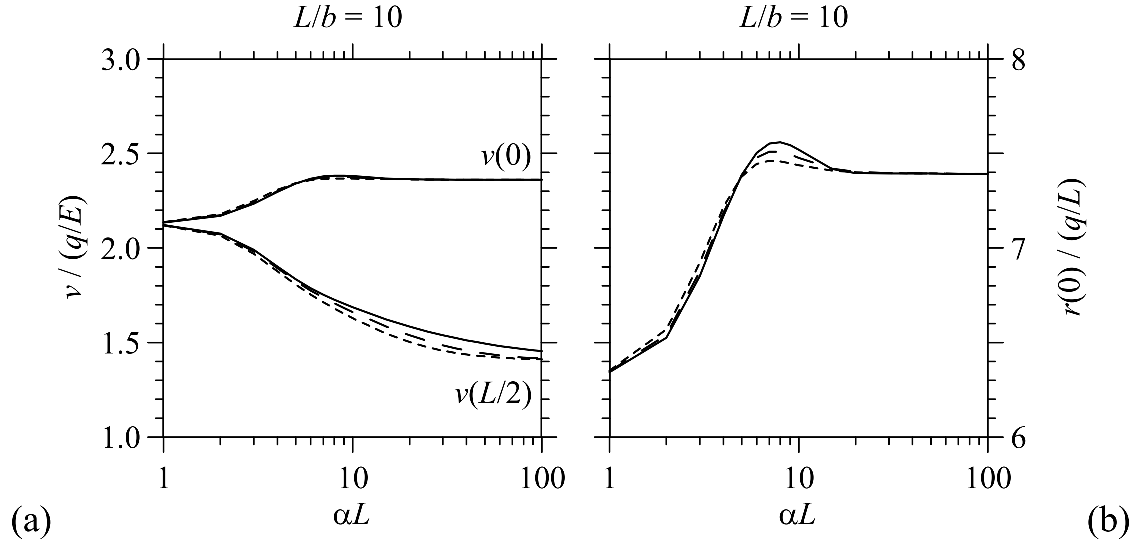

Fig. 4.34 – Beam on half space loaded by a uniform force distribution. Displacement at midpoint and at beam end, half-space pressure at midpoint for increasing αL.

Fig. 4.34a shows beam displacement at midpoint and at beam ends for increasing αL. For beam on stiff soil, both displacement tend to be similar, due to the rigid punch behaviour assumed by the beam. Increasing αL, displacement at midpoint tend to converge to a constant value close to 2.4 q/E, which is smaller than 2.51 $q/E = 0.8\ \pi\ q/E$, which is the solution of a rectangular loaded area having $a/b = 10$ (Love 1929), whereas displacement at beam ends is quite close to the analytic solution (1.48 $q/E = 0.47\ \pi\ q/E$).

4.6.3 Foundation beam loaded by a concentrated moment at midpoint

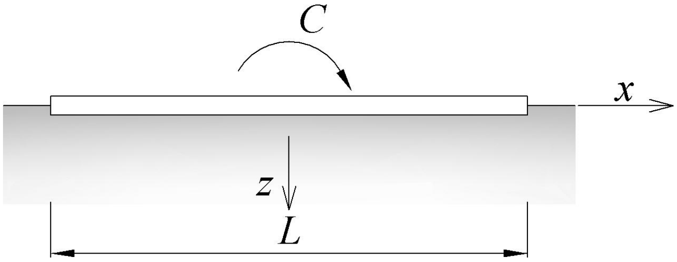

Fig. 4.35 – Foundation beam loaded by a concentrated moment C at midpoint.

The case of a foundation beam loaded by a concentrated moment C at midpoint is finally considered. Adopting $n_x = 2^8$, $n_{x,end} = 1$ and $n_y = 3$, beam displacements, surface pressures and bending moments along beam length are determined for $\chi = 10$ and different αL values.

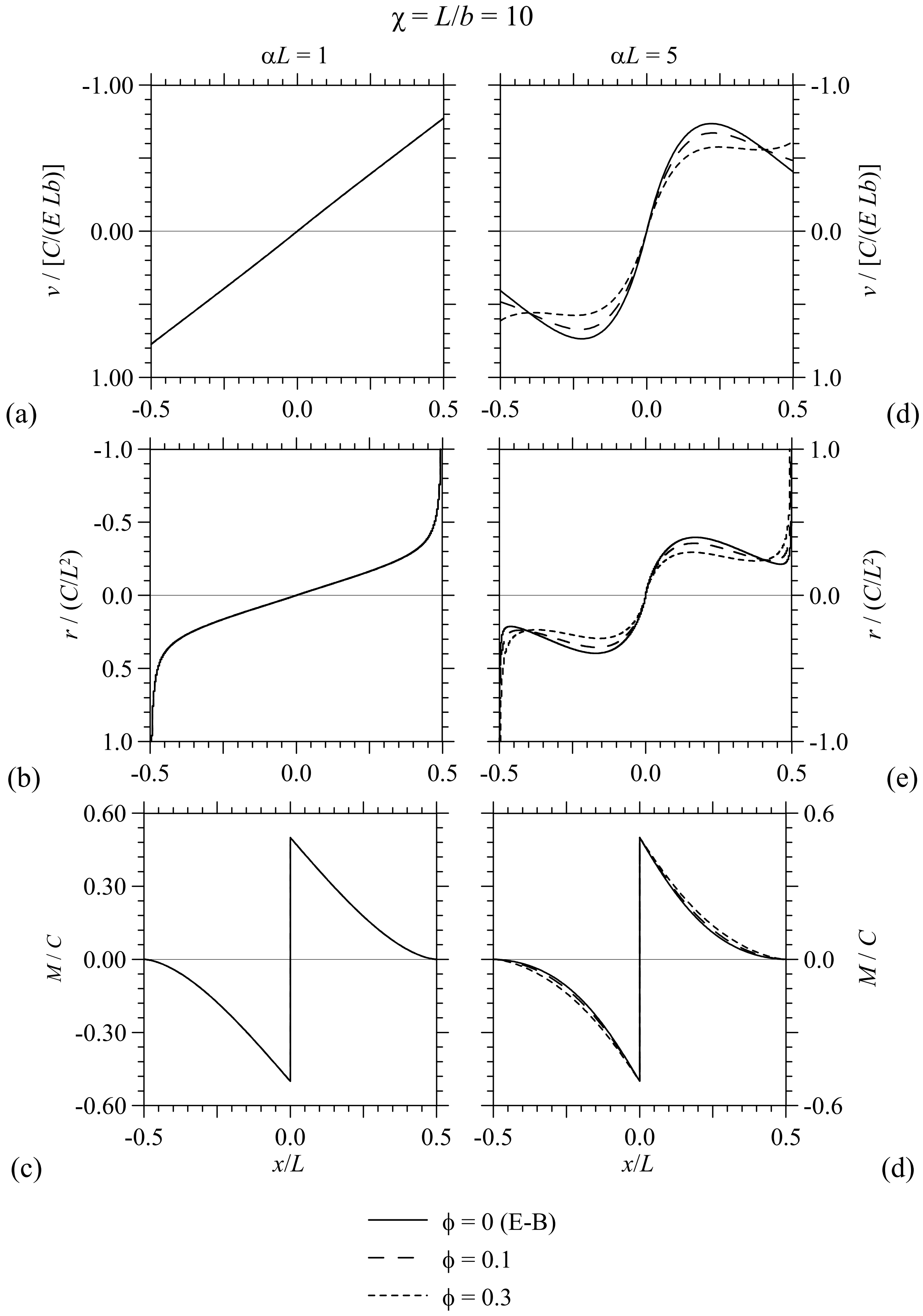

Fig. 4.36 – Foundation beam loaded at midpoint. Vertical displacement (a, d), half-space reactions (b, e) and bending moment (c, f) along the beam for $\alpha L = 1$ (a, b, c) and $\alpha L = 5$ (d, e, f).

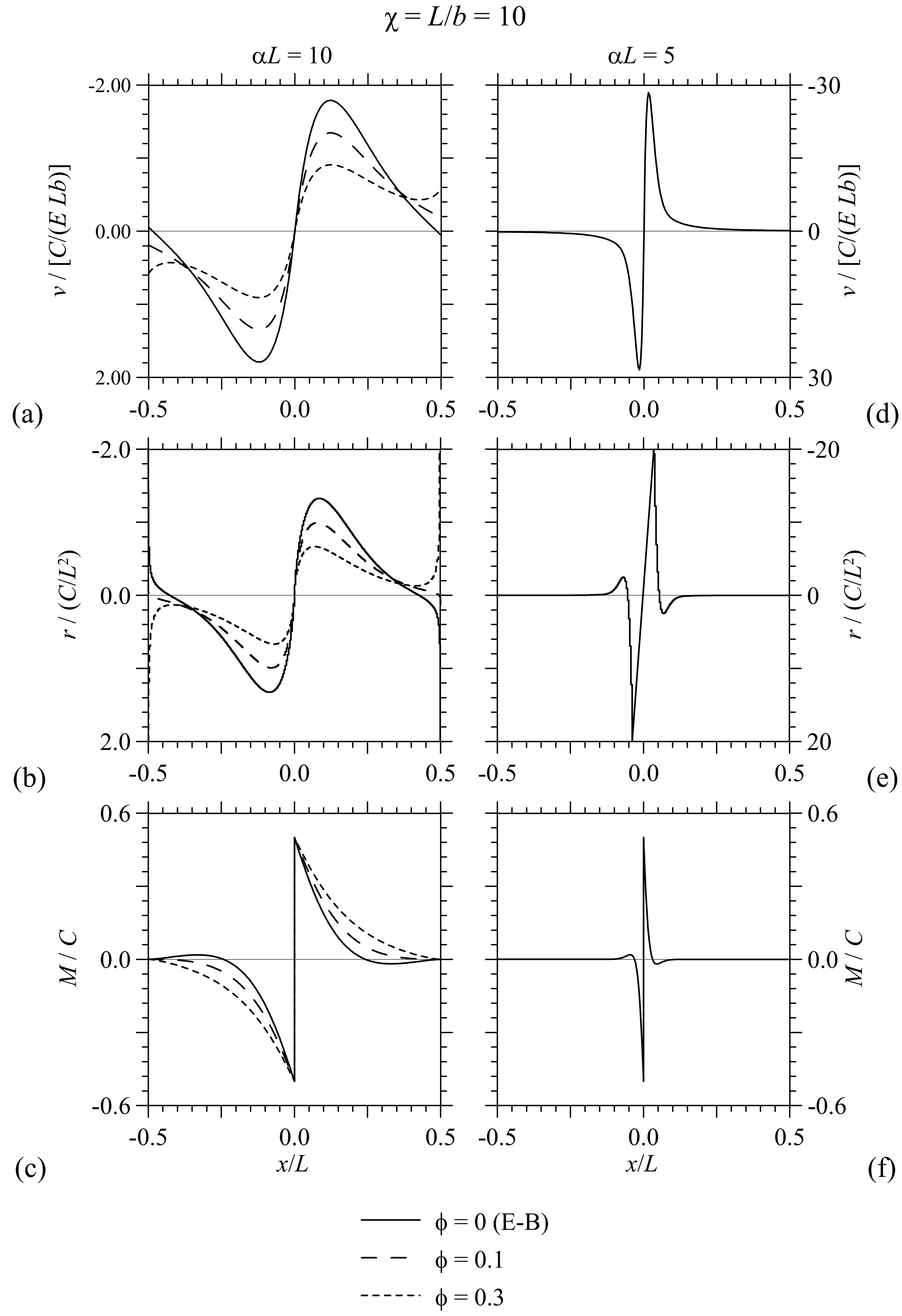

Fig. 4.37 – Foundation beam loaded at midpoint. Vertical displacement (a, d), half-space reactions (b, e) and bending moment (c, f) along the beam for $\alpha L = 10$ (a, b, c) and $\alpha L = 100$ (d, e, f).

Figs. 4.36a-c show results relative to αL = 1. In this case results do not depend appreciably on ϕ. Beam displacement is a rigid body rotation, whereas reactions present singularities near beam ends. For αL = 10, Figs. 4.37a-c show results quite different and depending on ϕ. For αL = 100, Figs. 4.37 d-f show results obtained with $\phi = 0$ (Euler-Bernoulli beam). In this case, the displacement, reaction and bending moment are concentrated close to beam midpoint, then a large number of subdivisions along x axis is necessary in order to obtain accurate results.

4.7 Buckling analysis of beams on 3D elastic half-space

The buckling of Euler-Bernoulli beams ($\phi = 0$) is considered. In order to obtain accurate results, the following examples adopt the same beam and surface discretizations considered for the static cases. Starting from a beam with aspect ratio χ = 10, critical loads and mode shapes are determined for increasing αL while considering three different end restraint cases. Then, similar analyses are carried out varying parameter χ.

4.7.1 Beam with sliding ends

The buckling of a beam with sliding ends on elastic half-space is considered. In Figs. 4.38a and b dimensionless critical loads $P_{\mathrm{cr}}/P_{\mathrm{cr,E}}$ are plotted versus αL^3 and αL, respectively. The curves appear to have a behaviour quite similar to the results obtained for the same beam on elastic half-plane. Critical loads increase for increasing αL and present crossing points and curve veering.
For αL equal to zero, critical loads converge to the values:

$$P_{\mathrm{cr},m}(0)/P_{\mathrm{cr,E}} = m^2 \quad \text{with } m = 1, 2, 3\ldots \tag{4.75}$$

typical of a beam with pinned or sliding ends without supporting medium. Fig. 4.38a clearly shows that each critical load is linearly dependent on αL^3, then an expression similar to the one defined by Reissner (1937) or Gallagher (1974) may be found. Normalized critical loads turn out to be proportional to the square of the beam-subgrade parameter αL. Fig. 4.38c shows the ratio $P_{\mathrm{cr}}/[P_{\mathrm{cr,E}}\,(\alpha L)^2]$ versus the parameter αL; for increasing αL, the ratios corresponding to the first eigenvalue converge to

$$P_{\mathrm{cr,3}} = 0.143\,P_{\mathrm{cr,E}}\,(\alpha L)^2\,. \tag{4.76}$$

which is obviously different with respect to the corresponding one determined for the case of the beam on elastic half-plane.
Figs. 4.39a-d show first and second mode shapes for increasing αL. Similarly to the case of the beam with sliding ends on elastic half-plane, mode shapes are sinusoidal and characterized by an increasing number of half-waves for

increasing αL. Moreover, half-waves amplitude is not uniform along beam length, but it is bigger close to beam midpoint with respect to its ends.

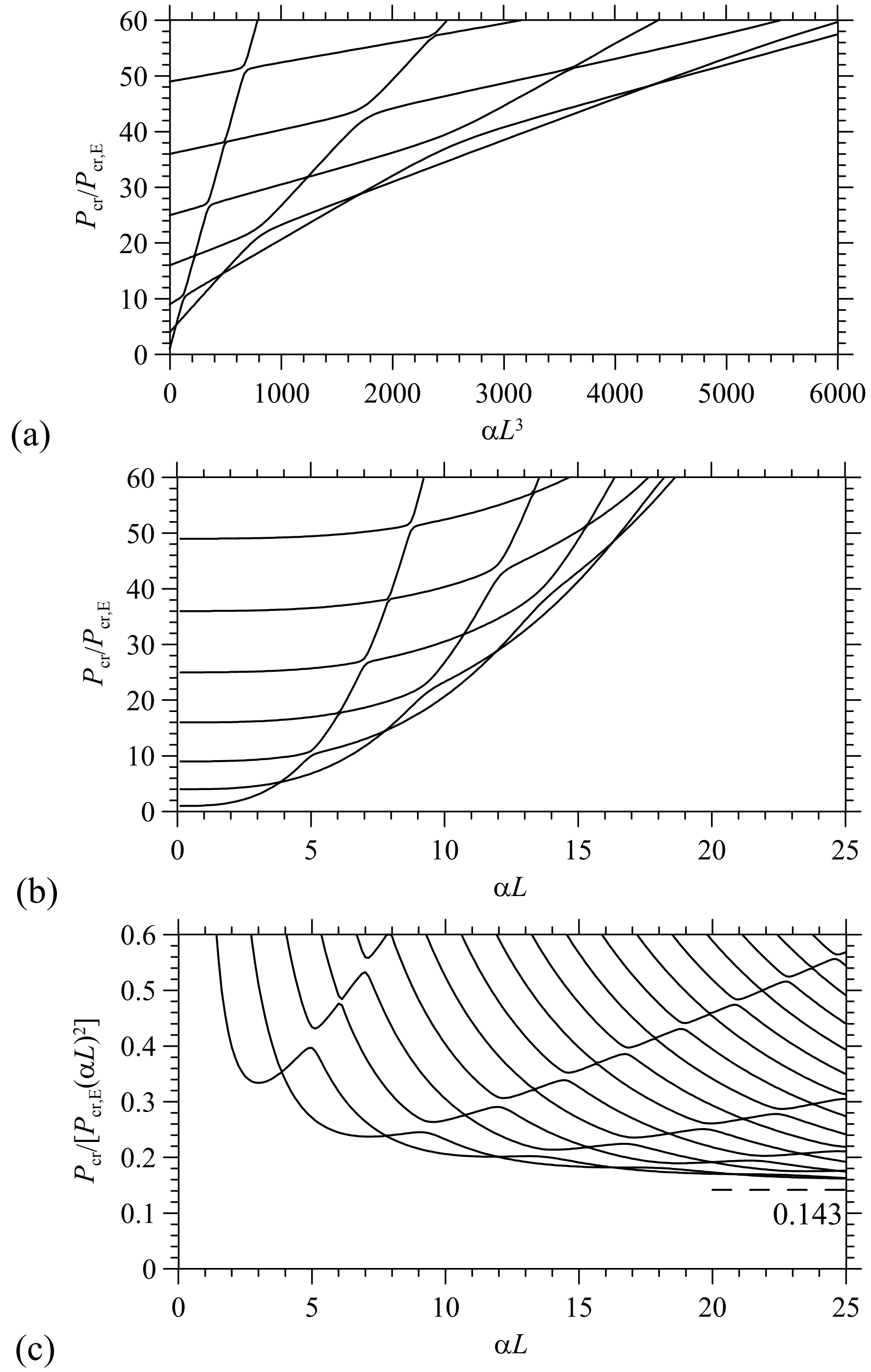
$\chi = L/b = 10$

Fig. 4.38 – Dimensionless critical loads P_{cr} versus αL for a beam with sliding ends on elastic half-space.

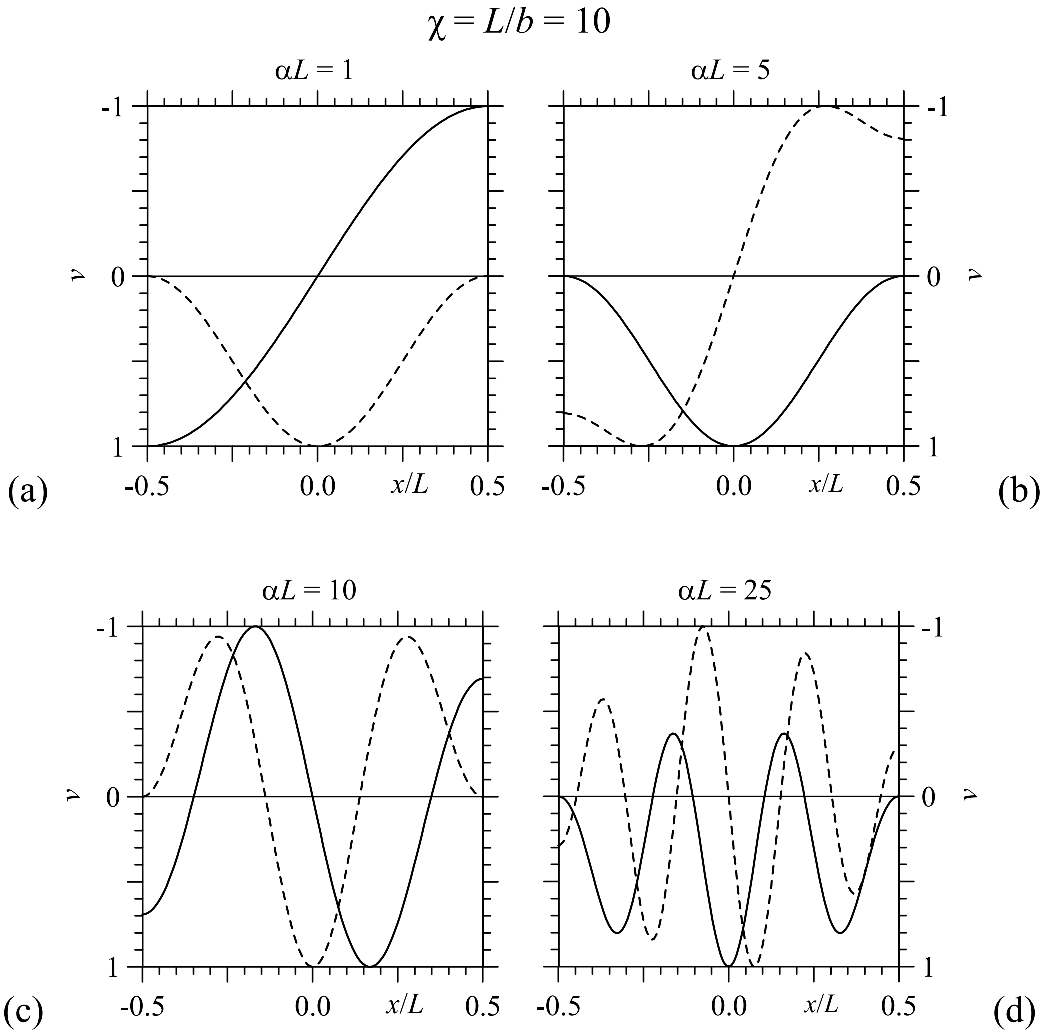

Fig. 4.39 – First (continuous line) and second (dashed line) mode shapes for a beam with sliding ends and αL equal to 1 (a), 5 (b), 10 (c) and 25 (d).

4.7.2 Beam with pinned ends

The buckling of a beam with pinned ends on elastic half-space is considered. In Figs. 4.40a and b, dimensionless critical loads $P_{\mathrm{cr}}/P_{\mathrm{cr,E}}$ are plotted versus αL^3 and αL, respectively. For αL equal to zero, critical loads converge to the values given in Eq. 30. Critical loads increase for increasing αL and present crossing points and curve veering, however first critical load appears quite far from other results, whereas second critical load is quite close to the third and fourth ones, differently with respect to the beam with pinned ends on elastic half-plane.

Considering Fig. 4.40c, for increasing αL, the first critical load converges to the following value:

$$P_{\mathrm{cr,1}} = 0.095 P_{\mathrm{cr,E}} (\alpha L)^2, \tag{4.77}$$

whereas the second critical load converges to

$$P_{\mathrm{cr,2}} = 0.136 P_{\mathrm{cr,E}} (\alpha L)^2, \tag{4.78}$$

which is smaller but quite close to Eq. 4.76, reached by the third and fourth critical loads. In particular, $P_{\mathrm{cr,2}}\,(\alpha L)^2$ is 95% of $P_{\mathrm{cr,3}}\,(\alpha L)^2$, this ratio is bigger with respect to the corresponding critical loads obtained for the beam on elastic half plane (0.106 / 0.121 = 88%). It is worth noting that values in Eqs. 4.78 and 4.76 are reached for large values of αL and in Fig. 4.40c, the second, third and fourth critical loads can not be distinguished.

Figs. 4.41a-f show first and second mode shapes for increasing αL. For $\alpha L = 5$ (Fig. 4.41a), first and second mode shapes are sinusoidal, whereas for $\alpha L = 10$ (Fig. 4.41b), first and second mode shapes can not be described by sinusoidal functions, similarly to the case of a beam with pinned ends on elastic half-plane. For $\alpha L = 15$ (Fig. 4.41c), the first mode shape is characterized by large deflection at beam ends, but the second mode shape is sinusoidal. Increasing αL, the first mode shape has the same behaviour found for the beam with pinned ends on elastic half-plane, characterized by large deflections at beam ends and negligible displacements near beam midpoint. In this case however, for $\alpha L = 20$, 25 and 50 (Fig. 4.41d-f), the second mode shape is characterized by large deflections at beam ends and sinusoidal deflections not negligible along its length. This behaviour may justify the corresponding critical load (Eq. 4.78), which is quite close to the third and fourth critical loads and to Eq. 4.76.

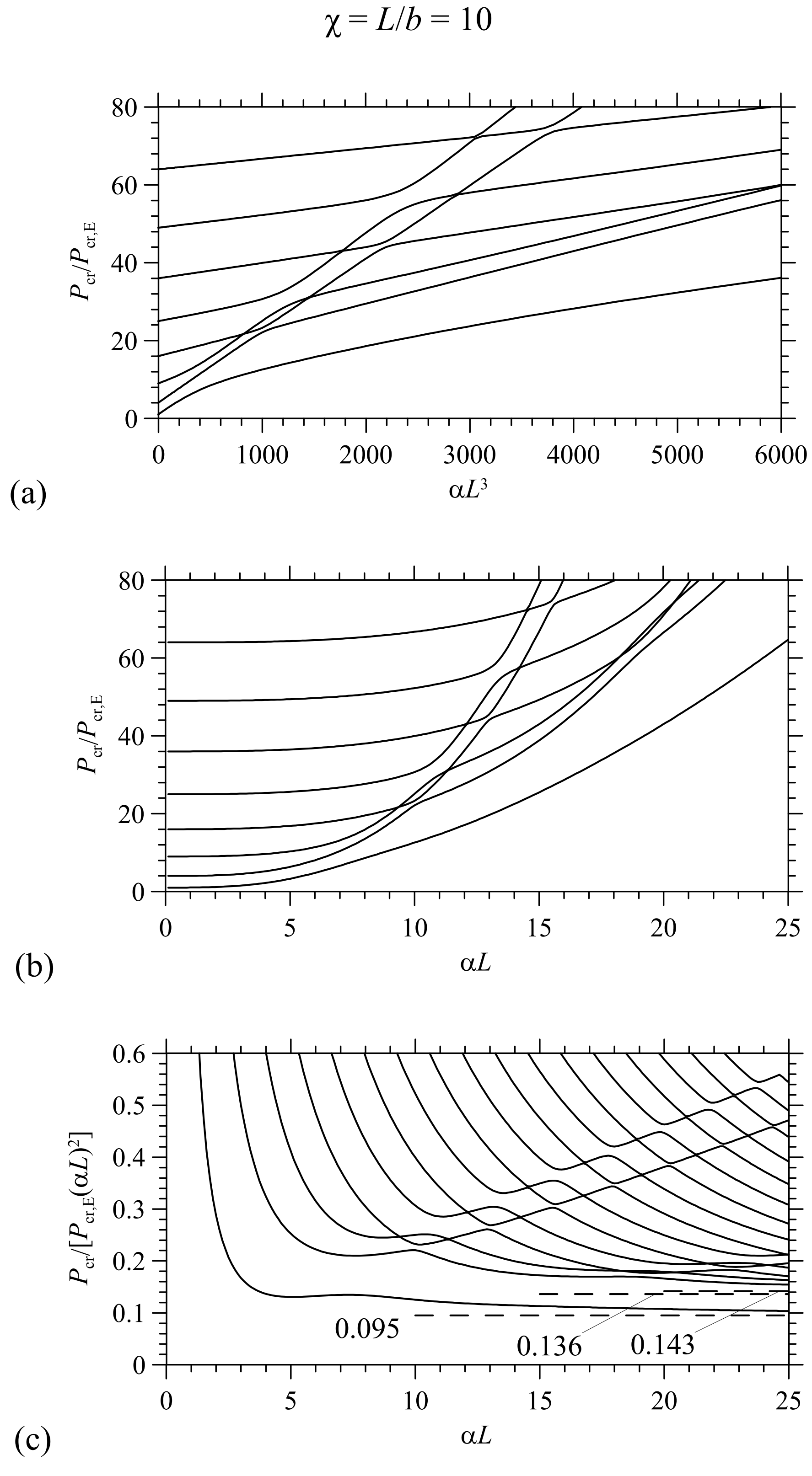

Fig. 4.40 – Dimensionless critical loads P_{cr} versus αL for a beam with pinned ends on elastic half-space.

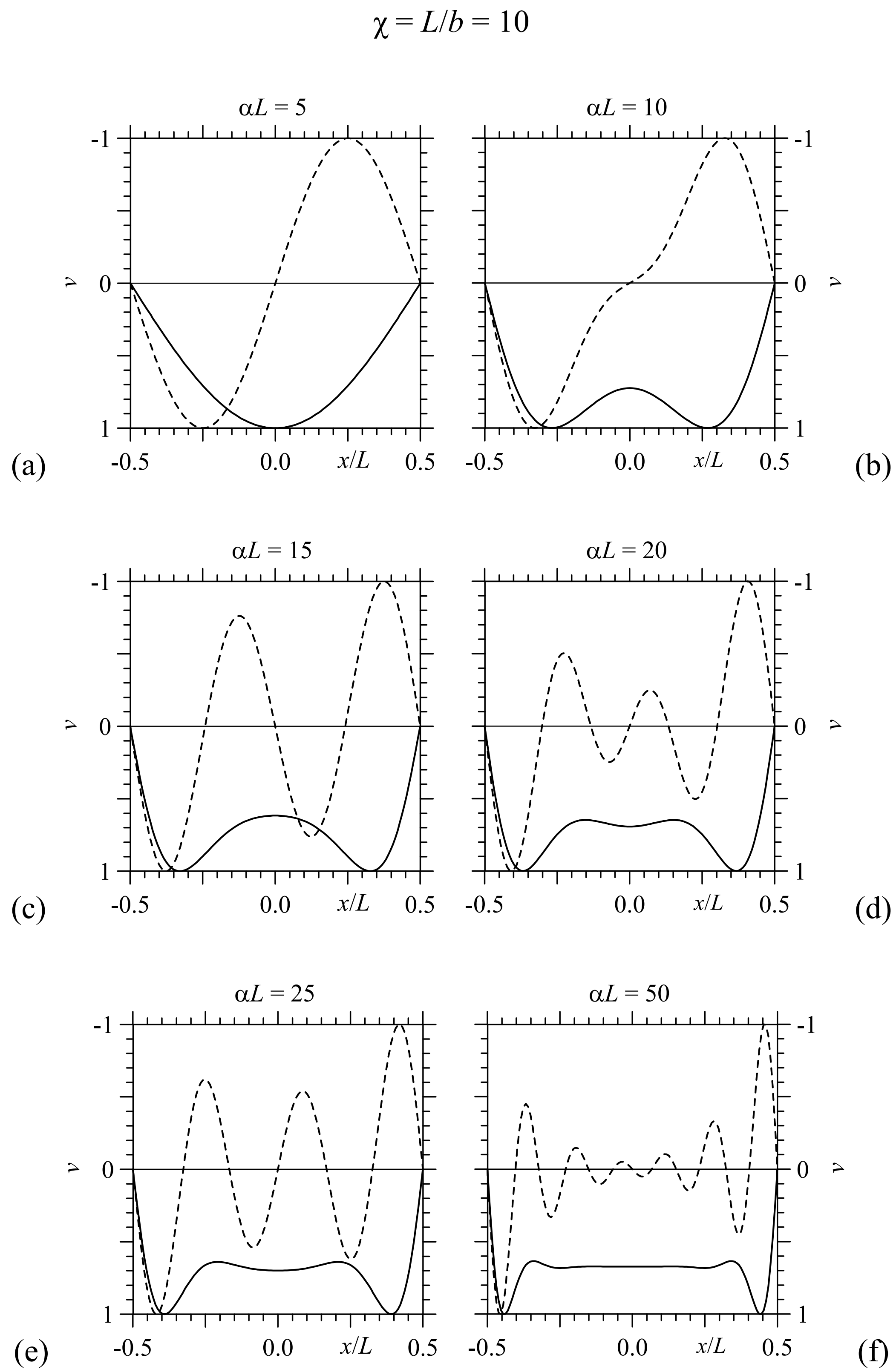

Fig. 4.41 – First (continuous line) and second (dashed line) mode shapes for a beam with pinned ends and αL equal to 5 (a), 10 (b), .15 (c) and 20 (d), 25 (e) and 50 (f).

4.7.3 Beam with free ends

The buckling of a beam with free ends on elastic half-space is finally considered. In Figs. 4.40a and b, the dimensionless critical loads $P_{\mathrm{cr}}/P_{\mathrm{cr,E}}$ are plotted versus αL^3 and αL, respectively. Fig. 4.40c shows the ratio $P_{\mathrm{cr}}/[P_{\mathrm{cr,E}}\ (\alpha L)^2]$ versus the parameter αL. Critical loads increase for increasing αL and present crossing points and curve veering. First and second critical loads, which are separated with respect to other results, present some crossing points and both converge to the value given in Eq. 4.77 for increasing αL, whereas the third and fourth eigenvalues converge to Eq. 4.76.

Figs. 4.43a-d show first and second mode shapes for increasing αL. Similarly to the case of the beam with free ends on elastic half-plane, for $\alpha L = 1$ (Fig. 4.43a) the first mode shape represents a rigid body rotation and the corresponding critical loads tends obviously to zero, whereas the second mode shape is sinusoidal. For $\alpha L = 5$ (Fig. 4.43b), after the first intersection point between first and second critical load curves, the fist mode shape is sinusoidal, but the second one is antisymmetric and characterized by large displacements at beam ends. Increasing αL (Figs. 4.43c and d), both mode shapes are characterized by large displacements at beam ends and negligible deformations close to beam midpoint. The symmetric mode shapes presented in Figs. 4.43a-d turn out to be obviously coincident with the first mode shape obtained for the beam with pinned ends.

$\chi = L/b = 10$

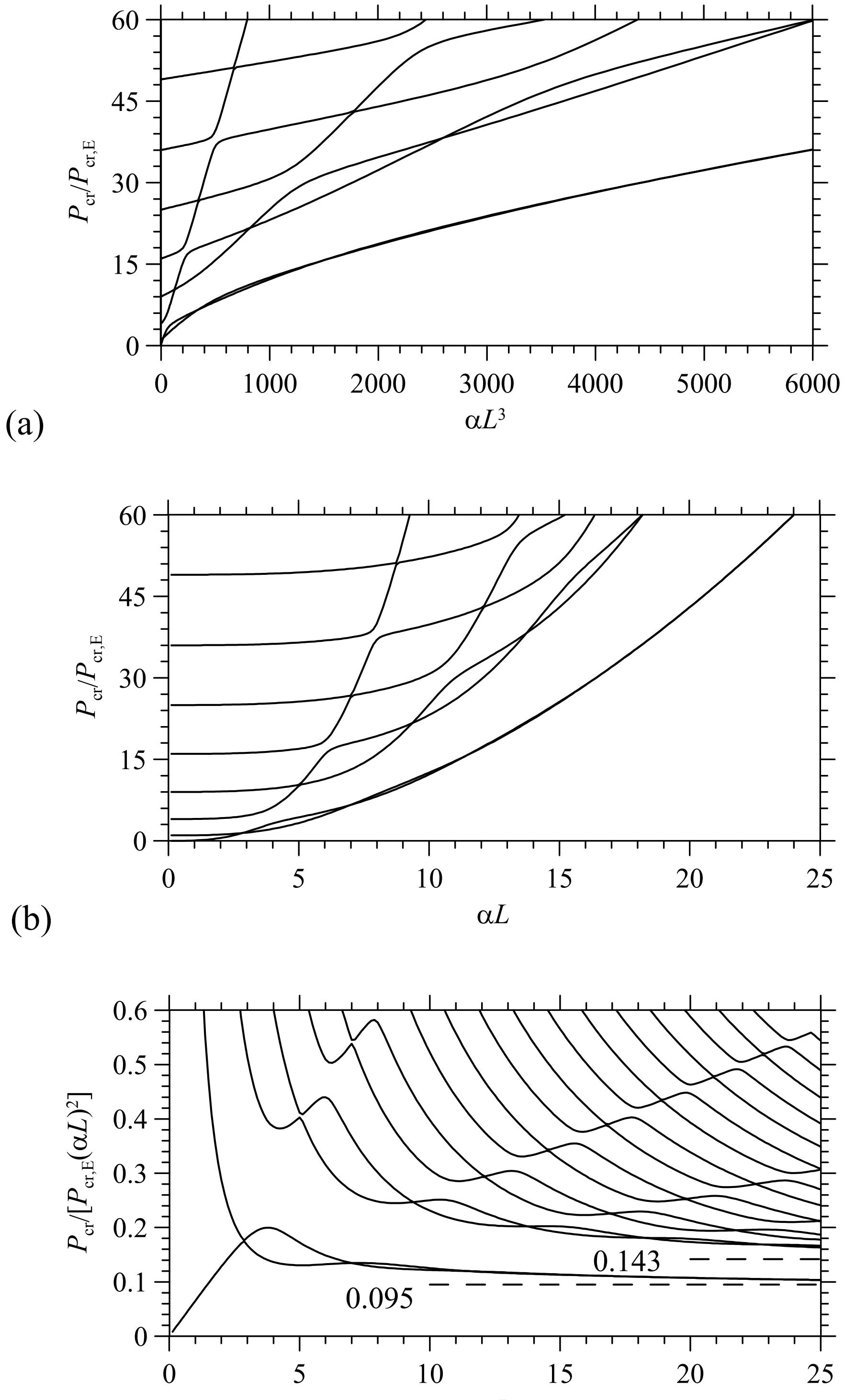

Fig. 4.42 – Dimensionless critical loads P_{cr} versus αL for a beam with free ends on elastic half-space.

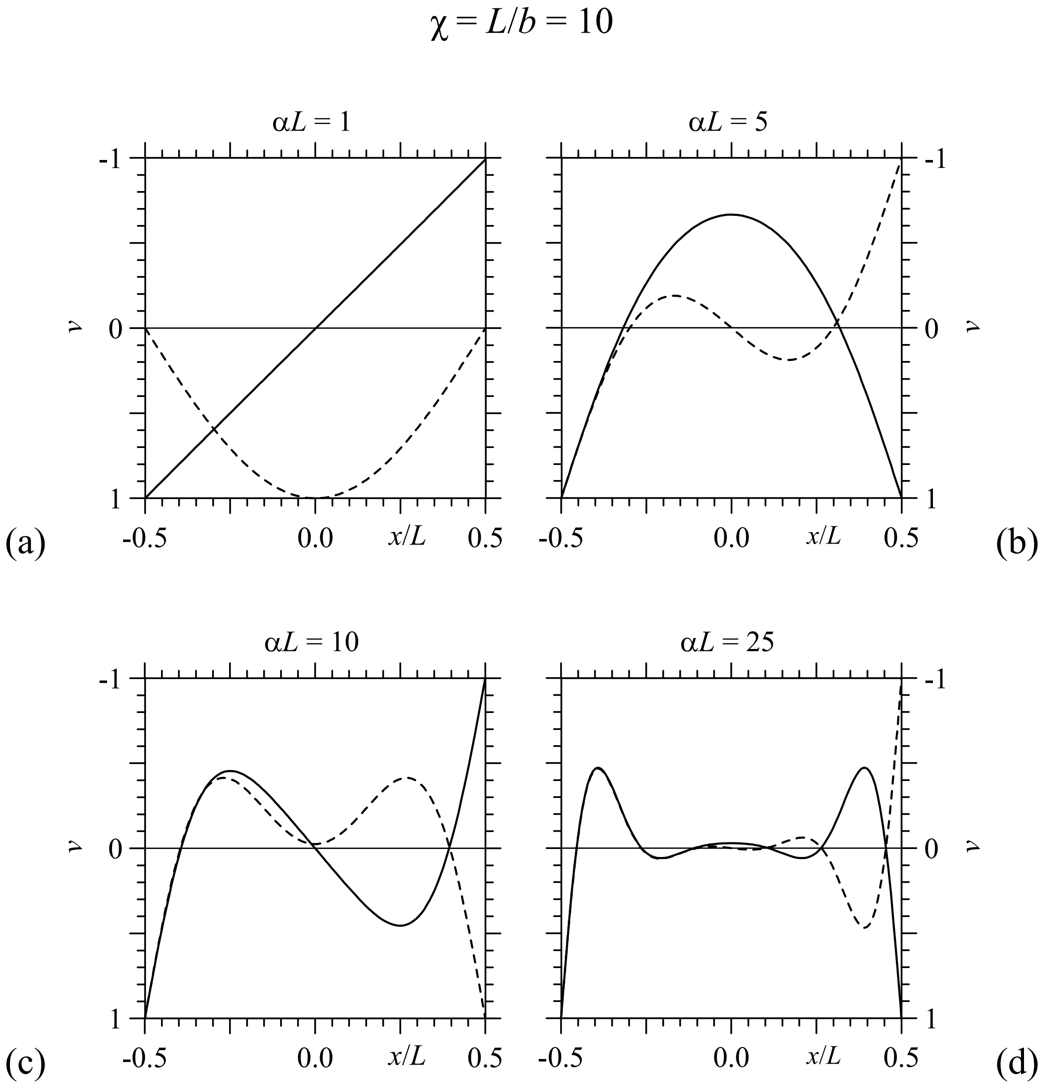

Fig. 4.43 – First (continuous line) and second (dashed line) mode shapes for a beam with free ends and αL equal to 1 (a), 5 (b), 10 (c) and 25 (d).

4.7.4 Critical loads of a beam on stiff half-space varying *L*/*b* ratio

Varying χ, critical loads follow the same behaviour described for $\chi = 10$ for all the beam cases considered. Then the buckling of a beam with a generic *L*/*b* ratio on a three-dimensional half-space turns out to be similar to the behaviour of any beam on an elastic support. However, the values presented in Eqs. 4.77, 4.78 and 4.76, which correspond to the dimensionless critical load of a beam on very stiff soil (large αL), strictly depend on χ. Then, varying χ, dimensionless critical loads are determined for increasing αL. Tab. 4.4 collects $P_{\mathrm{cr},1}/[P_{\mathrm{cr,E}}\,(\alpha L)^2]$, $P_{\mathrm{cr},2}/[P_{\mathrm{cr,E}}\,(\alpha L)^2]$, and $P_{\mathrm{cr},3}/[P_{\mathrm{cr,E}}\,(\alpha L)^2]$ values varying χ.

$P_{\mathrm{cr},i}/[P_{\mathrm{cr,E}}\,(\alpha L)^2]$	2D (§1)	$\chi = L/b$								
		0.1	1	2	3	4	5	10	50	100
1	0.083	0.083	0.084	0.086	0.087	0.088	0.089	0.095	0.124	0.147
2	0.106	0.107	0.112	0.115	0.119	0.122	0.125	0.136	0.194	0.240
3	0.121	0.122	0.124	0.126	0.128	0.130	0.133	0.143	0.199	0.244

Tab. 4.4 – Dimensionless critical loads varying χ.

Dimensionless critical loads increase for increasing χ; moreover, the second dimensionless critical load tends to be more and more close to the third one increasing χ. For example, for $\chi = 1$ the ratio between $P_{\mathrm{cr},2}$ and $P_{\mathrm{cr},3}$ is close to 0.9, whereas for $\chi = 100$ the same ratio is close to 0.98. Then, increasing χ, the second critical load tends to converge to the third and fourth one. This behaviour is clearly shown in Fig. 4.45 as, where, for increasing χ, the curves corresponding to the second and the third critical load tend to converge.

Figs. 4.44a-f show the second mode shapes for a beam with pinned ends for $\alpha L = 50$ and increasing χ. It is clear that the large beam deflections are located close to beam ends in all the cases considered, but, increasing χ, beam displacements along beam length become bigger and bigger. In particular, Figs. 4.44e and f show that beam deflections turn out to be sinusoidal with different amplitude along beam length and half-wave length appears to be constant. This behaviour is quite similar to the one that can be obtained with a beam with sliding ends and increasing αL. Moreover, this behaviour turns out to be quite similar to the one of the beam with pinned ends on Winkler half space (§ 1.5.3.4), which is characterized by the second critical load converging to the same value of the third and fourth eigenvalues and the corresponding mode shape is sinusoidal over the entire beam length.

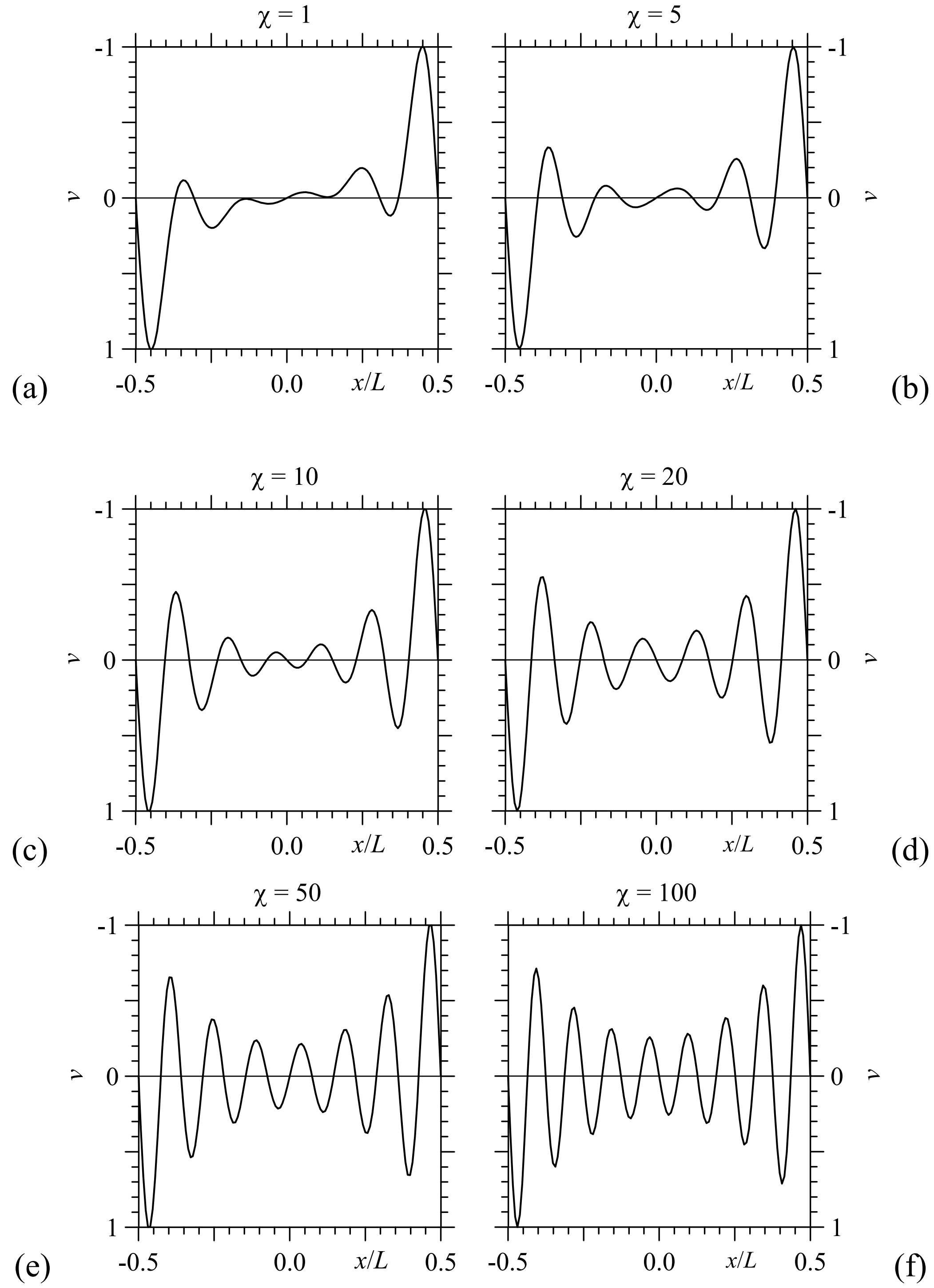

Fig. 4.44 – Second mode shape for a beam with pinned ends, αL = 50 and χ = 10 (a), 20 (b), 50 (c) and 100 (d).

For low values of χ, the beam is characterized by a very short length with respect to its width. However, buckling modes along beam width are not allowed by the model adopted; then, dimensionless critical loads for $\chi < 1$ can be also determined. Results are shown in Fig. 4.45 together with values collected in Tab. 4.4.

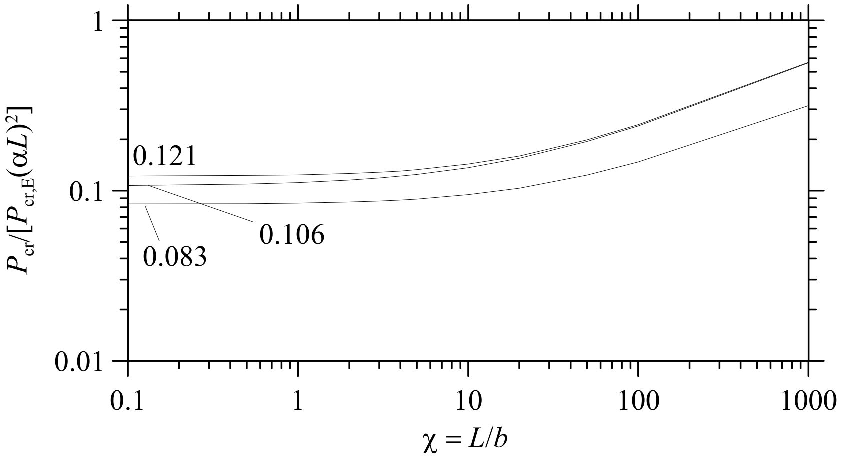

Fig. 4.45 – First three dimensionless critical loads of a beam on stiff half-space versus χ

The case of a beam having a large width with respect to its length, neglecting deformations along beam width, is quite close to a plane strain condition. In fact, for χ tending to zero, critical loads $P_{\mathrm{cr},i}$ for i = 1, 2 3, are very close to the corresponding ones obtained for the beam on elastic half plane:

$$P_{\mathrm{cr},1}^{\mathrm{PA\,2D}} = 0.083\, P_{\mathrm{cr,E}} (\alpha L)^2 , \tag{4.79a}$$

$$P_{\mathrm{cr},2}^{\mathrm{PA\,2D}} = 0.106\, P_{\mathrm{cr,E}} (\alpha L)^2 , \tag{4.79b}$$

$$P_{\mathrm{cr},3}^{\mathrm{PA\,2D}} = 0.121\, P_{\mathrm{cr,E}} (\alpha L)^2 . \tag{4. 79c}$$

Conclusions

In the first chapter of this thesis, the simple and effective FE-BIE coupling method proposed by Tullini and Tralli (2010) is applied to stability problems of Euler-Bernoulli beams on elastic half-plane with finite length, different end restraints and for a beam with a weak section at midpoint. The parameter αL has been adopted to describe the interaction between beam and half-plane; low values of αL represent short beams on soft half-plane, whereas large values of αL represent long beams on stiff half-plane. The present model has turned out to be effective in evaluating buckling loads and the corresponding mode shapes; moreover, the model has turned out to be faster than traditional models, characterized by the half-plane modelled by 2D FEs. For increasing beam slenderness and/or soil stiffness, a variation of critical loads proportional to $(\alpha L)^2$ has been found. For low values of αL, the well-known analytic results derived by Reissner (1937) and Murthy (1973) for a beam of infinite length on elastic half-plane are quite similar to those of a beam with either pinned or sliding ends; whereas, for large values of αL, Reissner results are well achieved by beams with sliding ends. Comparing the smallest critical load of a beam with sliding ends on half-plane with that of a beam on Winkler half-space, a relation between half-plane parameters and Winkler subgrade constant has been determined. Then, analyses performed for beams with pinned or free ends show that the first two critical loads are smaller than those obtained by Reissner. The corresponding mode shapes are characterized by large amplitudes close to beam ends, whereas third and fourth critical loads converge to the value given by Reissner. Similar behaviour has been found for beams with pinned or free ends on Winkler half-space, if rigid body vertical displacements are allowed, as it was underlined by Goodier and Hsu (1954). Moreover, the solution derived by Gallagher (1974) for the buckling of a beam with pinned ends on elastic half plane has found to be almost coincident with the results obtained with the present model for a beam with sliding ends. Then, the present model has been used for performing nonlinear incremental analysis of beams including second order effects and finally, nonlinear incremental analyses of rectangular frames with compressed columns and free or pinned foundation ends have been considered. As for pipes with pinned foundation ends, snapthrough instability is significant for pipes stiffer than the soil. The most important results showed in this chapter, such as the new critical load values related to mode shapes with large displacements close to beam ends and the nonlinear analysis of pipes, have recently been presented in Tullini et al. (2013).

Then, in the second chapter, the simple and effective finite element model adopted in Tullini and Tralli (2010) has turned out to be fast and effective also for the determination of critical loads of Timoshenko beams. In particular, two beam slenderness cases have been considered (L/h = 5 and 15). The results of the present model have been compared with those obtained with a traditional 2D FE model. For a simply supported beam without supporting soil, numerical results are in excellent agreement with the classical analytical solutions. For beams on stiff soil, i.e. for large values of αL, the buckling loads converge to the critical load $P_{\mathrm{cr},\infty}$, which is also reached by beams on Winkler half-space increasing Winkler subgrade constant. However, buckling loads determined with the 2D finite element model converge to values smaller than $P_{\mathrm{cr},\infty}$. In particular, for the slender beam on stiff soil (L/h = 15, $\alpha L = 25$), the first and second buckling modes are characterised by localization of deformations near beam ends; whereas, for short beams on stiff soil (L/h = 5, $\alpha L = 25$), the first two buckling modes present short wavelength depending on mesh size. In this case the buckling mode is localized in the upper part of the beam and a beam model is unable to describe such a behaviour. Nonetheless, the Timoshenko beam model appears to be very useful in determining buckling loads in good agreement with the reference solutions. Conversely, the Euler-Bernoulli beam model provides satisfactory results for long beams on soft soil. The results obtained in this chapter have recently been proposed and discussed by Tullini et al. (2012b).

In the third chapter, analyses of slender beams and frames on elastic half-plane have been performed including material nonlinearity for the structure. For this purpose, the efficient procedure proposed by Hasan et al. (2002) for pushover analysis of frames has been adopted. Material nonlinearity has been introduced into the discrete model by lumping it at the end of beam FEs without increasing the total number of degrees of freedom, but simply modifying the stiffness matrices of the FEs, adopting the procedure commonly used for modelling semi-rigid connections introduced by Monforton and Wu (1963), Xu (1992) and improved by Shakourzadeh et al. (1999). Incremental analyses of beams including material nonlinearity have been carried out up to the development of a three-hinge mechanism. Then, a pipe on half-plane representing a reinforced concrete box culvert, built to grant the flow of a stream under a railway, has been studied. Potential plastic hinges have been placed at beam-column connections and at beams midpoint. Three incremental analyses have been performed by increasing service loads and lateral earth pressures up to the development of a collapse mechanism. The present model has turned out to be simple and effective for the determination of the ultimate loads of the structure, which are smaller than the corresponding limit loads, determined applying the collapse mechanism to a portal frame, due to the soft soil support under the pipe. Finally, in the fourth chapter, the static and buckling analyses of beams on a 3D half-space have been considered. Starting from Boussinesq solution for the displacement generated by a normal force acting on half-space surface, the Galerkin boundary element method has been considered by discretizing surface pressures and displacements with a piecewise constant function. The problem of the indentation of a rigid punch on the half-space has been solved and the stiffness of a square foundation turned out to be in excellent agreement with other numerical solutions. Moreover, displacements generated by a uniform pressure over a rectangular area turned out to be in good agreement with Love (1929) analytic solution. Then, a Timoshenko beam with finite length on elastic half-space has been studied by extending the approach proposed by Tullini and Tralli (2010) to the half-space case. The parameter αL has been considered together with the new parameter χ, representing the ratio between beam length and width. Several examples have been performed in order to determine beam displacement, beam bending moment and half-space reactions. Finally, buckling analyses of Euler-Bernoulli beams on elastic half-space with different end restraints have been performed. Critical loads and mode shapes turned out to have a behaviour similar to that found in the first chapter and, for decreasing χ, the values of the first three critical loads of a beam with pinned ends turned out to be quite close to those of the same beam on half-plane.

It is worth noting that a traditional model for representing structures on elastic half-space is very difficult to realize and study. Therefore, the present model represents a promising tool for studying three dimensional frames on half-space, performing elastic analyses or including second order effects due to axial loads.

4.8 Appendix A1 – Discrete model for a beam on 2D half-space

For a prismatic Timoshenko beam element having length l_i, subjected to uniform loads $p(x)$ and with a constant soil pressure, element matrices are:

$$\tilde{\mathbf{K}}_{bi} = \frac{L^3}{(1+\phi_i)l_i^3}\begin{bmatrix} 12 & -6l_i & -12 & -6l_i \\ & (4+\phi_i)l_i^2 & 6l_i & (2-\phi_i)l_i^2 \\ & & 12 & 6l_i \\ \text{sym} & & & (4+\phi_i)l_i^2 \end{bmatrix}, \tag{A.1}$$

$$\tilde{\mathbf{K}}_{gi} = \frac{L}{(1+\phi_i)^2 l_i}\begin{bmatrix} \frac{6}{5}+a_i & -\frac{l_i}{10} & -\left(\frac{6}{5}+a_i\right) & -\frac{l_i}{10} \\ & \left(\frac{2}{15}+\frac{a_i}{12}\right)l_i^2 & \frac{l_i}{10} & -\frac{l_i^2}{30}\left(1+\frac{5a_i}{2}\right) \\ & & \frac{6}{5}+a_i & \frac{l_i}{10} \\ \text{sym} & & & \left(\frac{2}{15}+\frac{a_i}{12}\right)l_i^2 \end{bmatrix}, \tag{A.2}$$

with $\phi_i = 12D_b/(k_b G_b A\, l_i^2)$, $a_i = (2+\phi_i)\,\phi_i$,

$$\mathbf{F}_i = p\,[l_i/2,\ -l_i^2/12, l_i/2,\ l_i^2/12]^{\mathrm{T}}, \tag{A.3}$$

$$\mathbf{H}_i = [l_i/2,\ -l_i^2/12, l_i/2,\ l_i^2/12]^{\mathrm{T}}, \tag{A.4}$$

$$\tilde{g}_{ii} = \frac{2}{\pi} l_i^2\left(\frac{3}{2}-\ln l_i\right), \tag{A.5}$$

$$\tilde{g}_{ij} = \frac{2}{\pi}\left[\frac{3}{2}l_i l_j + G(x_{j+1}-x_{i+1}) - G(x_{j+1}-x_i) - G(x_j - x_{i+1}) + G(x_j - x_i)\right] \quad \text{for } i \neq j \tag{A.6}$$

where $G(x) = x^2/2\ \ln|x|$.

Setting $\phi_i = 0$, $\tilde{\mathbf{K}}_{bi}$ and $\tilde{\mathbf{K}}_{gi}$ turn out to be equal to the stiffness and geometric matrix o fan Euler-Bernoulli beam element.

4.9 Appendix A2 – Discrete model for a beam on Winkler half-space

The idealized model of half-space proposed by Winkler (1867) assumes that the deflection v at a point of the surface is directly proportional to the stress or soil pressure r applied at the same point and independent of stresses applied at other locations:

$$r(x) = c \cdot v(x) \tag{A.7}$$

where c is a constant known as the Winkler constant or the modulus of subgrade reaction. Physically, Winkler's half-space idealization model consists on a system of elastic springs mutually independent and having elastic constant equal to c.

The potential energy of a beam resting on a Winkler soil and considering second order effects due to axial load is given by same expression adopted for the beam on elastic half-plane, however in this case reactions r are given by Eq. A.1.32, then the total potential energy becomes:

$$\Pi(v) = \Pi_e - b\int_L p(x)\, v(x)\, \mathrm{d}x + \int_L c\,[v(x)]^2\, \mathrm{d}x\,, \tag{A.8}$$

where Π_e is the energy of the Timoshenko beam.

Adopting the same discrete model defined for the half-plane case, the total potential energy, written in discrete form, is given by:

$$\Pi(\mathbf{q}) = \frac{1}{2}\mathbf{q}^T(\mathbf{K}_b + \mathbf{K}_W)\,\mathbf{q} - b\mathbf{q}^T\mathbf{F} \tag{A.9}$$

Where $\mathbf{K}_W$ is the stiffness matrix of the Winkler half-space.

Considering a generic Timoshenko beam element of length l_i, the corresponding foundation stiffness matrix is (Yokoyama 1987):

$$\mathbf{K}_{Wi} = \frac{c l_i}{840(1+\phi_i)^2}\begin{bmatrix} 4\,k_{wi,11} & -l_i\,k_{wi,12} & 4\,k_{wi,13} & l_i\,k_{wi,14} \\ & l_i^2\,k_{wi,22} & -l_i\,k_{wi,23} & -l_i^2\,k_{wi,24} \\ & & 4\,k_{wi,33} & l_i\,k_{wi,34} \\ \text{sym} & & & l_i^2\,k_{wi,44} \end{bmatrix} \tag{A.10}$$

$$
\begin{aligned}
k_{wi,11} &= k_{wi,33} = 78 + 147\phi_i + 70\phi_i^2 \\
k_{wi,12} &= k_{wi,34} = 44 + 77\phi_i + 35\phi_i^2 \\
k_{wi,13} &= 27 + 63\phi_i + 35\phi_i^2 \\
k_{wi,23} &= k_{wi,14} = 26 + 63\phi_i + 35\phi_i^2 \\
k_{wi,22} &= k_{wi,44} = 8 + 14\phi_i + \phi_i^2 \\
k_{wi,24} &= 6 + 14\phi_i + 7\phi_i^2
\end{aligned}
\tag{A.11}
$$

4.10 Appendix A3 – Discrete model for a layer on 2D half-space

A simple discretization of the layer can be created by subdividing the domain horizontally and vertically in $n_{el,x}$ and $n_{el,y}$ subdivisions, respectively, obtaining a mesh of $n_{el} = n_{el,x} \times n_{el,y}$ quadrilateral elements having length l_i and height h_i. For simplicity, a mesh of equal quadrilateral elements is considered (Fig. 27), in order to adopt isoparametric quadrilateral elements to represent layer behaviour.

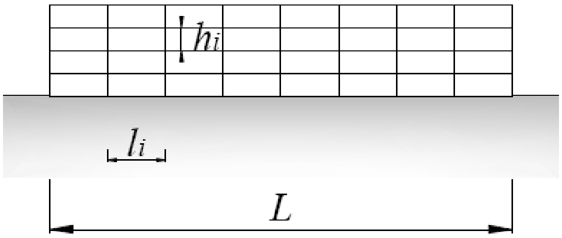

Fig. A.1 – Layer subdivided into 4 × 8 = 32 equal quadrilateral elements.

Each quadrilateral element is defined by four nodes in natural coordinates (ξ,η), which are interpolated as

$$\xi = \sum_{i=1}^{4} N_i \, \xi_i; \quad \eta = \sum_{i=1}^{4} N_i \, \eta_i \tag{A.12}$$

where N_i are the Lagrange shape functions:

$$N_1(\xi,\eta) = \frac{1}{4}(1-\xi)(1-\eta), \quad N_2(\xi,\eta) = \frac{1}{4}(1+\xi)(1-\eta), \tag{A.13a,b}$$

$$N_3(\xi,\eta) = \frac{1}{4}(1+\xi)(1+\eta), \quad N_4(\xi,\eta) = \frac{1}{4}(1-\xi)(1+\eta), \tag{A.13c,d}$$

which are also adopted for interpolating the displacement field in each element by the nodal displacements:

$$u^e = \sum_{i=1}^{4} N_i \, u_i; \quad v^e = \sum_{i=1}^{4} N_i \, v_i \, . \tag{A.14}$$

Displacements can also be expressed in matrix form as

$$\begin{bmatrix} u^e \\ v^e \end{bmatrix} = \begin{bmatrix} N_1 & 0 & N_2 & 0 & N_3 & 0 & N_4 & 0 \\ 0 & N_1 & 0 & N_2 & 0 & N_3 & 0 & N_4 \end{bmatrix} = \mathbf{N}\,\mathbf{q}_e \, . \tag{A.15}$$

And the strain vector is obtained by derivation of the displacements:

$$\begin{bmatrix} \varepsilon_x \\ \varepsilon_y \\ \gamma_{xy} \end{bmatrix} = \begin{bmatrix} \dfrac{\partial N_1}{\partial x} & 0 & \cdots & \dfrac{\partial N_4}{\partial x} & 0 \\ 0 & \dfrac{\partial N_1}{\partial y} & \cdots & 0 & \dfrac{\partial N_4}{\partial y} \\ \dfrac{\partial N_1}{\partial y} & \dfrac{\partial N_1}{\partial x} & \cdots & \dfrac{\partial N_4}{\partial y} & \dfrac{\partial N_4}{\partial x} \end{bmatrix} \mathbf{q}_e = \mathbf{B}\,\mathbf{q}_e\,. \tag{A.16}$$

The potential energy in discrete form can be defined at each element by

$$\Pi_e(\mathbf{q}) = \frac{1}{2}\mathbf{q}_e^T \mathbf{K}_{be}^{2\text{D}}\,\mathbf{q} - b\,\mathbf{q}_e^T \mathbf{F}_e^{2\text{D}}\,. \tag{A.17}$$

The element stiffness matrix and the vector of nodal forces are obtained as:

$$\mathbf{K}_{be}^{2\text{D}} = b \int_{A,e} \mathbf{B}^T C \mathbf{B}\, dA, \quad \mathbf{F}_e^{2\text{D}} = b \int_{s,e} \mathbf{N}^T t\, ds\,, \tag{A.18}$$

where A and s are the area and the boundary of the generic element of the layer. The integral in the stiffness matrix is computed numerically by Gauss quadrature in two dimensions. Considering 2×2 Gauss points, for example, the stiffness matrix turn out to be:

$$\mathbf{K}_{be}^{2\text{D}} = b \int_{A,e} \mathbf{B}^T C \mathbf{B}\, dA = b \int_{-1}^{1}\int_{-1}^{1} \mathbf{B}^T C \mathbf{B} \det \mathbf{J}\, d\xi\, d\eta = b \sum_{i=1}^{2}\sum_{j=1}^{2} \mathbf{B}^T C \mathbf{B} \det \mathbf{J}\; w_i w_j\,, \tag{A.19}$$

where det **J** is the determinant of the Jacobian matrix, introduced for relating natural coordinates and global coordinates and w_i, w_j are the Gauss weights.

4.11 Appendix A4 – Discrete model for a beam with semi-rigid ends (Monforton-Wu-Xu)

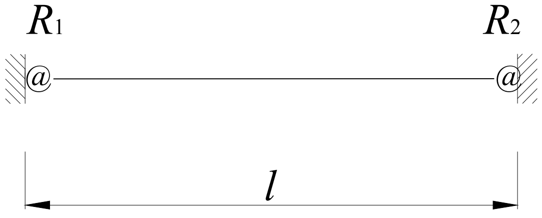

Fig. A.2 – Beam-column element with semirigid ends.

Considering a generic beam-column element having semi-rigid connections at its ends (Fig. A.2), r_1 and r_2 are the flexural rigidity factors at each end:

$$r_i = \frac{\phi_i}{\theta_i} = \frac{1}{1+(3D_b / R_i l)} \quad i = 1, 2, \tag{A.20}$$

Where D_b and l are beam bending stiffness and length, respectivel
Then, first and second order correction matrices $\mathbf{C}_e$ and $\mathbf{C}_g$ are given by (Monforton and Wu 1963, Xu 1992, Hasan et al. 2002):

$$\mathbf{C}_e = \frac{1}{4-r_1 r_2}\begin{bmatrix} 4-r_1r_2 & 0 & 0 & 0 & 0 & 0 \\ 0 & 4r_2-2r_1+r_1r_2 & -2l\, r_1(1-r_2) & 0 & 0 & 0 \\ 0 & 6(r_1-r_2)/l & 3r_1(2-r_2) & 0 & 0 & 0 \\ 0 & 0 & 0 & 4-r_1r_2 & 0 & 0 \\ 0 & 0 & 0 & 0 & 4r_1-2r_2+r_1r_2 & 3l\, r_2(1-r_1) \\ 0 & 0 & 0 & 0 & 6(r_1-r_2)/l & 3r_2(2-r_1) \end{bmatrix} \tag{A.21}$$

$$\mathbf{C}_g = \frac{1}{5(4-r_1r_2)^2}\begin{bmatrix} 0 & 0 & 0 & 0 & 0 & 0 \\ 0 & 1 & 0 & 0 & 0 & 0 \\ 0 & g_{32} & g_{33} & 0 & g_{35} & g_{36} \\ 0 & 0 & 0 & 0 & 0 & 0 \\ 0 & 0 & 0 & 0 & 1 & 0 \\ 0 & 0 & 0 & 0 & g_{65} & g_{66} \end{bmatrix} \tag{A.22}$$

where

$$\begin{aligned}
g_{32} &= -g_{35} = -4(8r_1^2 r_2 - 13r_1 r_2^2 - 32r_1^2 - 8r_2^2 + 25r_1 r_2 + 20)/l \\
g_{33} &= r_1(16r_2^2 + 25r_1 r_2^2 - 96r_1 r_2 + 128r_1 - 28r_2) \\
g_{36} &= 4r_2(16r_1^2 + 5r_1^2 r_2 + 9r_1 r_2 - 28r_1 + 8r_2) \\
g_{62} &= -g_{65} = -4(8r_1 r_2^2 - 13r_1^2 r_2 - 32r_2^2 - 8r_1^2 + 25r_1 r_2 + 20)/l \\
g_{63} &= 4r_1(16r_2^2 - 5r_1 r_2^2 + 9r_1 r_2 + 8r_1 - 28r_2) \\
g_{66} &= r_2(16r_1^2 + 25r_1^2 r_2 - 96r_1 r_2 - 28r_1 + 128r_2)
\end{aligned} \tag{A.23}$$

4.12 Appendix A5 – Discrete model for a beam on 3D half-space

Matrix G

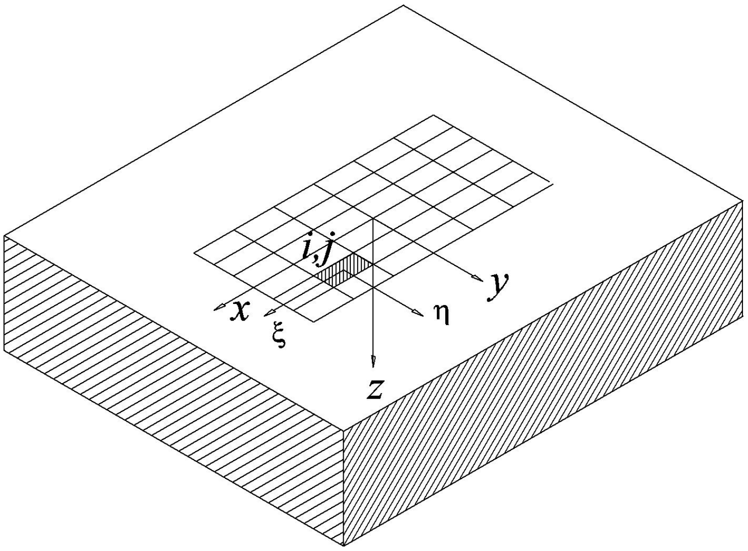

Fig. A.3 – Rectangular half-space surface, subdivided in rectangular sub-elements.

Considering a half-space surface subdivided by rectangular elements (Fig. A.3), the components of the flexibility matrix **G** of the half-space are:

$$g_{ij} = -\frac{(1-\nu_s^2)}{\pi E_s}\int_{y_i}^{y_{i+1}}\int_{x_i}^{x_{i+1}} \mathrm{d}x\,\mathrm{d}y \int_{\eta_j}^{\eta_{j+1}}\int_{\xi_j}^{\xi_{j+1}} \frac{1}{d(x,y;\xi,\eta)}\,\mathrm{d}\xi\,\mathrm{d}\eta\,. \qquad \text{(A.24)}$$

where $d = [(x-\xi)^2 + (y-\eta)^2]^{1/2}$ represents the distance from the origin of the global coordinate system of a generic point into the surface sub-element. The solution of the quadruple integral on a generic subdivision is:

$$g_{ij} = \frac{(1-\nu_s^2)}{\pi E_s}\left[\left[\left[\left[F(x,y;\xi,\eta)\right]_{\xi_j}^{\xi_{j+1}}\right]_{\eta_j}^{\eta_{j+1}}\right]_{x_i}^{x_{i+1}}\right]_{y_i}^{y_{i+1}} =$$

$$= \frac{(1-\nu_s^2)}{\pi E_s}\Bigg[\Bigg[F(x_i,y;\xi_j,\eta) - F(x_i,y;\xi_{j+1},\eta) +$$

$$-F(x_{i+1},y;\xi_j,\eta) + F(x_{i+1},y;\xi_{j+1},\eta)\Bigg]_{\eta_j}^{\eta_{j+1}}\Bigg]_{y_i}^{y_{i+1}} =$$

$$
\begin{aligned}
&=\frac{(1-\nu_s^2)}{\pi E_s}\{F(x_i,y_i;\xi_j,\eta_j)-F(x_i,y_i;\xi_{j+1},\eta_j)-F(x_{i+1},y_i;\xi_j,\eta_j)+F(x_{i+1},y_i;\xi_{j+1},\eta_j)+\\
&-[F(x_i,y_{i+1};\xi_j,\eta_j)-F(x_i,y_{i+1};\xi_{j+1},\eta_j)-F(x_{i+1},y_{i+1};\xi_j,\eta_j)+F(x_{i+1},y_{i+1};\xi_{j+1},\eta_j)]+\\
&-[F(x_i,y_i;\xi_j,\eta_{j+1})-F(x_i,y_i;\xi_{j+1},\eta_{j+1})-F(x_{i+1},y_i;\xi_j,\eta_{j+1})+F(x_{i+1},y_i;\xi_{j+1},\eta_{j+1})]+\\
&+F(x_i,y_{i+1};\xi_j,\eta_{j+1})-F(x_i,y_{i+1};\xi_{j+1},\eta_{j+1})-F(x_{i+1},y_{i+1};\xi_j,\eta_{j+1})+F(x_{i+1},y_{i+1};\xi_{j+1},\eta_{j+1})\}
\end{aligned}
\tag{A.25}
$$

where

$$F(x,\xi)=F_0(x,\xi)+F_1(x,\xi) \tag{A.26}$$

$$F_0(x,y;\xi,\eta)=\frac{d^3}{6} \tag{A.27}$$

$$F_1(x,y;\xi,\eta)=-\frac{1}{4}|x-\xi||y-\eta|\left[|y-\eta|\ln\frac{d+|x-\xi|}{d-|x-\xi|}+|x-\xi|\ln\frac{d+|y-\eta|}{d-|y-\eta|}\right]\quad \text{for } x\neq\xi,\ y\neq\eta \tag{A.28a}$$

$$F_1(x,y;\xi,\eta)=0\quad \text{for } x=\xi \quad\text{or}\quad y=\eta \tag{A.28b}$$

Matrix H

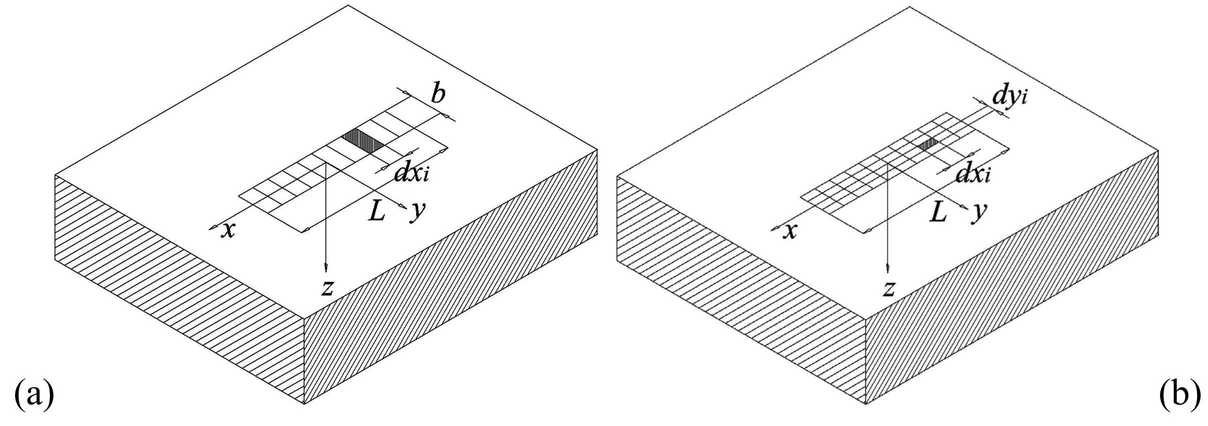

Fig. A.4 – Discretization of the contact surface between beam and half-space. One element along beam width (a), four equal elements along beam width (b).

Considering one subdivision ($ny = 1$) along beam width (Fig. A.22a), matrix **H** for the generic ith element is:

$$\mathbf{H}_i^1 = b\,[l_i/2,\ -l_i^2/12, l_i/2,\ l_i^2/12]^{\mathrm{T}}, \tag{A.29}$$

where $l_i = dx_i$.

Considering several subdivisions ny along beam width (Fig. A.22b), the generic matrix **H** is given by the following expression:

$$\mathbf{H}_i^{ny} = \begin{bmatrix} l_i/2 \\ -l_i^2/12 \\ l_i/2 \\ l_i^2/12 \end{bmatrix} \left[dy_1, dy_2, \dots dy_{ny}\right] = \begin{bmatrix} dy_1\, l_i/2 & .. & .. & dy_{ny}\, l_i/2 \\ -dy_1\, l_i^2/12 & .. & .. & -dy_{ny}\, l_i^2/12 \\ dy_1\, l_i/2 & .. & .. & dy_{ny}\, l_i/2 \\ dy_1\, l_i^2/12 & .. & .. & dy_{ny}\, l_i^2/12 \end{bmatrix}, \tag{A.30}$$

Then, adopting a power graded mesh with $\beta = 3$ and $n = 4$ and joining the subdivisions close to beam y axis, $ny = 3$ subdivisions are obtained (Fig. A.5a) and the corresponding width turn out to be:

$$dy_1 = dy_3 = b/16, \quad dy_2 = 7\,b\,/\,8. \tag{A.31}$$

For $ny = 5$ (Fig. 5b), dy_i values are:

$$dy_1 = dy_5 = b/54, \quad dy_2 = dy_4\ 7\,b\,/\,54, \quad dy_3 = 19\,b\,/\,54 \tag{A.32}$$

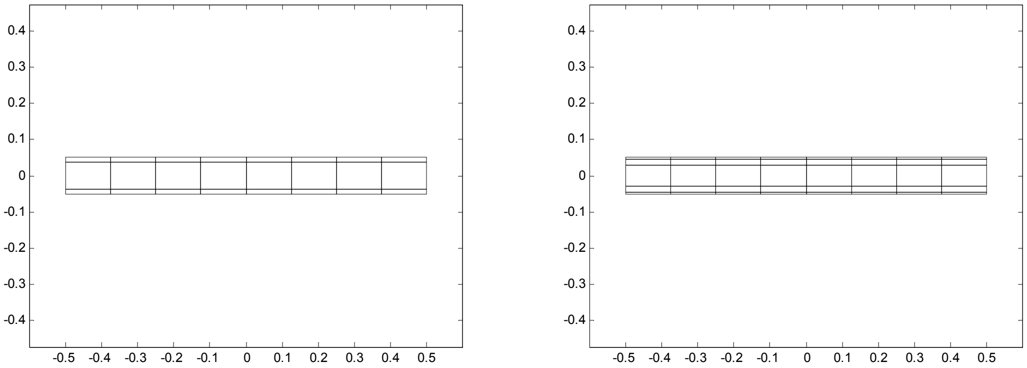

(a) (b)

Fig. A.5 – Contact surface between a foundation beam and the half-space subdivided into 8 elements along its length and 3 (a), 5 (b) elements along its width.

References

Abbas, B. A. H., Thomas, J. Dynamic stability of Timoshenko beams resting on an elastic foundation. *Journal of Sound and Vibration*. 1978; 60(1), 33-44.

Ainsworth M., McLean W., Tran T. Diagonal scaling of stiffness matrices in the Galerkin boundary element method. *The ANZIAM Jorunal*. 2000; 42(1): 141-150.

Allen HG. *Analysis and design of structural sandwich panels*. Oxford: Pergamon Press; 1969.

Amanat K. M., Enam B. Study of the semi-rigid properties of reinforced concrete beam-column joints. *Journal of Civil Engineering.* 1999; CE27 (1): 59-69.

Arboleda-Monsalve, L.G., Zapata-Medina, D.G., Aristizabal-Ochoa, D. J. Timoshenko beam-column with generalized end conditions on elastic foundation: Dynamic-stiffness matrix and load vector. *Journal of Sound and Vibration*. 2008; 310 (4-5): 1057-1079.

Argyris J. An excursion into large rotations. *Computer Methods in Applied Mechanics and Engineering*. 1982; 32: 85-155.

Aristizabal-Ochoa, D. J. Slope-deflection equations for stability and second-order analysis of Timoshenko beam-column structures with semi-rigid connections. *Engineering Structures*.2008; 30 (9): 2517-2527.

Augusti G. Mode approximations for rigid-plastic structures supported by an elastic medium. *International Journal of Solids and Structures*, 1970; 6, 809–827

Barden L. Distribution of contact pressure under foundations. *Géotechnique*. 1963; 12: 181-188.

Barsoum R. S., Gallagher R. H. Finite element analysis of torsional-flexural stability problems. *International Journal for Numerical Methods in Engineering*. 1970; 2: 335-352.

Basaga H. B., Kartal M. E., Bayraktar A. Reliability analysis of steel braced reinforced concrete frames with semi-rigid connections. *International Journal of Structural Stability and Dynamics*. 2012; 12 (5): 1-20.

Batoz JL, Dhatt G. Incremental displacement algorithms for non-linear problems. *International Journal for Numerical Methods in Engineering.* 1979; 14(8): 1262-1267

Bazant ZP, Cedolin L. *Stability of structures*. New York: Oxford University Press; 1991.

Belenkiy, L. M. Upper-Bound Solutions for Rigid-Plastic Plates and Slabs on Elastic Foundation by the Principle of Stationary Total Energy. *Journal of Structural Engineering*. 2007; 133(2), 305–307.

Bhat, S. Xirouchakis, P. Plastic Analysis of Floating Beams. *Journal of Engineering Mechanics.* 1986; 112 (2): 198–214.

Biot MA. Bending of an infinite beam on an elastic foundation. *Journal of Applied Mechanics - Transactions of the ASME* 1937; 4: A1-A7.

Bielak J., Stephan E. A modified Galerkin procedure for bending of beams on elastic foundations. *SIAM Journal on Scientific and Statistical Computing.* 1983; 4 (2): 340-352.

Blaauwendraad, J. Timoshenko beam-column buckling. Does Dario stand the test? *Engineering Structures*. 2008; 30 (11): 3389-3393.

Borodachev N. M. Contact problem for a stamp with a rectangular base. *PMM Prikladnaya Matematika i Mekhanika.* 1976; 40 (3): 554-560.

Bosakov S. V. Variational approach to the solution of a contact problem for an elastic half-plane. *International Applied Mechanics.* 1994; 30(7): 535-538.

Bosakov S. V. Solving the contact problem for a rectangular die on an elastic foundation. *International Applied Mechanics*. 2003; 39 (10): 1188-1192.

Boussinesq J. *Application des potentials à l'etude de l'équilibre et du mouvement des solides élastiques*. Gauthier Villars. Paris; 1885.

Bowles E. J. *Foundation analysis and design*. McGraw Hill 1997.

Brebbia C. A., Georgiou P. Combination of boundary and finite elements in elastostatics. *Applied Mathematical Modelling.* 1979; 3 (3): 212-220.

Brothers, P. W., Sinclair, G. B., Segedin, C. M. Uniform Indentation of the Elastic Half-Space by a Rigid Rectangular Punch. *International Journal of Solids and Structures*. 1977; 13: 1059–1072

Cerruti V. Acc. Lincei, Roma, *Mem. fis. mat*. 1882.

Chang S. P. , Kim S. B., Kim M.Y. Stability of shear deformable thin-walled space frames and circular arches. *Journal of Engineering Mechanics.* 1996; 122: 844-854.

Chen W. F., Lui E. M. *Handbook of Structural Engineering 2nd ed.* CRC press. 2005.

Cheng, F. Y., Pantelides, C. P. Static Timoshenko Beam-Columns on Elastic Media. *Journal of Structural Engineering*. 1988; 114 (5): 1152-1172.

Cheung Y. K., Nag D. K. Plates and Beams on Elastic Foundations–Linear and Non-Linear Behaviour. *Géotechnique*. 1968; 18 (2): 250 –260.

Cheung Y. K., Zienkiewicz O. C. Plates and tanks on elastic foundations - an application of finite element method. *International Journal of Solids and Structures.* 1965; 1 (4): 451-461.

Clough R., Johnston S. Effect of stiffness degradation on earthquake ductility requirements. *Transactions of Japan Earthquake Engineering Symposium*, Tokyio. 1967; 195-198.

Cortínez V. H., Piovan M. T. Stability of composite thin-walled beams with shear deformability. *Compututers & Structures*. 2006; 84: 978-990.

Cowper, G. R. The shear coefficient in Timoshenko's beam theory. *Journal of Applied Mechanics - Transactions ASME*. 1966; 33(2): 335–340.

Criesfield M. A. *Non-linear finite element analysis of solid and structures, volume 2: advanced topics*. Wiley: Chichester, 1991.

Dauge M. Elliptic boundary value problems on corner domains. *Lecture Notes in Mathematics.* Springer-Verlag. 1988.

Davies JM. *Lightweight sandwich construction*. Oxford: Blackwell Science; 2001.

Dempsey J. P., Li H. A rigid rectangular footing on an elastic layer. Technical note. *Geotechnique*. 1989; 39 (1): 147-152.

Erwin V. J., Stephan E. P., El-Seoud A. S. An improved boundary element method for the charge density of a thin electrified plate in R^3. *Mathematical Methods in the Applied Sciences.* 1990; 13: 291-303.

Erwin V. J., Stephan E. P. Adaptive approximations for 3-D electrostatic plate problems. *Advances in Engineering Software*. 1992; 15: 211-215.

FIB Féd. Int. du Béton. *Structural concrete. Textbook on behaviour, design and performance: updated knowledge of the CEB/FIP Model Code* 1990, Vol. 3. 1999.

Filippou F. C., Popov E. P., Bertero V. V. Modeling of R/C joints under cyclic excitations. *Journal of Structural Engineering ASCE*. 1983; 109 (11): 2666-2684.

Frangi A., Novati G., Springhetti R., Rovizzi M. 3D fracture analysis by the symmetric Galerkin BEM. *Computational Mechanics*. 2002; 28, (220-232).

Frangi A., Novati G., BEM-FEM coupling for 3D fracture mechanics applications. *Computational Mechanics*. 2003; 32: 415-422.

Gallagher A P. *Buckling of a beam under axial compression with elastic support. Studies in Numerical Analysis*, Scaife, B. K. P., Academic Press, London and New York, 1974.

Giberson, M. F. Two Nonlinear beams with definition of ductility. *Journal of the Structural Division*. 1969; 95, ST7.

Giroud J. P. Settlement of an embankment resting on a semi-infinite elastic soil. *Highway Research Record*. 1968; 223: 18-35.

Graham I. G., McLean W. Anisotropic mesh refinement: the conditioning of Galerkin boundary element matrices and simple preconditioners. *Journal on Numerical Analysis.* 2006; 44(4): 1487-1513.

Gonzalez J. A., Park K. C., Felippa C. A. FEM and BEM coupling in elastostatics using localized Lagrange multipliers. *International Journal for Numerical Methods in Engineering.* 2007; 69 (10): 2058-2074.

Goodier JN, Hsu CS. Nonsinusoidal buckling modes of sandwich plates. *Journal of Aeronautical Science.* 1954; 21: 525-532.

Gorbunov-Posadov M. I., Serebrjanyi R. V. Design of structures on elastic foundations. *Proceedings 5th International Conference in Soil Mechanics and Foundation Engineering.* 1961; 1: 643-648.

Gough GS, Elam CF, de Bruyne NA. The stabilisation of a thin sheet by a continuous supporting medium. *Journal of the Royal Aeronautical Society* 1940; 44: 12-43.

Guarracino F., Minutolo V., Nunziante L. A simple analysis of soil-structure interaction by BEM-FEM coupling. *Engineering Analysis with Boundary Elements*. 1992; 10 (4): 283-289.

Guzina B. B., Pak R. Y. S., Martínez-Castro A. E. Singular boundary elements for three-dimensional elasticity problems. *Engineering Analysis with Boundary Elements*. 2006, 30: 623-639.

Hasan R., Xu L., Grierson D. E., Push-over analysis for performance based-seismic design. *Computers & Structures.* 2002; 80, 2483-2493.

Hetenyi M. *Beam on elastic foundation*. Ann Arbor: The University of Michigan Press; 1946.

Hlaváček, I. Buckling of a Timoshenko beam on elastic foundation with uncertain input data. *IMA Journal of Applied Mathematics.* 2003; 68 (2): 185–204.

Ibrahimbegović A. On FE implementation of geometrically nonlinear Reissner's beam theory: three-dimensional curved beam elements. *Computer Methods in Applied Mechanics and Engineering.* 1993; 122: 11-26.

Johnson KL. *Contact Mechanics*, Cambridge: Cambridge University Press; 1985.

Kerr A D. The stress and the stability analyses of railroad tracks. *Journal of Applied mechanics* 1974; 41(4): 841-848.

Kerr A D. Analysis of thermal track buckling in the lateral plane. *Acta Mechanica*1978; 30: 17-50.

Kerr A D. Analysis of concrete pavement blowups. *Acta Mechanica.* 1984; 52: 201-224.

Kerr A D. Response of floating ice beams and plates with partial flooding. *Proceedings 1st International Conference on Ice Technology*, Cambridge. 1986. 75-86.

Kikuchi N. Beam bending problems on a Pasternak foundation using reciprocal variational-inequalities. *Quarterly of Applied Mathematics.* 1980; 38 (1): 91-108.

Kim M-Y, Chang S-P and Kim S-B. Spatial stability analysis of thin-walled space frames. *International Journal for Numerical Methods in Engineering*. 1996; 39: 499-525.

Kim N. I. , Kim M. Y. Exact dynamic/static stiffness matrices of non-symmetric thin-walled beams considering coupled shear deformation effects. *Thin-Walled Structures*. 2005; 43: 701-734.

Kosmatka, J. B. An improved two-node finite element for stability and natural frequencies of axial-loaded Timoshenko beams. *Computer & Structures*. 1995; 57 (1): 141-149.

Lai S., Will G., Otani S. Model for inelastic biaxial bending of concrete members. *Journal of Structural Engineering*. 1984; 110, ST11: 2563-2584.

Laudiero F and Zaccaria D. A consistent approach to linear stability of thin-walled beams of open section. *International Journal of Mechanical Sciences*. 1988; 30: 503-515.

Lee I. K. Elastic settlements in footings with a rough interface. *Proceedings 4th Australia New Zealand Conference of Soil Mechanics and Foundation Engineering*. 1963; 225.

Love A. E. H. The Stress Produced in a Semi-Infinite Solid by Pressure on Part of the Boundary. *Philosophical Transactions of the Royal Society of London*. 1929 228 659-669 377-420.

Leung K. L., Zavareh P. B., Beskos D. E. 2-D elastostatic analysis by a symmetrical BEM/FEM scheme. *Engineering Analysis with Boundary Elements* 1995; 15 (1): 67-78.

Ley R P, Lin W, Mbanefo U. *Facesheet wrinkling in sandwich structures*. CR-1999-208994; Virginia: NASA; 1999.

Maier G., Novati G. Boundary element elastic analysis of layered soils by a successive stiffness method. *International Journal for Numerical and Analytical Methods in Geomechanics*. 1987; 11 (5): 435–447

Mendonca A. V., Paiva J. B. An elastostatic FEM/BEM analysis of vertically loaded raft and piled raft foundation. *Engineering Analysis with Boundary Elements* 2003; 27 (9): 919-933.

Meyerhof G. G. Load carrying capacity of concrete pavements. *Journal of the Soil Mechanics and Foundations Division*. 1962; 88 (SM3): 89–115.

Minghini, F., Tullini, N., Laudiero, F. Locking-free finite elements for shear deformable orthotropic thin-walled beams. *International Journal for the Numerical Methods in Engineering.* 2007; 72 (7): 808–834.

Minghini F., Tullini N., Laudiero F. Buckling analysis of FRP pultruded frames using locking-free finite elements. *Thin-walled Structures*. 2008; 43: 223-241.

Monfortoon G. R., Wu T. S., Matrix analysis of semi-rigidly connected steel frames. *Journal of the Structural Division*. 1963; 89 (6) 13-42

Mukherjee S., Reddy J. N., Krishnamoorthy C. S. Convergence properties and derivative extraction of the superconvergent Timoshenko beam finite element. *Computer Methods in Applied Mechanics and Engineering*. 2001; 190: 3475-3500.

Mullan S. J., Sinclair G. B., Brothers P. W. Stresses for an elastic half-space uniformly indented by a rigid rectangular footing. *International Journal for Numerical and Analytical Methods in Geomechanics*. 1980; 4 (3): 277-284.

Murthy G K N. *Buckling of continuously supported beams*. Ph.D. thesis, School of Engineering and Science, New York University, New York; July 1970.

Murthy G K N. Buckling of beams supported by Pasternak Foundation. *Journal of the Engineering Mechanics Division* 1973a; 99 (3): 565-579.

Murthy G K N. Buckling of continuously supported beams. *Journal of Applied Mechanics* 1973b; 50 (2): 546-551.

Muskhelishvili N I. *Some basic problems of the mathematical theory of elasticity*. Noordhoff, Groningen; 1963.

Naraynaswami, R., Aldeman, H. M. Inclusion of transverse shear deformation in finite element displacement formulations. *AIAA Journal.* 1974; 12 (11): 1613-1614.

Noble B. The numerical solution of the singular integral equation for charge distribution on a flat rectangular lamina. *Symposium on numerical treatment of ordinary differential equations and integral integro-differential equations*. 1960; 530-543.

Otani S. Inelastic analysis of R/C frame structures. *Journal of the Structural Division*. 1974; 100, ST7.

Pais, A. Kausel E. Approximate formulas for dynamic stiffnesses of rigid foundations. *Soil Dynamic & Earthquake Engineering*. 1988; 7 (4), 213-227.

Pasternak P. L. On a new method of analysis of an elastic foundation by means of two foundation constants. (in Russian), *Gosudarstvennogo Izatelstvo Literaturi po Stroitelstvu i Architakutre*, Moscow, U.S.S.R., 1954.

Piovan M. T., Cortínez V. H. Mechanics of shear deformable thin-walled beams made of composite materials. *Thin-Walled Structures*. 2007; 45: 37-62.

Prager W (1927). Zur Theorie elastische gelagerter Konstruktionen. *ZAMM - Zeitschrift für Angewandte Mathematik und Mechanik.* 1927; 7(5): 354-360.

Przemieniecki, J. S. *Theory of matrix structural analysis*. McGraw Hill, New York. 1988.

Rajapakse R. K. N. D., Selvadurai A. P. S. On the performance of Mindlin plate elements in modelling plate-elastic medium interaction: A comparative study. *International Journal for Numerical Methods in Engineering*. 1986; 23 (7): 1229-1244.

Rao, K. Singh, S. Concentrated Load-Carrying Capacity of Concrete Slabs on Ground. *Journal of Structural Engineering*. 1986; 112 (12): 2628–2645.

Ratzersdorfer J. *Die Knickfestigkeit von Staben und Stabwerken*. J. Springer. Wien; 1936.

Rayleigh J. W. *Theory of Sound*. Dover Publications, New York. 1929.

Reddy, J. N. On locking-free shear deformable beam finite elements. *Computer Methods in Applied Mechanics and Engineering*. 1997; 149 (1-4): 113-132.

Reddy J. N. *An Introduction to the Finite Element Method* (3rd Ed.). Singapore; McGraw Hill; 2006.

Reissner M. E. On the theory of beams resting on a yielding foundation. *Proceedings of the National Academy of Sciences of the United States of America* 1937; 23(6): 328-333.

Reissner M. E. On non-uniform torsion of cylindrical rods. *Journal of Mathematics and Physics*. 1952; 31: 214-221.

Ruta, G. C., and Elishakoff, I. Buckling of a column on a Wieghardt foundation. *ZAMM - Zeitschrift für Angewandte Mathematik und Mechanik*. 2006; 86(8): 617-627.

Rvachev V. L. The pressure on an elastic half-space of a stamp with a wedge-shaped planform. *PMM Prikladnaya Matematika i Mekhanika*. 1959; 23 (1): 169-171.

Sadowsky M. Zweidimensionale Probleme der Elastizitatstheorie. *ZAMM - Zeitschrift für Angewandte Mathematik und Mechanik.* 1928; 8(2): 107-121.

Sapountzakis, E. J., and Kampitsis, A. E. Nonlinear dynamic analysis of Timoshenko beam-columns partially supported on tensionless Winkler foundation. *Computers & Structures*. 2010; 88 (21-22): 1206-1219.

Sapountzakis, E. J., and Kampitsis, A. E. Nonlinear analysis of shear deformable beam-columns partially supported on tensionless three-parameter foundation. *Archive of Applied Mechanics.* 2011; 81(12): 1833-1851.

Sapountzakis, E. J., and Kampitsis, A. E. Nonlinear dynamic analysis of shear deformable beam-columns on nonlinear 3-parameter viscoelastic foundation. Part I: Theory and numerical implementation. *Journal of Engineering Mechanics*. 2012, dx.doi.org/10.1061/(ASCE)EM.1943-7889.0000369

Selvadurai A. P. S., *Elastic analysis of soil-foundation interaction*. Elsevier. Amsterdam; 1979.

Shakourzadeh H., Guo Y. Q., Batoz J. L. Modelling of connections in the analyses of thin-walled space frames. *Computers & Structures*. 1999; 71, 423-433.

Shield TW, Kim KS, Shield RT. The buckling of an elastic layer bonded to an elastic substrate in plane strain. *Journal of Applied Mechanics - Transactions of the ASME* 1994; 61: 231-235.

Simitses G. J. *An introduction to elastic stability of structures*. Englewood Cliffs: Prentice-Hall; 1976.

Simo J.C. and Vu-Quoc L. A geometrically-exact rod model incorporating shear and torsion-warping deformation. *International Journal of Solids and Structures*. 1991; 27: 371-393.

Smith T. E. Buckling of a beam on a Wieghardt-type elastic foundation. *ZAMM - Zeitschrift für Angewandte Mathematik und Mechanik.* 1969; 49(11): 641-645.

Springhetti R., Novati G., Margonari M. Weak coupling of the symmetric Galerkin BEM with FEM for potential and elastostatic problems. *CMES-Computer Modeling in Engineering & Sciences* 2006; 13 (1): 67-80.

Stafford C. M, et al. A buckling-based metrology for measuring the elastic moduli of polymeric thin films. *Nature Materials.* 2004; 3(8): 545-550.

Takeda T., Sozen M. A., Nielsen N. Reinforced concrete response to simulated earthquakes. *Journal of Structural Engineering*. 1970; 96, ST12: 2557-2573.

Timoshenko S. P., Gere J. M. *Theory of elastic stability*. New York: McGraw-Hill; 1961.

Timoshenko S. P., Goodier J. N. *Theory of elasticity*. New York: McGraw-Hill; 1951.

Tullini N., Tralli A. Static analysis of Timoshenko beam resting on elastic half-plane based on coupling of locking-free elements and boundary integral. *Computational Mechanics.* 2010; 45(2-3): 211-225.

Tullini N., Tralli A., Lanzoni L. Interfacial shear stress analysis of bar and thin film bonded to 2D elastic substrate using a coupled FE-BIE method. *Finite Elements in Analysis and Design*. 2012a; 55: 42-51.

Tullini, N., Tralli, A., Baraldi, D. Buckling of Timoshenko Beams in Frictionless Contact with an Elastic Half-Plane. *Journal of Engineering Mechanics*. 2012b; doi: 10.1061/(ASCE)EM.1943-7889.0000529.

Tullini N., Tralli A., Baraldi D. Stability of slender beams and frames resting on 2D half-space. *Archive of Applied Mechanics*. 2013; 83 (3): 467-482.

Vesic A. B. Bending of beams resting on isotropic elastic solid. *Journal of Engineering Mechanics Division.* 1961; 87(EM2): 35-53.

Vlasov Z. Z. Thin-Walled Elastic Beams. *Israel Program for Scientific Translations*. Jerusalem, 1961.

Vlasov V. Z., Leonitiev U. N. Beams, plates and shells on elastic foundations. *Israel program for scientific translations.* Jerusalem, 1966.

Volynskii A. L., Bazhenov S, Lebedeva O. V., Bakeev N. F. Mechanical buckling instability of thin coatings deposited on soft polymer substrates. *Journal of Materials Science.* 2000; 35: 547-554.

Wang C. M., Xiang Y., Kitipornchai S. Buckling of restrained columns with shear deformation and axial shortening. *Journal of Engineering Mechanics*. 1991; 117 (9): 1973-1989.

Wang C. M., Wang C. Y., Reddy J.N. *Exact Solutions for Buckling of Structural Members*. CRC Press; 2005.

Wang C.Y. Buckling of a weakened infinite beam on an Elastic Foundation. *Journal of Engineering Mechanics.* 2010; 136 (4): 534-537.

Whitman R. V., Richart F. E. Design procedures for dynamically loaded foundations. *Journal of the Soil Mechanics and Foundations Division*. 1967; 93 (SM6): 169-191.

Wieghardt K. Über den Balken auf nachgiebiger Unterlage. *ZAMM - Zeitschrift für Angewandte Mathematik und Mechanik.* 1922; 2(3): 165-184.

Winkler, E. *Die Lehre Von Elasticitaet Und Festigkeit*. 1st Ed., H. Dominicus, Prague; 1867.

Xu L. Geometric stiffness and sensitivity matrices for optimization of semirigid steel frameworks. *Structural Optimization*. 1992; 5 (1-2): 95-99.

Yankelewsky D. Z., Eisenberger M. Analysis of a beam column on elastic foundation. *Computers & Structures* 1986; 23(3): 351-356.

Yokoyama T. Parametric instability of Timoshenko beams resting on an elastic foundation. *Computers & Structures*. 1988; 28 (2), 207-216.

Zenkert, D. An *introduction to sandwich construction*. Emas Publ. 1997, London.